



Thèse

2021

Open Access

This version of the publication is provided by the author(s) and made available in accordance with the copyright holder(s).

---

## Rare earth quantum memories: spectroscopy of a new platform and quantum storage implementations

---

Ortu, Antonio

### How to cite

ORTU, Antonio. Rare earth quantum memories: spectroscopy of a new platform and quantum storage implementations. Doctoral Thesis, 2021. doi: 10.13097/archive-ouverte/unige:158720

This publication URL: <https://archive-ouverte.unige.ch/unige:158720>

Publication DOI: [10.13097/archive-ouverte/unige:158720](https://doi.org/10.13097/archive-ouverte/unige:158720)

UNIVERSITÉ DE GENÈVE  
Département de Physique Appliquée

FACULTÉ DES SCIENCES  
MER Mikael Afzelius

---

RARE EARTH QUANTUM MEMORIES: SPECTROSCOPY OF  
A NEW PLATFORM AND QUANTUM STORAGE  
IMPLEMENTATIONS

THÈSE

Présentée à la Faculté des sciences de l'Université de Genève  
Pour obtenir le grade de Docteur ès sciences, mention Physique

par  
**Antonio Ortu**  
d'Italie

Thèse N° 5627

GENÈVE  
2021



**UNIVERSITÉ  
DE GENÈVE**

**FACULTÉ DES SCIENCES**

**DOCTORAT ÈS SCIENCES, MENTION PHYSIQUE**

**Thèse de Monsieur Antonio ORTU**

intitulée :

**«Rare Earth Quantum Memories: Spectroscopy of  
a New Platform and Quantum Storage  
Implementations»**

La Faculté des sciences, sur le préavis de Monsieur M. AFZELIUS, docteur et directeur de thèse (Groupe de physique appliquée), Monsieur H. ZBINDEN, professeur associé (Département de physique appliquée), Monsieur C. GALLAND, professeur (Laboratory of Quantum and Nano-Optics, École Polytechnique Fédérale de Lausanne, Lausanne), Madame M. MAZZERA, professeure (Institute of Photonics and Quantum Sciences, Heriot-Watt University, Edinburgh, United Kingdom), autorise l'impression de la présente thèse, sans exprimer d'opinion sur les propositions qui y sont énoncées.

Genève, le 22 décembre 2021

**Thèse - 5627 -**

**Le Doyen**

# Résumé de la thèse

D'un point de vue technologique, le mot *mémoire* fait en général référence aux composants électroniques permettant le stockage de l'information numérique. Des efforts considérables en recherche fondamentale et appliquée sur ces composants ont permis la manipulation de quantité de données très importante tout en réduisant leur taille, ce qui a accompagné l'augmentation de la qualité des images numériques, de la vitesse de calcul des processus et le développement du "big data".

La mécanique quantique permet d'envisager un nouveau type d'information basé sur l'utilisation de *qubit*. Nous sommes aujourd'hui au début du développement technologique en vue de manipuler et stocker ces qubits. Encoder cette information sur un photon est un bon moyen pour transmettre l'information quantique comme cela se fait déjà pour l'information classique via les réseaux de fibre optique. Utiliser les propriétés quantiques des photons aurait l'avantage de permettre des communications sécurisées de manière inconditionnelle. En revanche, il est plus difficile de préserver cette information sur de longues distances.

Une façon de prévenir ces pertes d'informations est d'implémenter des *répéteur quantiques* pour diviser un canal de communication trop long en canaux plus courts. Pour fonctionner, le répéteur repose sur des mémoires quantiques capables de stocker les états quantiques le temps nécessaire à la synchronisation des nœuds du réseau.

Au cours de mon travail doctoral, je me suis occupé de deux plateformes particulièrement prometteuses pour l'implémentation de mémoires quantiques, basées sur des ions de terre rares dans une matrice cristalline. Dans une première phase, nous avons réalisé une étude spectroscopique du Yb:YSO. Le matériau est intéressant pour sa structure hyperfine qui permet d'interfacer des photons très large spectralement. Les photons utilisés peuvent donc être très courts temporellement, ce qui permet l'augmentation du taux de répétitions du répéteur.

Après avoir caractérisé l'interaction hyperfine en présence d'un champ magnétique compris entre 0 et quelques centaines de milli-Tesla, nous avons découvert qu'à champ nul, toutes les transitions optiques et micro-ondes sont des transitions d'horloge : les énergies des états de spin résultant d'une hybridation des spins nucléaires et de spins électroniques sont insensibles au premier ordre aux fluctuations du champ magnétique ce qui permet d'obtenir des temps de co-

hérence allant jusqu'à la milliseconde. Les résultats sont prometteurs quant au stockage de l'information quantique sur de longues durées. De plus, ce matériau permet aussi d'interfacer des systèmes opérants dans le domaine micro-onde comme les qubits supraconducteurs.

La deuxième partie de ce travail a été dédiée à l'Eu:YSO, matériau déjà très populaire pour les longs temps de cohérence et de stockage qu'il permet d'obtenir. Nous avons réalisé plusieurs améliorations techniques qui ont permis l'augmentation de l'efficacité et du temps de stockage d'un protocole de mémoire quantique en utilisant les niveaux de spin. Nous avons aussi montré que notre mémoire est capable de stocker des impulsions optiques avec un bruit suffisamment bas pour permettre l'écriture, la préservation et la lecture d'un qubit temporel après une dizaine de millisecondes. Enfin, nous avons mesuré des corrélations quantiques entre deux photons générés à 20 ms d'intervalle par la même mémoire ce qui permet d'envisager la réalisation de répéteurs quantiques basés sur l'intrication.

En résumé, le travail présenté ici montre l'importance de la recherche fondamentale sur ces matériaux impliquant des ions de terres rares qui révèlent souvent des propriétés inattendues et utiles aux nouvelles technologies quantiques. Ainsi, les mémoires quantiques sont encore loin d'avoir atteint leurs limites fondamentales, et avec des efforts techniques on continue de les rapprocher aux performances nécessaires pour devenir des dispositifs utiles.

Thank you,

my supervisor Mikael Afzelius, for having welcomed me in the group and for your constant presence, support and help in everything that involved my work in Geneva;

Alexey Tiranov and Jean Etesse, for having been my everyday reference and inspiration in the lab as great postdocs;

all the people of GAP, for making it a great place to work and having fun in;

Kasia and my family, for always being there.



# Contents

<b>1</b>	<b>Introduction: quantum memories and communication</b>	<b>1</b>
1.1	Rare earth ions in solid state crystals . . . . .	3
1.2	Inhomogeneous broadening . . . . .	4
1.3	Storage protocols for ensembles . . . . .	6
1.4	A repeater of entanglement . . . . .	7
1.5	Thesis outline . . . . .	9
<b>2</b>	<b>Yb:YSO - Introduction</b>	<b>11</b>
2.1	Properties of ytterbium in yttrium orthosilicate . . . . .	12
2.2	Experimental setup . . . . .	14
<b>3</b>	<b>Low magnetic field spectroscopy of Yb:YSO</b>	<b>17</b>
3.1	Spectroscopic techniques . . . . .	19
3.2	Spectroscopy results . . . . .	20
3.3	Conclusion . . . . .	26
<b>4</b>	<b>Coherence dynamics of Yb at low field</b>	<b>29</b>
4.1	Zero field clock transitions (ZEFOZ) . . . . .	29
4.2	Near-ZEFOZ . . . . .	31
4.3	Coherence dynamics techniques . . . . .	32
4.4	Coherence results . . . . .	33
4.5	Conclusions and outlook . . . . .	38
<b>5</b>	<b>Eu:YSO - introduction</b>	<b>41</b>
5.1	Properties of europium in yttrium orthosilicate . . . . .	42
5.2	Experimental setup . . . . .	44
5.2.1	Frequency filtering through Eu:YSO crystals . . . . .	48
<b>6</b>	<b>The atomic frequency comb</b>	<b>51</b>
6.1	Introduction . . . . .	51
6.2	Practical implementation and improvements . . . . .	53
6.2.1	New crystal . . . . .	54
6.2.2	New reference cavity . . . . .	55
6.2.3	Vibration attenuation . . . . .	55



6.2.4	Beam geometry considerations . . . . .	57
6.3	Updated AFC . . . . .	57
6.4	Photon echoes and homogeneous linewidth . . . . .	60
6.5	Multimodality . . . . .	63
6.6	Conclusions and outlook . . . . .	64
<b>7</b>	<b>The spin transition</b>	<b>67</b>
7.1	Spin-wave storage, rephasing and dynamical decoupling . . . . .	67
7.2	Spin resonance . . . . .	72
7.3	The resonator circuit . . . . .	73
7.4	Population error estimation and Rabi frequency . . . . .	77
7.5	Effects of a controlled low magnetic field . . . . .	79
7.6	Spin-wave storage with bright pulses . . . . .	80
7.7	Conclusion . . . . .	84
<b>8</b>	<b>Single photon-level experiments</b>	<b>85</b>
8.1	Multimode spin-wave storage . . . . .	85
8.2	Time-bin qubit storage . . . . .	88
8.3	AFC-DLCZ . . . . .	91
8.3.1	Introduction . . . . .	91
8.3.2	AFC-DLCZ implementation . . . . .	94
8.3.3	Results . . . . .	99
8.4	Eu:YSO - Conclusion . . . . .	101
	<b>Conclusions and outlook</b>	<b>103</b>
<b>A</b>	<b>List of publications</b>	<b>107</b>
A.1	Paper I: Simultaneous coherence enhancement of optical and microwave transitions in solid-state electronic spins . . . . .	108
A.2	Paper II: Spectroscopic study of hyperfine properties in $^{171}\text{Yb}^{3+}:\text{Y}_2\text{SiO}_5$ . . . . .	118
A.3	Paper III: Optical and spin manipulation of non-Kramers rare-earth ions in a weak magnetic field for quantum memory applications . . . . .	131
A.4	Paper IV: Storage of photonic time bin qubits up to 20 ms in a rare-earth doped crystal . . . . .	151
A.5	Paper V: Multimode capacity of atomic frequency comb quantum memories . . . . .	165
	<b>Bibliography</b>	<b>203</b>

# Introduction: quantum memories and communication

Memory, in its most general meaning, is the ability of a system to *store*, *retain* and *recall* information over time. When used in general speech, it makes us think of the thoughts and experiences that we humans and animals can remember, as they are tucked in some way in our brains, involving electrical configurations of neurons and their network patterns. But also micro-organisms, plants, and inorganic systems can have a memory, as long as they display a behavior described by the three magic words highlighted above. In all these examples, information storage boils down to changing the initial *state* of some inner components of the system, given an external stimulus, from which they can recover after some time. Put in this way, the concept of memory seems quite ubiquitous and not very special after all. However, often memory systems are quite specialized in storing specific types of information and not others.

For instance, we learned quite well how to store the *bits* used in every digital device and transmission over the Internet, basically encoded as two states (labeled typically 0 and 1). Tailored for this type of information, we made devices such as hard disks, RAM modules, DVDs and so on. Normally, 0 and 1 states correspond here to localized magnetized areas, electrical currents or microscopic deformations in a metallic surface.

Then we got quantum information. In quantum mechanics, particles can assume *coherent superpositions* and *entangled states*. For instance, a state analogous to the 0 and 1 of classical bits can be stored in an atom by setting it into its lowest energy state and a higher, excited state, respectively. In addition, the atom can assume a superposition, which in mathematical notation we write as a vector  $\alpha|0\rangle + \beta|1\rangle$ , with specific coefficients  $\alpha$  and  $\beta$  indicating the relative orientation in analogy to a tridimensional space (figure 1.1). This is the quantum version of a bit, namely a *qubit*. With two particles  $a$  and  $b$ , entangled states can be achieved when the state of one particle is always correlated to a specific state of the other one, as in  $\alpha|0\rangle_a|0\rangle_b + \beta|1\rangle_a|1\rangle_b$ . All these states can be obtained by controlling

atoms with external electromagnetic fields, in particular coherent light as the one generated by a laser.

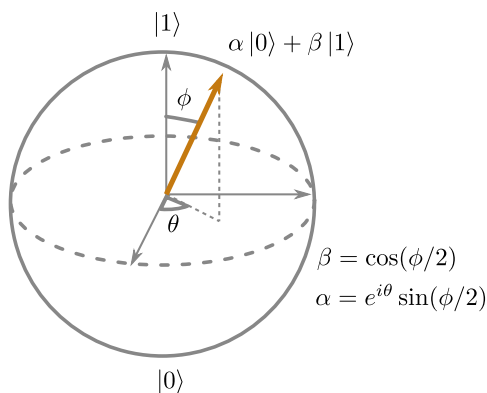


Figure 1.1: A qubit can be represented as a vector in the *Bloch sphere*. Here, the  $|0\rangle$  and  $|1\rangle$  states correspond to the poles.

These peculiar states are a promising resource to store information for specific applications. In computing, for instance, huge boosts in computational speed are enabled by the increase of the number of states that even a few particles can be set in<sup>1,2</sup>. In communication, quantum states allow to confirm that an eavesdropper is not intercepting information shared in a secured channel<sup>3,4</sup>.

However, information encoded in such states is very fragile. As the few particles we might have chosen to store information in will still interact with their surrounding environment, they will superpose and en-

tangle with many other particles, mixing their states in a much broader system that we cannot control, and eventually making the recall of that information practically impossible. From the point of view of the initial few particles, we say they experience *decoherence*. Various techniques are being continuously developed and improved to counteract decoherence, which often involve lowering the temperature of the system to a few Kelvin, putting it in deep vacuum and isolating it from vibrations and uncontrolled electromagnetic fields.

Given the difficulty in preventing decoherence, for now quantum memories can store quantum information for fractions of a second, which however is long from the point of view of the fastest particles out there: photons. Given their ultimate traveling speed, photons are an ideal carrier of information, and they have been employed already for centuries as radio waves and for decades in optical frequencies in data transmission over long distances. Optical fiber networks are widely used over the world to carry 0s and 1s through the Internet, in the so-called *telecom* band at about  $1.5\ \mu\text{m}$  of wavelength.

For this reason, there is an ongoing effort dedicated to exploiting the full features of the quantum states of photons for communication purposes. In particular, the very fragility of quantum states can be used, together with the no-cloning theorem<sup>5</sup>, to secure communication channels by alerting the users when an eavesdropper is intercepting their transmissions<sup>3,4</sup>. However, at distances beyond hundreds of kilometers, quantum-secured communication rates become impracticable due to the exponential losses over length characteristic of even the best optical fibers<sup>6-8</sup>. In classical communication, the problem is overcome by simply amplifying the signal in repeaters, but this cannot be done with quantum states, for the same no-cloning theorem mentioned above. Here is where quantum mem-

ories enter the game, as they can be used in networks as buffers in the quantum version of a repeater node<sup>9–11</sup>.

The atomic systems typically used for this application will need to have specific properties that define their performance as storage devices. First of all, they will need to interface with photons, though in most cases additional frequency conversion techniques will be needed in case the specific atoms used do not have a telecom transition. Their internal degrees of freedom should also include states with *long lifetimes* and allow the *preservation of coherence* information for some time. A certain *bandwidth* is also required to interface with short optical pulses in order to enable higher communication rates, and hence a wide separation between the optical level transitions, and all this needs to come with a good *efficiency*, so that the probability of recalling a previously stored state is as close to one as possible. Specifically for quantum states, the *fidelity* measures how close a recalled state is to its previous input. Finally, an additional desirable feature is a *multi-mode capacity*, that is the possibility of storing simultaneously more than one state. Finding a system with a good performance in all these factors is, however, still a challenge.

A variety of platforms have been proposed and still being improved for memories in quantum communication<sup>11,12</sup>, often with different strengths and weaknesses. Atoms and ions can be used as single units, allowing a high degree of control. Examples include trapped ions<sup>13,14</sup>, neutral atoms in cavities<sup>15</sup> and nitrogen- and silicon- vacancy centers in diamond<sup>16,17</sup>. Atoms can also be collectively interfaced as ensembles. Clouds of alkaline atoms like rubidium or cesium can be employed in warm clouds<sup>18,19</sup> and in magneto-optical traps<sup>20–22</sup> and typically offer a strong light absorption. Solid state materials can work as "natural traps" for optical centers and emitters, enabling also a high level of engineering of artificial structures with atom-like behavior, such as quantum dots<sup>23</sup> and optomechanical resonators<sup>24</sup>.

In this work, we will focus on yet another family of ensembles: rare earth ions in a solid state host.

## 1.1 Rare earth ions in solid state crystals

Rare earth optical centers have been explored since the 60s<sup>25</sup>, as it became quickly evident that when embedded into certain host crystals and cooled down to few Kelvin, they presented properties close to the ones of single, isolated atoms. The main reason for this is that their optical transitions are internal to their incomplete  $4f$  electronic shell, which is relatively screened out from external perturbations by complete shells with higher orbital radii. As the techniques of investigation progressed, part of the research community started focusing on the rare earth species that displayed particular features that could be used one day for applications. A typical example is erbium, which is the only rare earth

with a relatively long lived optical transition at exactly the wavelength used in telecommunications, namely 1550 nm. In particular for coherence preservation, praseodymium and europium were identified quite early as promising, thanks to their spin levels relatively insensitive to environmental perturbations. Other popular elements included neodymium, holmium and thulium, though at first they did not display such striking properties as the ones mentioned above.

These examples have their weak points: even at a few Kelvin, the ground states of erbium have population lifetimes easily perturbed by the lattice, unless the temperature is lowered to the order of millikelvin and an oriented bias field of few Tesla is applied<sup>26</sup>. Praseodymium and europium would require additional frequency conversion systems to be used in communication networks<sup>27–29</sup>, as their most useful transitions are at 606 nm and 580 nm respectively. Moreover, their insensitivity to magnetic fields makes them also slower if their spin transitions needs to be addressed directly, as in many forms of coherence extension, and their low nuclear state splittings limit their bandwidth. The exploration of different host crystals helped attenuate some of these drawbacks. Yttrium orthosilicate ( $\text{Y}_2\text{SiO}_5$ ) became one of the most popular, as its components exhibit relatively low magnetic moments (yttrium has the highest among them). In any case, it became clear quite quickly that finding a rare earth and a host crystal with all the good properties combined would be a big challenge.

This is why the search for new materials and the need for fundamental spectroscopy is still very important. The first part of my doctoral work focused on a more detailed characterization of a relatively unexplored material,  $^{171}\text{Yb}^{3+}:\text{Y}_2\text{SiO}_5$ . The second part will instead report the work done on  $^{151}\text{Eu}^{3+}:\text{Y}_2\text{SiO}_5$ , a material relatively more known and on which several memory protocols had already been tested.

## 1.2 Inhomogeneous broadening

An common feature of atomic ensembles is the *inhomogeneous broadening*, that is an enlarged frequency width observed in energy transitions. In solid state media, the effect originates in variations of the local field to which the optical centers are subjected when spread over the crystalline lattice. This produces a variation of the energy levels along a distribution, which appears continuous when the ensemble is composed of billions of atoms (figure 1.2a). The inhomogeneous broadening is an important resource in bandwidth, as it allows an interface over a broad range of frequency, but it is also a source of dephasing for the atoms involved in a storage process. However, thanks to the long-lived ground states of rare earth ions, the inhomogeneous broadening can be controlled to some degree.

For this purpose, most techniques involve *optical pumping* or *spectral hole burning* procedures<sup>30</sup> (see figure 1.3), which is based on applying a strong laser pulse over an optical transition in order to excite a portion of atoms in a ground

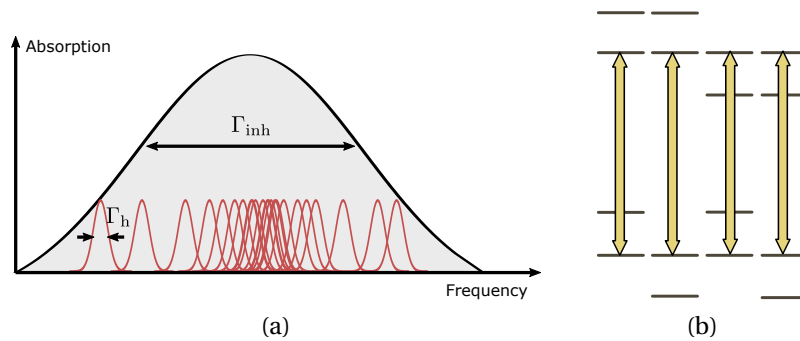


Figure 1.2: (a) Sketch of the formation of inhomogeneous broadening (gray area), of width  $\Gamma_{inh}$ , from the sum of the contributions of many atoms with different transitions distributed over the ensemble, with homogeneous linewidth  $\Gamma_h$  (red curves). (b) Example of the effect of one optical transition on different classes in an ensemble of 4-level systems. A single laser frequency can excite atoms at different transitions.

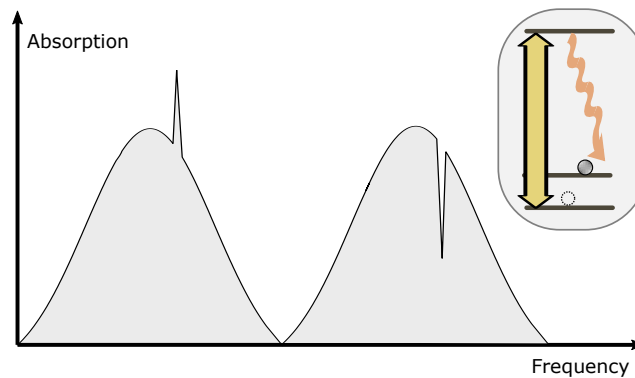


Figure 1.3: Example of a hole burning procedure. A strong laser pulse, resonant with one transition of part of the atoms in an ensemble, excites part of the population from a ground state. The atoms then redistribute on the other levels after the spontaneous decay. When the lifetime of the excited state is much shorter than the ground ones, a hole of enhanced transmission will appear on the absorption profile at the frequency of the laser pulse. The transitions at the other frequencies will instead appear more absorptive due to the accumulated population. If the laser pulse is chirped over a frequency range, the peaks and troughs of absorption will display a corresponding width. This principle is used for instance in spectroscopy to obtain information on the energy level splittings (as we did in chapter 3) and for the initialization of memory protocols (as for the AFC in chapter 6)

state and letting them fall into other long-lived levels, so to create features like *spectral holes* and *pits*. As a consequence, we can engineer the absorption of specific transitions. Most storage techniques in rare earth ensembles involve spectral hole burning in an initialization stage, as is our case.

An important application of spectral hole burning is *class cleaning*. As the atoms in the broadened transitions have relatively shifted transitions, the same optical pulse with a specific frequency might excite different transitions for atoms with different shifts, as in figure 1.2b. This is a problem when the storage protocols involves the manipulation of several energy levels, and for this reason the initialization of an ensemble memory requires to isolate a single class of atoms by optically pumping all the other ones until their overlapping transitions become transparent.

### 1.3 Storage protocols for ensembles

Even when focusing our view on ensembles in particular, many ways of storing information can be used, of which we mention here just a few examples. One of the earliest concepts is to slow down the input light in the atomic medium to practically stop it. This is roughly what happens in *Electromagnetically induced transparency* (EIT), where a strong optical control pulse resonant on a second transition with the same excited state is used at the same time as the input to temporarily modify the light dispersion, effectively decreasing the input pulse group velocity<sup>31</sup>. *Raman memories* also use a control pulse on a connected transition, but to induce an off-resonant Raman absorption of the input excitation into a spin state<sup>32</sup>. *Controlled reversible inhomogeneous broadening* (CRIB) protocols instead involve the manipulation of the inhomogeneous broadening through electric or magnetic fields to force a rephasing of the atoms<sup>33,34</sup>.

Our memory protocol of choice is the *atomic frequency comb* (AFC)<sup>35</sup>. It makes use of pit burning at multiple frequencies in a certain range of the inhomogeneous broadening to create a periodic structure in the absorption spectrum of a transition, which resembles a comb. In this case, only atoms remaining in the teeth of absorption will participate in the storage of an input pulse with a frequency profile overlapping them. The excited atoms will initially dephase according to their specific transition energies, but the periodic relationship between them will force a rephasing after a time equal to the inverse of the periodicity. The bandwidth of the comb is defined by the position of the teeth with lowest and highest frequency. An additional feature of the AFC is the intrinsic multimodality. The high number of atoms in the ensemble enables multiple consecutive pulses to be stored, with their related excited atoms rephasing independently after the storage time. We will discuss the AFC in detail in chapter 6.

The AFC is limited in storage time by the coherence lifetime of the excited state used. Moreover, the stored state cannot be read out on-demand, as the

storage time needs to be pre-programmed during pit burning. For these reason, we will extend it with a *spin-wave* protocol. With an additional optical pulse, the AFC excitation can be transferred into an empty ground spin state, and read out on-demand by a second transfer pulse. The phase of the ensemble during spin storage will evolve according to the spin transition, which normally is less sensitive to external perturbations and allows longer population and coherence lifetimes than the optical transitions. Our implementation of the protocol in europium can be found in chapter 7.

## 1.4 A repeater of entanglement

Quantum memories do not necessarily need a prepared external input state to be useful in quantum communication. In some protocols based on entanglement, the state shared along the links of a network can be created in the memory devices composing a repeater node. This is the idea behind the DLCZ proposal<sup>36</sup> (from the names of its authors Duan, Lukin, Cirac and Zoller), based on the probabilistic creation of a single photon from a pair of memories with their output modes interfering on a detection setup.

Figure 1.4 illustrates the principle. Let us say that we want to connect two nodes A and B, placed so far at a distance  $d$  that direct transmission of a quantum state between them is not practical. The general idea of a repeater scheme is to split the long link in smaller sub-links of length  $d_0$ <sup>9</sup>, over which losses are acceptable. At each intersection, the repeater scheme is composed of two steps, a first generation of entanglement along a sub-link and the following connection with adjacent sub-links to create a single shared state from A to B. The last step is referred to as *entanglement swapping*, which consists in the interference of two entangled states at a common measurement station to create a single entangled state out of them<sup>37</sup>. To do this, each repeater node contains two quantum memories, and two detection stations are place between each pair of memories.

The first step involves the application of excitation pulses to two memories from two different nodes, in a way that with some probability the excitation will decay into a second internal state with the emission of a single photon. The internal state of the memory will then be strongly correlated with the photon emission as

$$|\phi\rangle = |0_a\rangle |0_p\rangle + \sqrt{p_c} |1_a\rangle |1_p\rangle + o(p_c), \quad (1.1)$$

where the first component indicates no photon emission with no atomic excitation, the second a single excitation with one emission with probability  $p_c$ , and higher order terms with multiple emissions have smaller probabilities.

The output paths of the two memories, labeled left ( $L$ ) and right ( $R$ ), are overlapped at a beam splitter, with the other two ports directed on two single-photon detectors. In the DLCZ in particular, the probability of emission of this



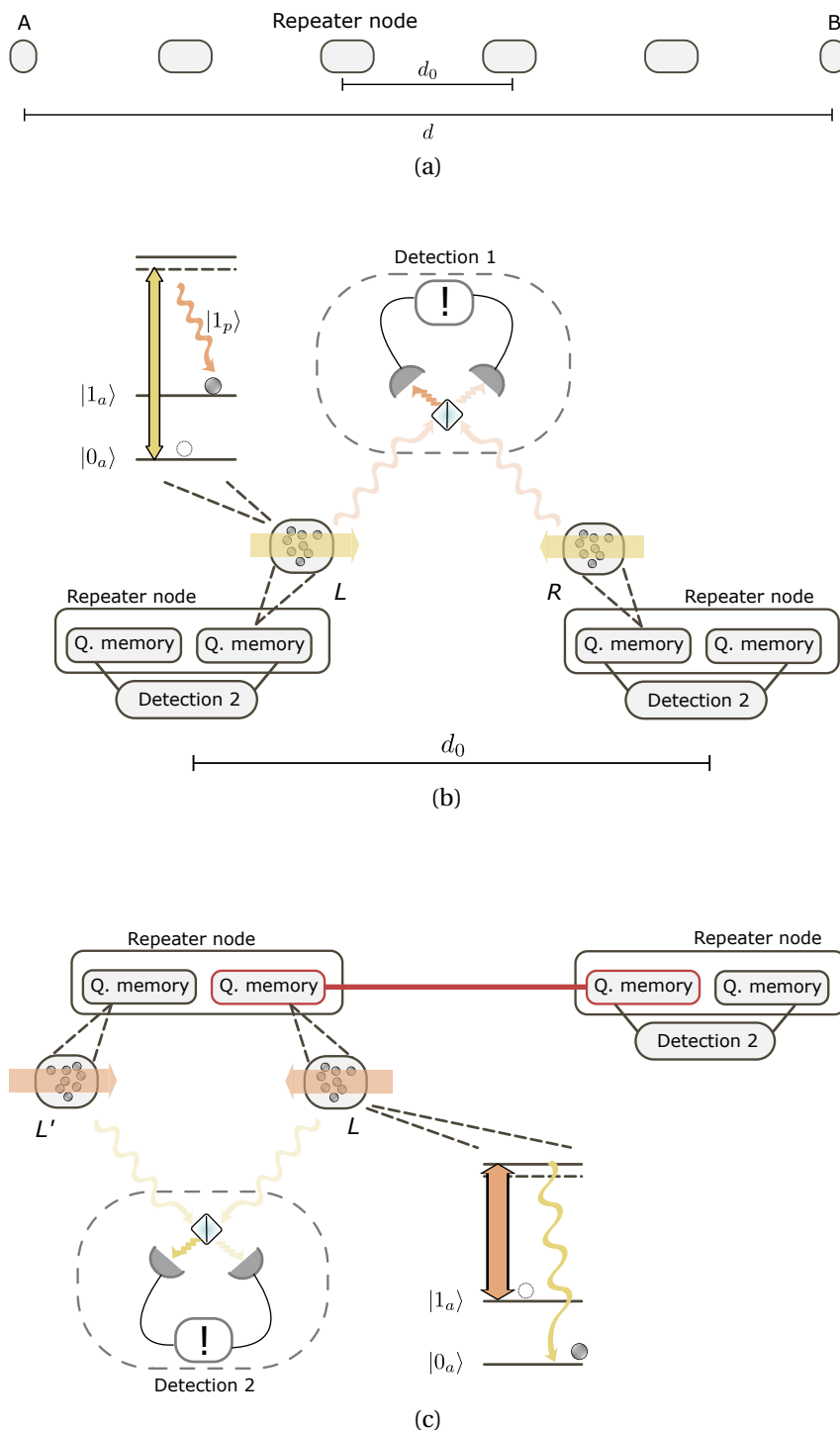


Figure 1.4: Concept of a repeater scheme for communication between two far nodes  $A$  and  $B$ . (a) The link is split into smaller sub-links to reduce the distance that each photon has to travel. (b) Example of a DLCZ concept. Each repeater includes two memories. One memory of each repeater is used to generate the first entanglement link via the detection station 1. An inset with a simplified energy level structure of a memory is shown with a possible choice of transitions. The two memories are optically excited at the same time and their output modes overlapped on a beam splitter with two detectors. A single click from one of them heralds the entangled state  $1,2$ . (c) The entanglement can then be swapped and extended to the other adjacent memories by a second detection stage close to the repeater node. The memories are read out by a re-excitation and their outputs interfere at the detection stations 2 similarly to the step in (a). The process is repeated for all sub-links until the whole link over the distance  $d$  shares the same entangled state.

first photon is tuned to be so low that most of the time only one is emitted from the pair of memories. Here, a single detection heralds the creation of entanglement between the internal states of the memories,

$$|\psi\rangle_I = \frac{1}{\sqrt{2}} \left( |1_a\rangle_L |0_a\rangle_R \pm e^{i\theta} |0_a\rangle_L |1_a\rangle_R \right), \quad (1.2)$$

and establishes the creation of the sub-link of length  $d_0$ .

After this has been done to all sub-links, they can all be merged in an entanglement swapping step. However, given the probabilistic nature of the state creation process, different sub-links will be ready at different times. This is why memories are necessary, so that they can store the entangled states until they can be read out once the adjacent sub-links have been established. To do this, a strong second pulse is applied to the loaded memories to re-excite their internal state and emit a second photon with the highest probability possible. The path of this second emission is sent on the remaining detection stations close to the repeater nodes, so that at each node the memories at the edges of two independent sub-links are coupled. Similarly to the first step, a detection of a single photon from the memory pair will herald a shared entangled state between them, effectively entangling the adjacent sub-links and by consequence the end-nodes  $A$  and  $B$  after the procedure is done in all repeaters.

We will see in section 8.3 how the DLCZ scheme can be combined with the AFC protocol to work in rare earth-doped crystals.

## 1.5 Thesis outline

This work can be divided in two main parts, corresponding to the two materials I worked on during my doctoral work. The first one is Yb:YSO, which we explored in detail at low magnetic fields in its spectroscopic properties and coherence dynamics. The second one is Eu:YSO, a well known material on which we investigated several paths for improvements with the demonstration of quantum storage protocols. The manuscript is composed of the following chapters:

- chapter 2 introduces Yb:YSO in its fundamental properties and the motivation behind our investigations. The experimental setup used for our measurements is also briefly explained.
- Chapter 3 delves into the spectroscopy at low magnetic field, including the characterization of the full Hamiltonian of the system.
- Chapter 4 reports our findings on the coherence dynamics of Yb:YSO, with the discovery of a zero-field clock transition (ZEFOZ) and a second low-field regime (near-ZEFOZ) with enhanced coherence preservation.

- Chapter 5 changes topic and introduces Eu:YSO, with its fundamental properties and the description of the lab setup.
- Chapter 6 contains an introduction of the atomic frequency comb (AFC) protocol, data on several improvements on its performance, and discussions on its limitations.
- Chapter 7 focuses on the spin transition and the AFC spin-wave. Here we investigate the extension of the coherence time, improvements on the control of spin transitions, and a characterization of the storage performance with bright pulses.
- Chapter 8 concludes the work on storage in Eu:YSO with a characterization at the single-photo level, storage of time-bin qubits, and the observation of non-classical correlations in the AFC-DLCZ protocol beyond tens of milliseconds.
- A final short chapter concludes the thesis with a general discussion on the results and on possible future developments.

## Yb:YSO - Introduction

Rare earth ions can be split in two families with very different features by just counting the number of unpaired electrons in their open  $4f$  shell, as a consequence of the more fundamental Kramers theorem<sup>38</sup> when they are hosted low symmetry doping sites in crystals such as YSO. With an even number of electrons, non-Kramers ions are subject to a quenching of their electronic spin, with consequent weaker interactions with external magnetic fields and hence display very long coherence lifetimes. Kramers ions, on the other hand, have a paramagnetic character given by their odd number of electrons, which gives rise to energy level doublets when accounting for the crystal field. They are more sensitive to field perturbations but at the same time display much larger hyperfine and Zeeman splittings, which are interesting for broadband memories and fast trains of pulses. With their complementary features, both families were intensely investigated in quantum memory research.

When I first arrived in Geneva, the subjects of the ongoing projects reflected this idea. Europium was the non-Kramers ion of choice and already hosted experiments on  $\sim$ ms-long storage protocols, as we will see in detail in the second part of this thesis, while neodymium was the Kramers ion of choice and protagonist of the first demonstrations of entanglement storage<sup>39</sup> (in parallel with another work in a Tm-doped waveguide<sup>40</sup>) and teleportation in rare earths<sup>41</sup>.

My first months in the lab were then dedicated to the goal of measuring a spin echo on Nd:YSO via Raman heterodyne scattering (RHS), on which we obtained the results in figure 2.1 and extracted a coherence decay time of  $(1.55 \pm 0.15) \mu\text{s}$ . These measurements probed the coherence between the  $m_S = \pm 1/2$  electronic spin states at about 1 mT. To our knowledge, this was the first time an RHS signal was observed in a Kramers ion, and for me personally served as an introduction to what was to come with ytterbium.

Similarly to neodymium, ytterbium in YSO is a Kramers ion, with the additional advantage of a much simpler hyperfine energy structure in its isotopes with non-zero nuclear spin. While neodymium has a nuclear spin of  $7/2$ , the  $^{171}\text{Yb}$  isotope has only  $I = 1/2$ , which makes things easier when engineering a memory

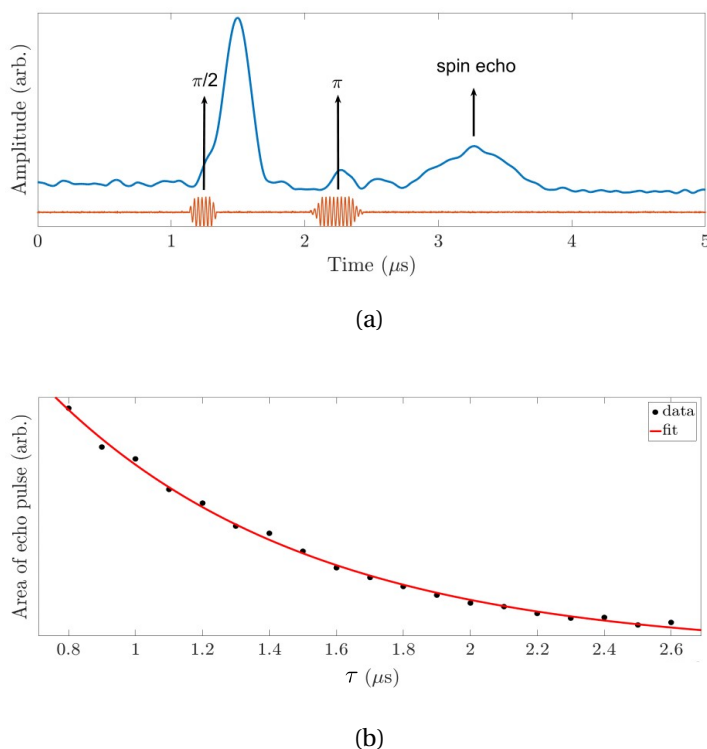


Figure 2.1: Spine echo measurements in Nd:YSO. (a) Example of an optically detected spin echo signal (blue) and the sequence of microwave pulses used (orange). This technique was used later on Yb:YSO, as we will see in chapter 4. (b) Echo signal decay as a function of the time separation  $\tau$  between the microwave pulses (black dots) and related exponential fit (red line), from which a coherence lifetime of  $(1.55 \pm 0.15) \mu\text{s}$  is obtained.

protocol. As it was largely unexplored in its hyperfine structure, the potential of having another Kramers ion with possibly higher spin coherence times at some field (the limit in Nd:YSO was  $100 \mu\text{s}$  for electronic and  $9 \text{ ms}$  for nuclear spins<sup>42</sup>) initially motivated the investigations that followed. At low fields, we expect similar coherence times as the ones of neodymium above, but as we will see things turned out to be quite different.

## 2.1 Properties of ytterbium in yttrium orthosilicate

Ytterbium is one of the heaviest lanthanoids, sitting at the end of the dedicated periodic table row with atomic number 70. As a dopant in  $\text{Y}_2\text{SiO}_5$ , it ionizes to a trivalent state like most rare earths, totaling 13 electrons in its open  $4f$  shell. As its most similar element in size in the host lattice is yttrium, Yb replaces it in two possible crystal sites of  $C_1$  symmetry. In each crystal site, its magnetic moment can assume two different orientations, originating two inequivalent sub-sites that appear aligned if the magnetic field is oriented orthogonal or parallel to the  $b$  crystal axis.

The crystal field perturbs the free ion and spin-orbit components of the Hamil-

tonian and gives rise to two multiplets, the ground  $^2F_{7/2}$  and excited  $^2F_{5/2}$ , connected by an optical transition at 981.46 nm (site I) and 978.85 nm (site II). The internal structure of these transitions depends on the specific isotopes, of which 7 different ones are stable in nature. Most of them have a nuclear spin  $I = 0$ , while  $^{171}\text{Yb}$  and  $^{173}\text{Yb}$  have respectively  $I = 1/2$  and  $I = 5/2$  and exhibit a hyperfine structure. Our work will focus on the former, which at zero field has the simplest possible hyperfine structure among stable isotopes of rare earths because  $S = I = 1/2$ . We will refer to the effective spin Hamiltonian in a field  $\mathbf{B}$

$$\mathcal{H}_{\text{Yb}} = \mathbf{I} \cdot \mathbf{A} \cdot \mathbf{S} + \mu_{\text{B}} \mathbf{B} \cdot \mathbf{g} \cdot \mathbf{S} - \mu_{\text{n}} \mathbf{B} \cdot \mathbf{g}_{\text{n}} \cdot \mathbf{I} \quad (2.1)$$

which also includes the electronic and nuclear Zeeman interactions via the tensors  $\mathbf{g}$  and  $\mathbf{g}_{\text{n}}$  in addition to the hyperfine interaction via the tensor  $\mathbf{A}$ . The quadruple interaction, relevant in systems with  $I \geq 1$  (as we will see with europium), is here not present, further simplifying the spectroscopy. Most of the time, the nuclear Zeeman effect will also be ignored, as the overall Zeeman effect is dominated by the contribution of the electrons.

Investigations on  $^{171}\text{Yb}^{3+}$  in  $\text{Y}_2\text{SiO}_5$  started from a collaboration between our group and Philippe Goldner's team at Chimie ParisTech<sup>1</sup>. Sacha Welinski et al.<sup>43</sup> initially performed electron paramagnetic resonance (EPR) and optical spectroscopic measurements on a crystal containing Yb ions in natural isotope concentrations. At the values of field magnitude explored, ranging from 50 mT to 200 mT, the electronic Zeeman effect is the dominant term of the Hamiltonian 2.1 and the hyperfine interaction can be treated as a weaker perturbation. From their results, the eigenvalues of the  $\mathbf{g}$  and  $\mathbf{A}$  tensors were obtained, together with the Euler angles of their principal axes with respect to the crystal axis. Numerical calculations extrapolated to lower fields indicated the possible presence of a partial clock transition, or partial ZEFOZ point (from ZEro First Order Zeeman), slightly below the range of fields explored when the hyperfine and Zeeman interactions would become comparable. As we will see in the following sections, this approximation breaks down at lower fields and we will need to complement the spectroscopy with other tools.

What makes this platform interesting in quantum communication is the peculiar hyperfine properties and an energy level structure that makes it a unique hybrid, in which some of the good properties typical of both Kramers and non-Kramers ions can coexist, namely a large bandwidth due to  $\sim$  GHz spin transitions and the quenching at first order of the effect of electronic dipole moment on magnetic field perturbations. Moreover, its large hyperfine splittings support high bandwidth, time multi-mode quantum memories, as indicated by the later works of Welinski, Businger et al.<sup>44,45</sup>, with the additional potential of interfacing directly with superconducting qubits at zero magnetic field via microwaves.

<sup>1</sup>[www.cqsd.fr](http://www.cqsd.fr)

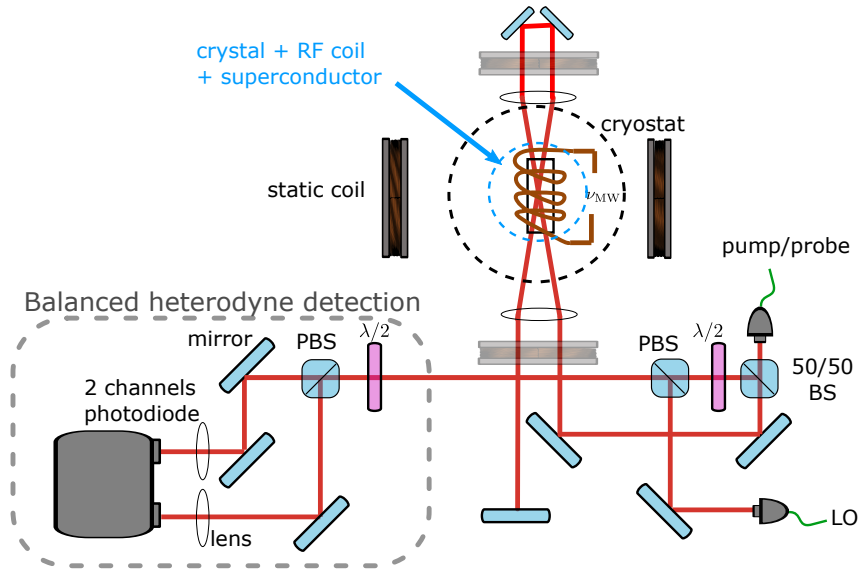


Figure 2.2: Sketch of the setup used in experiments on Yb:YSO.

## 2.2 Experimental setup

The particular crystal we investigated was a 10 ppm-doped  $^{171}\text{Yb}^{3+}:\text{Y}_2\text{SiO}_5$ , isotopically enriched to 95 % in terms of  $^{171}\text{Yb}$ . It was cut along the polarization extinction axes  $D_1$ ,  $D_2$  and  $b$ <sup>46</sup> with dimensions respectively of 5.7 mm, 5.6 mm and 9.5 mm, and polished on the  $D_1$ - $D_2$  side for optical access. Another crystal with dimensions 10.0 mm, 4.6 mm and 4.5 mm and polished on the  $D_2$ - $b$  side was used for coherence measurements on site I, for reasons that will become clearer in chapter 4.

The setup of the experiment is displayed in figure 2.2. The crystal is installed in a closed-cycle helium cryostat and typically used at a temperature of 3.5 K, enveloped by a coil for generating the microwave (MW) fields necessary to address the spin transitions. Of the 2 W of maximum power we could get from our MW wave generator and amplifier system, only about 0.5 % of it actually arrived at the crystal, given our estimate for the inductance of 0.2 nH. The electron spin coupling was strong enough for not needing an impedance matching circuit, something that is not trivial as for exemplified by our experience with europium in chapter 7.

To apply an external static magnetic field, we used a superconducting coil along one direction that enabled amplitudes up to 2 T, while the other axes were covered by a set of four homemade coils in a Helmholtz configuration capable of inducing a few mT.

The 980 nm transition of Yb:YSO is accessible with commercially available diode lasers, which is one of the reasons why it is interesting to study (in addition to its simple hyperfine structure). Such a laser is the source of our optical setup, with two beams that were separated into two acousto-optic modulators to generate

the probe and pump pulses on one path and a local oscillator on the other. The former passed through the crystal four times to increase the total optical depth, as it is meant to prepare the atomic population when required and for readout. The local oscillator is used instead to enhance the detected signals by heterodyne interference on a balanced silicon photodetector, after overlapping the probe at a polarized beam splitter.





# Low magnetic field spectroscopy of Yb:YSO

*This chapter describes our work reported in **Paper II**, published in *Physical Review B*, "Spectroscopic study of hyperfine properties in  $^{171}\text{Yb}^{3+}$ ".*

To complement the work done so far at higher magnetic field values and with the possibility of finding ZEFOZ points for some fields<sup>43</sup>, we conducted spectroscopic investigations at low magnetic fields up to 100 mT with a variety of complementary techniques. First of all, scanning our laser over the optical resonance  $^2F_{7/2}(0) \leftrightarrow ^2F_{5/2}(0)$  of the two sites at zero field allowed us to observe an interesting structure of partially resolved optical transitions between different hyperfine levels in the ground and excited states, as shown in figure 3.1, for light polarization parallel to  $D_1$  and  $D_2$ . We can see that the two sites behave differently: site II displays a drop in absorption over the whole spectrum when changing polarization alignment from  $D_1$  to  $D_2$ , while in site I this is not true for the group of transitions around the center of the spectrum. What is also interesting is one line in particular, the lowest frequency one of site II (at  $-4$  GHz in the relative scale of figure 3.1), which proved to be well separated from the others. This is useful for some applications in which it is important that a single class of ions is excited, removing the need for class cleaning and simplifying the preparation necessary for most memory protocols. We used this feature for instance when probing the coherence dynamics of Yb:YSO, as we will see in chapter 4.

The absorption spectra alone cannot give us all information on the energy structure as the transitions are only partially resolved. More generally, optical transitions depend on both the ground and excited state splittings, which were unknown for both ground and excited states before this work.

We need then some more elements. At zero magnetic field, the Hamiltonian 2.1 we have seen in the previous chapter has only one non-zero term, the hyperfine interaction  $\mathbf{I} \cdot \mathbf{A} \cdot \mathbf{S}$ . The hyperfine tensor  $\mathbf{A}$  can be diagonalized and its three

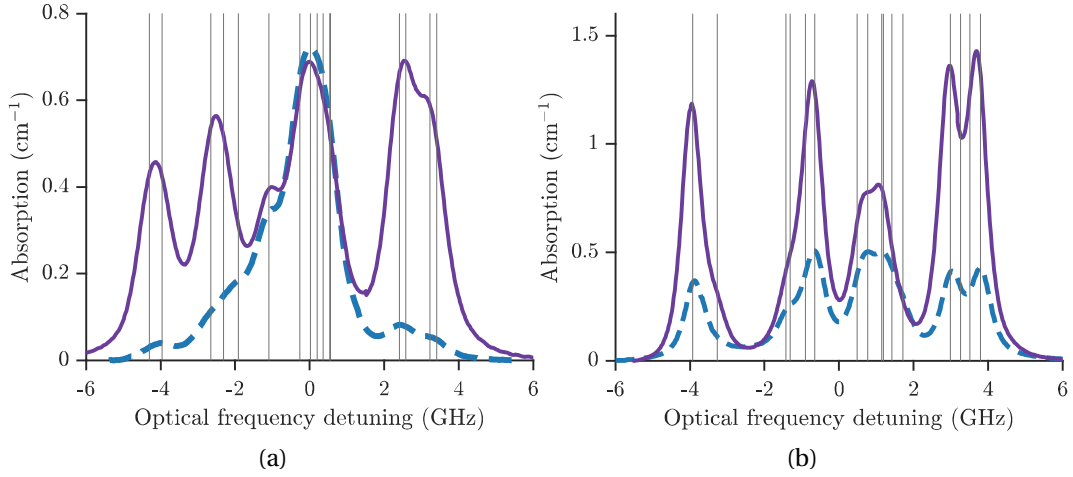


Figure 3.1: Absorption spectra of optical sites I (a) and II (b). The solid purple line indicates data collected with light linearly polarized along  $D_2$ , the dashed blue line along  $D_1$ . Gray vertical lines represent the positions of the hyperfine transitions calculated from the  $\mathbf{A}$  tensor obtained in this work with equation 3.1.

eigenvalues  $A_i$  are found to be related to the energy of the four hyperfine states as

$$E_{\phi^\pm} = \frac{1}{4} [-A_z \pm (A_x + A_y)] \quad \text{and} \quad E_{\psi^\pm} = \frac{1}{4} [A_z \pm (A_x - A_y)]. \quad (3.1)$$

These can be calculated starting from measurements of the energy splittings of the hyperfine levels, both for the ground and excited states. The orientation of the spatial basis that diagonalizes the  $\mathbf{A}$  matrix might however be different than the  $D_1$ ,  $D_2$  and  $b$  crystal axes, given the very low symmetry of the Yb sites ( $C_1$ ). This means we will have to find also the three Euler angles ( $\alpha_A, \beta_A, \gamma_A$ ) (in  $zxz$  convention) that will allow to express  $\mathbf{A}$  in the crystal frame ( $D_1, D_2, b$ ), starting from its diagonalized form:

$$\mathbf{A} = R(\alpha_A, \beta_A, \gamma_A) \begin{pmatrix} A_x & 0 & 0 \\ 0 & A_y & 0 \\ 0 & 0 & A_z \end{pmatrix} R^T(\alpha_A, \beta_A, \gamma_A). \quad (3.2)$$

where  $R$  indicates the rotation matrix

$$R(\alpha, \beta, \gamma) = R_z(\alpha) \cdot R_x(\beta) \cdot R_z(\gamma),$$

with

$$R_z(\alpha) = \begin{pmatrix} \cos(\alpha) & -\sin(\alpha) & 0 \\ \sin(\alpha) & \cos(\alpha) & 0 \\ 0 & 0 & 1 \end{pmatrix} \quad \text{and} \quad R_x(\beta) = \begin{pmatrix} 1 & 0 & 0 \\ 0 & \cos(\beta) & -\sin(\beta) \\ 0 & \sin(\beta) & \cos(\beta) \end{pmatrix}.$$

The angles can be found by applying an external magnetic field  $\mathbf{B}$  and study the change in splittings as a function of field intensity and direction. In this

we are aided by the fact that the  $g$  tensor is fully characterized from the EPR measurements in a regime where the Zeeman interaction is dominant with respect to the hyperfine one.

To understand how we obtained the following results, we have to take a look first at the two main techniques we used, spectral hole burning and optically detected magnetic resonance.

### 3.1 Spectroscopic techniques

Spectral hole burning (SHB) is a common technique in the spectroscopy of solids with inhomogeneously broadened transitions<sup>47</sup>. It exploits the long hyperfine population lifetime, or  $T_1^s$ , of certain states at low temperature in order to highlight the different transitions arising from finer structures that normally would be hidden by the inhomogeneous broadening, such as the hyperfine, quadrupolar or Zeeman splittings.

SHB makes use of a first strong pulse, called *pumping* or *burning* pulse, with power and/or duration high enough to excite a fraction of the population to the excited state. Assuming that the excited state optical  $T_1$  is shorter than the hyperfine  $T_1^s$ , after some time after the burning procedure the excited state will be empty again and the population will be redistributed among all other ground sub-states according to the branching ratios of their respective transitions.

If we now use a weaker, chirped probe pulse spanning the whole range of frequencies we are interested in, the absorption spectrum will be partially transparent at the frequency burned (the *main hole*) and at all other frequencies corresponding to transitions between the same ground sub-state and any of the excited states (the *side holes*)<sup>48</sup>. Hence, the difference in frequency between the main hole and the side-holes will provide in principle the splittings within the excited state.

At the same time, the additional population that decayed from the excited state into the other hyperfine states that were not excited by the burn pulse will appear as peaks of stronger absorption (*anti-holes*). These will differ in frequency from the main hole by the respective frequency splitting in the ground state, but additionally other anti-holes will originate from transitions between all other combinations of ground and excited state hyperfine levels. To further complicate the picture, the inhomogeneous broadening will cause different transitions from different atoms (classes) to overlap, adding even more anti-holes.

As the position of side-holes and anti-holes depends on the ground and excited state hyperfine splittings, in principle the SHB is enough to extract the hyperfine transitions frequencies. However, without additional information, it is difficult to assign each hole and anti-hole to their correct transitions.

To aid us in assigning the holes and anti-holes, we can address the hyperfine transitions of the ground or excited states directly with an AC field generated by a coil around the crystal. Optically detected magnetic resonance (ODMR) in

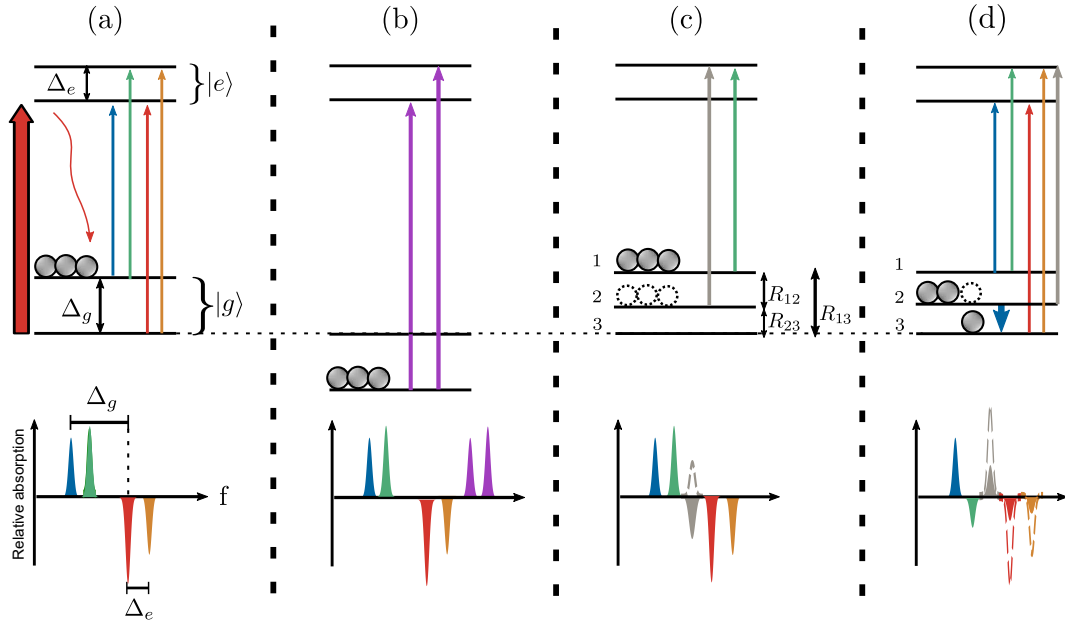


Figure 3.2: Principle of spectral hole burning on an optical transition with hyperfine splitting (a). The optical pump (wide red arrow) excites the atoms, which then fall into other ground states (wavy arrow). When probing the spectrum (bottom plot), peaks (anti-holes) and troughs (holes) of absorption appear at transitions connecting full and empty ground states respectively. Hyperfine splittings can be extracted in principle by the difference in frequency between the peaks and troughs of the absorption spectrum. (b) Effect of additional classes of atoms due to inhomogeneous broadening. The optical pumping populates different ground states in different classes, which add absorption features at different frequencies. (c) If more ground states are involved with fast relaxation rates between them, initially populated levels might be empty by the time the probe is applied, making a hole appear (green trough) where an anti-hole is expected (dashed green line). In the example depicted, the rate  $R_{23}$  is much smaller than  $R_{13}$  and  $R_{12}$ , so atoms initially on level 2 fall rapidly on level 3 and are repumped before readout. (d) Effect of an MW pulse applied between pumping and readout, like in ODMR. The population of a full level (2) is partially transferred into an empty one (3), reducing the contrast of the related holes and anti-holes and allowing to detect the spin resonance.

particular consists in probing optically the anti-holes after the application of a strong MW pulse (figure 3.2d). When the MW has a frequency corresponding to a spin transition, part of the population will be moved between states and the absorption will be reduced, indicating the presence of a resonance.

Finally, cross-relaxation rates between ground-substates might be high enough to lead to direct spontaneous population transfers during the burning process, which might transform anti-holes into holes<sup>48</sup> as we will see later. These mechanisms are sketched in figure 3.2.

## 3.2 Spectroscopy results

Normally, spectral hole burning would give us the information on splittings we are looking for at all fields. However, SHB spectra can get very complicated

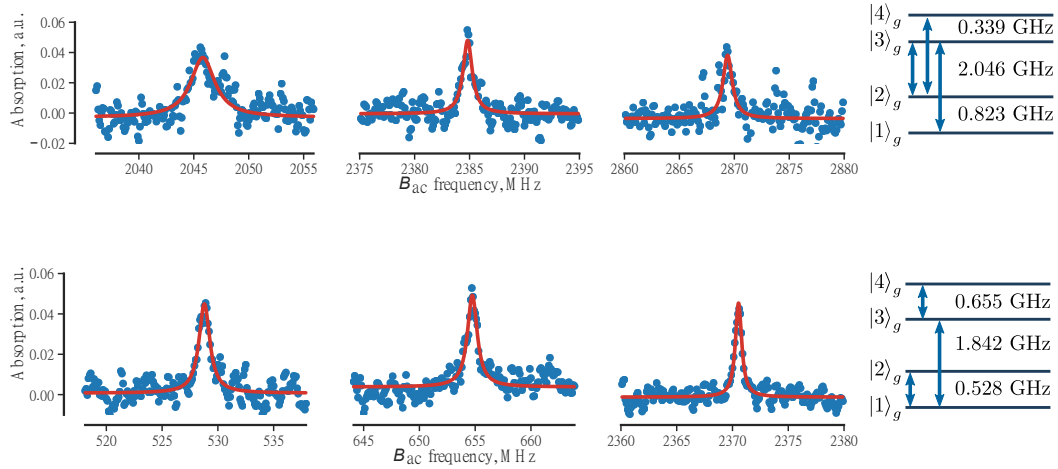


Figure 3.3: Examples of ODMR signal as a function of the frequency of the MW field  $\mathbf{B}_{ac}$ , displaying some of the spin resonances (left), and respective transition sketch (right) for site I and II (top and bottom figure respectively). The red solid lines indicate Lorentzian fits from which the central frequencies and widths are extracted.

as we have seen in the previous section. We start then at zero magnetic field and try to measure the frequency spin transitions directly by ODMR. Figure 3.3 displays some of the resonances observed. In total, we detected resonances at the frequencies 2046, 2385, 2869 and 3208 MHz for site I and 528, 655, 2370 and 3025 MHz for site II, corresponding to transitions within the ground state, with fitted widths between 0.5 and 1.2 MHz. From these, we can use the relations 3.1 to obtain the eigenvalues  $A_i$  of the hyperfine tensor. These differ considerably from the ones found by the EPR measurements<sup>43</sup>, possibly because ODMR at zero field has the advantage of being independent on a field direction, thus excluding the Euler angles from the equations and the need for a nonlinear fit which could introduce larger errors. This discrepancy arises in the special case of the lowest possible degree of symmetry ( $C_1$ ) of the doping sites of the YSO host, which does not impose any specific orientation on the  $\mathbf{A}$  and  $\mathbf{g}$  tensors, while in most host crystals some restriction on the components of the tensors depends on higher symmetries. A similar situation is observed in Er:YSO<sup>49</sup>.

Now we can add to the picture the data obtained by SHB, which we performed for a range of magnetic field amplitudes up to about 100 mT by optical burning at the center of the absorption spectrum. Examples of spectral maps as a function of the magnetic field are shown in figure 3.4, in which dark and bright lines indicate holes and anti-holes respectively, with  $\mathbf{B} \parallel D_1$  on site I and  $\mathbf{B} \parallel D_2$  for site II. A lot of other details can be extracted from these datasets after combining them with the ODMR data, a process thoroughly described in *Paper II*. We can summarize here the key points, using site I with  $\mathbf{B} \parallel D_1$  as an example.

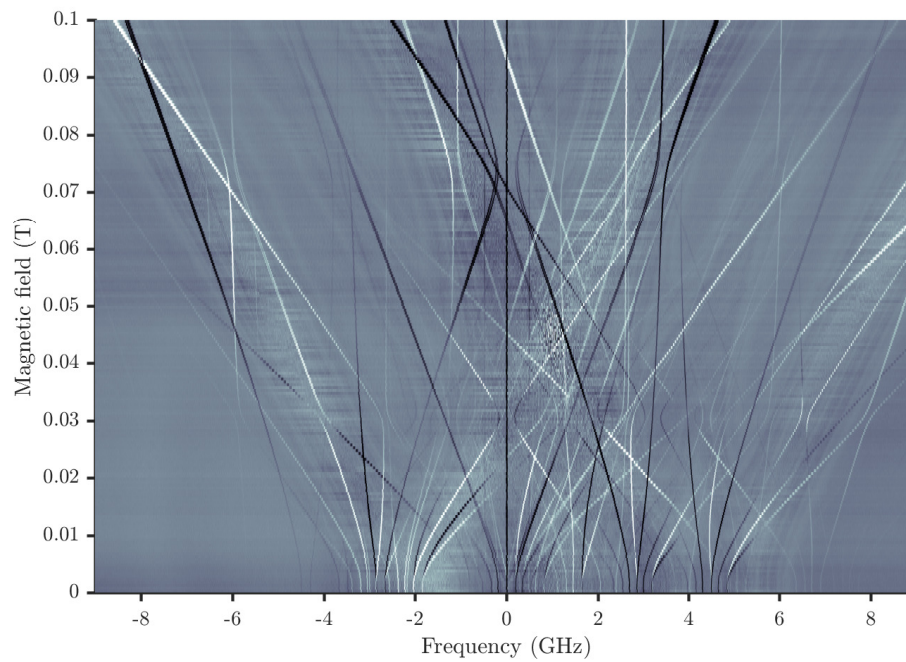
Using the splitting found by ODMR for the ground state, we can unambigu-

ously identify some of these transitions at zero field in the SHB spectra with their anti-holes, and follow the lines at higher fields to observe the electronic Zeeman effect on them (while the nuclear Zeeman effect can be neglected). These lines display a first nonlinear region visible at about 30 mT, which by consequence must be due to avoided crossings of the ground state hyperfine levels. The behavior induced by the excited state requires however several steps to identify the correct lines:

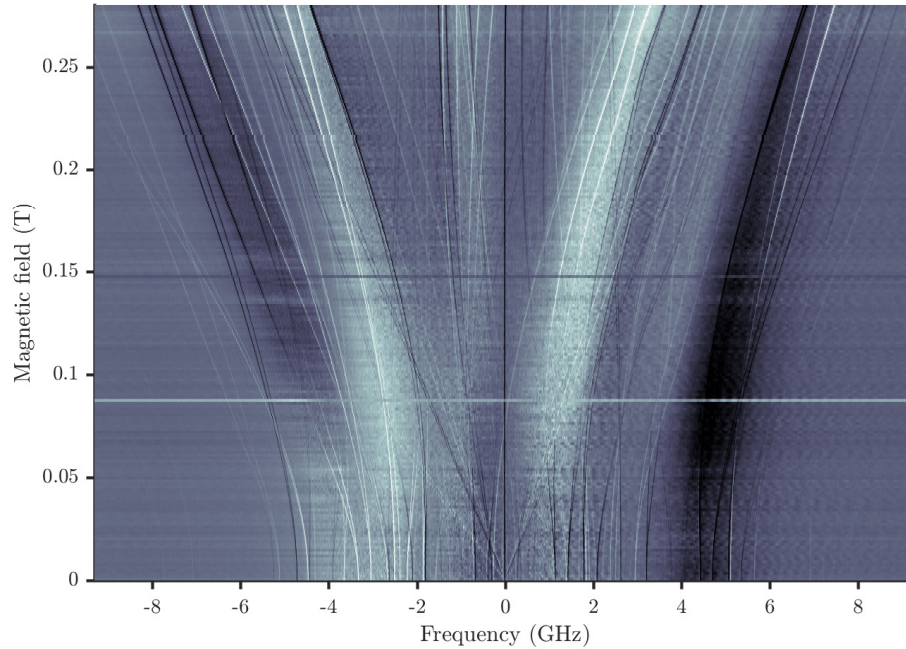
- Another nonlinear region is visible at 80 mT, which by exclusion must be due to avoided crossings of the excited state levels.
- Some lines switch character from absorption to transparency after crossing these nonlinear regions. This is due to the change of rate of relaxation of ground hyperfine states with the level being pumped. If the decay is faster than the burning time (about 100 ms), hyperfine states can be indirectly emptied and appear as *pseudo-holes*. Other pseudo-holes never change character, but some of them can be identified as they display a nonlinear bent at both the 30 and 80 mT field regions. This cannot happen for "true" side-holes, as they should depend only on the excited state splittings and hence have only one non-linear region at 80 mT as seen above.
- True side holes related to different excited state levels can be distinguished from the remaining pseudo-holes and other classes by considering the strongest side holes having non-linearities only at 80 mT. This can be confirmed by using their corresponding splittings to calculate the position of all expected anti-holes.
- From the splittings at zero field of the true side-holes thus identified, we can calculate the excited state hyperfine eigenvalues as in 3.1.

Once the correct transitions are identified, we can extract them and fit their frequency variation with field as in figures 3.5 and 3.6, using the Hamiltonian 2.1. At this point, we have all the necessary information to build the full structure of the  ${}^2F_{7/2}(0) \leftrightarrow {}^2F_{5/2}(0)$  transition, including the hyperfine splittings, as shown in figure 3.7. The order of the levels can be inferred by comparing the various ordering possibilities of the splittings found at zero field with the absorption spectra first observed in figure 3.1. Only the ordering in figure 3.7 is in good agreement with the optical spectrum.

A particularly interesting feature involves the hole/anti-hole transformations that some lines undergo. As an example, we can follow the path of the  $|2\rangle_g \leftrightarrow |3\rangle_g$  transition of site I for increasing field along  $D_1$ , seen in detail in figure 3.8a. In the middle of the nonlinear region around 30 mT, the anti-hole gradually loses contrast until it becomes a side-hole at the closest point to an anti-crossing with the main hole (visible in figure 3.4a). Increasing even more the field brings the hole



(a)



(b)

Figure 3.4: (a) SHB map for varying magnetic field along  $D_1$  and frequency, on site I, and (b) for field along  $D_2$  on site II. The dark regions are absorption holes, the bright ones are absorption anti-holes. Some of these lines are reported along with their fitted curves in figures 3.5 and 3.6.



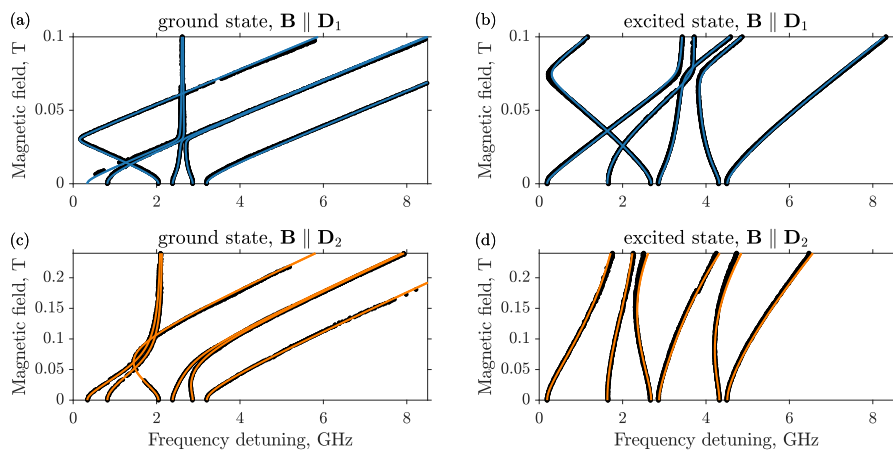


Figure 3.5: Detail of SHB lines extracted from the maps as the examples in figure 3.4, for site I with field along  $D_1$  (top) and  $D_2$  (bottom), corresponding to the ground (left) and excited states (right). Solid lines represent the corresponding calculated transition frequencies.

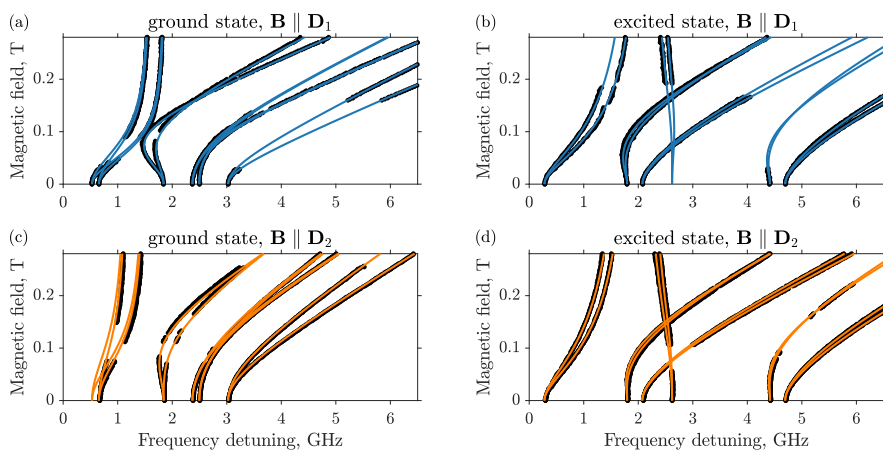


Figure 3.6: Detail of SHB lines extracted from the maps as the examples in figure 3.4, for site II with field along  $D_1$  (top) and  $D_2$  (bottom), corresponding to the ground (left) and excited states (right). Solid lines represent the corresponding calculated transition frequencies.

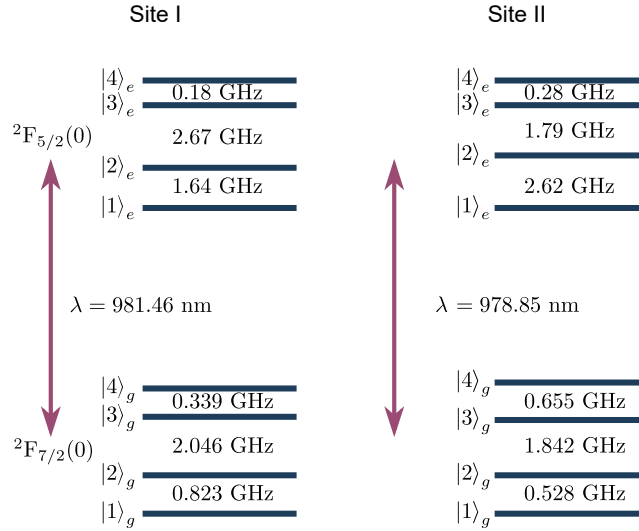


Figure 3.7: Final hyperfine energy structure of the  ${}^2F_{7/2}(0) \leftrightarrow {}^2F_{5/2}(0)$  transition on the two crystal sites.

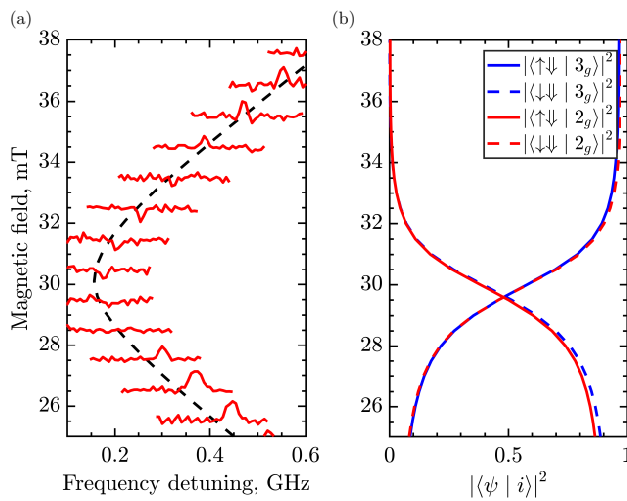


Figure 3.8: Transformation between hole and anti-hole characters of the  $|2\rangle_g \leftrightarrow |3\rangle_g$  transition ( $\mathbf{B} \parallel D_1$ , site I). (a) Hole burning spectra transition in the region around 30 mT, showing a dip in absorption at the anti-crossing. (b) Overlap of the two states with the  $|\uparrow\downarrow\rangle$  and  $|\downarrow\downarrow\rangle$  spin eigenstates (the two remaining ones have always negligible amplitude), showing an increased mixing in the nonlinear region and a full swap at higher fields.

to transform back into an anti-hole and continue its path in frequency linearly. This phenomenon could be attributed to a change in the relaxation rates, as sketched in figure 3.2c. The mixing of state wave functions of different spin character can drive such a change, as suggested by the results in figure 3.8b. By diagonalizing the Hamiltonian in equation 2.1, we find that the eigenstates change their overlap amplitudes with the eigenstates of the  $\sigma_z^e \otimes \sigma_z^n$  tensor product of electronic and nuclear Pauli operators, namely  $|\uparrow\uparrow\rangle$ ,  $|\uparrow\downarrow\rangle$ ,  $|\downarrow\uparrow\rangle$  and  $|\downarrow\downarrow\rangle$ , in which the thin and wide arrows indicate the electronic and nuclear spin respectively. The state labeled as  $|3\rangle_g$  starts at low field with a very strong overlap with the  $|\uparrow\downarrow\rangle$  state, while  $|2\rangle_g \approx |\downarrow\downarrow\rangle$ . As they cross the nonlinear region, the two states completely mix with equal components of the two spin eigenstates, possibly inducing an increase in their cross-relaxation rate. At higher fields,  $|2\rangle_g$  and  $|3\rangle_g$  completely swap components. Phenomena like this have been observed for instance in ruby<sup>50</sup> and Er:YSO<sup>48</sup> with similar interpretations involving state mixing.

With the eigenvalues cleared for both ground and excited states, what remains to be found is the orientation of the hyperfine tensors with respect to the crystal axes, that is the Euler angles in equation 3.2. By using the  $\mathbf{g}$  tensor obtained without hyperfine state with the  $I = 0$  isotope and the high field EPR data in Welinski's work, we can fit the orientation with respect to  $\mathbf{g}$ , which in turn was expressed in Euler angles with respect to the crystal frame.

Interestingly we find that, similarly to  $\mathbf{g}$ , also  $\mathbf{A}$  has one component much stronger than the other two. Moreover, the strongest components of the two tensors are almost parallel, and very close to  $D_1$  in site I and  $b$  in site II. These considerations are true for both ground and excited states, and they will lead to important consequences for the coherence dynamics that we will see in the next chapter.

### 3.3 Conclusion

We have seen how Yb:YSO has a surprisingly rich spectroscopy at low magnetic field, with nonlinear Zeeman regions and strong wave function admixing capable of changing the population dynamics. Nonetheless, we were able to extract all the relevant information necessary to completely characterize the hyperfine interaction, correcting the first estimations obtained at higher fields and complementing the results on the Zeeman tensor. Finally, we identified a strong asymmetry of the hyperfine tensor  $\mathbf{A}$ , similar to the one affecting  $\mathbf{g}$ , which will enable the excellent coherence properties we will find from our experiments on the coherence dynamics.

	Site I		Site II	
	ground	excited	ground	excited
$A_x$ (GHz)	0.481	1.44	-0.1259	2.34
$A_y$ (GHz)	1.159	1.82	1.1835	2.90
$A_z$ (GHz)	5.251	7.20	4.8668	6.49
$\alpha_A$ ( $^\circ$ )	72.25	73.88	45.86	51.07
$\beta_A$ ( $^\circ$ )	92.11	84.76	11.13	14.11
$\gamma_A$ ( $^\circ$ )	63.92	90.13	2.97	-0.67
$ g_x $	0.31	0.8	0.13	1.0
$ g_y $	1.60	1.0	1.50	1.4
$ g_z $	6.53	3.4	6.06	3.3
$\alpha_g$ ( $^\circ$ )	72.8	77	59.10	54
$\beta_g$ ( $^\circ$ )	88.7	84	11.8	23
$\gamma_g$ ( $^\circ$ )	66.2	-7	-12.6	-10

Table 3.1: Summary of the hyperfine tensor eigenvalues  $A_i$  and Euler angles, in  $xxz$  convention and with respect to the crystal frame ( $\mathbf{D}_1$ ,  $\mathbf{D}_2$ ,  $\mathbf{b}$ ), obtained in this work by SHB and ODMR. The lower part reports also the properties of the  $g$  tensor obtained at higher field by Welinski et al.<sup>43</sup>



## Coherence dynamics of Yb at low field

*This chapter describes our work reported in **Paper I**, published in *Nature Materials*, "Simultaneous coherence enhancement of optical and microwave transitions in solid-state electronic spins".*

### 4.1 Zero field clock transitions (ZEFOZ)

At zero magnetic field, we saw in chapter 3 how the effective Hamiltonian is composed of the hyperfine interaction alone and can be easily diagonalized, with eigenvalues as in equation 3.1. We also found that the hyperfine tensor  $\mathbf{A}$ , like the Zeeman  $\mathbf{g}$ , is fully anisotropic. As we will see, this particular feature has interesting consequences on  $^{171}\text{Yb}^{3+}$ , which is a general feature of systems with highly anisotropic hyperfine interactions.

Up to now we labeled the hyperfine states by their ordering in energy, as in figure 3.7. However, we already mentioned in the context of the wave function mixing (figure 3.8) that we can express them on the  $z$  electronic and nuclear spin basis. At zero field, they become (see also figure 4.1)

$$|\phi^\pm\rangle = \frac{1}{\sqrt{2}}(|\uparrow\uparrow\rangle \pm |\downarrow\downarrow\rangle) \quad \text{and} \quad |\psi^\pm\rangle = \frac{1}{\sqrt{2}}(|\uparrow\downarrow\rangle \pm |\downarrow\uparrow\rangle), \quad (4.1)$$

with

$$|\uparrow\rangle = \left|S_z = \frac{1}{2}\right\rangle, \quad |\downarrow\rangle = \left|S_z = -\frac{1}{2}\right\rangle, \quad |\uparrow\rangle = \left|I_z = \frac{1}{2}\right\rangle, \quad |\downarrow\rangle = \left|I_z = -\frac{1}{2}\right\rangle.$$

These are all maximally entangled Bell states, all composed by an equal mixture of spins of opposite signs of both electrons and nucleus. By calculating the expectation value for both spins in any of these states, we obtain  $\langle \mathbf{S} \rangle = 0$  and  $\langle \mathbf{I} \rangle = 0$ .

To see the implications of this, let us think what happens to the energy of a transition when put under a small variation of the magnetic field  $\Delta\mathbf{B}$ . The resulting decoherence rate due the Zeeman effect can be expanded as

$$\frac{1}{\pi T_2} = \mathbf{S}_1 \cdot \Delta\mathbf{B} + \Delta\mathbf{B} \cdot \mathbf{S}_2 \cdot \Delta\mathbf{B} + \dots \quad (4.2)$$

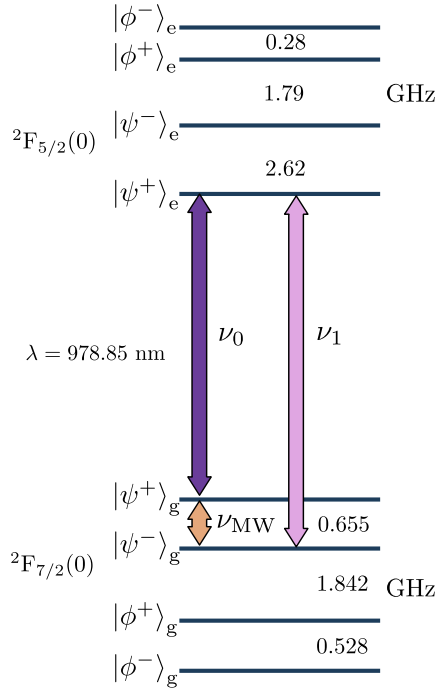


Figure 4.1: Zero-field structure of site II of  $^{171}\text{Yb}^{3+}:\text{Y}_2\text{SiO}_5$  with hyperfine levels labeled as the definitions 4.1. The transitions used for most of the coherence experiments are also shown:  $\nu_0$  (purple) is used for the photon echo sequence and as probe in the optically detected spin echo,  $\nu_1$  (pink) is the transition on which the RHS signal is emitted and  $\nu_{\text{MW}}$  (orange) is the spin transition. Other combinations were used to confirm the generality of our results, for instance the 528 MHz spin transition and analogous ones on site I.

where the  $\mathbf{S}_i$  tensors have for components the  $i$ -th derivatives of the transition energy with the field in all directions. In particular, the gradient  $\mathbf{S}_1$  is defined, to first order for a transition between two generic states  $|\xi_1\rangle$  and  $|\xi_2\rangle$ , as

$$\mathbf{S}_1 = \begin{pmatrix} \frac{\partial(\langle \xi_1 | \mathcal{H}_{\text{Yb}} | \xi_1 \rangle - \langle \xi_2 | \mathcal{H}_{\text{Yb}} | \xi_2 \rangle)}{\partial B_x} \\ \frac{\partial(\langle \xi_1 | \mathcal{H}_{\text{Yb}} | \xi_1 \rangle - \langle \xi_2 | \mathcal{H}_{\text{Yb}} | \xi_2 \rangle)}{\partial B_y} \\ \frac{\partial(\langle \xi_1 | \mathcal{H}_{\text{Yb}} | \xi_1 \rangle - \langle \xi_2 | \mathcal{H}_{\text{Yb}} | \xi_2 \rangle)}{\partial B_z} \end{pmatrix}. \quad (4.3)$$

Here the field-independent hyperfine terms cancel and each argument of the partial derivatives reduces to the difference of the expectation values of the Zeeman terms of the two states. Using the definitions 4.1 however leads to all terms being zero simply because

$$\langle \xi_i | \Delta \mathbf{B} \cdot \mathbf{g} \cdot \mathbf{S} | \xi_i \rangle = \langle \xi_i | \Delta \mathbf{B} \cdot \mathbf{g} \cdot \mathbf{I} | \xi_i \rangle = 0 \quad (4.4)$$

for all levels in both the ground and excited states.

In other words, the first order Zeeman effect is canceled simultaneously for all transitions, including the optical ones. The canceling of the first term in 4.2 defines the zero first order Zeeman (ZEFOZ) condition, or clock transitions. This is the first hint at the potential of Yb:YSO for coherence preservation, as often ZEFOZ points are typically reached in rare earths at much higher magnetic field intensities<sup>51</sup> and only for one particular transition at a time.

A second important finding is that the low perturbation insensitivity does not come at the cost of a low MW coupling with the spin transitions. For instance, in

non-Kramers ions, the MW coupling is typically weaker as their magnetic interactions are given mostly by the nuclear spins (we will have to face this problem on europium in chapter 7). In Yb:YSO, the transition amplitudes between states that involve spin flips are still allowed and proportional to the Bohr magneton, a feature typical of Kramers ions. More explicitly, for a generic  $\xi = \psi, \phi$ ,

$$\langle \xi^\pm | \mathbf{B}_{ac} \cdot \mathbf{g} \cdot \mathbf{S} | \xi^\mp \rangle \propto g\mu_B, \quad (4.5)$$

with  $g$  indicating the resulting constant from the component of the  $\mathbf{g}$  tensor parallel to the alternate field  $\mathbf{B}_{ac}$ .

A third important finding is how this ZEFOZ condition can be generalized to any system with  $S = 1/2$  and half-integer  $I$  if the eigenvalues of the hyperfine tensor are all different and non-zero. In these conditions, the hyperfine levels are always non-degenerate and can be expressed as maximally entangled eigenstates similarly to the set 4.1. Even an additional quadrupolar interaction of the form  $\mathbf{I} \cdot \mathbf{Q} \cdot \mathbf{I}$  does not change the symmetry of the wavefunctions.

Before comparing these theoretical results with the experiments, we still have another interesting field regime that requires our attention.

## 4.2 Near-ZEFOZ

Even at a non-zero field, if it is applied along specific directions, the coherence can be preserved. Though not fulfilling exactly the ZEFOZ condition, we find that the gradient of the magnetic sensitivity of the transitions can be kept small with respect to the second order term. The phenomenon has its origin in the strong anisotropy of the  $A$  tensors. As already mentioned in chapter 3, both  $A$  and  $g$  have one component much stronger than the other two, and they are almost parallel. This can be seen by writing the magnitude of the gradient  $\mathbf{S}_1$  explicitly, assuming  $A_z$  and  $g_z$  are the strongest components and that they are parallel. Firstly, the contribution of a small magnetic field can be treated as a perturbation to the zero-field Bell states 4.1. Then, we can make use of equation 4.3 and calculate the first order energy shifts to the perturbed states, finally obtaining, for the specific case of the 655 MHz hyperfine transition <sup>1</sup>:

$$|\mathbf{S}_1| = 2\mu_B^2 \sqrt{\frac{B_z^2 g_z^4}{(A_x - A_y)^2} + \frac{B_y^2 g_y^4 A_x^2}{(A_x^2 - A_z^2)^2} + \frac{B_x^2 g_x^4 A_y^2}{(A_y^2 - A_z^2)^2}}. \quad (4.6)$$

A way of seeing the effect of the strong asymmetry is by enforcing the conditions  $A_z \gg A_x, A_y$  and  $g_z \gg g_x, g_y$ . It then becomes clear that to minimize  $\mathbf{S}_1$  the field needs to be oriented on the plane orthogonal to  $z$ . In this case, the equation above becomes

$$|\mathbf{S}_1| = 2\mu_B^2 \frac{B}{A_z^2} \sqrt{g_y^4 A_x^2 \sin^2(\phi) + g_x^4 A_y^2 \cos^2(\phi)}. \quad (4.7)$$

<sup>1</sup>In *Paper I*, a similar equation is reported, valid in particular for the 528 MHz transition instead



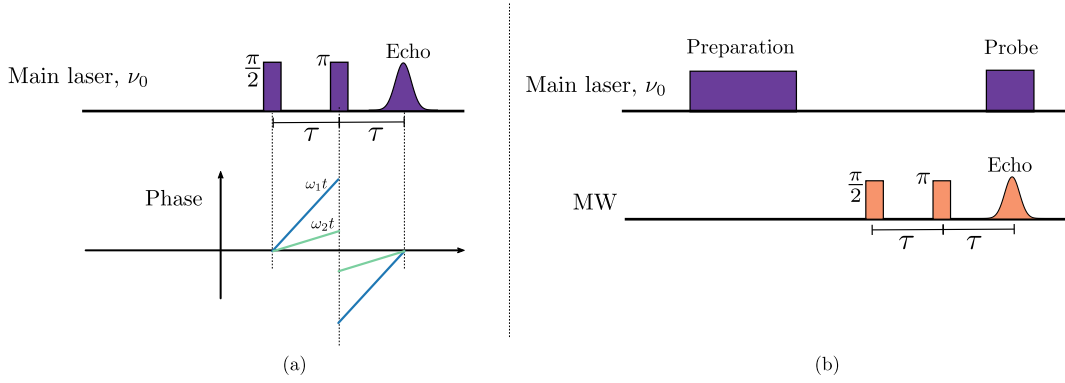


Figure 4.2: (a) Pulse sequence for photon echo experiments, with a sketch of the phase evolution of two random atoms below. After the  $\pi/2$  pulse, two atoms will evolve differently in phase due to the inhomogeneous broadening. After a time  $\tau$ , the  $\pi$  pulse inverts all phases, so that they converge again after another interval  $\tau$  and an echo is emitted. For convenience, a local oscillator separated by 3 MHz is always on and overlapped with the path of the emission from the crystal, and their interference is monitored. (b) Analogous sketch of the optically detected spin echo sequence. Here, the laser at  $\nu_0$  is used to pump the ions from the  $|\psi^+\rangle_g$  state to  $|\psi^-\rangle_g$  (see for reference figure 4.1). Then, a spin echo sequence is performed on the MW spin transition between the two states, with a similar induced phase evolution as for the photon echo in (a). At the time of echo emission, a probe pulse on  $\nu_0$  coherently scatters part of the emission into the optical  $\nu_1$  transition. A separate optical local oscillator at  $\nu_1 + 3\text{MHz}$  interferes on a balanced detector with the emitted signal, which is recorded from the corresponding beat.

The minima of this expression as a function of the angle  $\phi$  in the  $x - y$  plane give us conditions similar to a ZEFOZ in character but with non-zero, though weak,  $\mathbf{S}_1$  components. An explicit approximate calculation yields

$$|\mathbf{S}_1| \approx 2B\mu_B^2 g_x^2 \frac{A_y}{A_z^2} \sim 0.001\mu_B \sim \mu_N, \quad (4.8)$$

which means that, even if we are dealing with a Kramers ion with non-zero electronic spin, the actual sensitivity appears of the same order of magnitude as the nuclear moment. On the other hand, the considerations made for the zero-field ZEFOZ about the addressing of the spin transitions in equation 4.5 still hold, and the spin transitions involving spin flips still behave like purely electronic ones. Amazingly, it seems that Yb:YSO can offer the good properties of both Kramers and non-Kramers ions in low fields.

With this framework, we can now explain what happens in the laboratory. Before looking at the results, it is useful to have an overview of the techniques necessary for observing the coherence dynamics.

### 4.3 Coherence dynamics techniques

The most basic method of probing the evolution of coherence in atomic ensembles is the Hahn echo technique, developed initially in the field of nuclear

magnetic resonance<sup>52</sup>, and also called *spin echo* when applied to spin transitions or *photon echo* when in the optical range. Its main feature is the compensation of the dephasing induced by inhomogeneous broadening, which normally dominates the dynamics of an ensemble in its unprepared state. It starts by exciting part of the ensemble into a superposition of a ground and an excited state with a  $\pi/2$  pulse (in the sense of the rotation done by the Bloch vector of the atoms in the Bloch sphere). The different energies of each atom will make their phases evolve differently, leading to a loss of coherence. A  $\pi$  pulse at a time  $\tau$  after the first excitation with the same phase will invert the phase of each atom and allow a refocusing at a time  $2\tau$ , as shown in figure 4.2. By measuring the echo intensity as a function of  $\tau$ , the coherence time  $T_2$  of the transition can be extracted from the intensity of the signal

$$I(\tau) = I_0 e^{-4\frac{\tau}{T_2}}. \quad (4.9)$$

This coherence time can still be limited by other phenomena not due to inhomogeneous broadening affecting the dynamics in a timescale comparable to or smaller than the experiment duration.

The intensity of the echo can be read out directly on a photon detector or, in the case of spin echoes in our Yb-doped crystal, through interference with a reference signal as in Raman heterodyne scattering (RHS), as sketched in figure 4.2. In that case, a weak light pulse is applied to an optical transition connecting one of the ground sub-states of the spin transition with an excited state. Part of the spin superposition will be temporarily transferred and quickly fall back into the other ground sub-state while emitting coherently in the optical range.

Normally, one could use the beat of the scattered signal with the one at the probing frequency and detect the beat. For non-Kramers ions (nuclear spins) the RHS beat signal using the standard method is at a few tens of MHz, thus easily detectable with a photodiode with reasonable gain. The microwave-level splittings of Kramers (above  $\sim 0.5$  GHz) imply less detection gain, and the RHS beat signal becomes harder to detect. Our earlier attempts at detecting RHS were severely hampered by this effect, which led us to develop the following detection scheme: by using a local oscillator (LO), we can tune the frequency between the LO and the RHS signal, to obtain a beat signal in the range 1-10 MHz. This method allows an easy detection of RHS signals up to many GHz of spin transitions.

More in general, RHS has been used in similar investigations to probe the coherence of MW or microwave transitions from the optical domain<sup>53-56</sup>. With Hahn echo sequences and RHS, we collected all data in the following section.

## 4.4 Coherence results

Let us now look at the results obtained in the ZEFOZ and near-ZEFOZ regimes. Figure 4.4 shows some demonstrations of what a ZEFOZ means at the level of

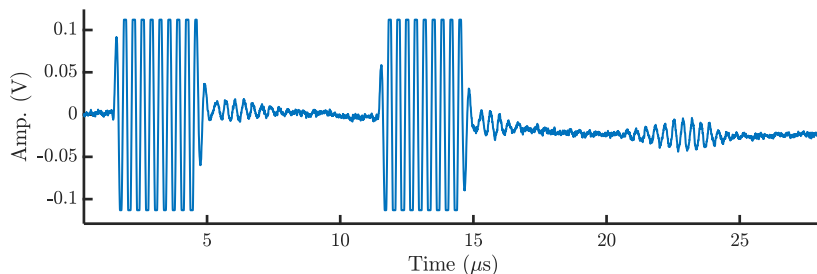


Figure 4.3: Example of the first spin echo signals obtained with the RHS technique, here at about  $23 \mu\text{s}$ , with the signal generated by the microwave pulses on the left. The echo intensity is measured from the frequency peak produced by recording an FFT around the echo pulse.

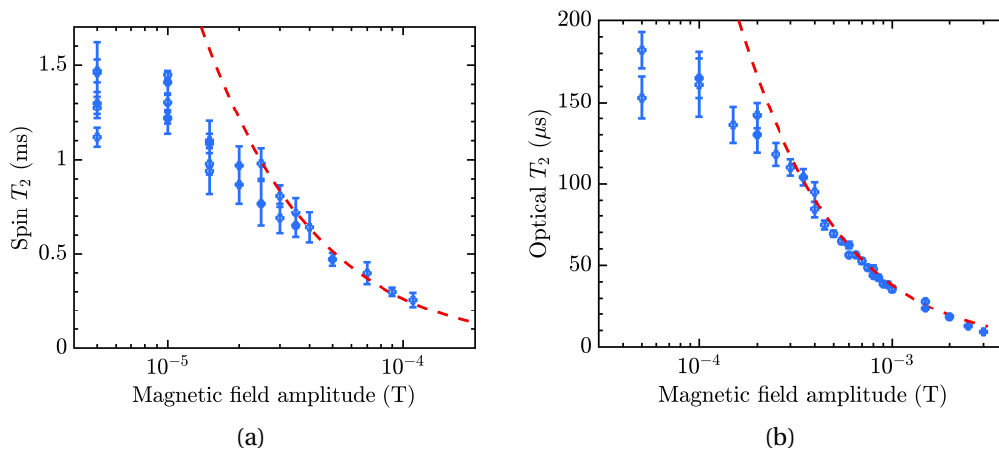


Figure 4.4: (a) Experimental spin  $T_2$  of the 655 MHz (blue dots), extracted from the decay of optically detected spin echoes, for small fields approaching the ZEFOZ condition along the  $b$  axis. Scattered points are due to measurement taken in different days, showing anyway consistent results. The dashed red line results from calculations of the  $T_2$  obtained from the model 4.2 and the  $\mathbf{A}$  tensor obtained in chapter 3, showing a mismatch possibly due to a residual bias magnetic field. (b) Optical  $T_2$  of the  $\nu_0$  transition from photon echo measurements for fields along  $D_1$  (blue dots) and related calculations (red dashed line) showing a similar mismatch between data and the model.

	Site I, 339 MHz	Site I, 823 MHz	Site II, 528 MHz	Site II, 655 MHz
$T_2$ (ms)	$1.30 \pm 0.05$	$1.47 \pm 0.08$	$2.4 \pm 0.4$	$1.47 \pm 0.12$

Table 4.1: Collection of spin coherence times extracted from spin echo measurements at different sites. The 655 MHz is the highest value of figure 4.4a, while the others were measured only once to confirm the ZEFOZ conditions for other transitions and sites.

the coherence time in our crystal. In this case, spin echoes on the  $|\psi^+\rangle_g \leftrightarrow |\psi^-\rangle_g$  transition at 655 MHz are optically detected via RHS and the corresponding coherence time extracted for each field amplitude from 0 to about 1 mT. Similarly, the optical coherence is probed by photon echoes on the  $|\psi^+\rangle_g \leftrightarrow |\psi^+\rangle_e$  transition. Close to zero, we measure the highest spin and optical  $T_2$  values of about 1.5 ms and 200  $\mu$ s respectively. The static field was oriented along the  $b$  crystal axis for the spin echo measurements and along  $D_1$  for the photon echo. Similar results were found for other configurations, including the 528 MHz transition of site II and the 339 and 823 MHz of site I, and summarized on table 4.1. The dashed lines in the figure show the results of fits of the magnetic noise magnitude  $|\Delta\mathbf{B}|$  from equation 4.2 and with  $\mathbf{S}_1$  and  $\mathbf{S}_2$  obtained from the full Hamiltonian characterized in chapter 3. The fits result in a field perturbation of about 3  $\mu$ T, though the data deviates as the external applied field magnitude approaches zero. This might be due to a residual bias field that we were not able to compensate with our coils, estimated to be lower than 15  $\mu$ T, which might have prevented us from reaching the full ZEFOZ condition.

Let us now increase a bit the magnetic field. The first order Zeeman term will now cease to be negligible. However, we have seen in section 4.2 that, if we avoid to point the field along the axis with the strongest  $\mathbf{A}$  and  $\mathbf{g}$  components, we can get away with a very weak linear sensitivity  $|\mathbf{S}_1|$  by finding the minima of equation 4.7. In practice, finding these minima is complicated by the mismatch between the reference frame in which  $\mathbf{A}$  is diagonal and the laboratory one. We can however build a section of a map as in figure 4.5a, where a "valley" of minima can be seen in a plane intersecting the  $x - y$  one above. The map is obtained by numerically calculating  $|\mathbf{S}_1|$  from the full Hamiltonian at each coordinate. This new plane is matched to the points of maximum spin coherence time we measured, indicated in the same figure. The main axes of the laboratory frame roughly corresponds to the extinction axes  $(D_1, D_2, b)$ , with  $\theta$  the angle of the field along the  $D_1 - b$  plane and  $\varphi$  on the  $D_1 - D_2$  plane (see also figure 4.6). We can also see the good matching of the optical and spin minima of the sensitivity in figure 4.5b, where the optimal angle for  $\theta$  is plotted against  $\varphi$ . The measured points for the spin echo perfectly align with the model and similarly for the calculated positions of the minima for the optical transition  $\nu_0$ .

More details on what happens around a near-ZEFOZ, for fixed  $\varphi$  and varying  $\theta$ , are shown in figure 4.5c, highlighting the directional dependence of  $T_2$  and a

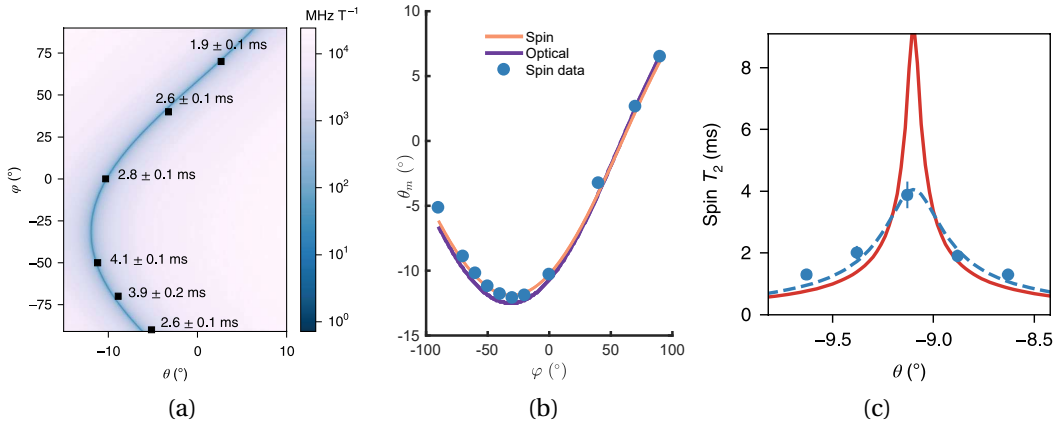


Figure 4.5: (a) Map in spherical coordinates (defined in figure 4.6) of the calculated first order Zeeman variation  $|S_1|$ , showing the "valley" of minima with some of the coherence times we measured, with a 5 mT field amplitude. (b) Position of the optimal angle  $\theta_m$  leading to a minimum of  $|S_1|$  as a function of the other angle  $\varphi$ , measured for the spin transition (blue dots) along with its model (orange line) and the calculated results for the optical transition  $\nu_0$  (purple line), showing matching orientations. (c) Spin  $T_2$  as measured in a small range of angles  $\theta$  around a maximum for fixed  $\varphi = -70^\circ$  (blue dots). The red solid line results from our model, showing a peak at more than double the maximum value we measure. The model can be matched to the data by assuming an inhomogeneity of the generated static field of about  $0.5\%/\text{cm}^3$ .

maximum coherence time of 4 ms. The data can be compared to a simple model based on equation 4.2 with the calculated  $S_1$  and assuming a noise magnitude of  $|\Delta B| = 3\mu\text{T}$  (solid line). The mismatch in maximum achievable coherence time can be explained by the inhomogeneity of the field generated by the coils on the crystal, which in the calculations corresponding to the dashed line is  $0.5\%/\text{cm}^3$ .

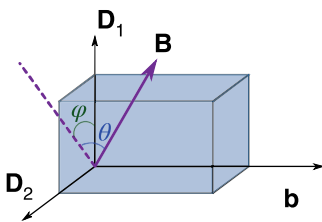


Figure 4.6: Sketch of the crystal with its polarization extinction axes and the  $\theta$  and  $\varphi$  angles used approximately as the lab reference frame for the magnetic field studies.

More explicit examples of echo decays can be seen in figure 4.7. The spin  $T_2$  can change of a factor of 3 by moving away of just  $0.5^\circ$  from the near-ZEFOZ. On the other hand, the optical coherence seems more resilient, as shown by a similar curve collected at slightly different field conditions in figure 4.8a, with a  $T_2$  of  $200\mu\text{s}$ . Going back to the spin echo decay, a more detailed analysis as in figure 4.7b highlights the presence of fast oscillations, which we attribute to a possible spin super-hyperfine interaction between  $^{171}\text{Yb}^{3+}$  and neighboring  $^{89}\text{Y}^{3+}$  ions. In that case, the oscillations would arise as a beat due to an additional splitting of the hyperfine levels from to the field generated by the yttrium. Similar effects have been observed in other Kramers ions<sup>57</sup>.

Besides technical issues such as field misalignment and inhomogeneity, the coherence time can be limited by relaxation processes. Figure 4.8b compares data acquired at the near-ZEFOZ condition from spin echoes curves with what

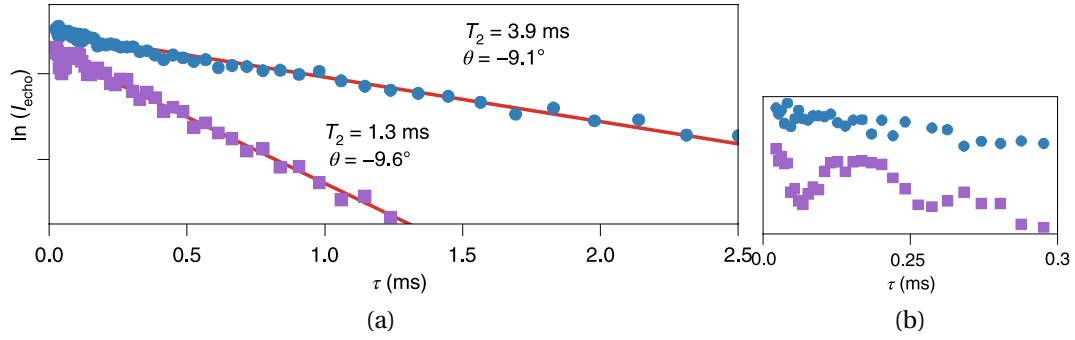


Figure 4.7: (a) Examples of spin echo decay curves in logarithmic scale, with dots and squares indicating data points and solid lines indicating linear fits. A variation of  $0.5^\circ$  is capable of changing the  $T_2$  by a factor 3. (b) Zoom on the first  $300\ \mu\text{s}$  of (a), showing oscillations possibly originating from a super-hyperfine interaction between  $^{171}\text{Yb}^{3+}$  and  $^{89}\text{Y}^{3+}$  ions of the host lattice.

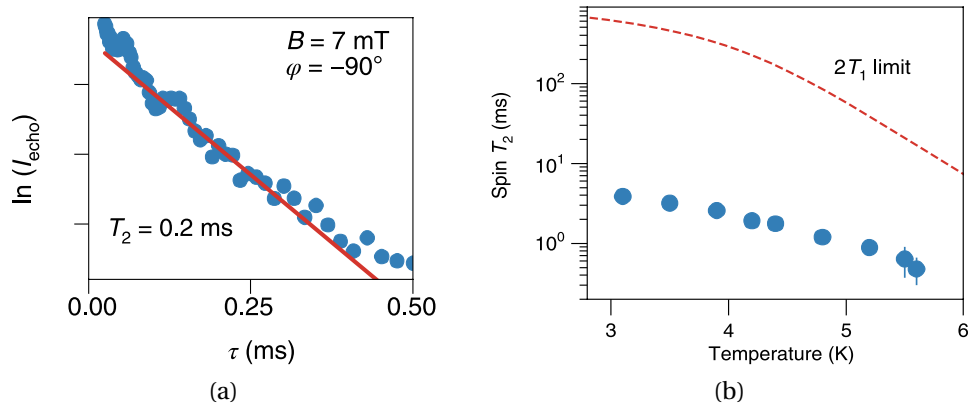


Figure 4.8: (a) Example of photon echo decay at close to the near-ZEFOZ condition. The optical transition seems to be less sensitive to the angle variations with respect to the spins. (b) Spin  $T_2$  measured at near-ZEFOZ as a function of temperature (blue dots) compared to the spin-lattice population lifetime limit obtained from the measurements of Lim et al.<sup>58</sup> (red dashed line). The mismatch could be given by additional spectral diffusion and Yb-Yb spin interactions.

we expect from spin-lattice relaxation processes measured by Lim et al.<sup>58</sup> up to a temperature of about 5.5 K. The gap might be explained by spin-spin interactions between adjacent Yb ions, leading a decrease in  $T_1$  of the ground hyperfine states and spectral diffusion. Additionally, the aforementioned super-hyperfine interaction can also modify the transition gradients, though the oscillations appear to be quenched when the field approaches the near-ZEFOZ condition.

We briefly attempted dynamical decoupling (DD) of the spin transitions, which can help attenuate the decoherence induced by spectral diffusion (we will see more details on DD in chapter 7). As shown in figure 4.9, if we align a  $-300\ \mu\text{T}$  field with the  $b$  axis, we obtain a spin  $T_2$  of  $114\ \mu\text{s}$ , in agreement with the behavior we saw on the plot 4.4b. However, by repeating  $N$  times a decoupling pulse after the first excitation while keeping the distance between pulses  $\tau = 20\ \mu\text{s}$ , we are able to increase the coherence time to  $658\ \mu\text{s}$ , a factor of 6. This is just a proof of

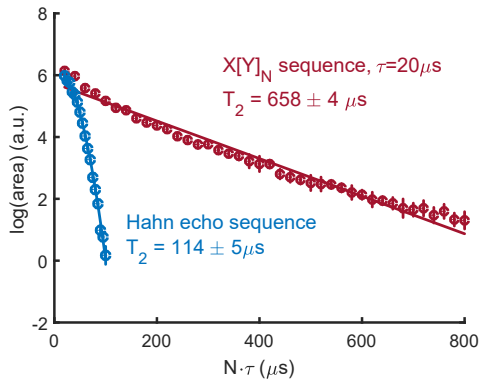


Figure 4.9: Example of dynamical decoupling effect outside of the coherence enhancement regions, with  $-300 \mu\text{T}$  along the  $b$  axis. By applying an  $X[Y]_N$  sequence, the coherence time is enhanced by a factor of 6.

concept showing that spectral diffusion is present at least outside of the ZEFOZ and near-ZEFOZ conditions. On the other hand, DD did not produce a measurable difference in the coherence time of the spins when already at the enhancement conditions.

Spectral diffusion and dynamical decoupling in Yb:YSO are discussed more in detail in the aforementioned work of Lim et al.<sup>58</sup> and later in our group by Businger et al.<sup>45</sup> and Welinski et al.<sup>44</sup> In the latter work in particular, other diffusion processes due to spin flip-flops are identified as the limiting contributions to the coherence time of both optical and spin transitions at ZEFOZ, while instantaneous spectral diffusion was not observed on photon echoes.

To conclude this chapter on coherence dynamics, we give an overview of the results obtained at different conditions in table 4.2.

	ZEFOZ		near-ZEFOZ		DD test	
	Spin	Optical	Spin	Optical	Spin, no DD	Spin, DD
$T_2$ (ms)	1.3-2.4	0.15-0.18	1.9-4.1	0.20	0.114	0.658

Table 4.2: Summary table with ranges of coherence time measured for spin and optical transitions at ZEFOZ, near-ZEFOZ and the spin dynamical decoupling test.

## 4.5 Conclusions and outlook

This concludes the part of this thesis on ytterbium. We have seen that complementing the high field results of Welinski et al.<sup>43</sup> with spectral hole burning and magnetic resonance at low field leads to rich spectral features in chapter 3. The exploration of the coherence dynamics by means of Hahn echoes and RHS revealed the potential of such a hybrid system of electronic and nuclear spins, which at zero field and at specific directions of low fields offers a combination of what makes Kramers and non-Kramers ions good for coherence preservation and manipulation. Parallel work also explored population and coherence dynamics at

higher fields, finding extensions of the spin-lattice relaxation lifetimes up to 5 s and coherence times up to 0.5 ms via dynamical decoupling<sup>58</sup>.

Our findings opened  $^{171}\text{Yb}^{3+}:\text{Y}_2\text{SiO}_5$  to several prospective applications and developments. Quantum memories can benefit from the long coherence times, relatively simple hyperfine structure, accessible MW transitions for efficient rephasing and dynamical decoupling, and the field conditions that make superconducting coils and high fields unnecessary. But another precious feature, painfully lacking in other promising species such as europium and praseodymium, is given by the large zero-field hyperfine splittings, which make this platform compatible with broadband optical inputs and hence a high time multimode capacity. The importance of these properties will become clearer in the second part of this thesis, when described in the context of the memory protocol implemented in  $^{151}\text{Eu}^{3+}:\text{Y}_2\text{SiO}_5$ .

The spectroscopy of  $^{171}\text{Yb}^{3+}$  developed into more findings from another collaboration with Goldner's group<sup>44</sup>, leading to the characterization of a collective pumping effect due to spin-spin interactions that extended the optical coherence time to 0.8 ms. Businger et al.<sup>45</sup> finally implemented a full AFC spin-wave memory protocol in  $^{171}\text{Yb}^{3+}:\text{Y}_2\text{SiO}_5$  with a storage time of 1.2 ms and a bandwidth of 10 MHz, limited at the time by the maximum power of the optical pulses. This proof of concept was the first demonstration of memory involving the electronic spin states in a Kramers ion, which paved the way for future work at the single photon level with improvements in bandwidth and efficiency.

The generality of the conditions giving rise to the ZEFOZ regime are promising for other similar species, like other Kramers ions such as  $^{167}\text{Er}^{3+}$ <sup>26,56,59</sup> and single molecule magnets with rare earths<sup>60,61</sup>. NV centers in diamonds can also show simultaneous ZEFOZ for multiple transitions<sup>62,63</sup>, though arising from different fundamental reasons. Additionally, the possibility of strong coupling with MW signals and the zero-field operative conditions are an opportunity for interfaces with superconducting qubits<sup>64,65</sup>.





## Eu:YSO - introduction

When I started working in the europium lab, the setup was more or less the same that led to the results of Jobez et al. in 2015<sup>66</sup> for the spin-wave memory and Laplane et al. in 2017<sup>67</sup> for the AFC-DLCZ. We knew that some limitations were purely technical, and some others a bit less understood. In particular, there were three main aspects that needed some work:

1. The atomic frequency comb efficiency was still far from the theoretical limit of 54 %<sup>35</sup> and its effective coherence lifetime was below the more fundamental bound of  $380 \mu\text{s}$  imposed by the latest photon echo measurement<sup>68</sup>, which in turn was much lower than the population lifetime of the excited state of  $1.9 \text{ ms}$ <sup>69</sup>.
2. Similarly, the lifetime of the storage efficiency was abysmally lower than the population lifetime of 20 days observed in Eu:YSO<sup>70</sup>, or even than the more approachable coherence times measured with dynamical decoupling sequences<sup>71</sup>. Moreover, the transfer of coherence into the spin transition and following readout was done with sub-optimal efficiency, with an estimated 50 % optical-to-spin population transfer, while spin rephasing error rates of 3.6 and 0.2 % were obtained depending on the rephasing sequence<sup>66</sup>.
3. Noise at the single photon level limited the SNR in the spin-wave memory and the cross correlation between the two delayed photons in the AFC-DLCZ.

In the following chapters, these three problems will be addressed separately. The last chapter of this part will instead focus on the experiments on single photon-level spin storage, time-bin qubit storage, and the AFC-DLCZ protocol.

## 5.1 Properties of europium in yttrium orthosilicate

With atomic number 63, europium is halfway through the row of the lanthanoids in the periodic table. I will give here a brief summary of its spectroscopic properties when used as a dopant in host crystal, while more details can be found in more general literature<sup>72</sup>. When doping a  $\text{Y}_2\text{SiO}_5$  crystal, it ionizes to a 3+ configuration, keeping six unpaired electrons in the  $4f$  shell, and it takes the place of Y (the most similar species in the host in size, also with a 3+ state) in two possible crystallographic sites with  $C_1$  symmetry, each of which can have two possible magnetically inequivalent sub-sites. The crystal field, considered as a perturbation to the free ion and spin-orbit Hamiltonian components, completely lifts the degeneracy of the spin-orbit levels ( $\text{Eu}^{3+}$  is a non-Kramers ion given its even number of electrons in its open  $4f$  shell), among which we find the ground level  ${}^7F_0$  and the excited  ${}^5D_0$  used in our applications. Although transitions between  $4f$  states, as well as states with both  $J = 0$ , are normally forbidden, the crystal field in  $\text{Y}_2\text{SiO}_5$  partially mixes the  ${}^7F_0$  state with other electronic states of different  $J$  and parity, making the  ${}^7F_0 \rightarrow {}^5D_0$  transition weakly allowed. The zero angular momentum of both ground and excited states makes this transition peculiar among rare earths as it results in small magnetic and crystal field interactions with the host species, enabling in principle higher optical coherence times. This transition can be addressed with yellow light at slightly different wavelengths for the two crystallographic sites. At a few Kelvin, the two are spectrally well separated, with a FWHM of about 2.5 GHz, and centered at 580.04 nm and 580.21 nm in vacuum<sup>70</sup>, respectively. In literature, the sites are indicated namely as *site I* and *II*, the former being the most used in quantum information applications given its higher absorption coefficient<sup>70</sup>. In fact, all the optical transitions we will see in the following chapters occur between the  ${}^7F_0$  and  ${}^5D_0$  of site I, of which we can see the absorption resonance in figure 5.1b for light linearly polarized along the  $D_1$  axis of  $\text{Y}_2\text{SiO}_5$ .

At a finer level, we find substructures dominated by nuclear spin effects, since the crystal field effectively quenches the contributions to the Hamiltonian of the electronic Zeeman and electronic-nuclear hyperfine interactions at first order. This is why we can simplify the Hamiltonian of the system for our applications as<sup>73,74</sup>:

$$\mathcal{H}_{\text{Eu}} = \mathbf{I} \cdot \mathbf{Q} \cdot \mathbf{I} + \mathbf{B} \cdot \mathbf{Z} \cdot \mathbf{I}, \quad (5.1)$$

where  $\mathbf{I}$  indicates the nuclear spin vector ( $I = 5/2$  in  ${}^{151}\text{Eu}^{3+}$ ),  $\mathbf{Q}$  the quadrupolar interaction matrix,  $\mathbf{Z}$  the nuclear Zeeman interaction matrix and  $\mathbf{B}$  the external magnetic field vector. Even without a field, the quadrupolar interaction partially lifts the degeneracy given by the nuclear spin. The dominance of nuclear effects over hyperfine and electronic Zeeman interactions is typical of non-Kramers ions

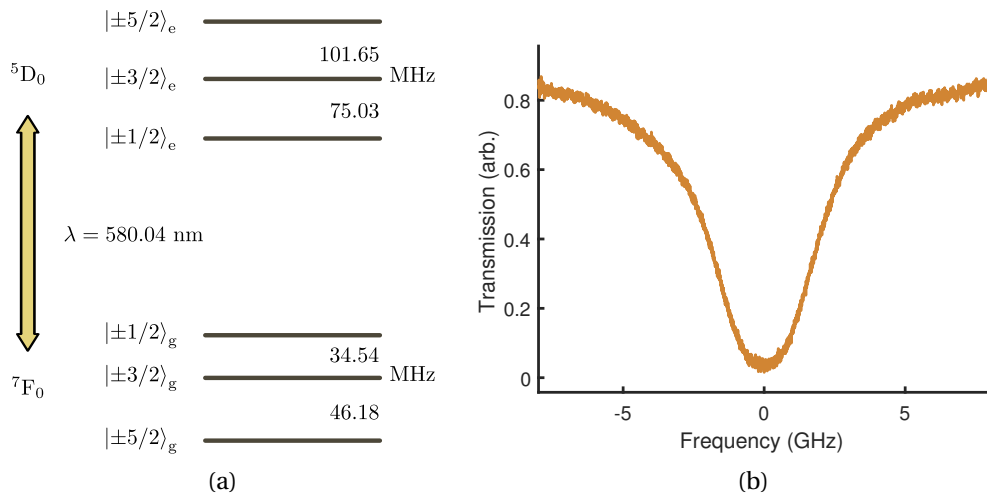


Figure 5.1: (a) Energy structure diagram of  $^{151}\text{Eu}^{3+}:\text{Y}_2\text{SiO}_5$  at zero field, corresponding to the effective Hamiltonian 5.1. (b) Transmitted signal through our memory  $^{151}\text{Eu}^{3+}:\text{Y}_2\text{SiO}_5$  crystal swept over the  ${}^7\text{F}_0 \rightarrow {}^5\text{D}_0$  resonance of site I. The nuclear structure is completely hidden by the inhomogeneous broadening.

and it makes their nuclear spin sub-states particularly insensitive to magnetic field perturbations, hence excellent candidates for long storage memories, although this also reduces the interaction strength with controlled RF and microwave fields for active decoupling and spin rephasing. Even among non-Kramers, the ground state of Eu:YSO has an unusually weak magnetic sensitivity, thanks to compensating effects coming from the mixing to other states induced by the crystal field<sup>75,76</sup>. The excited state, which is subject to less mixing, has wider splittings.

The magnitudes of the nuclear interactions depend also on the specific isotope. Natural europium comes with an almost even balance between isotopes  $^{151}\text{Eu}$  and  $^{153}\text{Eu}$ , both with total nuclear spin  $I = 5/2$ , but crystal samples for applications are often enriched specifically with one of them with percentages close to 99%. The main differences relevant for our applications are the different quadrupolar splittings, as they fundamentally limit the maximum bandwidth of a memory (see for instance section 6.1), and the sensitivity to external magnetic field perturbations which can affect the spin coherence time. In this work, we will use the isotope  $^{151}\text{Eu}$ , though investigations on  $^{153}\text{Eu}$  can be also found in other publications (see for instance Timoney et al., 2012<sup>77</sup>).

At this point, we can specify the relevant energy level structure as in figure 5.1a that will accompany us for all the experiments we are going to see here. With no magnetic field, both the ground and the excited states will have three doublets, one for each value  $|m_I|$  of the nuclear magnetic number. The latter is not a good quantum number due to mixing, particularly for the ground state, so it is to be considered as a qualitative character of the energy level. Starting from separations of tens of MHz, the doublets split under a constant magnetic field with gradients of about  $\sim 10\text{MHz/T}$ . The nuclear energy structure remains however covered at low



Figure 5.2: Custom isolation box for two 1160 nm laser sources (stacked vertically on the right of the picture) and the high finesse optical cavity used for frequency stabilization (inside a vacuum chamber, on the left). Of the two lasers, only the one below, not visible here, is used in the experiments described in this thesis. This arrangement allows to spatially decouple the sources from the rest of the setup, connected via optical fibers, and improve thermal and acoustic stability. As a results, the frequency lock could operate continuously without human intervention for multiple consecutive months.

fields by the optical inhomogeneous broadening, requiring a full class cleaning procedure for the memory protocols we will see in the next chapters.

## 5.2 Experimental setup

The general setup for the experiments on Eu:YSO was revisited during this work, involving in particular improvements in the management of the optical power reaching multiple experiments in the same laboratory and a complete redesign of the part dedicated to the frequency stabilization of the laser sources. For the works presented in this thesis, the setup used for europium experiments starts with a Toptica external cavity laser diode with a wavelength of 1160 nm. The output beam is split into two paths, one directed to the locking system and one to the frequency conversion system. The locking setup consists of a Pound-Drever-Hall system<sup>78,79</sup> with an optical cavity of finesse around  $\sim 10^5$ . The cavity and source laser are placed in a custom made box to isolate it from the lab environment and to enhance thermal and acoustic stability (see also section 6.2.2). The component of light to be converted is firstly amplified to about 10 W by a fiber-based ytterbium Raman amplifier from MPB Communications and converted to a wavelength of 580 nm via second harmonic generation in a bulk PPLN crystal. At this point, the optical power is typically 1.8 W and the polarization

linear. The beam is then directed through a cascade of acousto-optic modulators (AOM) to generate the various optical channels needed for the experiments. Each AOM is set in a double-pass configuration, so that when a channel is on, the first diffracted mode (+1) is back-reflected and its polarization rotated so that it can be separated from the main beam at a polarized beam splitter (PBS) and coupled into a polarization-maintaining optical fiber with its output on a specific spatial mode of the experiment. The AOMs are controlled electronically by programmable arbitrary wave generators (AWG) and are capable to generate signals as fast as  $\sim 10$  ns (rise and fall times) in a range of about 400 MHz in double pass.

Though the specific number and use of each optical channel may vary depending on the experiment, the setup thus built is capable of controlling up to 5 independent optical channels, corresponding to separate spatial modes:

- the *transfer*, typically used for high-efficiency transfer of atoms in the spin-wave memory, or *read* in the AFC-DLCZ protocol
- the *memory preparation* for wide frequency tailoring of the inhomogeneous broadening in the memory crystal, e.g. class cleaning, pit burning, AFC
- the *filter preparation*, for tailoring of the absorption and transparency windows of the filter crystals used in photon-counting experiments
- the *input*, used mainly to create the pulses to be stored in AFC and spin storage and as a probe in frequency-swept readouts
- the *write*, specifically made for the write pulse of the AFC-DLCZ experiment.

On a separate optical table, the outputs of the optical fibers of the channels are arranged depending on their role around the memory and filter crystals, which are placed inside a cryostat with access windows on two directions and on two optical planes. The upper one (figure 5.3a) includes the memory crystal used in all experiments with the  $D_1$  axis oriented vertically in the lab frame. The transfer, memory preparation and input beams all overlap on the crystal with different waist sizes to maximize preparation homogeneity and transfer efficiency, and they propagate along the  $b$  axis within a couple of degrees. In order to enhance the overall optical depth of the memory, the input beam can be deflected to re-enter the cold chamber from the same side with appropriate mirrors. For experiments with bright pulses, the input path ends on a linear photodetector, while when photon counting is necessary it is redirected with a flip mirror into a fiber with output on the filter setup on the lower optical plane. This same path is used for the Stokes emission of the DLCZ experiment of section 8.3, while its anti-Stokes counterpart is collected in the backwards direction from a combination of a waveplate, Faraday rotator and polarized beam splitter (PBS). Always for the DLCZ, the read beam corresponds to the transfer, and the write beam path overlaps the read in the opposite direction.

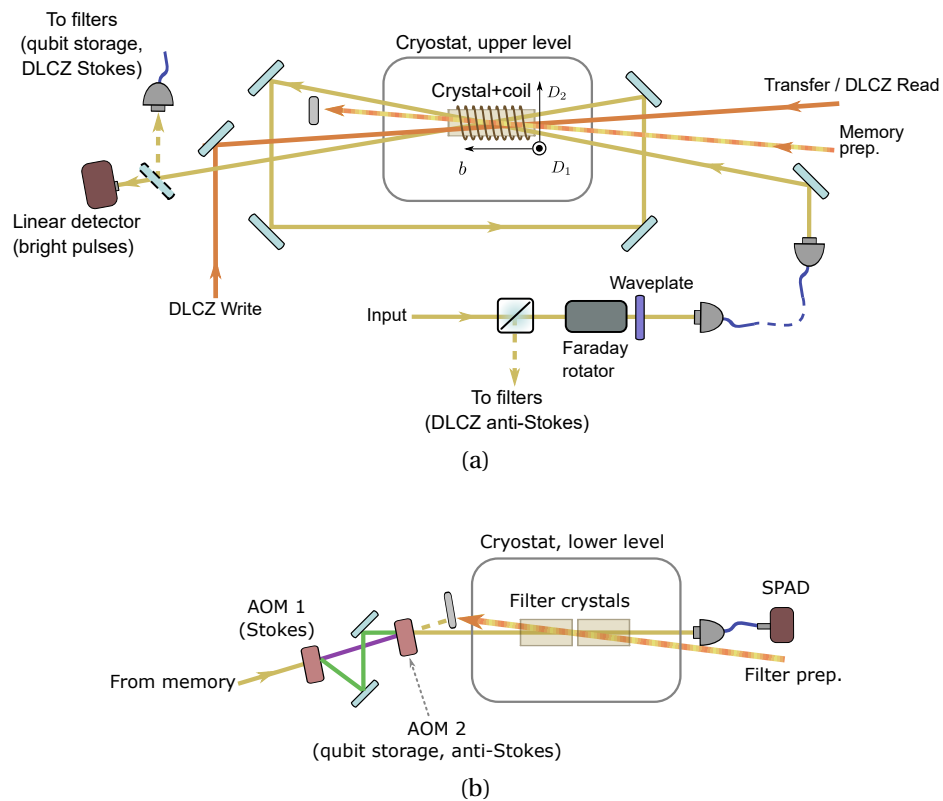


Figure 5.3: Simplified sketch of the experimental setup around the cryostat (all angles between optical paths are exaggerated for clarity). (a) Upper optical plane, on which the memory crystal is placed with the orientation of the axes indicated and the RF coil, as well as all the optical beams interacting with it. For photon counting experiments, spin storage output and Stokes photons of the DLCZ are redirected with a flip mirror into a filtering setup. Similarly, anti-Stokes of the DLCZ are separated from the input path by a polarization rotation assembly. (b) The lower optical plane on which the filtering crystals are located, used only in experiments with single-photon level light. When reading out the output of the spin storage or anti-Stokes, only AOM 2 is active and the light takes the path highlighted in purple. When detecting Stokes photon, light is deflected only by AOM 1 and it follows the green path. The two paths overlap after AOM 2, cross the crystals, and finally reach the fiber-coupled single photon detector.

The lower optical plane hosts the optical filter setup, with the filter crystals at its core (figure 5.3b). AOMs are used here to gate in time and shift in frequency the output photons, before re-entering the cold chamber of the cryostat. Here, two Eu:YSO crystals are used in series for a higher optical depth. They have their inhomogeneous linewidth tailored by the filter preparation beam and act as frequency band-pass filters with up to two simultaneously transparent spectral regions depending on the experiment. After this, the beam is finally coupled into a fiber connected directly to a single photon avalanche detector (SPAD).

As we have seen, this overall configuration of the optical setup is designed for flexibility between different types of experiments, given by the possibility of diverting the paths on different detectors, with large sections of bulk optics connected by polarization maintaining fibers to aid spatial path and polarization stability.

The custom copper mount holding the crystals is thermally connected to a cold platform and placed on top of a soft layer to dampen vibrations (more on this in section 6.2.3). A coil for radio-frequency generation surrounds the memory crystal around the  $b$  axis without touching it, anchored on a separate custom copper mount and electrically connected to a resonator circuit (characterized in detail in section 7.3). The cryostat (Montana Cryostation, 2012 year model) is based on a closed-cycle helium cryocooler, capable of reaching a minimum temperature of about 3 K on its last platform (about 3.5 K on the anti-vibration crystal mount). The setup is completed with a *coil hat*, a set of coils mounted on a custom structure fitted for the cold chamber of the cryostat as visible in figure 5.4, used to apply magnetic static fields up to about 2 mT.

Data collection is carried out by an oscilloscope for bright pulses experiments, controlled by Matlab scripts for long and repetitive acquisition sessions. When photon counting, an ID Quantique ID900 controls the gating of the filter AOMs and the single photon detector, while at the same time collecting detections and transferring them to the computer for storage. Our implementation of the DLCZ experiment additionally requires conditional triggers based on the detection of

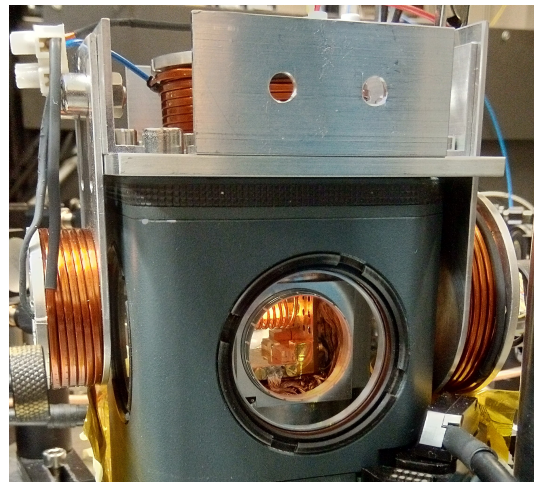


Figure 5.4: Cryostat cold chamber with coil hat, capable of generating static bias fields up to a couple of millitesla. Only the top one, with its axis aligned to the  $D_1$  extinction axis of the crystal, is used in the experiments reported in the following chapters. Inside the cold chamber, the memory crystal is illuminated by the laser. The small coil used to generate our RF pulses is also visible, enveloping the crystal along the  $b$  axis. The two filter crystals are glued on the level just below with their  $b$  axis orthogonal to the memory one.



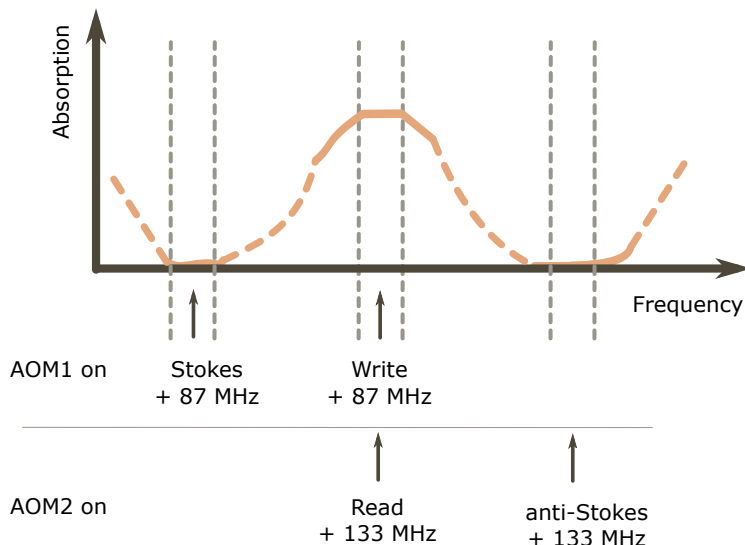


Figure 5.5: Sketch of the absorption spectrum of the filter crystals after preparation for the AFC-DLCZ experiment. The dashed portions of the absorption line indicate untailored regions. Portions enclosed within gray dashed lines indicate the tailored windows for optimal absorption or transparency. Below, the signals of the DLCZ experiment are matched to the tailored frequency windows by different AOMs depending whether the Stokes or anti-Stokes detection gate is active. For single-photon level input-output memories other than the DLCZ, the transparency at the lowest frequency is not needed and only AOM2 is used.

a Stokes photon, again controlled by the ID900. More details on the use of the beams, electronics and pulse sequences are provided in the chapters dedicated to the respective experiments.

### 5.2.1 Frequency filtering through Eu:YSO crystals

The same type of crystals used as a memory can be easily employed as optical filters<sup>80–83</sup>. The inhomogeneous absorption spectrum can be tailored by selecting to pump specific frequencies similarly to what we do during pit burning and class cleaning. For the input-output protocols at the single photon level such as those presented in sections 8.1 and 8.2, we need just one transparency window at the frequency of the AFC emission,  $|g\rangle \leftrightarrow |e\rangle$ , and an absorption window at optical transfer frequency  $|s\rangle \leftrightarrow |e\rangle$  to absorb any scattered components. In this case, we measured a maximum optical depth of 7.4 in the absorption window, which brings an extinction ratio of 1636 : 1. The two filtering crystals in figure 5.3b are prepared by pumping all atomic classes in order to have population accumulating at the transfer transition frequency plus a shift of 133 MHz, corresponding to the shift applied by the AOM on the scattered mode when the detection temporal gate is open. Similarly, the frequency of the AFC emission plus the same shift is burned to make sure the output photons from the memory will not be absorbed. The two tailored windows also need to have a width at least matching the AFC bandwidth, which was typically of 2 MHz.

In the case of the AFC-DLCZ of section 8.3, the situation is a bit more complicated. When the anti-Stokes detection gate is open, we need to do the same thing as before. However, when the Stokes gate is open, the absorption and transmission frequencies of the filters need to be inverted. Instead, we decided to apply a lower shift to the Stokes photons so that they will match a separate transparency at a frequency lower than the absorption one. The latter, at the same time, will be matched by the same shift to any scattered light at the AFC frequency. This is the reason why we use two different AOMs: AOM1 is turned on only during Stokes acquisition and applies a different shift of 87 MHz, while AOM2 operates exactly as for the standard storage. The frequency shifts of the two AOMs are chosen so to use two transparency windows and only one absorption window, making the pumping of all classes contributing to the absorption simpler. The situation is schematized in figure 5.5.



## The atomic frequency comb

*Some of the results of this chapter are reported in our publications labeled as **Paper IV**, submitted to *npj Quantum information*, "Storage of photonic time bin qubits up to 20 ms in a rare-earth doped crystal", and **Paper V**, "Multimode capacity of atomic frequency comb quantum memories" (manuscript to be submitted).*

### 6.1 Introduction

The atomic frequency comb (AFC) is a protocol for rephasing excited atoms in an inhomogeneous broadened transition. It has been introduced by Afzelius et al.<sup>35</sup> back in 2009 and demonstrated experimentally first in Nd:YVO in 2008<sup>84</sup>. Since then it has been used in many other experiments of light storage in various types of rare earth ensembles, e.g. Tm:YAG<sup>85</sup>, Nd:YLF<sup>86</sup>, thulium in Ti:LiNbO<sub>3</sub> waveguides<sup>87</sup>, Yb:YSO<sup>45</sup> to name a few, including the storage of entanglement in Nd:YSO<sup>88</sup> and Pr:YSO<sup>89</sup>.

The AFC consists in burning several pits in the inhomogeneous broadening of a transition  $|g\rangle \rightarrow |e\rangle$  so to leave equally distanced peaks of absorption, in a structure resembling a comb. All atoms but the ones satisfying a periodicity condition in frequency  $\delta = m\Delta$ , with  $m$  an integer and  $\Delta$  the spacing between the "teeth" of the AFC, are pumped away into an auxiliary state  $|aux\rangle$ , so that in theory the remaining frequency spectrum in  $|g\rangle$  becomes a series of equally spaced delta functions. The whole width of the periodic structure defines the bandwidth of the comb  $\Gamma$ .

If we now consider a single photon impinging on the AFC structure along a transition  $|g\rangle \rightarrow |e\rangle$ , at the condition that the spectral width of the photon is lower than the total AFC bandwidth, it will be absorbed by the ensemble of all  $N$  atoms in a collective Dicke state,

$$|\psi\rangle_{\text{AFC}} = \sum_{j=1}^N c_j e^{2\pi i \delta_j t} e^{2\pi i k z_j} |g_1, \dots, e_j, \dots, g_N\rangle, \quad (6.1)$$

which is a superposition of all possible states in which an atom is excited and all

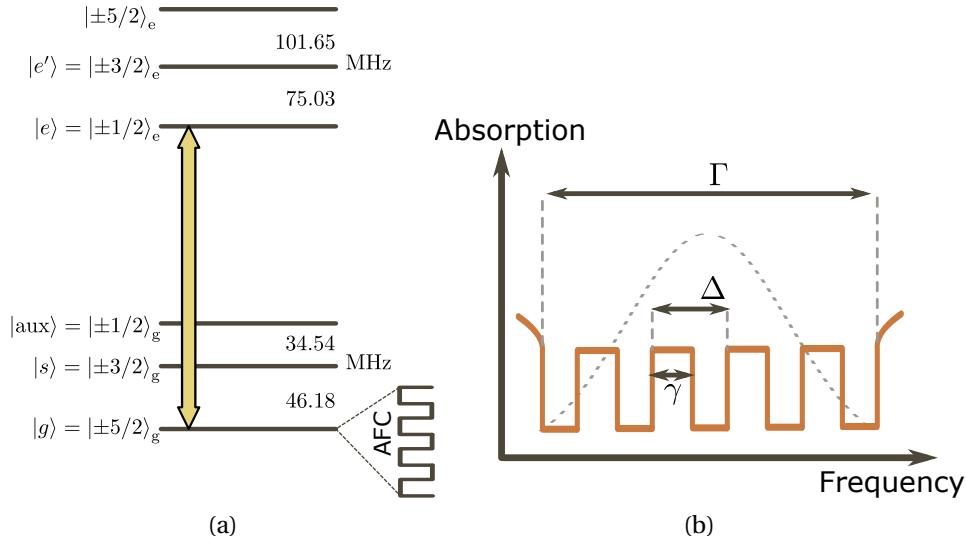


Figure 6.1: (a) Eu:YSO hyperfine structure with the AFC transition and the relevant states. (b) Sketch of an AFC absorption profile with square teeth, as it would be seen on the  $|g\rangle \leftrightarrow |e\rangle$  transition, with the bandwidth  $\Gamma$ , teeth width  $\gamma$  and periodicity  $\Delta$ . The dashed curve indicates the how the profile of an input photon to be stored can overlap the comb along its bandwidth.

others on the ground, with their respective amplitudes  $c_j$  and phase coefficients due to different detuning  $\delta_j$  and position  $z_j$ . By preparing the teeth structure with a specific periodicity  $\Delta$ , we make sure that all atoms will rephase after a time  $1/\Delta$ , thus inducing a constructive interference of their emission probabilities and generating an echo<sup>35</sup>.

This type of ensemble composed of delta-shaped teeth has a vanishing absorption, so in practice the teeth will have some finite width  $\gamma$  and shape (we use rectangular teeth in this work, though other shapes can be implemented, like Gaussian) as sketched in figure 6.1b. On the other hand, too broad peaks will make reabsorption of the echo after emission more likely, since the absorptive medium has a finite length that photons have to travel after emission. In theory, these effects compete against each other and limit the efficiency to 54 %, unless we change the configuration to a backwards emission<sup>35</sup> or use an impedance-matched optical cavity<sup>90</sup>.

When optimizing the AFC preparation, it is important for these reasons to control the ratio of periodicity over width, which defines the comb finesse,  $F = \Delta/\gamma$ . An optimal efficiency  $\eta_{\text{AFC}}(0)$  can be found as a function of finesse as<sup>85</sup>

$$\eta_{\text{AFC}}(0) = \tilde{d}^2 e^{-\tilde{d}} \text{sinc}^2\left(\frac{\pi}{F}\right), \quad \text{with} \quad \tilde{d} = \frac{d}{F} \quad (6.2)$$

with an optimal finesse  $F$  for each optical depth  $d$

$$F = \frac{\pi}{\text{atan}(2\pi/d)}.$$

The efficiency bound above still does not include the effects of decoherence.

Even considering atoms distributed in deltas, fundamentally they have a finite homogeneous linewidth. It follows that, if we would like the echo to be emitted at later times  $1/\Delta$ , the efficiency will decrease accordingly. This usually translates into an exponential decay

$$\eta_{\text{AFC}} = \eta_{\text{AFC}}(0) e^{-4\frac{1}{\Delta} \frac{1}{T_2^{\text{AFC}}}} \quad (6.3)$$

in which the starting zero-time efficiency  $\eta_{\text{AFC}}(0)$  is reduced by a factor depending on an effective coherence time of the atoms  $T_2^{\text{AFC}}$ . This characteristic time is ultimately limited by the optical coherence time  $T_2$  of the transition, but it can be further reduced by environmental and technical sources.

There are several reasons for having a good efficiency and long coherence time of the AFC. The AFC is in itself a memory protocol, although with a pre-programmed readout, so it could be used directly to delay the emission of previously absorbed photons. Other indirect advantages include the multi-mode capacity. Since billions of atoms participate to the AFC, if the input light pulses are not too bright they will not modify its structure. A train of multiple pulses can thus be stored without re-preparing the ensemble, and each of them will be read out at their respective rephasing times. To avoid cross-talks between modes, they will need to be all absorbed before the re-emission of the first pulse of the train, hence the need for an adequate  $1/\Delta$  so that the sum of the temporal widths of all input temporal modes will not exceed it. The bandwidth of the AFC also plays a role here, since the wider the comb is in frequency, the shorter the input pulses can be in the time domain.

Another example of use of a long AFC delay time comes with the combination of more advanced protocols, such as spin-wave storage and AFC-DLCZ, as we will see later in detail. In the former, in addition to multi-mode capacity, a long AFC rephasing time allows the use of more efficient transfers into spin states for a limited optical Rabi frequency. In the AFC-DLCZ protocol, it leads to an increase of the success probability of an entanglement attempt between two repeaters.

## 6.2 Practical implementation and improvements

An AFC can be prepared in different ways. Two in particular were described and compared by Jobez et al.<sup>91</sup>. The simplest method consists in sending a chirped optical pulse for each interval between two adjacent spectral teeth, in series. A more refined technique involves a series of identical pulses with Fourier spectrum corresponding to the whole comb spectral shape. The latter method is the one used in the works of our group since 2016, including the ones described in this thesis, as it allows to produce more accurate combs. In the PhD dissertation of Laplane<sup>68</sup>, we find the parameters of the AFC that will be our reference for gauging the improvements we will see shortly. The zero delay efficiency was close to 35 %

and the effective coherence time of  $130\ \mu\text{s}$ . To understand how close this is to an ideal comb, we can compare the zero-delay efficiency with the prediction of the model described in Afzelius et al.<sup>35</sup>, given a maximum optical depth attainable in the optical transition  $|g\rangle \leftrightarrow |e\rangle$ . First of all, even in the limit of infinite optical depth, we saw in the previous section that the theoretical efficiency is limited to 54 % in the forward configuration. Given the optical depth of 2 attainable with the crystal of 1 cm used at the time<sup>91</sup>, which becomes 4 at best in double pass, the expected efficiency at zero delay is then 32 %, according to the model 6.2. This means that the preparation of the AFC for short  $1/\Delta$  is not an issue.

How the efficiency decreases with  $1/\Delta$  is however a very different thing to judge. We know that the experimental  $T_2^{\text{AFC}}$  is far from optimal because in the case of a perfectly isolated system the coherence lifetime  $T_2$  is twice the population lifetime  $T_1$ , and for our system  $T_1 = 1.9\ \text{ms}$ <sup>69</sup>. The coherence of the atoms may be affected by other perturbations such as fluctuating magnetic fields in the lab, interactions with neighboring atoms of the host material and vibrations of the mount holding the crystal. Photon echo measurements can be sensitive to these phenomena, and at the time yielded a coherence time of  $380\ \mu\text{s}$ <sup>68</sup>, which however is far from the  $T_1$  limit, while still leaving room for improvement from the  $130\ \mu\text{s}$  mentioned by Laplane. There are also other technical issues that might affect the AFC but not the coherence time of photon echoes. For instance, when using separate beams to prepare the comb and to generate the input pulses respectively, their overlap and different spot sizes also play a role. A longer AFC delay requires the preparation of combs with higher teeth density, i.e. a finer spectral resolution, up to a point where the width of our laser is not sufficiently narrow to burn perfectly square holes and the effective optical depth will eventually decrease. We addressed some of these issues during my doctoral work and we will see the results in the following sections of this chapter.

### 6.2.1 New crystal

First of all, we acquired a new crystal from our group of collaborators at Chimie ParisTech<sup>1</sup>. As for the crystals used by Laplane<sup>68</sup> and Jobez<sup>66,91</sup>, we use isotopically enriched  $^{151}\text{Eu}^{3+}:\text{Y}_2\text{SiO}_5$  with a doping concentration of 0.1 %. The crystal is cut along the  $b$ ,  $D_1$  and  $D_2$  polarization extinction axes with dimensions 12 mm, 2.9 mm and 2.5 mm respectively. With respect to older crystals, this one is longer along the direction we typically use for the input light ( $b$ ) and shorter along the others, with the practical consequences of having a slightly higher optical depth (measured up to 3 in a single pass after class cleaning and pit burning) and allowing an RF coil with shorter radius to be wrapped around the  $b$  axis to increase the RF field intensity for the same power.

<sup>1</sup>led by Philippe Goldner in Paris, ([www.cqsd.fr](http://www.cqsd.fr))

### 6.2.2 New reference cavity

In our previous works, an homemade optical cavity in a custom-made vacuum chamber was used as a frequency reference for the source laser at 1160 nm, leading to a laser spectral width of about 3 kHz at 580 nm in a timescale of few milliseconds<sup>91</sup>. This is roughly the timescale of one preparation pulse. However, since we need tens of repetitions to optimally prepare the AFC, long term drifts should also be considered. On the same cavity, we observed also linear drifts of about 20 kHz/s possibly due to temperature variations, measured in a timescale of a few seconds. To do this, we prepared a spectral hole on the sample and then probed it multiple times with the same technique described later in section 6.2.3.

We acquired a new high-finesse cavity made from ultra-low expansion glass from Stable Laser Systems. For a good decoupling of the cavity from acoustic noise and thermal drifts, the cavity lays on top of four Viton spheres, lodged in four recesses of a Zerodur block. The block is then inserted into a cylindrical vacuum chamber at ionic pump-level vacuum. We further isolated the source and stabilization assembly in a custom-made box separated from the rest of the optical setup (see also 5.2). This choice helped decoupling the diode lasers and stabilization setup from the laboratory environment and led to an overall improvement in temperature and acoustic isolation, thus allowing the Pound-Drever-Hall frequency locking to continuously operate for months without intervention. Besides the obvious implications in long measurements, especially when collecting photon-counting data for multiple days, this solution eliminated any measurable drift in the central frequency of the laser.

We did not quantitatively characterize the bandwidth of the locking setup, nor the laser linewidth. However, we can say the latter is no larger than 13 kHz, estimated by hole burning. Independent ringdown measurements on the cavity led also to 13 kHz of the cavity resonance width, which however does not tell us directly the laser linewidth in the PDH locking scheme. To experimentally calibrate our ability to spectrally burn narrow features, we can perform in the future hole burning at different powers to exclude the effect of power broadening by extrapolating the linewidth of the spectral hole at zero power of the burning pulse.

### 6.2.3 Vibration attenuation

An important contribution to the effective spectral width in hole burning is given by vibrations arriving at the crystal through its copper mount. It is believed that this broadening stems from strain-induced spectral shifts caused by the vibrations<sup>92</sup>. Our cryostat (Montana Cryostation, 2012 year model) has an anti-vibration system which helps decoupling the cold chamber against the motion induced by the high pressurized helium of the closed-cycle cooling system. However, the standard isolation of the Cryostation proved insufficient as the



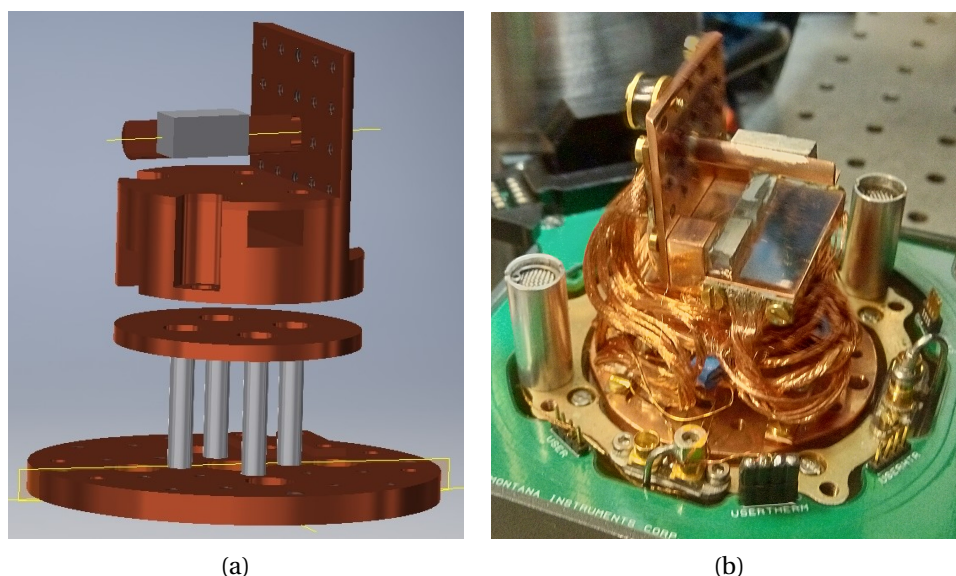


Figure 6.2: (a) Digital sketch of a crystal mount prototype and platform assembly. The empty space between the two is meant to be filled by the attenuation layer. (b) Photograph of the final crystal mount in position in the open cryostat cold chamber, on top of the attenuation layer and with thermal links attached.

perturbations were visible for instance when probing a spectral hole over a few seconds, as in figure 6.3a. Here, a narrow hole is burned and excited with a short pulse to create a free induction decay (FID) signal. The corresponding Fourier transform gives the central frequency and width of the hole. The FID is collected repeatedly with pairs of a weak excitation pulse (tens of  $\mu\text{W}$ ) and a few ms-long local oscillator, in a heterodyne scheme, with about 300 repeated excitation pulses per each hole preparation. The vibrations then appear as a frequency broadening and shift of the FID signal. In the past, using an electrical pulse synchronized with the helium cycle to trigger the experiment allowed to attenuate the problem, at least avoiding the time periods in which the vibrations are strongest. However, this imposed restrictions in the timing of the experiment that we wanted to avoid.

A simple improvement that we developed consists in decoupling the crystal mount from the 3 K platform by adding a soft cushion between them, made of scrambled thin copper wires (see figure 6.2). To keep a good thermal contact between crystal mount and platform, we use soft thermal links also made of copper wires, the extremes of which are soldered onto flat plates to increase the contact surface with the anchoring ends. The same FID method allows to see how the perturbations are completely removed, as in figure 6.3b. Besides freeing us from the need of synchronizing the experiment with the cryostat cycle, this simple solution enabled to use longer preparation sequences. We also observed direct effects on the AFC performance, as the efficiency decay curve could appear non-exponential if the cushion was not well positioned, indicating the presence of vibrations at specific frequency intervals.

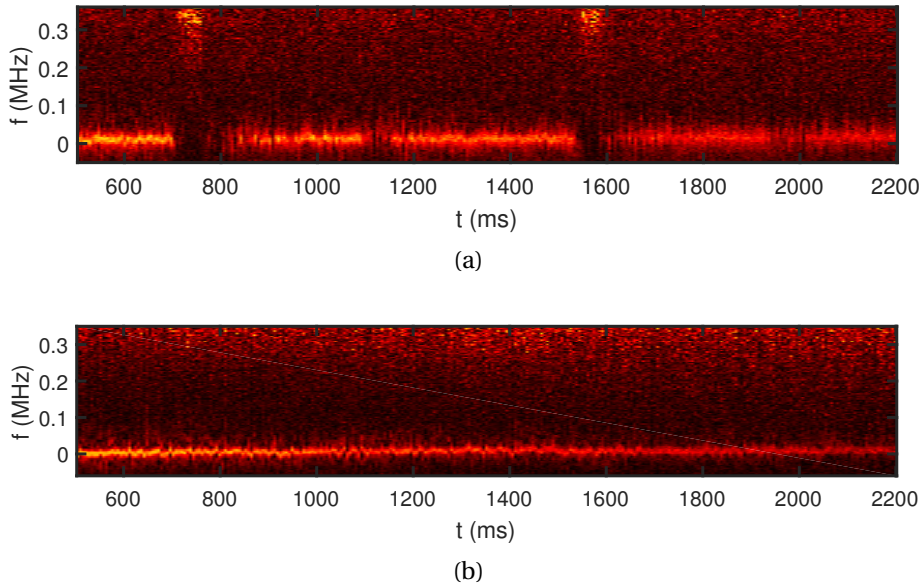


Figure 6.3: Maps of the fast Fourier transform of the FID emission over about 2 s. A brighter color indicates a stronger FFT signal. (a) Data acquired with the crystal holder hard-fastened to the cryo platform with a screw. The vibrations induced by the helium cycle are visible as breaks in the FID spectrum and a broadened line. (b) Same measurement as (a) with an attenuation layer. The cryostat cycle is no more discernible and the FID spectrum is visibly narrower.

### 6.2.4 Beam geometry considerations

To allow for an efficient preparation, the comb is burned by an optical beam independent on the one used for the input pulses, as it normally requires a higher intensity. This same beam was used in the past for the transfer pulses in spin-wave experiments, which require even higher intensity. For these reasons, the beam waist size in the crystal resulted in a compromise between intensity and homogeneity in the volume overlapping the input beam. After a general reorganization of the preparation setup, we split the transfer/preparation optical channels in two independent ones. This allowed to relax the intensity requirements on the preparation beam and to increase the homogeneity by increasing the spot diameter at the waist from  $250\ \mu\text{m}$  to  $700\ \mu\text{m}$ . We chose this value because, with quick measurements of efficiency decay, we could observe an increase of  $T_2^{\text{AFC}}$  with a saturation around this value of diameter.

## 6.3 Updated AFC

The elements described in the previous section enabled considerable improvements on the AFC. Figure 6.4a displays a typical AFC efficiency decay curve as a function of the delay time  $1/\Delta$  obtained in a double pass configuration, with a maximum optical depth of 6 and a total bandwidth of 2 MHz. The AFC is prepared on the state  $|g\rangle$  and the input is sent along the  $|g\rangle \leftrightarrow |e\rangle$  as shown in

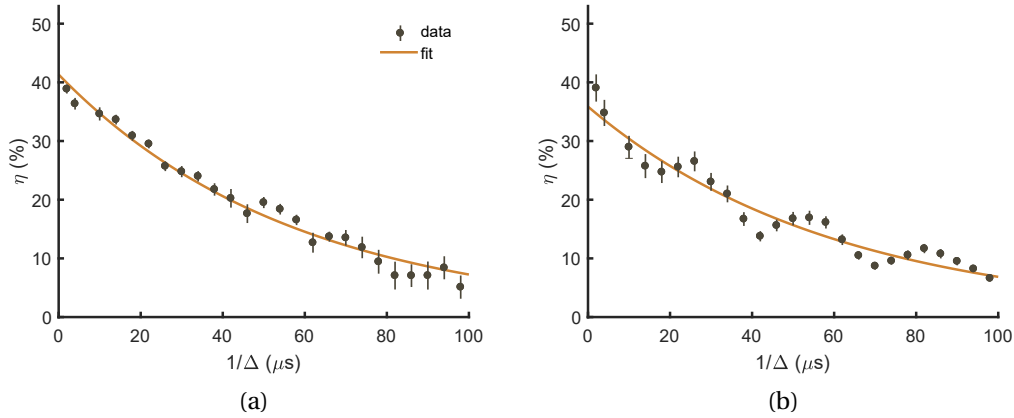


Figure 6.4: (a) typical AFC efficiency decay curve at environment magnetic field. (b) Same experiment with a magnetic field of 1.35 mT along  $D_1$ . The periodic modulation is a consequence of the splitting of the excited state as described in the main text. Solid lines indicate exponential fits to equation 6.3.

figure 6.1a. We can see that the data is well fitted by an exponential curve with parameters defined as in equation 6.3. The efficiency extrapolated at zero delay is  $\eta_{\text{AFC}}(0) = (41.3 \pm 1.7) \%$  and the effective coherence time  $T_2^{\text{AFC}} = (259 \pm 14) \mu\text{s}$ . The increase in zero-delay efficiency with respect to Laplane and Jobez et al. is mostly due to the increased optical depth, thanks to the longer crystal and the preparation beam homogeneity. The coherence time seems to have particularly benefited from the vibration attenuation and optical beam size increase, though it still remains far below both  $T_1$  and the photon echo coherence time of  $380 \mu\text{s}$  reported by Laplane<sup>68</sup>. The new optical cavity allows to prepare the comb with weaker and longer pulses, since frequency drifts are now negligible at the preparation timescale. This might have helped in increasing the comb coherence time by allowing to burn finer structures when repeating the preparation pulses for hundreds of times, though we did not perform specific measurements to distinguish this particular contribution. Given the general improvements, we decided to look closer at the coherence time as probed by photon echoes, the results of which are reported in the next section.

After the creation of a comb, we can observe its frequency profile by reading out the transmission of a weak frequency-chirped probe pulse. In figure 6.5, we can see several examples of comb profiles with  $1/\Delta$  ranging from 2 to  $75 \mu\text{s}$ . The preparation parameters were optimized so to maximize the AFC echo intensity, which did not always correlated to the maximum optical depth contrast between absorption peaks and troughs.

In particular, we note that the peak optical depth decreases for higher  $1/\Delta$ , while the shape of the teeth, initially square, gradually deteriorates in sharpness. Such effects might be a sign of power broadening during comb preparation, which however we believe it is avoided by the optimization of the preparation parameters,

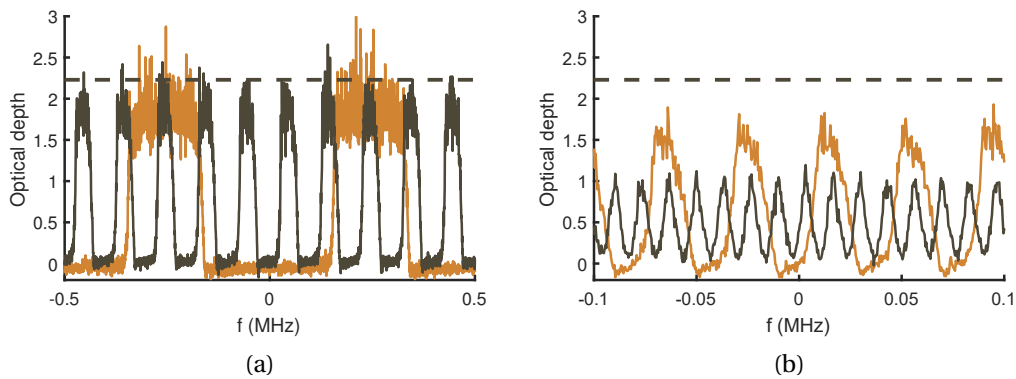


Figure 6.5: Readout of the centers of several AFC comb profiles. The range is adjusted to highlight the features of the teeth. (a)  $1/\Delta = 2\mu\text{s}$  for the orange curve and  $10\mu\text{s}$  for the black one. (b)  $1/\Delta = 25\mu\text{s}$  in orange,  $75\mu\text{s}$  in black. The dashed lines in both figures indicate the maximum optical depth measured as a reference with the same probe pulse, limited in this measurement by overburning of the probe pulse itself (it is actually 3 in this transition).

or a laser linewidth comparable to  $\Delta$ . The latter issue cannot be completely ruled out, as we have just a rough estimation of the linewidth by hole burning, a process which in itself can be affected by power broadening, unless an extrapolation to zero burning power is made by fitting the hole width at varying power of the pre-pulses.

The probe pulse itself might introduce problems in the readout, as it needs to be at the same time chirped slowly enough to not distort the teeth shapes, but not too powerful at each frequency to optically pump the atoms. The reference maximum optical depth of 2.25 measured with the same probe is an indication of this problem, as we know from independent measurements that it is 3 in single pass. More accurate investigations on these issues should be performed in the near future.

As we can see from the extrapolated  $\eta_{\text{AFC}}(0)$  and the optical readout at the shortest storage time of  $2\mu\text{s}$ , we reach the optimal efficiency given by equation 6.2, which is 40.7%. In principle, we should be able to obtain the best comb for any optical depth. Figure 6.6 shows the results of the AFC efficiency at  $1/\Delta = 2\mu\text{s}$  for a range of optical depth values obtained by emptying part of the initial population in  $|g\rangle$  after preparation, compared with the calculated efficiency at optimal finesse of equation 6.2. We can see

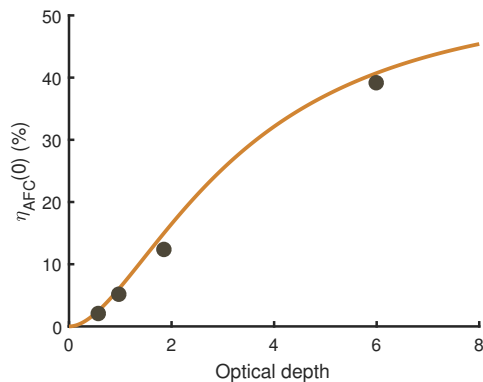


Figure 6.6: AFC efficiency at  $1/\Delta = 2\mu\text{s}$  for different optical depth values (black dots), compared to the theoretical optimal zero-time efficiency from equation 6.2 without any free parameters.

a good matching between theory and data, considering that the measurements are actually taken at a non-zero storage time to simplify the acquisition.

For reasons that will become clearer in chapter 8, it is interesting to see what happens to the AFC efficiency under a small constant magnetic field. In the case of figure 6.4b, a field of 1.35 mT is applied along the  $D_1$  axis, producing the periodic modulation of the efficiency over  $1/\Delta$ . This is a consequence of the nuclear Zeeman splitting of the excited state, which is dominant with respect to the one of the ground state. In this situation, burning a hole in the absorption spectrum inevitably leads to side-holes which reduce the absorption depth of the teeth in the comb when the splitting does not match its periodicity  $\Delta$  (*Paper III*, see chapter 7). This is not a problem if we are careful in choosing a field magnitude and a value of  $1/\Delta$  which correspond to one of the maxima in the efficiency decay curve, given by the Zeeman splitting:  $30.64 \text{ MHz T}^{-1} \cdot 1.35 \text{ mT} = 41.4 \text{ kHz}$ .

## 6.4 Photon echoes and homogeneous linewidth

As mentioned earlier, an important tool for distinguishing certain types of limitations affecting the coherence of our optical transition are photon echo sequences. The technique, described in detail already in 4.3, has been used for decades in spectroscopy to probe coherence and it consists in exciting a portion of the atoms of an ensemble and rephasing them with an inverting  $\pi$  pulse after a delay  $\tau$ . Measuring the decay of the intensity as a function of the time between the excitation and rephasing pulses can give us information on the coherence time of the transition. Photon echoes are sensitive to many effects that might limit also the AFC coherence, but they do not require the creation of narrow spectral features and thus will be less affected by the linewidth of the laser. More in general, different contributions to the homogeneous linewidth can be taken into account as

$$\Gamma_h = \Gamma_0 + \Gamma_{\text{ISD}} + \Gamma_p \quad (6.4)$$

in which the narrowest homogeneous linewidth possible  $\Gamma_0$  is summed to the contribution  $\Gamma_{\text{ISD}}$  of the instantaneous spectral diffusion (ISD), and the contribution from phonon coupling  $\Gamma_p$ . While in Eu:YSO the phonon component can be quenched at the lowest temperatures we can achieve, as we will show later, the ISD needs always to be taken into account. In short, the atoms excited by the rephasing pulse induce a shift in the transition frequencies of their neighbors, perturbing phase coherence and inducing an effective broadening of the transition.

The ISD contribution can be estimated separately, thanks to its linear behavior with respect to several parameters of the system. The most general way to do this is by means of the excitation density  $\rho_{\text{ex}}$ , defined by Könz et al.<sup>70</sup> as

$$\rho_{\text{ex}} = 3 \cdot 10^{12} I \tau_p \alpha \quad (6.5)$$

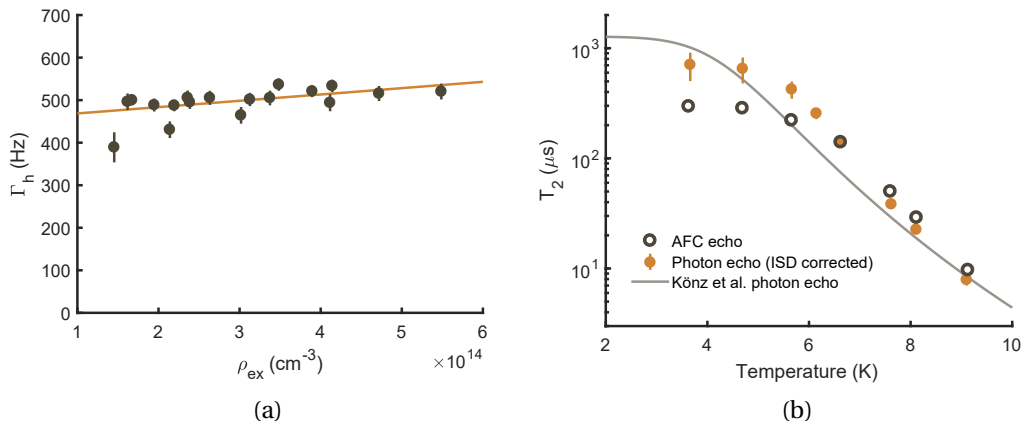


Figure 6.7: (a) Homogeneous linewidth extracted from photon echo sequences for different excitation density values  $\rho_{ex}$ . Black dots indicate the data used for the fit (gray line). (b) Comparison between effective coherence times as a function of the temperature on the crystal mount. Full and empty dots indicate our data for AFC and photon echoes respectively. The solid line is an experimental fit from photon echo experiments from Kőnz et al.<sup>70</sup>.

with  $I$  intensity of the beam in  $\text{W}/\text{cm}^2$ ,  $\tau_p$  duration of the pulse in  $\mu\text{s}$  and  $\alpha$  absorption coefficient in  $\text{cm}^{-1}$ . By varying this parameter, the  $\Gamma_0$  linewidth would then be interpreted as the extrapolated homogeneous width for an excitation density of zero.

The first explorations of the coherence time of Eu:YSO can be traced back to the work of Yano et al. in 1991<sup>93</sup>, in which photon echoes at 6 K indicated a homogeneous linewidth of about 667 Hz for site I and 387 Hz for site II. It was already indicated that interactions between  $\text{Eu}^{3+}$  ions were limiting the coherence time, as this varied with intensity and optical depth. Three years after, Equall and others<sup>69</sup> measured 122 Hz on site I and 167 Hz on site II, by reducing the laser intensity, the temperature to 1.4 K, shielding the sample from unwanted fields and applying a controlled 10 mT field to quench contributions from flips of  $\text{Y}^{3+}$  nuclear spins. After estimating the ISD contribution, they fitted a  $\Gamma_0$  of 105 Hz for both sites, effectively reaching the limit imposed by the population lifetime  $T_1$ . Later measurements from Graf et al.<sup>94</sup> and Kőnz et al.<sup>70</sup> yielded extrapolated values of  $\Gamma_0$  of 210 and 250 Hz respectively, compatible with what reported by Equall without the magnetic field correction. In the work of Kőnz, however, measurement performed on different Eu:YSO crystals led to different coherence times. Since our crystal was grown by a different team, it is necessary to properly investigate the coherence time in our case to set a baseline for the AFC.

In our latest experiments, we chose to repeat photon echo measurements at different values of the parameter  $\alpha$  in equation 6.5 by preparing a pit with an optical depth ranging from 0.5 to 2, while keeping the other parameters constant:  $\tau_p = 4 \mu\text{s}$  and  $I \approx 27.4 \text{ W}/\text{cm}^2$ . For each value of  $\rho_{ex}$ , we collected photon echo decay curves to extract the coherence time  $T_2^{\text{PE}}$  by linear regression, and equivalently

the homogeneous linewidth as  $\Gamma_h = 1/(\pi T_2^{\text{PE}})$ . Figure 6.7a displays the collected values of  $\Gamma_h$  as a function of  $\rho_{\text{ex}}$ . We extract  $\Gamma_0 = (450 \pm 40)$  Hz, roughly twice the values found by Könz without any shielding nor controlled magnetic field.

To observe the phonon contribution, which according to Könz et al.<sup>70</sup> should be of Raman type and thus vary as  $\sim T^7$ , we repeated the measurements of both  $T_2^{\text{AFC}}$  and  $T_2^{\text{PE}}$  for a range of temperatures, controlled by a heater and thermometer in the cold chamber. The results, visible in figure 6.7b and in our work *Paper V*, show the onset of the phonon contribution to the homogeneous linewidth above 5 K. Below this threshold, the coherence times reach a plateau compatible with the previous measurements, which indicate a range with negligible broadening from phonon coupling. For this reason, the data shown was shifted according to a value of  $\Gamma_{\text{ISD}}$  estimated by subtracting the previously measured  $\Gamma_0$  from the  $\Gamma_h$  of the point at the lowest temperature. Since all photon echoes at the other temperatures were taken at the same approximate excitation density ( $2 \times 10^{14} \text{ cm}^{-3}$ ), the same  $\Gamma_{\text{ISD}}$  contribution can be subtracted from all points, to express only the fundamental linewidth given by  $\Gamma_0 + \Gamma_p$  without the component dependent on the excitation parameters. The longest  $T_2$  we measured, collected at 3.6 K, is  $(620 \pm 60) \mu\text{s}$  for an optical depth of about 0.5 and excitation density  $\rho_{\text{ex}} \simeq 2 \times 10^{14} \text{ cm}^{-3}$ . After removing the ISD component, this corresponds to  $(700 \pm 200) \mu\text{s}$ , with the increase in uncertainty due to the ISD estimation.

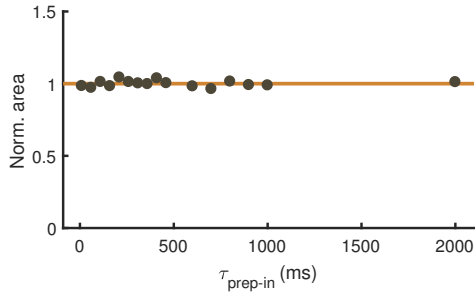


Figure 6.8: AFC echo area as a function of the delay between the preparation and the input pulses  $\tau_{\text{prep-in}}$ . The comb is prepared with a single pulse with  $1/\Delta = 20 \mu\text{s}$ . The solid line indicates the average of the data normalized to the mean, equal to 1. The scattering of the data around this value has a standard deviation of 2%. The absence of a visible decline of the signal up to 2 s indicate the absence of significant spectral diffusion at this timescale.

might be due to the measured temperature depending on the exact position and thermal contact of the thermometer, which in our case is anchored on the crystal mount.

Another important factor to consider is the possible presence of spectral diffu-

The AFC coherence time in the low temperature range is shorter by a factor of  $\sim 2.5$  with respect to the photon echo, while the data converge to compatible values when dominated by phonon coupling. This gap is unexplained by fundamental limitations and we believe it is due to technical problems in the preparation of the AFC. As an additional qualitative reference, the gray line shows the model reported by Könz et al.<sup>70</sup>. While the general shape of the curve seems to match our results, there might be a systematic error in estimating the temperature, indicated for instance by the different threshold at which the phonon coupling drives the change in  $T_2$ . This

sion, time-dependent random shifts in the energy of the optical transitions of the single ions. Such an effect has been observed in Eu in other host crystals, such as  $\text{YAlO}_3$ <sup>95</sup>, but not appreciably on  $\text{YSO}$ <sup>96</sup>. If present, it might effectively broaden the teeth of the comb structure if they are prepared with many pulse repetitions with a long total preparation time. To probe for spectral diffusion, we create a comb with a single preparation pulse of about 5 ms with fixed  $1/\Delta = 20\mu\text{s}$  and scan the delay  $\tau_{\text{prep-in}}$  between the preparation of the comb and the input pulse to be stored. In presence of spectral diffusion in that timescale, we should observe a decrease in the AFC efficiency. Figure 6.8 however shows that this is not the case, since delays as far as 2 s did not provide any measurable echo intensity change besides random fluctuations always within a standard deviation of 2% around the mean. This method is similar to the common three-pulse stimulated photon echo technique<sup>72</sup>, in which the coherence is first created by a  $\pi/2$  pulse, converted into a population grating with a second  $\pi/2$  pulse after a time delay, and then read out with a third  $\pi/2$  as an echo. In creating the population grating, the AFC  $1/\Delta$  is equivalent to the time delay between the first two  $\pi/2$  pulses, while the delay between preparation pulse and input takes the part of the delay between the second and the third  $\pi/2$  pulses. These results exclude the presence of spectral diffusion in the timescale affecting the AFC preparation and suggest that some other technical issue is to blame for the difference in coherence time with the photon echoes.

## 6.5 Multimodality

Back in section 6.1, we briefly mentioned that efficiency and effective coherence time have significant consequences on the multi-mode capacity of the AFC. This is important in particular for the implementation of entanglement-based repeaters, since allowing to store  $N_m$  input modes instead of just one for each entanglement attempt will scale up directly the rate of success by a factor  $N_m$ <sup>97</sup>.

Two main AFC parameters will affect directly the temporal mode capacity, namely the bandwidth of the comb and the storage time we choose. In atomic media, the most fundamental limitation to the bandwidth comes from the smallest separation between energy levels. For  $^{151}\text{Eu}^{3+}:\text{Y}_2\text{SiO}_5$  close to zero magnetic field, this is the spin transition of 35 MHz. However, the preparation procedure for the comb involves the simultaneous burning of wide sections of the spectrum which cannot overlap, with the result that, depending on the  $\Lambda$ -system we choose, the frequency separation can be further reduced. Unfortunately, the choice of transitions to be used in protocols based on spin-wave storage is governed by their oscillator strength. In our current  $\Lambda$ -system (figure 6.1a), the transitions  $|g\rangle \leftrightarrow |e\rangle$  and  $|\text{aux}\rangle \leftrightarrow |e'\rangle$  are only  $\sim 6\text{MHz}$  apart, which means the comb cannot be wider than that. For the moment, however, we are not too much bothered by this limitation, as the optimization of the spin-wave protocol will lead to an



effective memory bandwidth of 1.5 MHz in the current setup (see section 7.6). In our publication *Paper V*, we addressed this issue in detail. In the same paper, we also find a quantitative relation between the mode capacity of the AFC itself and its parameters, of which we can give here a brief summary.

From the Nyquist theorem, we know that in order to prevent information loss the mode size needs to be at least twice the inverse of the AFC bandwidth,  $T_m \geq 2/\Gamma$ . A high fidelity can be assured if we use a factor of 2.5 instead of just 2, and the number of such modes that can be stored at a fixed  $1/\Delta$  becomes

$$N_m = \frac{\Gamma}{2.5\Delta} \quad (6.6)$$

However the input pulse shape is not just square. We typically use Gaussian profiles, which can be shown to have an optimized temporal width without excessive cut-off, both in time and frequency domains, when the intensity FWHM is  $T_G = T_m/2.38$ .

Once the AFC bandwidth is fixed and so is the minimum temporal mode size, what limits the mode capacity is the storage time, which in turn has to be chosen in accord to the efficiency we would like at readout. We can then define an efficiency at fixed storage time and AFC coherence lifetime as (see equation 6.3)

$$\eta_{T_2} = \exp\left(-\frac{1}{\Delta T_2^{\text{AFC}}}\right) \quad (6.7)$$

from which we can obtain a new expression for the mode capacity directly in terms of the AFC parameters, namely

$$N_m = \frac{\ln(1/\eta_{T_2})}{2.5} \Gamma T_2^{\text{AFC}}. \quad (6.8)$$

This formula will be further extended in the case of the spin-wave storage in section 7.1.

Using the mode size optimization mentioned above, we implemented the storage of 100 temporal modes for  $50.7\mu\text{s}$  at the single photon level, with an average efficiency of  $(18 \pm 2)\%$  measured from the histograms in figure 6.9. The bandwidth of the comb is 5 MHz and the mode size 500 ns, which allow the storage of Gaussian pulses with intensity FWHM of 210 ns without additional losses in efficiency. Each input mode contains on average a mean photon number of  $0.99 \pm 0.05$  per experiment repetition. For the AFC as a stand-alone memory, this is just an example, as for instance the mode capacity-efficiency trade-off can be tuned by choosing a different storage time.

## 6.6 Conclusions and outlook

We can summarize the results reported in this chapter as an overall improvement on the AFC coherence time and efficiency, with effects on the performance

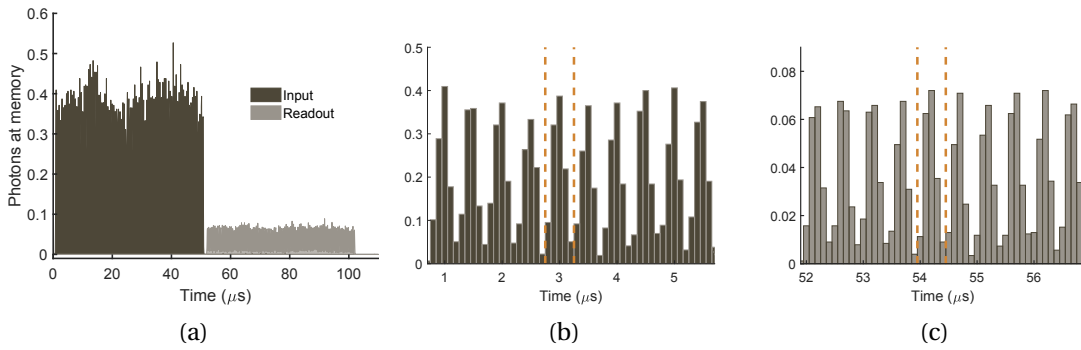


Figure 6.9: AFC storage for 50.7  $\mu\text{s}$  of 100 modes at the single photon level. (a) Input and readout collected counts (histograms not resolved). (b) Zoom on the first 10 modes, with example of 500 ns temporal mode indicated by the orange dashed lines. (c) Zoom on the retrieval of the same modes shown in (b).

as a stand-alone time-multimode memory and as a building block of more advanced protocols. While the role of every technical improvement might be hard to gauge, we can definitely observe a better long-term stability of the new laser stabilization setup and an increase of the effective coherence time due to the expansion of the preparation beam and additional decoupling from vibrations thanks to a new crystal holder system. We have also performed a detailed comparison with photon echo-based coherence times to better understand our current limitations. We also know that additional limitations need to be identified as the  $T_2^{\text{AFC}}$  remains far from the coherence time extracted from photon echo measurements, from which we excluded effects due to spectral diffusion. Possible future improvements might involve a further reduction in the laser linewidth with a more accurate characterization, and tests concerning the quality of the AFC preparation pulses. We also observed a  $T_2$  from photon echo measurements well below the best values obtained in other works, while keeping in mind some differences in the experiment execution. As for the zero-time efficiency, the values obtained are in line with what we could expect from the theory. We can further upgrade the setup by inserting the crystal in an optical cavity, similarly to what has been already demonstrated in other works<sup>98,99</sup>. For all these reasons, we are confident that the AFC has still a wide margin for improvements in its coherence time in Eu:YSO, which will lead to improvements also in its extension to other protocols like the spin-wave memory and the AFC-DLCZ repeater.



## The spin transition

*The topics of this chapter are discussed in our publications:*

- **Paper III**, published in *Physical Review A*, "Optical and spin manipulation of non-Kramers rare-earth ions in a weak magnetic field for quantum memory applications".
- **Paper IV**, submitted to *npj Quantum Information*, "Storage of photonic time bin qubits up to 20 ms in a rare-earth doped crystal".
- **Paper V**, "Multimode capacity of atomic frequency comb quantum memories" (to be submitted).

### 7.1 Spin-wave storage, rephasing and dynamical decoupling

The spin-wave protocol is normally used to extend the coherence time of memories above the millisecond regime<sup>45,100,101</sup> and even hours<sup>51,102</sup>, breaking the limitation of hundreds of microseconds typical of optical transitions. As an extension of the AFC, it was demonstrated first in 2010<sup>103</sup>. The coherence lifetime alone however does not make a good memory by itself, as the final purpose is to use it with quantum states. As we will see more in detail for our case, spin-wave storage protocols involve compromises with bandwidth (and hence multimodality) of the input signal and typically induce noise at readout for a variety of reasons. Obtaining a good signal-to-noise ratio at the single-photon level is still a challenge tackled in a few works in rare earths<sup>66,83,104</sup>.

The key advantage of a spin-wave is the relative robustness of the spin transitions to external perturbations. For this reason, it requires the existence of a finer structure such as the electronic-nuclear hyperfine we have seen for  $^{171}\text{Yb}^{3+}$  in chapter 2 or the nuclear quadrupolar we have in  $^{151}\text{Eu}^{3+}:\text{Y}_2\text{SiO}_5$ . For the latter at zero magnetic field, two spin transitions are available in the ground state of the type  $\Delta m_I = \pm 1$ , the  $|\pm 3/2\rangle_g \leftrightarrow |\pm 1/2\rangle_g$  at 35 MHz and the  $|\pm 5/2\rangle_g \leftrightarrow |\pm 3/2\rangle_g$

at 46 MHz. The latter will be at the center of the spin-wave and AFC-DLCZ experiments that will follow, in the context of the  $\Lambda$ -system depicted in figure 7.1.

In our case, the spin storage is meant as an extension to the AFC protocol, to which it adds the on-demand readout of the stored state besides enhancing the storage time. After coherence is created in the ensemble on an optical transition between a ground sub-state  $|g\rangle$  and an excited state  $|e\rangle$ , the spin-wave starts when the excited state component is transferred down onto a second ground sub-state  $|s\rangle$  by a tailored optical pulse applied at a time  $dt < 1/\Delta$ . After the spin-wave storage time  $T_s$ , the same pulse can be re-applied to get back the stored atoms onto the  $|e\rangle$  state, from which they will continue their phase evolution for a time  $1/\Delta - dt$  according to the AFC structure until the emission at the rephasing time  $T_s + T_{\text{AFC}}$ . The sequence and the corresponding phase evolution is represented in figure 7.3. Since the transfer pulse has a certain duration, already from this description we can see that part of the AFC rephasing time  $1/\Delta$  cannot be used for multiple mode storage, hence the final temporal multi-mode capacity will result from a compromise between AFC time and the bandwidth and efficiency of the transfer pulse.

The shape of the optical transfer pulses we use is the HSH<sup>105</sup>, sketched in figure 7.2. It is a chirped adiabatic pulse which in principle allows to transfer the whole population window with the same efficiency over its full bandwidth, set by the chirp width, as long as the adiabatic conditions are fulfilled. In our [Paper V], we discuss the effect of the HSH transfer pulse on the multimode capacity of a spin storage protocol. The temporal mode capacity can be written as the time remaining from the AFC rephasing after removing the cutoff size of the HSH  $T_c$ , divided by the input mode size  $T_m$ :

$$N_t^{\text{sw}} = \frac{1/\Delta - T_c}{T_m}. \quad (7.1)$$

We need then to consider the change in efficiency of the HSH pulse with its square duration  $T_{\text{squ}}$  (during which most of the optical power is focused), Rabi frequency  $\Omega$  and AFC bandwidth  $\Gamma$  (see also the supplementary materials of Businger et al.<sup>45</sup>)

$$\eta_{\text{HSH}} = 1 - \exp\left(-\pi^2 \frac{T_{\text{squ}} \Omega^2}{\Gamma}\right). \quad (7.2)$$

Using the two formulas, and assuming  $\pi^2 T_{\text{squ}} \Omega^2 / \Gamma = 4$  (condition for > 98% transfer), we can rewrite the mode capacity as

$$N_t^{\text{sw}} = \frac{1}{2.5} \left( \frac{\Gamma}{\Delta} - \chi \frac{4\Gamma^2}{\pi^2 \Omega^2} \right), \quad (7.3)$$

where  $\chi$  is a constant relating the cutoff and square parts of the HSH pulse,  $T_c = \chi T_{\text{squ}}$ . Using the result 6.8 obtained for the AFC, we finally obtain

$$N_t^{\text{sw}} = \frac{1}{2.5} \left( \frac{\ln(1/\eta_{T_2})}{4} \Gamma T_2^{\text{AFC}} - \chi \frac{4\Gamma^2}{\pi^2 \Omega^2} \right), \quad (7.4)$$

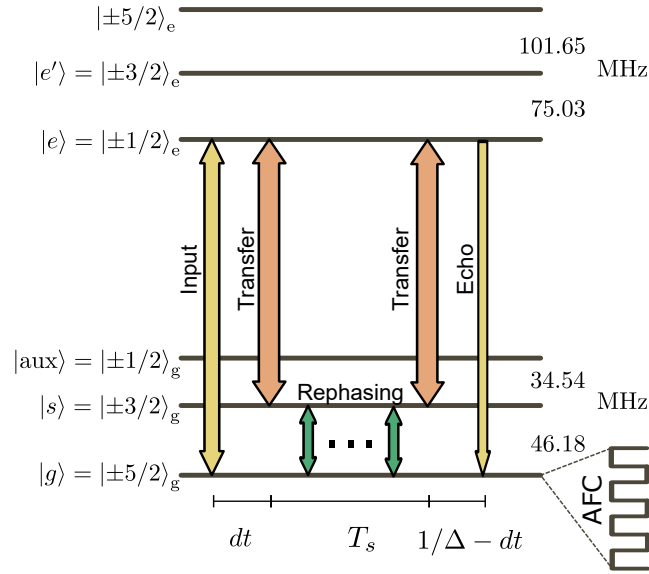


Figure 7.1: Schematic representation of the  $\Lambda$ -system involved in the spin-wave experiments and transitions of addressed in the pulse sequence. The  $|e'\rangle$  and  $|aux\rangle$  levels are used only in the class cleaning and preparation stages of the memory.

which gives us the multimode capacity of the full spin-wave protocol as a function of the AFC efficiency  $\eta_{T_2}$  at a fixed  $T_2^{\text{AFC}}$ , the bandwidth  $\Gamma$  and the transfer Rabi frequency  $\Omega$ .

The other main component of the spin storage protocol is the spin transition itself. A large part of my thesis work was dedicated to the study of its manipulation, which will be described in the following.

As also the spin transition has its own inhomogeneous broadening  $\Gamma_{\text{inh}}^s$ , the coherence should be lost quickly on a timescale  $\sim T_2^* = 1/(\pi\Gamma_{\text{inh}}^s)$ . The phase evolution can be inverted as a Hahn echo sequence (also seen in section 4.3) with a series of RF pulses which will result in a collective rephasing at a specific time. Each rephasing pulse effectively inverts the phase of an atom  $\omega_j t$  accumulated in a time  $t$ , but the timing of the sequence ensures that each atom comes back to its original phase at readout, as shown in figure 7.3. For this reason, the pulses are applied with a delay  $\tau$  between each other so that  $T_s = n\tau$ , with  $n$  even. The population can then be transferred back to the excited state, from which it will resume the phase evolution according to the AFC distribution and finally emit. With this procedure, the inhomogeneous contribution to the spin linewidth can in principle be eliminated and the new effective coherence time will be dominated by homogeneous processes alone as  $T_2^s = 1/(\pi\Gamma_h^s)$ .

The homogeneous linewidth however might hide other phenomena not due to the single ion. A typical example is the random fluctuations of the local magnetic field in the crystal, which might stem from the magnetic dipoles of other atoms in the host lattice like yttrium<sup>71</sup>, or even from electronic equipment in the lab environment. Often, and particularly for the host lattice dipoles, these

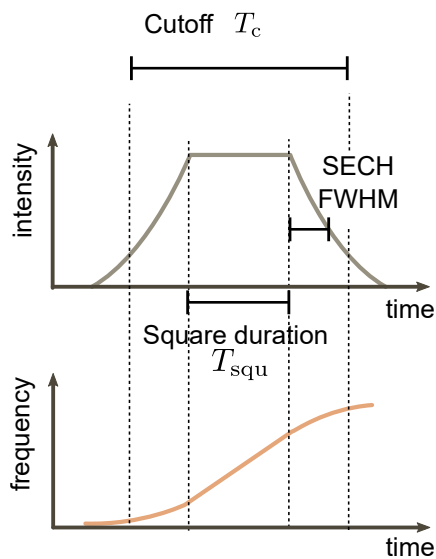


Figure 7.2: Sketch of an HSH pulse, used as an extension of the secant hyperbolic pulse (SECH) to increase the power over a limited time duration, while keeping an adiabatic character. It is composed of two sech-shaped rising and falling edges, defined by their full width at half maximum, and a central square part. A frequency chirp can be applied, linear in the central region and smoothed at the edges to ensure adiabaticity. When the central square part duration is zero, we obtain a SECH pulse<sup>106</sup>. An HSH pulse is always used in our case for the optical transfer, while both HSH and SECH were used for the RF rephasing depending on the particular constraints on the pulse duration. In practice, the total duration needs to be limited to a cutoff, which might introduce imperfections if too short with respect to the edges width.

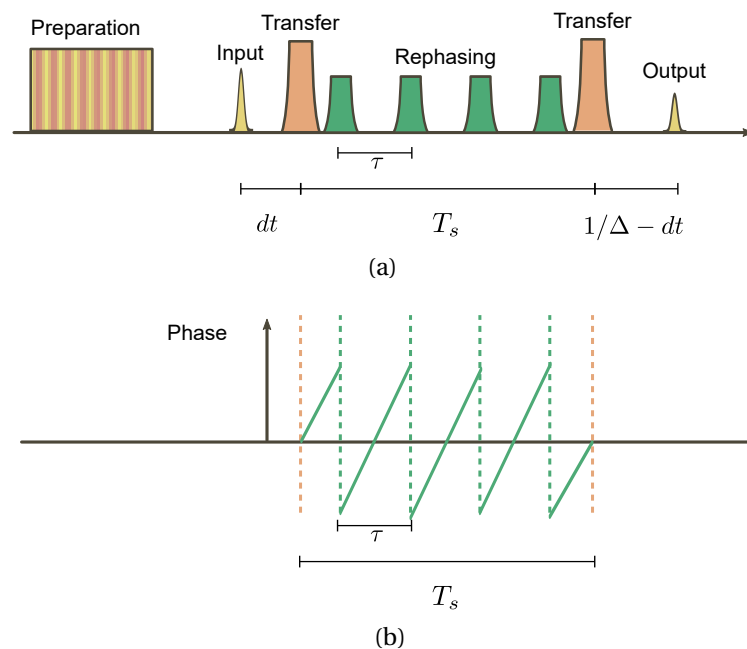


Figure 7.3: Temporal sequence of the spin-wave storage (a), with a representation of the phase evolution of a stored atom in a spin ground state (b).

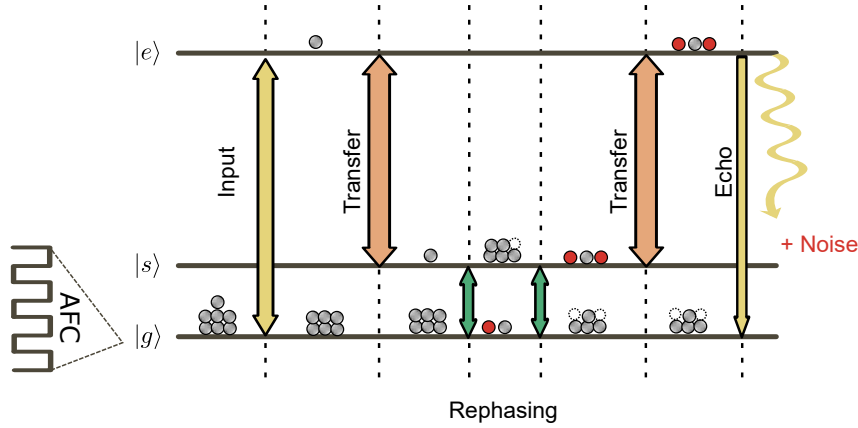


Figure 7.4: Simplified representation of how population errors might occur due to imperfect rephasing pulses. The single photon excitation is represented by the atom in the excited state after the input pulse, which is then transferred onto the storage state  $|s\rangle$ . At each rephasing pulse, even a small probability of mixing the populations of the two ground spin states might create a noise during the echo emission, as described by equation 7.5.

fluctuations occur in a characteristic timescale, so that their perturbation can be avoided by periodically addressing the ions with pulses separated by a shorter time. This is the motivation behind the research in dynamical decoupling (DD) techniques<sup>51,100,107–110</sup>.

In practice, some technical issues need to be faced when optimizing the spin-storage, which affect the final efficiency of the protocol and in particular the generated noise at the single-photon level. Population errors in particular are an important source of noise at the single-photon level. A population error occurs when some atoms are not brought back to their initial energy level at the end of the sequence, as sketched in figure 7.4. In particular in single-photon level spin wave storage, the weak excitation in the storage state  $|s\rangle$  is inverted multiple times with the large population left in  $|g\rangle$ , potentially leading to atoms remaining on  $|s\rangle$  at the end of the rephasing sequence and emitting spontaneously at readout. The problem can be quantified in principle by the probability of emitting a noise photon  $p_n$  along the same transition as the final echo in the formula<sup>110</sup>

$$p_n = \tilde{d}\rho_{ss}, \quad (7.5)$$

where  $\tilde{d}$  is the effective optical depth of the comb transition and  $\rho_{ss}$  the population component of the state density matrix related to  $|s\rangle$ . This is valid if we assume that the transfer from  $|s\rangle$  to  $|e\rangle$  is perfect and if  $p_n \ll 1$ . Since in our case  $\tilde{d} \simeq 2$ , this means that we must keep  $\rho_{ss}$  lower than 0.005 if we want to achieve a noise probability no higher than  $\sim 0.01$ , which is roughly what was obtained in previous experiments<sup>66</sup>.

Some more specific aspects that can influence the noise generation and rephasing efficiency in our system have to be considered:

- the inversion pulses for the rephasing and decoupling sequences have a



finite duration and spectral width. More in general, it is important that one pulse is capable of addressing the whole spin inhomogeneous linewidth with as constant an efficiency as possible

- the insensitivity typical of nuclear spin states, the main feature responsible for good coherence preservation, also makes them less sensitive to the excitation ac magnetic field, thus requiring a high RF power. Sometimes, this can induce excessive heat that might be hard to dissipate without affecting the crystal temperature
- given the high power required, the circuits used for the generation of the RF field need to be carefully designed to minimize unwanted reflections, restricting operations to a narrow band of frequencies.

To address these points, we first measured the linewidth of the spin transition at 46 MHz. We then built a new frequency-tunable circuit resonator to minimize signal reflections and enhance the effective power of the field reaching the crystal.

## 7.2 Spin resonance

The shape of a spin transition could be probed in principle by simply applying the spin-wave protocol without rephasing and observe the shape of the related echo decay curve<sup>103</sup>. However, this method can only probe a spin storage time  $T_s$  higher than zero, given the size of the transfer pulses. This is particularly problematic because it can prevent to distinguish a Gaussian from a Lorentzian shape, for example, which would show their distinct characters at very short rephasing times.

We then choose another method. The spin transition shape can also be observed by modifying a spin-wave storage experiment with RF pulses as in figure 7.5a. A delay  $\tau_2$  of the last transfer pulse with respect to the optimal rephasing time results in an additional accumulation of phase  $\omega_j \tau_2$ , different for each atom, according to the inhomogeneous broadening of the spin transition. This will result in an attenuation of the emitted echo. In the time domain, plotting the echo intensity as a function of  $\tau_2$ , which is varied from negative to positive values going through zero delay, will reveal a shape related in frequency to the spin line by a Fourier transform. Typically, the spectral resonance can appear Lorentzian or Gaussian in character, hence the coherence will decay respectively as a negative exponential or Gaussian when probed as a function of the readout time. Figure 7.5b shows our results on the  $|\pm 5/2\rangle \leftrightarrow |\pm 3/2\rangle$  resonance which indicate a predominantly Gaussian shape, fitted with the equation

$$a e^{-(\pi \Gamma_{\text{inh}}^s \tau_2)^2 / (2 \ln(2))},$$

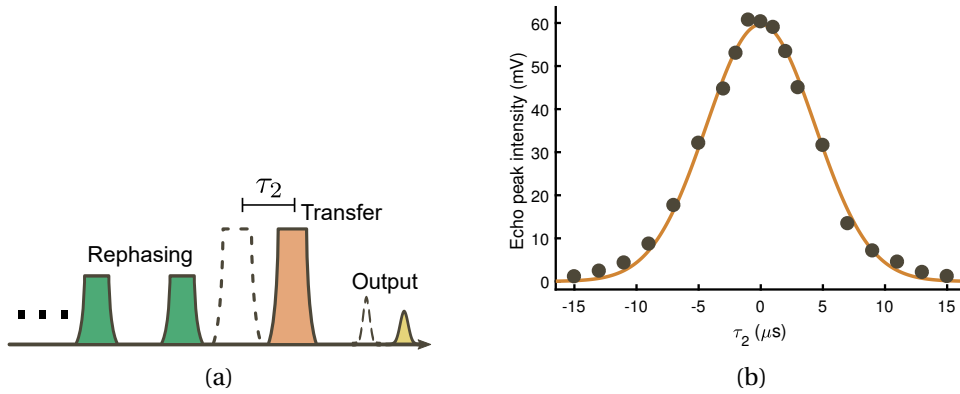


Figure 7.5: (a) Detail of the pulse sequence for read out of the spin resonance profile. A spin-wave sequence is applied, but the last transfer pulse is delayed by  $\tau_2$  with respect to its normal position in the rephasing sequence of figure 7.3. (b) The observed  $|\pm 5/2\rangle_g \leftrightarrow |\pm 3/2\rangle_g$  spin resonance in the time domain.

where  $a$  is a free amplitude parameter and  $\Gamma_{\text{inh}}^{\text{s}}$  the spin linewidth. We obtain from the fit a linewidth of  $\Gamma_{\text{inh}}^{\text{s}} = (61 \pm 2)$  kHz, where the error range is given by a 95 % confidence interval (the same results are published as supplementary material in our *Paper IV*). This value is relatively large: as a comparison, the  $|\pm 3/2\rangle \leftrightarrow |\pm 1/2\rangle$  transition yields with the same method a width of  $(13 \pm 2)$  kHz, though on a Lorentzian shape. This means that an efficient RF inverting pulse will have to cover at least twice this range, and probably even more, when applied in a storage sequence.

### 7.3 The resonator circuit

As compared to many other quantum systems, for instance single NV centers and single quantum dots, our crystals are macroscopic and generally on the order of 1 cm long. This poses a challenge if we want to generate a strong and homogeneous RF driving field over the entire length of the crystal. The homogeneity can be obtained by inserting the crystal in a solenoid with axial length at least as the one of the crystal. Coils of comparable dimensions however come with a large inductance, typically between hundreds of nH and 1  $\mu\text{H}$  depending on the exact geometry and number of spires. For this reason, the transmission of RF power through the coil from a standard  $50 \Omega$  generator becomes highly inefficient. To overcome the problem, we can use an impedance matching circuit, which typically means the transmission of power will be however restricted to one specific resonant frequency. This might be another problem, given the influence of the temperature on the coil and the electrical connections inside the cold chamber. Cooling from 290 K down to 3 K shifts the resonance frequency and changes the resonator quality factor, which is problematic especially when testing the opti-

mization of the physical parameters of the coil and when changing it to adapt to different crystal mounts and spin transitions. Some tunability of the resonance frequency of the circuit would hence be useful.

The previous version of the circuit consisted of two capacitors, one to be connected in series with the amplifier output,  $C^s$ , followed by one in parallel at the interface with the cryostat,  $C^p$ , as in figure 7.6a. The inductance  $L$  and resistance  $r$  of the coil are fixed by its geometry, which in turn is constrained by the dimensions of the crystal (namely radius, which affects the peak field magnitude, and length, to ensure homogeneity of the generated field over the whole ensemble). The generator-amplifier system  $E_0$  have always an output resistance  $R_0 = 50 \Omega$ , typical of commercially available setups. So in principle we can optimize the capacities  $C^s$  and  $C^p$  to maximize the current intensity flowing in the coil at a frequency corresponding to the spin transition we want to address. However, we also need to keep in mind that the parallel capacity is actually composed of the sum of the external tunable capacity we control and a fixed capacity given by the unavoidable interface with the stages of the cryostat. From the input of the vacuum chamber at room temperature, cryo-compatible cables bring the current to the coil, passing through thermalization connections at 30 and 3 K first to minimize heat leakage from the outside. The overall connection will give an unavoidable capacity which will effectively bound  $C^p$  to a value always larger than zero. Typical coaxial cables add between 50 and 100 pF m<sup>-1</sup>, and our overall connection path is on the order of 20 cm. This means we should expect a lower bound for  $C^p$  between 10 pF and 20 pF.

A simple model allowed us to design the circuit, starting from the Kirchhoff voltage law for the two loops in the sketch of figure 7.6a at an angular frequency  $\omega$

$$\begin{aligned} R_0 I_1 + E_0 + \frac{I}{i C^s \omega} + \frac{I - i}{j C^p \omega} &= 0, \\ r i + j L \omega i + \frac{i - I}{j C^p \omega} &= 0. \end{aligned}$$

The two combined equations lead to an expression of the coil current  $i$  that we want to maximize:

$$|i| = \frac{E_0 C^s \omega}{\sqrt{[1 - L\omega^2 (C^s + C^p) - R_0 r \omega^2 C^p C^s]^2 + [R_0 C^s \omega + r \omega (C^s + C^p) - R_0 L \omega^3 C^s C^p]^2}}$$

To simplify this expression, we can use the fact that the resistance of the coil  $r$  is typically very small. If  $r = 0$ , the current is maximized to infinity for  $C^s = 0$  and  $C^p = 1/(L\omega^2)$ . For a more realistic non-zero  $r \ll R_0$ , we can add correction terms to the two solutions found for  $r = 0$  to find, after some algebra,

$$|i_{\max}| = \frac{E_0}{2\sqrt{r R_0}} \quad \text{for} \quad C^s = \frac{1}{L\omega^2}, \quad C^p = \frac{1}{L\omega^2} \left(1 - \sqrt{\frac{r}{R_0}}\right).$$

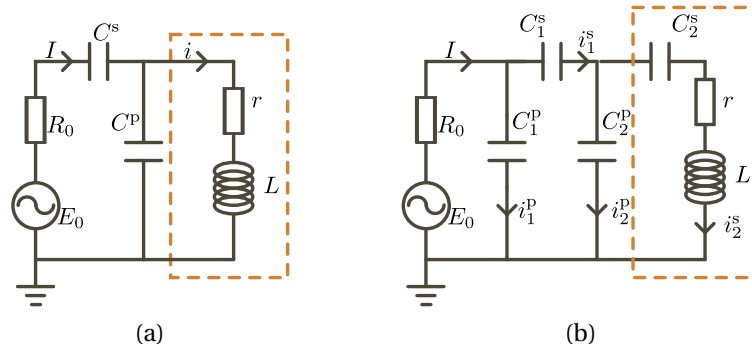


Figure 7.6: (a) Sketch of the original impedance-matching circuit. (b) New version, used for the measurement presented in this work. Regions encircled by the dashed orange line are inside the cryostat.  $C^p$  and  $C_2^p$  for the two versions include a component created by the electrical connections between the cryostat external interface and the 3 K platform.

This circuit allowed so far to obtain in our group Rabi frequencies of 60 kHz from a quality factor of about  $Q = 51.4$ <sup>68</sup>. As mentioned before,  $C^p$  will always have a component coming from the interface with the cryostation and will be lower-bounded. It then becomes clear that we need to find a compromise with the large inductance  $L$ , preferable for the generation of a strong field, if we want to keep the parallel capacity low enough to still match the impedance at our frequency  $\omega$ . As a result, this circuit has also a limited tunability, since once the inductance is fixed, the remaining degrees of freedom are not enough to fully control the frequency and quality factor of the resonance

We tried to ease these constraints with a new version of the resonator, inspired by Hu et al.<sup>111</sup>, and represented in figure 7.6b. With respect to the previous circuit, it adds a series capacitor  $C_2^s$  right before the RF coil inside the cryostat, responsible for the main tuning of the resonance and to be tuned at room temperature, and another parallel capacitor  $C_1^p$  right at the output of the amplifier. Kirchoff's law on the three loops now gives, renaming the previous  $C_p$  as  $C_2^p$  and  $C_s$  as  $C_1^s$ ,

$$\begin{aligned} E_0 - R_0 I - \frac{1}{jC_1^p \omega} i_1^p &= 0 \\ \frac{1}{jC_1^p \omega} i_1^p - \frac{1}{jC_1^s \omega} i_1^s - \frac{1}{jC_2^p \omega} i_2^p &= 0 \\ \frac{1}{jC_2^p \omega} i_2^p - \frac{1}{jC_2^s \omega} i_2^s - jL\omega i_2^s - r i_2^s &= 0, \end{aligned}$$

and the current law gives

$$i_1^s + i_1^p = I, \quad i_2^s + i_2^p = i_1^s.$$

The system can be solved analytically for the current in the coil  $i_2^s$  as a function of all other parameters. From there, we can try to maximize its magnitude starting from reasonable values of the capacities and coil inductance we can achieve in

the lab. We know that our RF coils give an inductance in the range of hundreds of nH up to about 1  $\mu$ H, given their typical dimensions comparable to the crystal and with tens of winding loops of the wire. We focus at first on allowing the highest impedance possible to get a higher field on the crystal. Next, we try to measure the contribution to  $C_2^p$  given by the cryostat connection, from which we obtain only an approximate result due to the very low capacity in the order of few to tens of pF, and due to the variations of it given by every slight change in position of the mount before cooldown.  $C_2^p$  and  $C_1^s$  are then initialized to similar values, while  $C_1^p$  is kept at any arbitrary value that allows to clearly see a peak in the current intensity spectrum. It can be optimized later once the resonant frequency is fixed.

Examples of numerical results for given sets of parameters are displayed in figure 7.8a. With a coil of 21 loops, 0.7 mm thick wire, 15 mm total length and 8 mm radius, we obtain an inductance of about 1.3  $\mu$ H for a target frequency of 46 MHz<sup>1</sup> with a resistance of  $\sim 1 \Omega$ . A qualitative optimization using our code results in a resonance at that frequency for the values  $C_1^p = 260$  pF,  $C_1^s = 12$  pF and  $C_2^s = C_2^p = 14$  pF. We also note that in the model we just need to change  $C_2^s$  to 41 and 4 pF to shift the resonance to 35 and 75 MHz respectively, highlighting the wide tunability of the resonator. These two frequencies correspond to the other spin transition of the ground state and the  $|e\rangle \leftrightarrow |e'\rangle$  of the excited state, which can be reached now with the same coil by mainly adjusting the serial capacitor. The great advantage of this circuit however can be seen when we consider a much more pessimistic estimate of the capacitance of the cable interfacing the cryostat. If we change  $C_2^p$  to 100 pF, we need simply to readjust  $C_2^s$  between 3 and 20 pF to obtain the same resonances, as shown in figure 7.8b. This allows a great range of use of the same circuit for cryostats which might require more cabling.

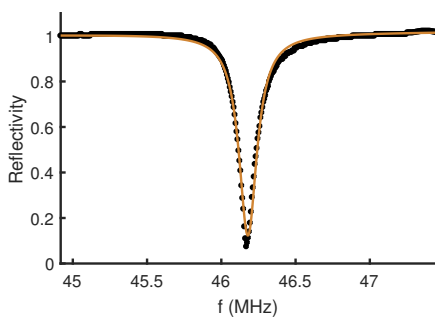


Figure 7.7: Measured circuit reflectivity after the circuit is tuned on the 46 MHz transition and fitted as a Lorentzian.

after which the parallel capacity  $C_2^p$  also needs to compensate the change in impedance. The capacity  $C_1^p$  instead is mostly responsible for the overall resonance quality factor and does not modify the resonance frequency.

The actual values used in the circuit we made had to be adjusted to obtain the same results with the aid of tunable, high voltage capacities, but stayed in the same order of magnitude as the ones from the model. Once the inductance is fixed, the series capacity  $C_2^s$  is used for tuning the resonance frequency before cooling down the cryostat, while the parallel  $C_2^p$  and serial  $C_1^s$  capacities are kept in the center of their tunable range between 5 and 20 pF. After cooldown, the unavoidable frequency shift is corrected roughly by  $C_1^s$ ,

<sup>1</sup>modeled with the online tool at [hamwaves.com](http://hamwaves.com) and then measured with a multimeter

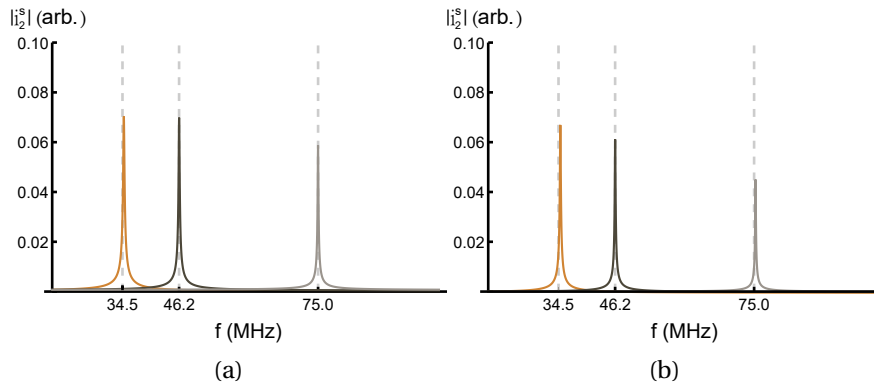


Figure 7.8: (a) Calculated absolute value of the current through the coil for the new circuit. Resonances corresponding to the spin transition frequencies of 35 (orange), 46 (black) and 75 MHz (gray) are obtained by varying  $C_2^s$  while all other values are fixed. (b) Same plot but with  $C_2^p = 100$  pF and readjusted  $C_2^s$

We tested the circuit in the lab and obtained the reflection spectrum of figure 7.7 with a vector network analyzer. The resonance corresponds to a reduction of the reflectivity of the whole circuit by roughly 90% and a fitted FWHM of  $(147 \pm 2)$  kHz. Additional ringdown measurements produced a quality factor estimation of about 220, with a similar width of roughly 200 kHz. This quality factor is roughly a factor 4 higher than the one reported for the old circuit. As mentioned before, however, the true strength of the resonator is its flexibility against different values of the parallel capacity that might arise from cable connections, without sacrificing the inductance.

## 7.4 Population error estimation and Rabi frequency

The effect of the new circuit on the spin storage can be tested by applying a series of inverting pulses on a prepared atomic population. If they are applied an even number of times in a spin transition, as it is typically the case in our experiments, at the end of the whole sequence the atoms should be back on their initial state. However, phase and population errors can occur due to imperfections, for instance if the atoms are not addressed uniformly by the pulse.

While both error types affect the efficiency of the storage, population errors in particular can be an important source of noise at the single-photon level. A population error occurs when some atoms are not brought back to their initial energy level at the end of the sequence. In particular in single-photon level spin wave storage, the weak excitation in the storage state  $|s\rangle$  is inverted multiple times with the large population left in  $|g\rangle$ , potentially leading to incoherent atoms remaining on  $|s\rangle$  at the end of the rephasing sequence and emitting spontaneously at readout. For this reason, a test for this type of error was already reported by our group in the work of Jobez et al.<sup>66</sup> for the 35 MHz transition. As a basic rephasing

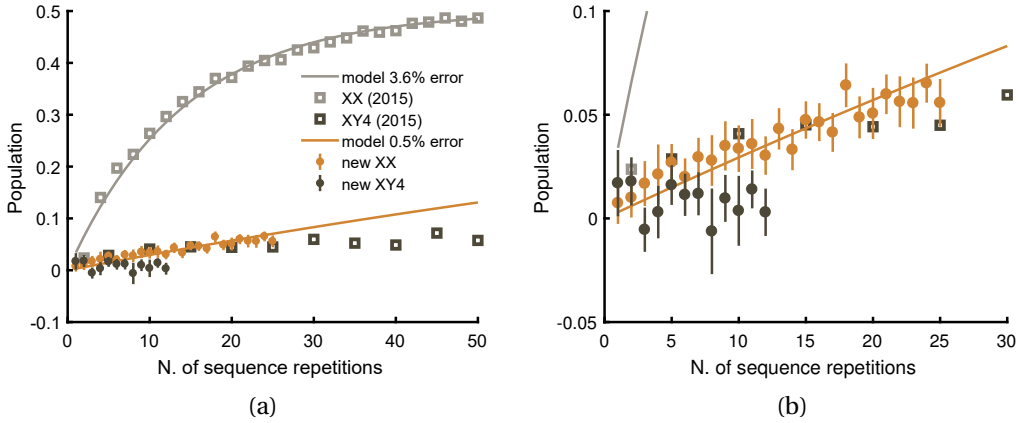


Figure 7.9: Population left in the  $|g\rangle$  state, initially empty, after repetitions of different rephasing sequences. (a) Gray and black squares display respectively the data for XX and XY-4 sequences from the 2015 work of Jobez et al.<sup>66</sup>, with a gray solid line representing a model for the error of XX pulses. Orange and black full circles represent the data obtained in our new setup, with the orange solid line reporting the model results for the XX sequence. (b) Detail of the same plot focusing on the new data. In particular, the XY-4 does not seem to yield measurable population errors for the number of sequences here tested.

sequence is repeated, the errors would accumulate as a function of the number of repetitions and an optical probe on the  $|s\rangle \leftrightarrow |e\rangle$  transition would show an increase in optical depth. The same concept is used here to look for improvements in our rephasing pulses after the implementation of the new resonator. Moreover, the shape of the pulses was re-optimized to efficiently transfer the different transition at 46 MHz. We use now adiabatic pulses with either a SECH or HSH shape, with a chirp including the whole width of the transition we characterized in section 7.2 (see also figure 7.2).

In figure 7.9 we see a comparison of our results with the old ones from Jobez et al. Two types of sequences were tested: a pair of pulses with the same phase (XX) and a quadruple with alternated shifts of  $\pi/2$  (XY4) capable of partially compensating the error of a sequence (see also 7.1). When repeating the sequence, the time interval between repetitions was always much longer than the coherence time, to make sure that the measured effects would depend only on the population. The results show a clear improvement in the error, estimated as the amount of optical depth present in a level that should be empty by the end of the repeated sequence. The solid lines indicate numerical calculations of the population components of the density matrix of the two-level system, with a population error induced per sequence repetition  $\epsilon$ . By visually comparing the numerical results with the measurements of the XX sequence type, the data of Jobez et al. proved compatible with a 3.6 % error per sequence repetition. Our results instead show compatibility with an error parameter of 0.5 %. As for the XY4 sequence, our new results do not show any sign of error within the estimated error bars of the experiment up to

12 repetitions, corresponding to a total number of 48 single pulses. In any case, we will not get to use this many repetitions in our storage experiments, as the rephasing constraints on timings require the pulses to be too close in time, leading to heating effects that will destroy the coherence. On the other hand, we will see how up to 16 pulses-long sequences could be effectively used in our storage experiments while keeping the noise stable at readout.

These results were obtained with a first prototype of the new circuit which was initially optimized for simultaneous addressing of multiple spin resonances at different frequencies, by means of an additional inductance, as it was the case for the original work of Hu<sup>111</sup>. For this reason, the Rabi frequency we used was 42 kHz. However, when the matching is optimized for one single resonance, we measured a maximum Rabi frequency of 130 kHz. This is what we can observe in figure 7.10 in the form of oscillations in the transmission signal from an originally full  $|g\rangle$  state, while being driven at 46 MHz for about 200  $\mu\text{s}$ . In the experiments of the following sections, the Rabi frequency was typically 120 kHz, as heating effects and electrical discharges in the custom circuit would sometimes prevent the use of the full power when using many pulses as in the more complex dynamical decoupling sequences.

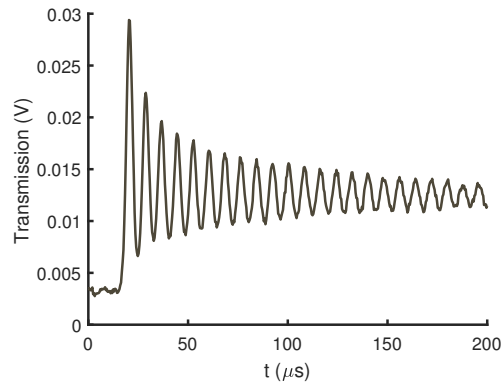


Figure 7.10: Rabi oscillations of the atomic population in the  $|g\rangle$  state, as probed optically from the  $|g\rangle \leftrightarrow |e\rangle$  transition, while driven at 46 MHz on the  $|g\rangle \leftrightarrow |s\rangle$  transition. The resulting Rabi frequency is 130 kHz.

## 7.5 Effects of a controlled low magnetic field

The last results from our group on Eu:YSO at the single-photon level were obtained with the natural magnetic environment of the lab<sup>66,67,112</sup>, which already allowed for efficient storage times up to 1 ms. However, measurements of the spin coherence decay<sup>68</sup> revealed revivals of coherence at longer times, attributed to the effect of the Earth's field on the nuclear spin doublets of the ground state, and a spin coherence time of 3.9 ms was extracted. On the other hand, positive effects of small fields on the spin coherence times of Eu:YSO were already observed in other works<sup>71,113</sup>. In agreement with this, applying even a small magnetic field of 4 mT allowed to glimpse at a more complicated picture at the time of Laplane's work in our group<sup>68</sup>, with longer decay processes with timescales approaching 1 s after a first quick dephasing of about 10 ms. Later, experiments at tens of millitesla performed by my colleague Adrian Holzäpfel<sup>100</sup> allowed to reach storage times of



half a second in a regime where single components of the split Zeeman doublets were used, though the AFC bandwidth was lower since the field did not allow to split the Zeeman doublets more than 100 kHz. It was clear at this point that this low-field range had yet a strong potential for long coherence times and possibly a valid alternative to the few Tesla-high fields used to reach the ZEFOZ points<sup>51,102</sup>.

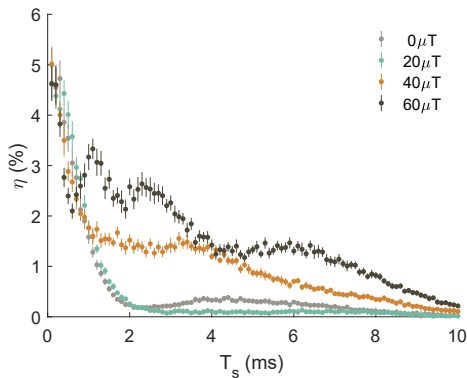


Figure 7.11: Spin storage decay curves with different magnetic field magnitudes up to  $60\ \mu\text{T}$  along  $D_1$ . With no applied magnetic field, a revival is visible after the first quick drop of  $\sim 1\ \text{ms}$ . The revival seems to be flattened to a constant plateau at  $20\ \mu\text{T}$ , while at higher fields a more complex pattern emerges. At the same time, on average the overall efficiency seems to increase with the magnetic field.

tribute part of the spectrum to the interference of the multiple paths of transfer that the atoms can follow when addressed by the RF pulses in a four-level system, made of the Zeeman-split  $|g\rangle$  and  $|s\rangle$  doublets. The role of the RF pulses in this is highlighted by the changes in the oscillatory pattern when an overall shift in time is added as in figure 7.12b, in a way that should not change the final rephasing in an ideal spin-wave storage without the Zeeman splittings. In the paper, the phenomenon is generalized and compared to a broader model, but much of the underlying physics is still unclear and need further investigations, as part of the calculated spectra do not match the results. The use of a controlled magnetic field for spin storage is also the main reason why we characterized the AFC efficiency curve at 1.35 mT back in section 6.3, as this will be the field finally used in the following experiments.

## 7.6 Spin-wave storage with bright pulses

Having tested our capability of addressing the spin transition, we finally put it at work in our full AFC spin-wave storage experiments. Figure 7.13a shows

This motivated us to explore qualitatively what happens to the efficiency decay curves of spin storage experiments for fields below the millitesla range. Figure 7.11 summarizes the results, which display the onset of complex modulations in a very small range of fields applied along the  $D_1$  axis. For fields above 1 mT, we will see in the next section how the oscillations will be attenuated in amplitude and not be distinguishable beyond a few milliseconds, allowing for an increase of the effective storage time. At intermediate timescales beyond 1 mT of field, fast beatings in efficiency are however still visible and with a rich frequency spectrum, displayed in figure 7.12. The phenomenon is addressed more in detail in our work *Paper III*, in which we at-

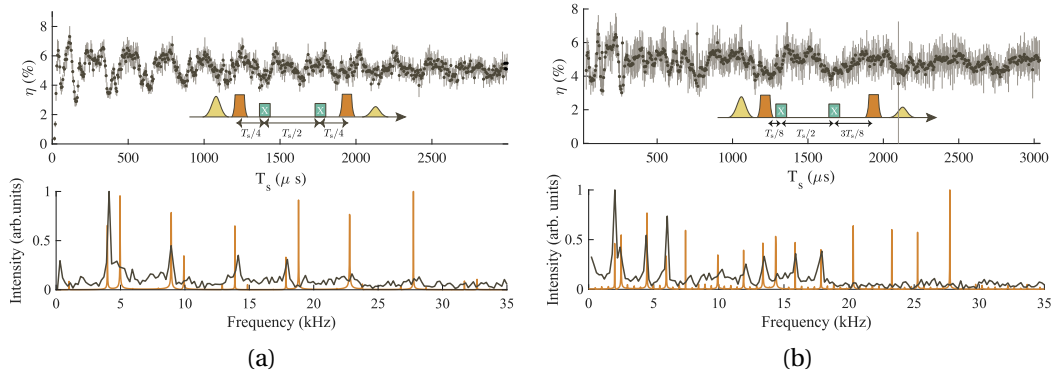


Figure 7.12: Above, spin storage efficiency with a controlled 1.4 mT magnetic field along  $D_1$ . Below, the result of fast Fourier transforms on the two traces (black), compared to the model in *Paper III* (orange). The difference between figures (a) and (b) is a shift in time of the whole XX rephasing sequence, while still respecting the ideal rephasing condition. The emergent patterns evidently differ, and their peaks in frequency partially correspond to some of the calculated ones.

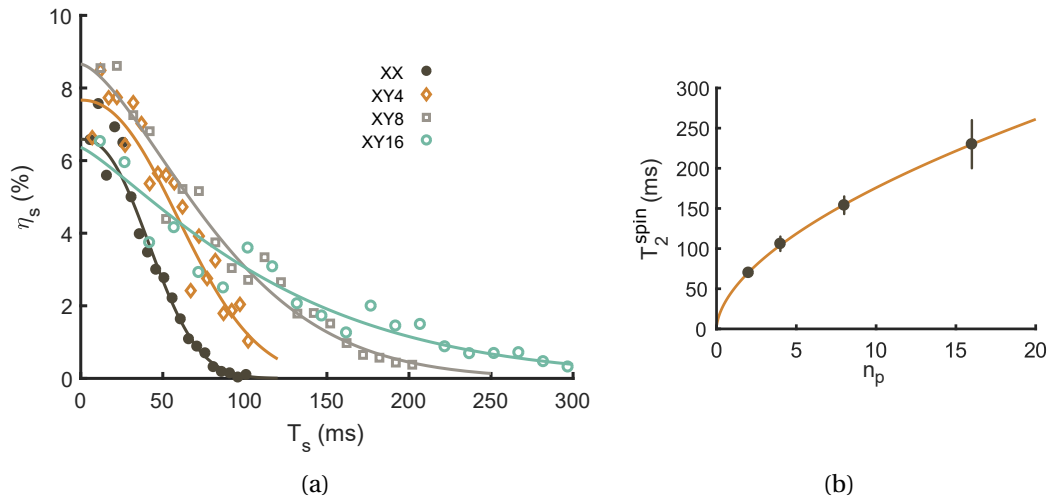


Figure 7.13: (a) Spin storage efficiency curves for four different rephasing sequences, with number of pulses up to 16. The solid curves indicate Mims fits according to equation 7.6 and the resulting parameters can be found in table 7.2. (b) Coherence time as a function of the number of pulses, showing a behavior in agreement with a decoupling effect from an Ornstein-Uhlenbeck type of perturbation, as described by equation 7.7 (solid line).

Sequence name	Phase vector
XX	[0 0]
XY-4	[0 $\pi/2$ 0 $\pi/2$ ]
XY-8	[0 $\pi/2$ 0 $\pi/2$ $\pi/2$ 0 $\pi/2$ 0]
XY-16	$2 \times [0 \ \pi/2 \ 0 \ \pi/2 \ \pi/2 \ 0 \ \pi/2 \ 0]$

Table 7.1: Schematic representation of the dynamical decoupling sequences. Each phase vector contains the phases applied to each pulse of a sequence in temporal order, all distanced by the same time delay  $\tau$ . The XY-16 is basically the XY-8 repeated twice.

DD type	$T_2^{\text{spin}}$ (ms)	$\eta_s(0)$ (%)	$m$
XX	$70 \pm 2$	$6.6 \pm 0.6$	$2.4 \pm 0.4$
XY-4	$106 \pm 9$	$7.7 \pm 1.6$	$2.2 \pm 0.9$
XY-8	$154 \pm 11$	$8.6 \pm 1.4$	$1.5 \pm 0.3$
XY-16	$230 \pm 30$	$6.4 \pm 1.7$	$1.2 \pm 0.3$

Table 7.2: Fitted parameters of the spin storage curves with bright pulses for different DD sequences, according to equation 7.6.  $T_2^{\text{spin}}$  is the effective spin coherence time,  $\eta_s(0)$  the extrapolated zero-time efficiency, and  $m$  the Mims factor.

examples of storage efficiency measurements as a function of the spin storage time  $T_s$  for various dynamical decoupling sequences, from XX to XY-16 in order of number of pulses  $n_p$ . Similarly to the XY-4 described in section 7.4, XY-8 and XY-16 contain pulses with the same intensity profile but with alternated phase shifts. Table 7.1 reports schematically the phase of each pulse in the sequences and more information can be found in the works cited in the previous discussion of section 7.1.

A static magnetic field of 1.35 mT is applied parallel to  $D_1$ , and the AFC is prepared with  $1/\Delta = 25 \mu\text{s}$ . To take into account spectral diffusion processes, the curves are fitted to the Mims equation<sup>114</sup>

$$\eta_s(T_s) = \eta_s(0) e^{-2(T_s/T_2^{\text{spin}})^m} \quad (7.6)$$

in which a Mims factor  $m$  higher than 1 indicates a deviation from a purely exponential coherence decay. Table 7.2 contains the fitted parameters, showing a  $T_2^s$  that ranges from  $(70 \pm 2)$  ms of the XX sequence up to the  $(230 \pm 30)$  ms of the XY-16. Together with the values of  $m \neq 1$ , this indicates the presence of spectral diffusion and an effective decoupling as the number of pulses increases. The behavior of  $T_2^{\text{spin}}$  as a function of  $n_p$  further confirms this conclusion, as it closely follows the power-law relation

$$T_2^{\text{spin}}(n_p) = T_2^{\text{spin}}(1) n_p^{\gamma_p} \quad (7.7)$$

with  $\gamma_p = 0.57 \pm 0.03$  and  $T_2^{\text{spin}}(1) = (47 \pm 2)$  ms, as expected from an Ornstein-

Uhlenbeck process<sup>108,109,115</sup>, also displayed in figure 7.13b. First of all, this tells us that further improvements in coherence time are possible by using sequences with more pulses. In order to do that, however, the effect on noise at the single photon level and technical issues such as heating of the crystal will need to be properly addressed.

On the other hand, this spin transition seems to have a slight advantage over the 35 MHz one. Holzäpfel et al. measured from a similar fit a value of  $T_2^{\text{spin}}(1) = (25 \pm 1)$  ms (in a 15 mT magnetic field oriented at  $65^\circ$  from the  $D_1$  axis), which is roughly half our value here. In principle, this means we could obtain twice the coherence time with the same number of pulses, or in other words use half the number of pulses to obtain the same coherence time. Especially at the single-photon level, this is important as it might help keeping a low noise from population errors with many DD pulses, besides less heating to be dissipated by the cryostat.

The efficiency data show some scattering around the expected behavior, in particular when using the XY-16 sequence. This could be a sign of the beatings resulting from the simultaneous manipulation of split doublets by the RF, as mentioned in the previous section. The maximum extrapolated efficiency at zero storage time  $\eta_s$ , on the other hand, is expected to be higher. If we model the total storage efficiency as a product of the separate efficiencies of the AFC  $\eta_{\text{AFC}}$ , optical transfer  $\eta_t$  and RF sequence  $\eta_{\text{RF}}$ , we should have:

$$\eta_s(0) = \eta_{\text{AFC}}(25\mu\text{s}) \eta_t^2 \eta_{\text{RF}}.$$

Since our previous tests suggest a negligible error in the rephasing sequence for just one repetition of XX and XY-4, most of the loss should come from the first two terms. To estimate the optical transfer efficiency, we can look at the residual AFC echo after the first transfer pulse, corresponding to a part of the population that remained in the excited state. With our best optical transfer pulses with an HSH shape with about  $15\mu\text{s}$  duration and 1.5 MHz frequency chirp, we are able to reduce the AFC echo by about 80 % of its normal amplitude, hence  $\eta_t \approx 0.8$ . Together with the AFC efficiency in double pass at  $1/\Delta = 25\mu\text{s}$  of 28 %, this would give us an expected spin storage efficiency of about 18 %. This is more than double the values we obtain from the data, a problem that we observed in all our spin-wave experiments to this date in both spin transitions. A possible explanation is that, although we might efficiently transfer the atoms between levels both optically and in RF, the coherence is not preserved. In fact, both tests of optical echo extinction and RF population transfer from the previous section do not give us any information on how well the relative phase of the atoms is maintained. Also in this case, the answer might lie in the assumption that each Zeeman doublet behaves like a single level when addressed by our RF pulses. This also holds for the optical pulses, which allow 16 different paths from  $|g\rangle$  to  $|s\rangle$  via the  $|e\rangle$  state. For now this question remains unanswered, but we hope we will be able to address

it in the near future. In any case, the results shown here are the basis for the single-photon level experiments of the next chapter.

## 7.7 Conclusion

The spin transition at 46 MHz, at the center of the enhancement of the storage time of our memory protocol, was the protagonist of this chapter. We have seen a new custom resonator that allowed to improve the RF power reaching the spins in our crystal and tested the improved population error rate of XX and XY-4 rephasing sequences. We briefly saw how the effects of a small magnetic field are yet to be fully understood, while at the same time we saw a definitely positive contribution to the spin-wave coherence performance above 1 mT, with a maximum measured coherence time of 230 ms. While increasing the number of pulses should extend even more the coherence time, we will have to address in the future the technical problems of heating dissipation from the RF and a yet unexplained loss of efficiency during storage.

## Single photon-level experiments

*The experiments reported in sections 8.1, "Multimode spin-wave storage", and 8.2, "Time-bin qubit storage", are the subjects of our arXiv **Paper IV**, submitted to npj Quantum Information, "Storage of photonic time bin qubits up to 20 ms in a rare-earth doped crystal".*

### 8.1 Multimode spin-wave storage

Having characterized the memory with bright pulses in section 7.6, we can lower the input power so to have an average number of photons of  $\sim 1$  per temporal mode and store multiple modes simultaneously, in order to evaluate the noise and signal-to-noise ratio (SNR) at the single-photon level, with the same pulse sequence described in figure 7.3. We performed storage experiments for  $T_s$  of 20, 50 and 100 ms, the results of which are reported in figure 8.1, with 6 temporal modes of size  $T_m = 1.65 \mu\text{s}$ . This particular choice stems from the discussion on the multimode capacity of a spin-wave storage in section 7.6, from which we optimize the HSH transfer pulse to a total duration of  $15 \mu\text{s}$ , 1.5 MHz of frequency chirp, and an AFC of  $1/\Delta = 25 \mu\text{s}$ .

For all values of  $T_s$  tested, the retrieved modes are well distinguishable from the background noise. The latter is mostly due to imperfections of the decoupling sequence that add unwanted population to the  $|s\rangle$  state in addition to the stored component. For each storage time, we adapted the decoupling sequence: XY-4 was used for 20 ms, XY-8 for 50 ms and XY-16 for 100 ms.

Table 8.1 shows the most relevant measured quantities at each storage time. We tried first of all to keep the input average number of photons per mode,  $\mu_{\text{in}}$ , close to one, though it slightly fluctuated and drifted during the long acquisition times of tens of hours. The probability of detecting a noise photon per mode, mostly generated by the RF and detected as spontaneous emission after readout, is indicated as  $p_n$  and was typically close to 0.01. Independent measurements with the RF signal off yielded an optics-only noise probability typically around 0.002. The value for  $p_n$  in the table in the 20 ms case is measured independently

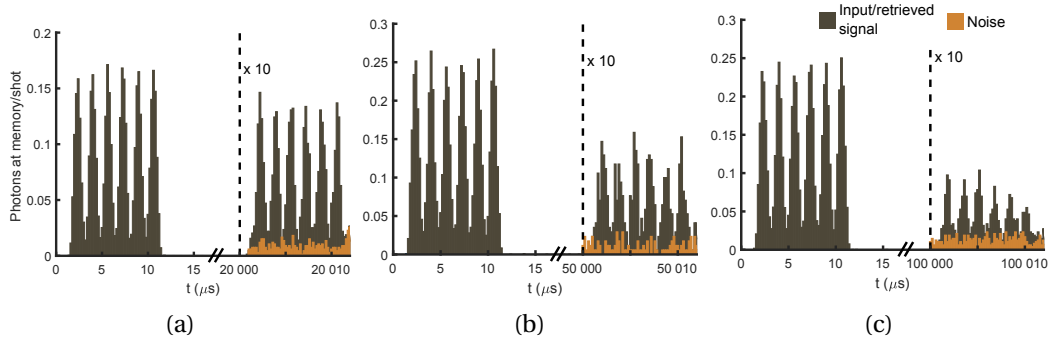


Figure 8.1: Spin-wave storage with single-photon-level input for (a) 20 ms, (b) 50 ms and (c) 100 ms. For each sub-figure, the left histogram shows the input signal for reference and the right shows the retrieved modes (black) and noise (orange).

$T_s$ (ms)	$\mu_{in}$	$p_n$	$\eta$ (%)	SNR	$\mu_1$
20	$0.711 \pm 0.006$	$0.0073 \pm 0.0012$	$7.39 \pm 0.04$	$7.4 \pm 0.5$	$0.098 \pm 0.002$
50	$1.21 \pm 0.01$	$0.009 \pm 0.002$	$4.37 \pm 0.04$	$5.6 \pm 0.7$	$0.218 \pm 0.008$
100	$1.062 \pm 0.007$	$0.0110 \pm 0.0015$	$2.60 \pm 0.02$	$2.5 \pm 0.2$	$0.445 \pm 0.008$

Table 8.1: Relevant quantities for single photon-level storage as described in the main text: spin storage time  $T_s$ , average input photon number  $\mu_{in}$ , noise detection probability  $p_n$ , storage efficiency  $\eta$ , signal-to-noise ratio SNR,  $\mu_1$  parameter. Each quantity is evaluated first separately in each mode of size  $T_m$ , then averaged over all six modes.

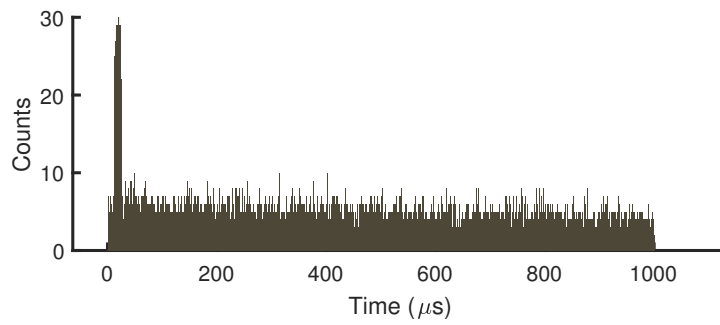


Figure 8.2: Noise photon counts after  $T_s = 20$  ms, with input optical pulses off. Right after the range in which the retrieved modes should appear, starting at  $\sim 10 \mu\text{s}$ , an echo of the readout transfer pulse is visible. This echo is present in all measurements, but always appears after the last stored mode and does not disturb the SNR. After that, the noise floor is again the same as the first  $10 \mu\text{s}$  and slowly decays according to the optical  $T_1 = 1.97$  ms (according to Könz et al.<sup>70</sup>).

by blocking the input pulse, so the detected counts must have been generated mainly by the memory protocol itself. This noise being incoherent, it produces a background with the shape of the spontaneous decay of few milliseconds, which appears flat in the  $\sim 100 \mu\text{s}$  range, as shown in figure 8.2. For this reason, to increase the detection rate of noise calibrations, we used the counts in a  $225 \mu\text{s}$  interval after the readout for the other two storage times reported in the table. In any case, an independent set of measurements collected on a different day for the noise generated by the various sequences up to the XY-8 confirms that the noise is independent on the number of decoupling pulses used. In fact, we found the values of  $p_n = 7.4 \times 10^{-3}$ ,  $8.1 \times 10^{-3}$  and  $8.6 \times 10^{-3}$  respectively for XX, XY-4 and XY-8, in all cases with an error of  $\pm 0.3 \times 10^{-3}$ . This means that we are not yet limited in the excess population by pulse area errors, as these should be reduced when using higher order pulse sequences. The exact cause of the population error is thus generally unclear at this point.

The efficiency  $\eta$  decreased from  $(7.39 \pm 0.04) \%$  of 20 ms to  $(2.60 \pm 0.02) \%$  at 100 ms. This is in agreement with what we have measured with bright pulses in section 7.6, though for the highest two values of  $T_s$  we find a slightly lower efficiency. It is possible that the generally long acquisition times between 20 and 70 hours exposed the experiment to long-term fluctuations of the general optical alignment. The SNR is well above 2 for all cases, which leads to the  $\mu_1$  parameter being between 0.4 and 0.1. This quantity indicates the minimum average value of  $\mu_{\text{in}}$  required in input to obtain an SNR= 1 in output, and is here derived as  $\mu_1 = p_n/\eta$ . In other words, we could in principle store a Fock single-photon state qubit if it can arrive at the memory with probability higher than  $\mu_1$ <sup>66</sup>.

From this experiment, we learned that our memory is capable of a good SNR up to at least 100 ms, which might be further improved by using more complicated decoupling sequences, since for now the number of RF pulses used does not yet increase the noise. In principle, to store for a longer time, a fixed distance between



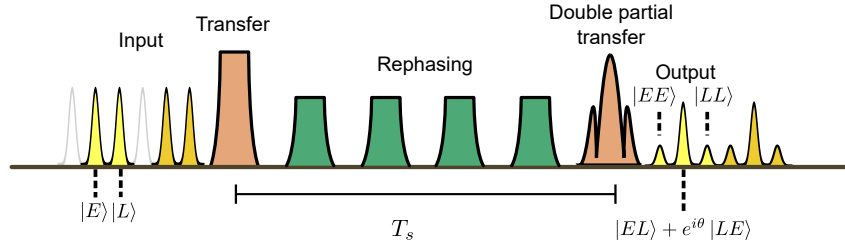


Figure 8.3: Time sequence of pulses for qubit storage. In total, four of the six input modes are used to encode two qubits at each storage attempt. A modified transfer pulse reads out partially the two qubits in two times separated by the mode size  $T_m$  to overlap the two components of each qubit in one temporal mode for interference.

DD pulses needs be kept and we could simply add more pulses<sup>100</sup>. However, this quickly leads to sequences with even hundreds of pulses. With our current setup this cannot be done at the single-photon level due to the heating beyond 16 pulses. This is a technical issue we hope to solve, after which storage in the range of hundreds of milliseconds will be feasible with the current coherence properties of our memory.

## 8.2 Time-bin qubit storage

We can now attempt the storage of a quantum state in the form of a time-bin qubit, for which we chose the storage time with highest efficiency we tested,  $T_s = 20$  ms. By separating an input pulse into two adjacent time modes, each one with an average number of photons of 0.5, we define a qubit in an early-late basis  $\{|E\rangle, |L\rangle\}$  (see figures 8.3 and 8.6a). After storage, a modified transfer pulse, qualitatively described by figure 8.4, reads out partially each component in two time instances, separated by a time delay corresponding to the bin size  $T_m$ . The relative phase between the two partial readouts can be changed by an internal parameter  $\theta$  of the pulse. This essentially works as an imbalanced interferometer, though it is embedded in the memory protocol and does not require particular stabilization or additional hardware. As a result, for each qubit, we will see at the output three occupied modes. In time order, the first one contains the early component of the qubit of the first partial readout  $|EE\rangle$ , the third one the late component from the second partial readout  $|LL\rangle$ , and the middle mode contains the coherent sum of early and late components  $1/\sqrt{2}(|EL\rangle + e^{i\theta} |LE\rangle)$ . This is exemplified by figure 8.6b for two qubits stored together and for the relative phases of  $\theta = 0$  and  $\theta = \pi$ .

We can generalize the framework by associating to each basis the respective Pauli matrices they diagonalize:  $\sigma_x$ ,  $\sigma_y$  and  $\sigma_z$  for  $1/\sqrt{2}(|EL\rangle \pm |LE\rangle)$  ( $x$  basis),  $1/\sqrt{2}(|EL\rangle \pm i|LE\rangle)$  ( $y$  basis) and  $\{|EE\rangle, |LL\rangle\}$  ( $z$  basis) respectively. In this sense, the input qubits were encoded as an eigenstate of operator  $\hat{\sigma}_x$ . From here, we can

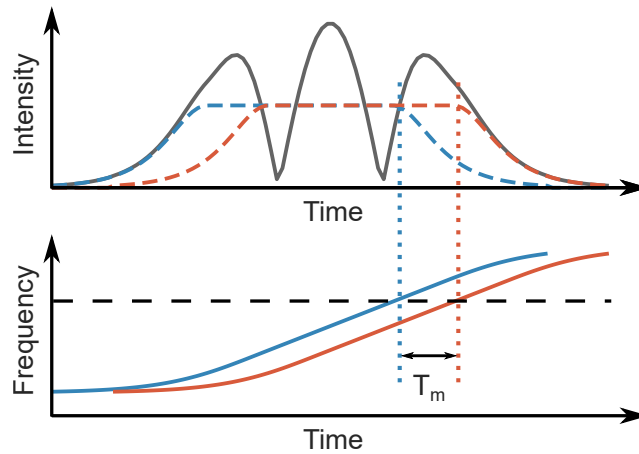


Figure 8.4: Sketch of the intuition behind the composite HSH pulse used for qubit readout. The fields of two standard HSH pulses are delayed by one mode size  $T_m$  and summed, with a relative phase  $\theta$  between the two. The intensity of the resulting pulse will depend on the phase and appear as an interference pattern (black line, in the top panel). The dashed blue and red lines indicate the intensity of the separated HSH pulses. The bottom panel shows the situation in the frequency domain, with the two independent chirps applied to the two HSH components. By calibrating the intensity accordingly, the stored state will be partially read out at two times delayed by the mode size.

associate to the system the density matrix

$$\rho = \frac{1}{2} (\mathbb{1} + \mathbf{r} \cdot \boldsymbol{\sigma}) \quad (8.1)$$

with  $\mathbf{r}$  the state vector in the Bloch sphere and  $\boldsymbol{\sigma} = (\sigma_x, \sigma_y, \sigma_z)$  the vector of the Pauli matrices.

The practical reason for this procedure is to tie the Pauli formalism to the measurable visibility values  $V_x$ ,  $V_y$  and  $V_z$  between the projections of the read-out state onto the two elements of each basis, as in the direct inversion method<sup>116</sup>. Here, they correspond to the expectation values of the Pauli operators, so that we can construct the Bloch vector of our state as

$$\mathbf{r} = (V_x, V_y, V_z). \quad (8.2)$$

Once the vector  $\mathbf{r}$  is characterized, we can obtain the measured fidelity through its definition, assuming the input state  $\rho_{\text{in}}$  is a pure state,  $\mathcal{F} = \text{tr}(\rho \rho_{\text{in}})$ . By using the Bloch vector associated to our input state  $\mathbf{r}_{\text{in}} = (1, 0, 0)$  and using the same form as in 8.1, we obtain

$$\mathcal{F} = \frac{1}{2} (1 + \mathbf{r} \cdot \mathbf{r}_{\text{in}}). \quad (8.3)$$

The visibility values are reported in table 8.2, from which we obtain a fidelity  $\mathcal{F} = (85 \pm 2) \%$ .

This value of fidelity should be limited by the same type of noise represented by  $p_n$ . A practical example of this is the completely destructive interference one

should observe in the central bin of figure 8.6 for  $\theta = \pi$ , which instead displays some residual detections. Another indication of this is the purity, defined as

$$\mathcal{P} = \text{tr}(\rho^2) = \frac{1}{2} (1 + |\mathbf{r}|^2), \quad (8.4)$$

and which, with our Bloch vector, results in  $\mathcal{P} = (76 \pm 3) \%$ . This indicates a white noise component to the retrieved state. Furthermore, we can independently measure a "classical" fidelity with bright pulses in order to have a negligible noise component, which yields in our case a fidelity of 96 %.

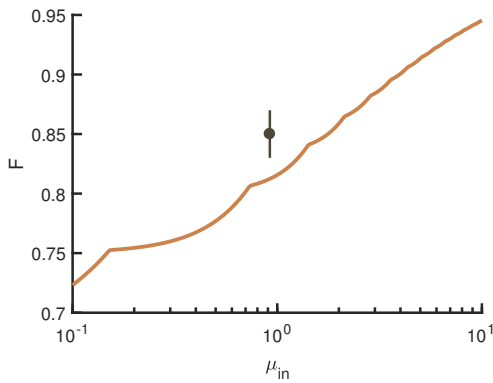


Figure 8.5: Fidelity threshold criterion for quantum storage of weak coherent states from Specht et al.<sup>117</sup> as a function of the input photon number  $\mu_{\text{in}}$ . Our measured fidelity surpasses the classical limit by more than one standard deviation, represented by the errorbars.

Even though coherent states are used as input to implement the qubit, we can show that several classical strategies cannot reach the fidelity we measure, even considering the efficiency and noise of our implementation. Specht et al.<sup>117</sup> introduced a criterion to distinguish a quantum storage from a measure-and-prepare strategy with a classical device. With this method, it would be possible to emulate the qubit storage up to a limited fidelity of 81.2 % with our same input photon number  $\mu_{\text{in}} = 0.92$ . Our fidelity however is well above this threshold as represented in figure 8.5.

Another method was derived for the case of storage of Fock states, for which the classical emulation limit on the fidelity is of  $2/3$ <sup>118</sup>. In this case, the limit can be violated by having a single photon at the input of the memory with a probability higher than  $\mu_1$ <sup>66,112</sup>. If we assume a realistic heralding efficiency of 19 %, demonstrated in quantum storage experiments with Pr:YSO<sup>89</sup>, with our settings we could obtain a fidelity of 75 %, higher than the classical  $2/3$  limit.

Basis	$V$
$ EL\rangle \pm  LE\rangle$	$0.70 \pm 0.04$
$ EL\rangle \pm i LE\rangle$	$-0.14 \pm 0.07$
$ EL\rangle,  LE\rangle$	$-0.06 \pm 0.03$

Table 8.2: Visibility values measured in three time-bin bases.

These results confirm the capability of our memory to store for tens of milliseconds at the quantum level, with margins of improvement mostly given by technical challenges. We also implemented a new type of readout procedure involving a composite HSH, which will be described more in detail and extended to the storage of more general quantum states in a future publication.

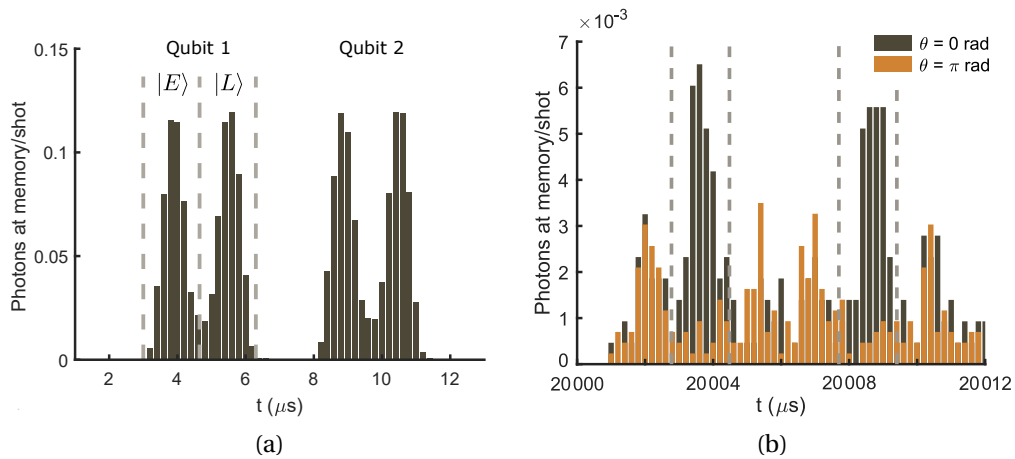


Figure 8.6: (a) Histogram of the input time-bin qubits. The dashed gray lines indicate the time modes in which the  $|E\rangle$  and  $|L\rangle$  are encoded, with an average of 0.5 photons in each, for a total of 1 per qubit. (b) Histograms displaying the average number of photons in output of the memory after storage and readout of the qubits in (a), for  $\theta = 0$  (black) and  $\theta = \pi$  rad (orange). The pairs of dashed gray lines identify the time bins in which the the  $|EL\rangle$  and  $|LE\rangle$  components interfere.

## 8.3 AFC-DLCZ

### 8.3.1 Introduction

So far, we have seen examples of input-output memories, that is storage devices meant to interface with externally generated arbitrary states, to be read out on-demand at a chosen time. There are protocols, however, that do not require external states, but only exploit the entanglement of two signals generated by the device itself and delay the emission of one of the two entangled components using their storage capabilities. These are called read-only memories, and they work as both the generators and time-buffer of the resource employed to secure communication in a network<sup>11</sup>.

The first practical proposal for a similar device was the one of Duan, Lukin, Cirac and Zoller, from which the DLCZ protocol takes its name<sup>36</sup>. The original paper considered clouds of neutral atoms, such as rubidium, on which an excitation pulse was tailored so to Raman-scatter a single emission on a second transition (in their example, a Stokes emission, since it had a lower frequency). Figure 8.7a displays the energy structure proposed. This single Stokes photon worked as a heralding signal for the generation of the entangled excitation that now remained in another hyperfine level  $|s\rangle$ . After some time, a strong read pulse would read out the excitation again by inverting the excitation process, producing an anti-Stokes signal. Since the two emissions are entangled, they can be used as a resource in proving the security of a quantum channel for communication. Examples of similar experimental implementations involved mostly neutral atoms in a variety of degrees of freedom<sup>119–127</sup>, with quantum correlations observed more in general

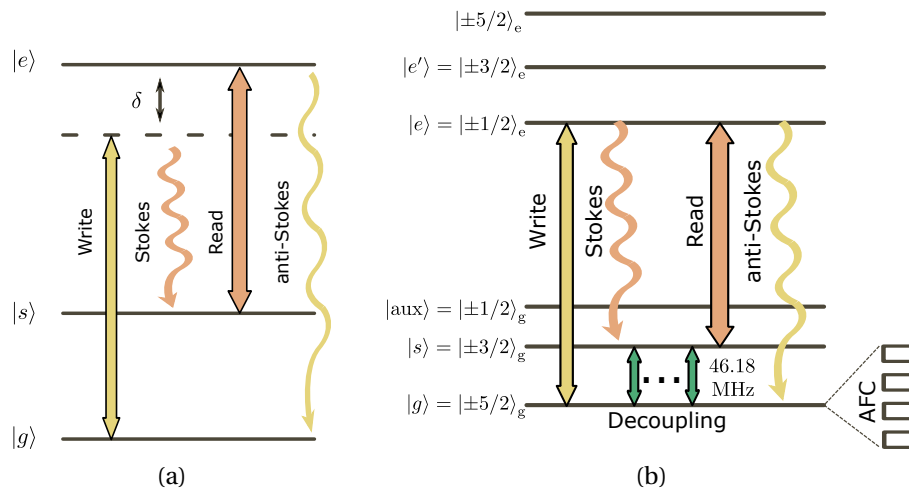


Figure 8.7: (a) Transitions for a DLCZ protocol as proposed in the original paper. The optical transitions are off-resonant to induce an instantaneous Raman scattering, and the ground states are typically spin states of atoms with a well defined quantum number. (b) Transitions for our AFC-DLCZ implementation in Eu:YSO. The main differences with the original proposal is the use of on-resonant transitions with an AFC on the write one and dynamical decoupling on the spin transition to extend the coherence time.

also in thin diamonds<sup>128–130</sup>, various molecules<sup>131</sup>, nanomechanical resonators<sup>132</sup> and even liquid water<sup>133</sup>. With some adaptations we will now discuss, the DLCZ protocol has also been applied to rare earths<sup>67,83,134</sup>.

The original protocol as it was conceived could not be executed in just any platform, as it made use of detuned optical pulses for the Raman emission and spin states for the long storage. While the latter is not an issue in rare earth-doped crystals, Raman scattering of highly detuned pulses is typically not possible given the mixing of the spin-orbit states by the crystal field and the consequent weakening of off-resonant transitions. The only way to transfer atoms between energy levels in these systems is with resonant pulses.

A solution to this problem was proposed in 2011 by Sekatski et al.<sup>135</sup>, involving the AFC in extending the coherence that would otherwise be quickly lost in a resonant inhomogeneously broadened optical transition. This is how the DLCZ was extended into the AFC-DLCZ protocol, and successfully used in generating first non-classical correlations in europium and praseodymium<sup>67,83</sup> and more recently proper time-bin entanglement with the violation of a CHSH inequality<sup>134</sup>. The goal of our prototype based on europium is to extend the protocol operation from the previous 1 ms of Laplane et al.<sup>67</sup> to at least tens of milliseconds, enabled by our improved spin-wave storage.

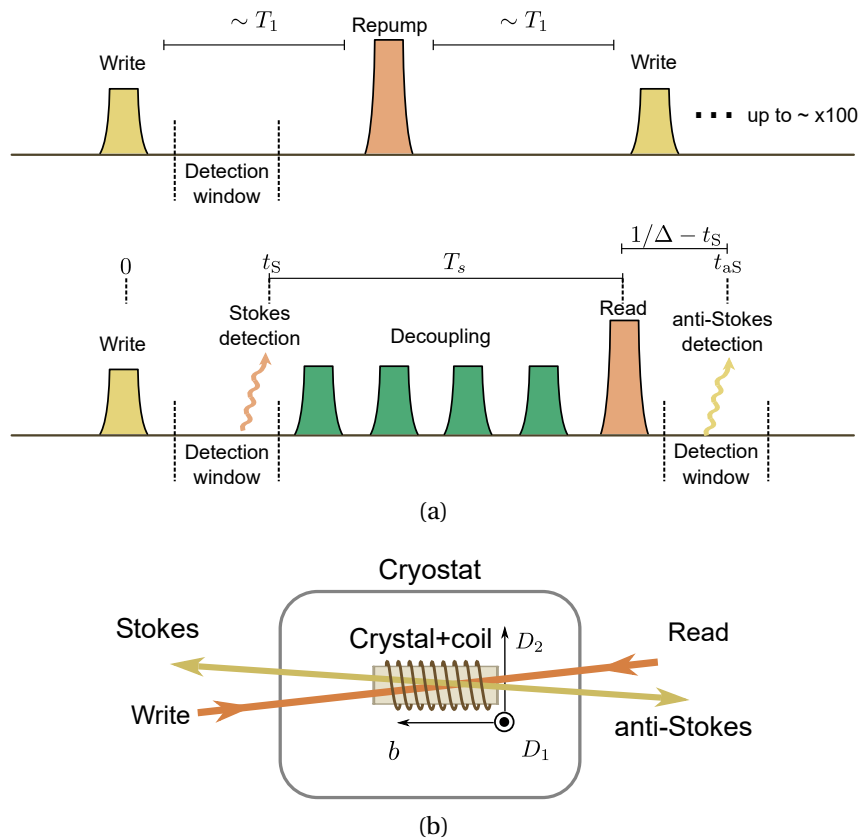


Figure 8.8: (a) Temporal sequence of the AFC-DLCZ protocol. (Top) Initially, the write creates the first excitation from which the Stokes can be created. If no Stokes is detected within a limited detection window, after the excited population fully decayed, the storage state  $|s\rangle$  is emptied by a repump pulse similar to the read. This can be repeated up to few hundreds of times before the optical depth of the AFC starts to be compromised and the memory is reprepared. (Bottom) If a Stokes is detected after the write, the storage starts with a  $T_s$  equal to the time separation between the detection and the read pulse. A correlated anti-Stokes should be detected at a second detection window. The memory is always reinitialized after. (b) Simplified sketch of the setup show in figure 5.3, highlighting the beam paths relevant to the DLCZ experiment.

### 8.3.2 AFC-DLCZ implementation

The AFC-DLCZ pulse sequence is sketched in figure 8.8 and the related transitions in figure 8.7b. After the same preparation undergone by the spin wave memory we have seen earlier, the AFC-DLCZ starts with a write pulse applied on the  $|g\rangle \leftrightarrow |e\rangle$  transition, tailored in temporal shape and frequency chirp so to match the read pulse to be used later. Atoms are excited in a collective way according to the usual AFC coherence rules, though instead of transferring them actively with an optical pulse into an empty spin state as in the standard spin-wave storage of the previous sections, we use the  $|e\rangle$  state as a reservoir of spontaneous emission. With a probability depending on the excited population fraction (which depends on the write pulse power) and the optical depth, a bunch of atoms will decay into all ground states according to the branching ratios, but we are interested in the ones that end up in the storage state  $|s\rangle$ , initially empty, before the AFC echo is emitted. With some probability  $p_s$ , we will detect the photon emitted during the spontaneous decay of one atom in a spatial mode with a small angle with respect to the write, in the opposite direction, which we call Stokes photon in analogy to a Raman scattering setting.

At this point, the spin storage starts, as we use this detection to trigger the dynamical decoupling sequence to extend the coherence time of the single excitation correlated with the detected Stokes. Note that an AFC echo of the write pulse will still take place at  $1/\Delta$ , but emitted in the same transition as the write and will not disturb the heralded single-excitation spin-wave in  $|s\rangle$ .

At a time  $T_s$  after the detection, a read pulse is applied in the opposite direction of the write at the maximum available power, which ideally should perform a 100% transfer of the spin excitation to the excited state. Similarly to the standard spin storage, the excited component continues the phase evolution dictated by the AFC and emits an anti-Stokes photon, but in the opposite direction to the Stokes.

Once both detections occurred and the corresponding detection timestamps saved, we can show the non-classical correlation between Stokes and anti-Stokes using the fact that they will always be emitted with a well defined time difference dependent on the storage parameters. The non-classical character of the correlations can be proved by violating a theoretical bound involving the cross-correlation function  $g_{s,as}$

$$g_{s,as}^{(2)} = \frac{\langle a_s^+ a_{as}^+ a_s a_{as} \rangle}{\langle a_s^+ a_s \rangle \langle a_{as}^+ a_{as} \rangle} \simeq \frac{p_{s,as}}{p_s p_{as}} \quad (8.5)$$

where  $a_i$  and  $a_i^+$  represent the annihilation and creation operators of the emitted fields,  $p_i$  the probability of their detection and  $p_{s,as}$  the probability of a coincident detection of two photons in the two fields. The approximation into the term on the rightmost side is valid when  $p_{s,as} \ll 1$ , which is typically the case. A more explicit derivation is presented in Etesse et al.<sup>136</sup>. In the works of Laplane<sup>67</sup>,

Kutluer<sup>83</sup> and their colleagues, a Cauchy-Schwartz inequality is used to show that the correlations are non-classical:

$$g_{S,aS}^{(2)} \leq \sqrt{g_{S,S}^{(2)} g_{aS,aS}^{(2)}}. \quad (8.6)$$

Any two fields  $S$  and  $aS$ , if classical in nature, must obey the inequality, while non-classical ones can yield cross correlations larger than this bound. This tool was first proposed by Clauser<sup>137</sup> to experimentally distinguish between quantum and classical fields. In principle, it requires to measure also the auto-correlation functions of each field, which for theoretical thermal states correspond to a value of  $g_{S,S} = g_{aS,aS} = 2$ , but in practice have even lower values<sup>67,83</sup>. Here, we will assume for the moment the upper bound of  $g_{S,S} = g_{aS,aS} = 2$ , which by the Cauchy-Schwartz inequality implies that, if  $g_{S,aS} > 2$ , the fields  $S$  and  $aS$  must have non-classical correlations.

The works on Eu:YSO and Pr:YSO mentioned above made use of the intrinsic multi-mode capability of the AFC. In short, the whole time frame between the application of the write pulse and the AFC delay  $1/\Delta$  is considered a useful detection gate for Stokes, and divided in time bins corresponding roughly to the bandwidth of the memory as fixed by the transfer pulse chirp (see also section 7.6). This effectively brings a linear scale-up of the detection rate over storage attempts, and hence the coincidence rate, similarly to what happens when using multiple input time modes in a input-output memory.

The absolute coincidence rate is however always limited, mainly because the cross-correlation depends inversely on the Stokes probability  $p_S$  due to noise generated by multiple excitations. As a result, the number of experiment trials in which a Stokes is detected is actually a small fraction of the total, and most of the time the storage protocol is applied on an "empty" memory. This generally lengthens the data acquisition process and leaves the experiment vulnerable to perturbations such as alignment drifts and power fluctuations.

The issue was partially attenuated in our past works by repeating the storage sequence multiple times before reinitializing the memory and reparing the AFC from scratch. Given our new RF resonator circuit and enhanced current into the memory coil, this is not viable anymore as we observed heating effects that would perturb the memory. Moreover, the absolute coincidence rate over time would be reduced even more if we extend the storage time of each trial to tens of milliseconds. This is what motivated us to implement a conditional storage on the actual detection on a Stokes photon during its dedicated detection time window<sup>138</sup>. If no Stokes is detected, the storage state is repumped and a new write pulse applied again, preventing the RF and readout sequence from happening and saving us some time per storage trial. This write-detection-repumping sequence can be repeated until a Stokes is detected up to a limit on the amount of repetitions, after which the memory is re-initialized anyway to avoid an excessive deterioration of the AFC, since part of the population is lost into the  $|aux\rangle$  state at every cycle.



Another important difference with our past implementation is the set of optical transitions used. In the work of Laplane et al., after the write pulse is applied on  $|g\rangle \leftrightarrow |e\rangle$  and the Stokes is emitted on  $|e\rangle \leftrightarrow |s\rangle$ , an odd number of rephasing pulses brings the stored population back to  $|g\rangle$  and the read pulse is applied on the same transition of the write, while the anti-Stokes has the same frequency as the Stokes. This simplified the optical filtering (an optical cavity was used for the purpose), but required some care in the RF sequence, as after the initial preparation, the AFC needed to be transferred along the spin transition and the rephasing sequence had to be modified for the correct rephasing with three pulses (details shown in Laplane's thesis<sup>68</sup>). In our new version, we kept the DLCZ protocol closer to a standard spin-wave storage, at the cost of a more complicated filtering setup, described in 5.2.1, which is able to filter both the Stokes and anti-Stokes photons while providing a high absorption of the read pulse.

The major obstacle in showing cross-correlation values significantly above the classical limit of 2 is given by the noise background, due to uncorrelated detections close in time to the anti-Stokes, which might originate from several sources:

- a fundamental one that cannot be completely removed is given by the probabilistic nature of the Stokes-spin excitation pair generation, as it comes from the spontaneous emission of a reservoir of atoms excited by the write pulse which will lead to an always non-zero multiple pair creation probability. The write pulse will need to be as low as possible to suppress this component, in a compromise with the coincidence rate. This component is intrinsic to any DLCZ scheme.
- Part of the reservoir will decay along different transitions than the Stokes, so spectral filtering is necessary to not count photons emitted to states other than  $|s\rangle$ . This is true also during anti-Stokes detection. We addressed the optical filtering in section 5.2.1.
- Imperfections of the rephasing/decoupling RF pulses will add errors due to unwanted mixing of the coherent excitation in  $|s\rangle$  with the large population left in  $|g\rangle$  once the spin storage starts. This problem is the same we faced with the multimode single-photon level and qubit storage in the previous sections, so all the work we have done on the control of the spin transition in chapter 7 will be useful also here.
- Other technical noise comes from the environment residual light and dark counts of the detector, though as for the previous sections they are dominated by noise generated by the memory. Write and read pulses need to be properly gated in time and filtered to avoid scattered components into the detection paths. The same filtering system in section 5.2.1 will help attenuate this issue, together with temporal gating of AOMs and the detector.

A more detailed analysis of the influence of these noise sources on the cross-correlation and their dependence on the Stokes detection probability can be found in Etesse et al.<sup>136</sup>.

In a plot of the coincidences as a function of a relative time delay with respect to the expect coincidence peak, the effects described above will add to the background, reducing the contrast of the peak due to useful detections coincidences. On the other hand, the height of this peak will be limited by the storage and readout efficiencies. This is slightly different than in the standard spin-storage because we use only one transfer pulse, but it needs to respect a more stringent phase matching condition. Expressed in  $\mathbf{k}$  vectors, this is given by the sum of write, Stokes, RF, read and anti-Stokes contribution as

$$\mathbf{k}_w + \mathbf{k}_S + \mathbf{k}_{RF} + \mathbf{k}_r + \mathbf{k}_{AS} = 0. \quad (8.7)$$

Here,  $\mathbf{k}_{RF}$  can be ignored given its wavelength  $c/46\text{MHz} = 6.5\text{m}$ , much larger than the crystal length of 1.2 cm. Since the Stokes emission is spontaneously emitted after the write pulse, we can choose its direction simply by fixing a certain collection path coupled eventually with the detector. For convenience, in our setup (see for reference figure 5.3a) this is the same direction on which we coupled the input beam of the spin-wave experiments. This way, we have to apply the read pulse to match exactly the write path in the opposite direction and have the anti-Stokes emitted counter-propagating to the Stokes. The phase matching condition can be checked with bright pulses by stimulating the Stokes emission with an input, while maximizing the correlated anti-Stokes pulse after storage. However, during the long data acquisition times, the coupling of the beams with the optical fibers and the overall optics might not stay perfectly aligned and the phase matching could deteriorate.

Given the conditional storage we implemented, also the data analysis will be different. While in the past the timing of the rephasing and read pulses would be fixed, now it varies depending on the detection of the Stokes. This means that the spin storage is triggered at different times of the AFC phase evolution, which however are compensated after readout, so that the emission time of the anti-Stokes will be fixed at  $t_{aS} = T_s + 1/\Delta$  (see for example figure 8.8). When enough data is accumulated, the anti-Stokes will directly form a peak in the acquisition window at a time  $t_{aS}$ , while the background takes a trapezoidal shape due to the convolution of the square Stokes and anti-Stokes detection windows. In short, the anti-Stokes detection gate directly shows coincidences between emissions in the two fields. In our case, the detection window was  $20\mu\text{s}$ , though only the first half was used for coherent detections while the second half would only detect incoherent photons as a probe for the noise background.

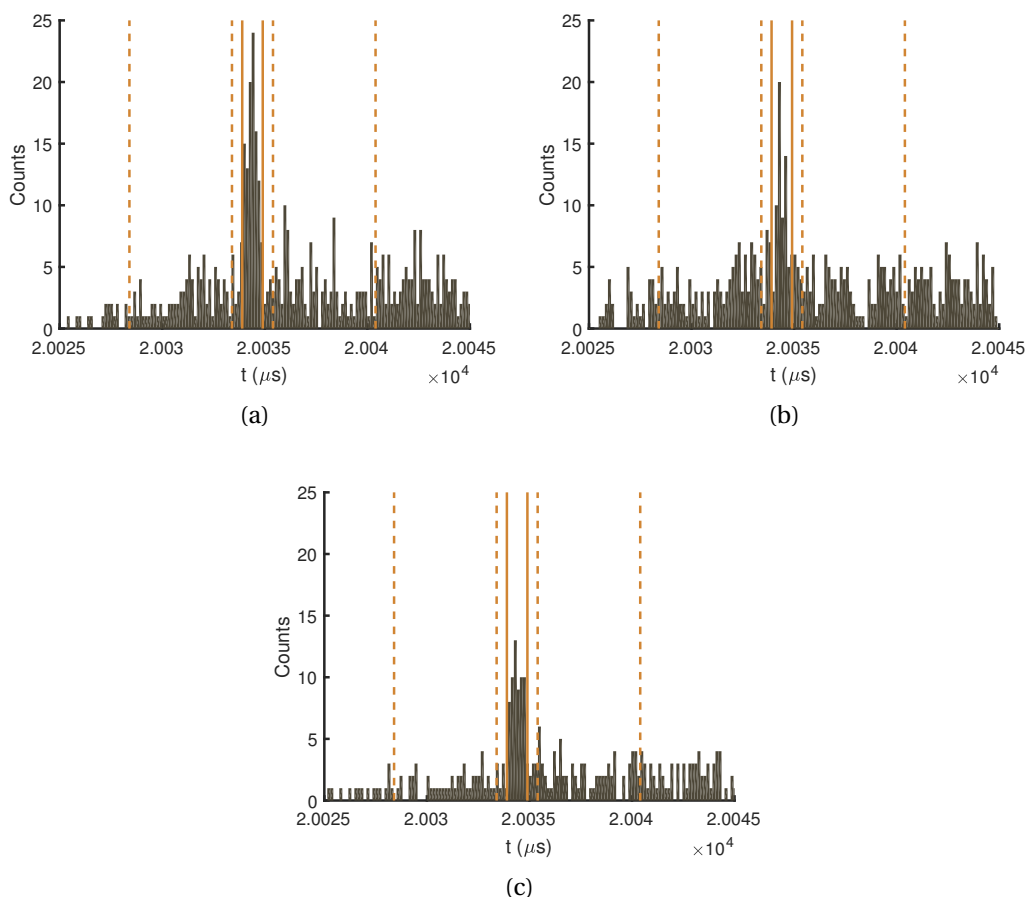


Figure 8.9: Examples of anti-Stokes counts obtained from the related detection window. Anti-Stokes are expected in the first  $10\mu\text{s}$ , but counts were collected for an additional time to monitor the noise background. The latter has a linear increase in the first half of the window, due to the time interval in which a Stokes can be detected in its on detection window. The orange solid lines delimit the  $1\mu\text{s}$  mode in which the correlated anti-Stokes should appear. The dashed lines instead delimit the ranges from which the noise background is estimated. The three examples are taken in different days and with slightly different experimental conditions, representative of the fluctuations we observed over time. The respective values of  $g_{\text{S,aS}}^{(2)}$  obtained are (a)  $5.0 \pm 0.7$ , (b)  $3.0 \pm 0.5$  and (c)  $5.1 \pm 0.9$ .

Measurement set	$g_{S,aS}^{(2)}$	$p_s$	$p_{aS}$	$\eta_{\text{out}}(\%)$	$R_c(\text{h}^{-1})$
a	$5.0 \pm 0.7$	0.006	0.004	$3.6 \pm 0.4$	1.18
b	$3.0 \pm 0.5$	0.008	0.008	$2.7 \pm 0.5$	1.46
c	$5.1 \pm 0.9$	0.005	0.005	$3.6 \pm 0.6$	1.01

Table 8.3: Examples of results from three measurement sets with a  $1 \mu\text{s}$  coincidence window. From the left column to right, the second order cross-correlation function  $g_{S,aS}^{(2)}$ , the probability of Stokes and anti-Stokes detections in their respective gates  $p_s$  and  $p_{aS}$ , the readout efficiency  $\eta_{\text{out}}$  and the absolute rate of coincidences over time  $R_c(\text{h}^{-1})$ .

### 8.3.3 Results

Figure 8.9 shows examples of coincidence histograms resulting from the experiment with  $T_s = 20 \text{ ms}$ ,  $1/\Delta = 25 \mu\text{s}$  and a bin resolution of  $100 \text{ ns}$ . As mentioned earlier, the peak is a sign of the successful storage and readout of a quantum state component correlated with the Stokes. To evaluate the cross-correlation function, we can calculate it as the ratio between the counts in the peak and an estimate of the accidental coincidences as an average of the ones coming right before and after the peak, in the positive linear slope. This gives us values ranging from  $5.1 \pm 0.9$  to  $3.0 \pm 0.5$ , with the coincidence detection window fixed at  $1 \mu\text{s}$ , accumulated in total measurement times between 45 h and 90 h (all errors of measurements based on counts are given by considering Poissonian statistics). These are independent measurements taken on separate days, with generally the same setup but with small variations of some conditions such as  $p_s$ , write-read phase matching optimization and adjustments in the complex electronics controlling the conditional detection method, in an attempt of optimizing the cross correlation function and coincidence detection rate. Other runs here not reported confirmed a fluctuating behavior, with  $g_{S,aS}^{(2)}$  values ranging between 3 and 5, also at a lower  $T_s$  value of  $10 \text{ ms}$ . The optimization of the experiment and troubleshooting of issues was made harder by our low coincidence rate, which required data accumulation for at least  $\sim 50 \text{ h}$  to get acceptable statistical errors. Nonetheless, the cross-correlation values given by the data show the detection of non-classical correlations.

Table 8.3 reports more details about the three sets. In particular, we can look at the values of one of the best cases (set c): the probability of detecting a Stokes in its  $10 \mu\text{s}$  detection gate is 0.005, equal to the anti-Stokes one. The readout efficiency can be estimated by the formula

$$\eta_{\text{out}} = \frac{N_{\text{cw}} - N_{\text{bg}}}{N_s \eta_t \eta_d}, \quad (8.8)$$

where  $N_{\text{cw}}$  stands for the counts in the coincidence window of the anti-Stokes,  $N_{\text{bg}}$  the number of background detections,  $N_s$  the total number of Stokes detections,  $\eta_t = 18\%$  the transmission efficiency of the path between memory output and

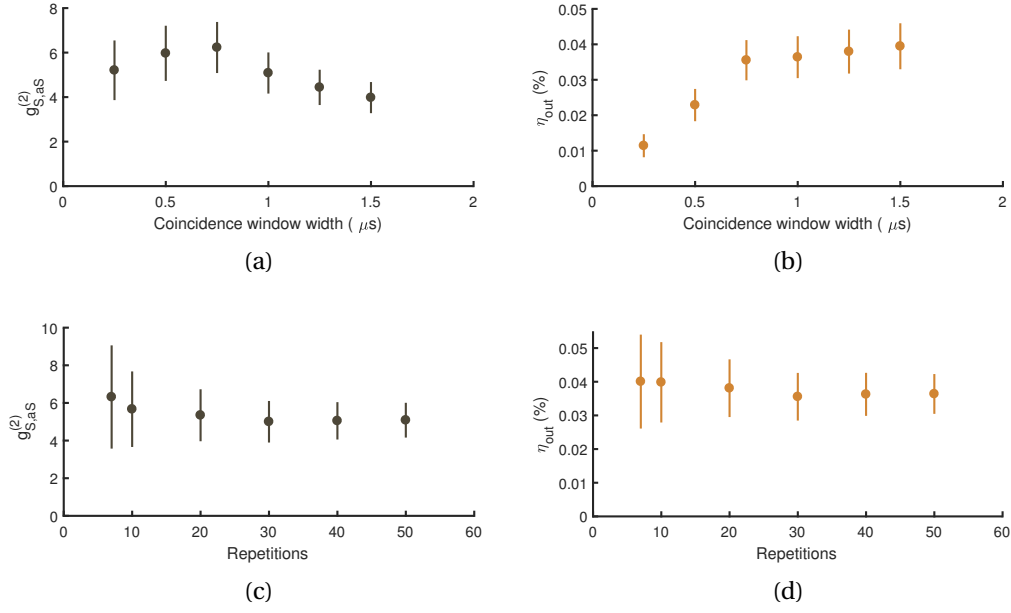


Figure 8.10: Variation of the second order cross correlation  $g_{S,as}^{(2)}$  (left panels, (a) and (c)) and readout efficiency (right panels, (b) and (d)) as a function of the coincidence window width (top panels) and write-repump cycle repetition number (bottom panels), for the dataset "c" in table 8.3 and figure 8.9c.

detector and  $\eta_d = 56\%$  the detection efficiency of the sensor.

With a  $1\ \mu s$  wide coincidence window, we get  $\eta_{out} = (3.6 \pm 0.6)\%$ . This value however changes as a function of the width of the window, typically increasing proportionally with it. Similarly,  $g_{S,as}^{(2)}$  changes if we modify the coincidence window, though inversely with the width. Examples of these trends are reported in figures 8.10a and 8.10b, showing a peak  $g_{S,as}^{(2)} = 6.2 \pm 1.1$  for  $0.75\ \mu s$  of coincidence window width. We also monitored the two quantities as a function of the write-repump repetition number (figures 8.10c and 8.10d) in which the Stokes detection occurred, to verify that the performance is not affected by a drop in the AFC efficiency. See figures 8.10c and 8.10d.

To compare with the results of Laplane et al.<sup>67</sup>, we need to take into account the different parameters used. In that work, with a  $T_s$  of 1 ms, a coincidence window size of 100 ns yields a readout efficiency of 0.45 % and a  $g_{S,as}^{(2)}$  of  $4.2 \pm 0.5$ . The choice of such a narrow coincidence window stems in fact from a compromise between the cross-correlation value and the efficiency, the latter increasing to  $(2.5 \pm 0.3)\%$  if the window is increased to 820 ns. In our last results, with a 10 times wider coincidence window, we typically obtain a similar value of cross-correlation, but without compromising too much the efficiency, normally around 3 %, and at 20 times the storage time.

It is clear that our experiment is not performing at ideal conditions. First of all, the estimated efficiency is lower than what we would expect from the previous AFC and spin-wave characterizations, which assuming no rephasing errors from

the RF pulses and the use of only one optical transfer, should be approximated by  $\eta_{\text{DLCZ}} \approx \eta_{\text{AFC}} \eta_{\text{t}}$ . Here, the AFC efficiency is 16 %, measured with bright pulses independently in a single pass configuration at 1.35 mT and  $1/\Delta = 25 \mu\text{s}$ . The read efficiency should be similar to the one estimated in section 7.6 as about 80 %. This would result in an efficiency of 13 %. However, we saw how even in the standard spin-storage the final efficiency was actually half the expected one. In the worst case of a factor of two dividing the DLCZ efficiency, the gap with the measured value is still too large. It is possible that our method of phase matching is not accurate enough, or that the same unknown effect limiting our input/output spin-storage efficiency affects more strongly the DLCZ. Another issue is the still limited acquisition rate over time, which exposes the experiment to fluctuations. To solve the issue, we need to reduce as much as possible the losses coming from the path from the output of the memory to the detector, which for now give about 18 % of transmission efficiency.

With more consistent measurement results, it should be possible to demonstrate, similarly to what has been done in Pr:YSO at  $T_s = 16 \mu\text{s}$ , a certain degree of entanglement of the Stokes and anti-Stokes fields, which later could be coupled to other quantum memories and frequency-converted to the telecom band. Parallel work is being carried out in our same laboratory involving a quantum frequency conversion setup for 580 nm light, which has been already characterized in the past<sup>29,139,140</sup> and improved further.

## 8.4 Eu:YSO - Conclusion

These results are the last ones obtained in my doctoral work, and in particular for Eu:YSO. As we have seen, the whole setup has been upgraded, which ultimately brought to improvements in the AFC and spin-wave memories. In this last chapter, we have applied our protocols at the single-photon level regime, characterizing the noise and SNR of multimode and qubit storage. We finally revisited the AFC-DLCZ and obtained preliminary results on non-classical correlations, similarly to what Laplane et al. demonstrated in 2017<sup>67</sup>, but at a delay between Stokes and anti-Stokes improved by a factor 20 and with a storage conditioned on the heralded creation of the spin excitation. Limitations in detection rate and readout efficiency should be overcome in the near future by a more systematic technical optimization of the setup.

In the future, possible lines of investigation involve exploring the role of the degeneracy of the nuclear spin states in the spin-wave storage by applying much higher fields, which might shed some light in particular on the missing storage efficiency. As for the DLCZ, after having addressed the technical issues of low coincidence rates, we could couple the Stokes field to a telecom converter setup, with the goal of demonstrating non-classical correlations between a telecom photon over tens of kilometers and stored spin excitation for 20 ms or more. We

would also need to demonstrate that the Stokes and the spin-wave excitation are actually entangled even at our long storage times, which would require to increase the cross-correlation function by solving the efficiency issue. All these improvements will bring our system closer to a functioning repeater prototype by showing all the features required to work in a quantum network setting.

# Conclusions and outlook

During my doctoral studies in Geneva, I had the chance to work at different phases of the evolution of a candidate material for a quantum memory device. After a brief introduction with neodymium, on which I learned about Raman heterodyne scattering and how to use spin echoes to probe the coherence dynamics of a spin system, I found myself exploring ytterbium in YSO at a stage in which many of its secrets were yet to be revealed. With my postdoc at the time, Alexey Tiranov, we performed a spectroscopic investigation at magnetic fields ranging from zero to few hundreds mT, complementing earlier work at higher fields and fully characterizing the hyperfine interaction between nuclear and electronic spins. Interestingly, these findings were later confirmed theoretically by independent investigations with numerical tools<sup>141</sup>. The exploration of the coherence dynamics led to the discovery of a simultaneous ZEFOZ condition for all optical and microwave frequencies at zero field, possible due to the complete anisotropy of the hyperfine interaction and the formation of maximally entangled Bell states. In some specific directions, the system retains some insensitivity to external fluctuations even at higher fields of a few mT.

The second part of my doctorate experience involved a general upgrade of a setup built for the implementation of memory protocols on europium in YSO. After having improved several technical aspects, we greatly improved on the state of the art of the AFC protocol in europium in both maximum efficiency and coherence lifetime. At the single photon level, we demonstrated the storage of 100 input modes, and investigated the multimode capacity dependence on the AFC parameters.

We also improved our degree of control of the spin transitions with the development of a new circuit resonator. Thanks to a low magnetic field and dynamical decoupling, we improved the coherence lifetime of our spin-wave protocol at the single photon level, reaching 100 ms of storage of 6 temporal modes with an SNR above 2. This allowed us to proceed with the demonstration of storage of a time-bin qubit, with high fidelity.

My last months in the lab involved the configuration of a new conditional DLCZ setup with a feed-forward feature based on the detection of a Stokes photon, which enabled to the implementation of conditional storage on the heralding of a single excitation in the memory. This led us to show non-classical correlations



between a heralding photon and the readout 20 ms apart.

From here, both systems I worked with still have large margins of improvements, and so do quantum memories in general. The characterizations on Yb:YSO and its surprisingly good properties highlight the importance of fundamental spectroscopy studies and research on new materials, especially after it led to the general finding that all systems with  $S = 1/2$ , half integer nuclear spin and anisotropic hyperfine interaction should have in principle a zero-field ZEFOZ. ZEFOZ transitions have indeed been found later in other Kramers ions such as Er in YSO<sup>59</sup> and in LiYF<sup>142</sup>, and more in general in Tm:YGG<sup>143</sup> and even transition metals like Cr:YSO<sup>144</sup>. More fundamental spectroscopy is being carried out in rare earths in other host materials, in particular erbium in silicon<sup>145,146</sup>, CaWO<sub>4</sub><sup>147</sup>, TiO<sub>2</sub><sup>148</sup> and many others<sup>149</sup>. Always newer platforms try to exploit the great optical properties of rare earths in hosts that allow a high degree of engineering and light manipulation, like molecular complexes<sup>150</sup> and nano-particles<sup>151–153</sup>.

On the applications side, Yb:YSO can be used as a broadband photonic memory, as exemplified by the work of my colleague Moritz Businger and others in a proof of concept<sup>45</sup>, with ongoing work to bring it at the single-photon level and quantum regime. A control and extension of the coherence time can be obtained by dynamical decoupling and the broad pumping effect<sup>44</sup>, which should enhance the spin-wave storage. The possibility of long coherence times at zero field opens up avenues for Yb as a transducer to microwaves<sup>154</sup>, interesting for instance to couple with systems operating at low fields like superconducting qubits. Transduction between microwave and optics is considered in general for rare earths, with potential efficiencies above 80 %<sup>155</sup>.

Eu:YSO too has not exhausted its potential. In chapter 6, the AFC coherence times proved to be still far from their fundamental limitation given by the optical coherence time. Extending it further would improve also the multi-mode capacity, which is the core strength of the AFC in view of applications for high-rate communication. We saw in chapter 7 how our dynamical decoupling is still elementary and could be extended to reach storage times of seconds, similarly to what has been done in Holzäpfel et al.<sup>100</sup>, but at a lower field and with a different spin transition that in principle should double the coherence time with a fixed number of decoupling pulses. Technical challenges like heating dissipation will need to be addressed, while keeping the noise produced by RF pulses at a minimum. For this purpose, new dynamical decoupling and pulse optimization techniques could be tested<sup>156</sup>. The identification of yet unknown problems affecting the spin-wave storage could potentially double the overall efficiency, of which we might have just started to scratch the surface with the hypothesis of the path interference illustrated in our *Paper III* and with further theoretical investigations currently in progress. This includes the role of the magnetic field on storage, which up to now has been used pragmatically and which still requires a more complete explanation for its positive contribution to the coherence time.

As a consequence, the DLCZ protocol would also benefit from this, and further technical improvements with boosts of the coincidence generation rate could lead in the near future to the demonstration of the storage of entangled states for hundreds of milliseconds, while interfacing with a quantum frequency conversion stage to bring Stokes photons into the telecom range<sup>29,139,140</sup>.

Another advantage of rare earths in solid materials that has not been fully exploited yet is the relatively easy integration on chips. In this sense, works already exist in implementing memory properties of ensembles in common optical waveguides, like LiNbO<sub>3</sub> doped with erbium<sup>157</sup> and thulium<sup>158</sup>. Taken from another point of view, waveguides can be directly laser-written on a rare earth-doped crystal to enhance light coupling<sup>159</sup>. For this approach, a great challenge will be to filter out the strong optical pulses used for transferring atoms in storage protocols, as they are typically used in a co-linear configuration. Single rare earth ions in optical micro-cavities are also a promising line of research for integrability, matching the potential of single ion control with the tunable optical coupling<sup>160,161</sup>. Integration is also useful for the prospect of embedding quantum memories in quantum repeaters based on satellites<sup>162</sup>.

Looking further ahead, rare earth memories might have a role one day in enhancing quantum computing, a possibility envisioned by recent proposals of techniques for quantum gates<sup>163,164</sup> and strategies for factorization involving multimodality<sup>165</sup>.

In conclusion, as highlighted by this range of applications and new avenues for improvements, I am convinced that rare earths will have a place in future quantum technologies, besides the very widespread use they already have in classical electronic devices.



## List of publications

- **Paper I**, A. Ortu, A. Tiranov, S. Welinski, F. Fröwis, N. Gisin, A. Ferrier, P. Goldner, and M. Afzelius, "Simultaneous coherence enhancement of optical and microwave transitions in solid-state electronic spins". *Nature Materials* 17, 671–675 (2018). [Link](#).
- **Paper II**, A. Tiranov, A. Ortu, S. Welinski, A. Ferrier, P. Goldner, N. Gisin, and M. Afzelius, "Spectroscopic study of hyperfine properties in  $^{171}\text{Yb}^{3+}$ ", *Phys. Rev. B* 98, 195110 (2018). [Link](#).
- **Paper III**, J. Etesse, A. Holzäpfel, A. Ortu, and M. Afzelius, "Optical and spin manipulation of non-Kramers rare-earth ions in a weak magnetic field for quantum memory applications", *Phys. Rev. A* 103, 022618 (2021). [Link](#).
- **Paper IV**, A. Ortu, A. Holzäpfel, J. Etesse, and M. Afzelius, "Storage of photonic time bin qubits up to 20 ms in a rare-earth doped crystal", arXiv:2109.06669 (2021) (submitted to *npj Quantum Information*). [Link](#).
- **Paper V**, "Multimode capacity of atomic frequency comb quantum memories", manuscript in preparation.

**A.1 Paper I: Simultaneous coherence enhancement of optical and microwave transitions in solid-state electronic spins**

# Simultaneous coherence enhancement of optical and microwave transitions in solid-state electronic spins

Antonio Ortu<sup>1,4</sup>, Alexey Tiranov<sup>1,4</sup>, Sacha Welinski<sup>2</sup>, Florian Fröwis<sup>1</sup>, Nicolas Gisin<sup>1</sup>, Alban Ferrier<sup>2,3</sup>, Philip Goldner<sup>2</sup> and Mikael Afzelius<sup>1\*</sup>

**Solid-state electronic spins are extensively studied in quantum information science, as their large magnetic moments offer fast operations for computing<sup>1</sup> and communication<sup>2–4</sup>, and high sensitivity for sensing<sup>5</sup>. However, electronic spins are more sensitive to magnetic noise, but engineering of their spectroscopic properties, for example, using clock transitions and isotopic engineering, can yield remarkable spin coherence times, as for electronic spins in GaAs<sup>6</sup>, donors in silicon<sup>7–11</sup> and vacancy centres in diamond<sup>12,13</sup>. Here we demonstrate simultaneously induced clock transitions for both microwave and optical domains in an isotopically purified <sup>171</sup>Yb<sup>3+</sup>:Y<sub>2</sub>SiO<sub>5</sub> crystal, reaching coherence times of greater than 100 μs and 1 ms in the optical and microwave domains, respectively. This effect is due to the highly anisotropic hyperfine interaction, which makes each electronic-nuclear state an entangled Bell state. Our results underline the potential of <sup>171</sup>Yb<sup>3+</sup>:Y<sub>2</sub>SiO<sub>5</sub> for quantum processing applications relying on both optical and spin manipulation, such as optical quantum memories<sup>4,14</sup>, microwave-to-optical quantum transducers<sup>15,16</sup>, and single-spin detection<sup>17</sup>, while they should also be observable in a range of different materials with anisotropic hyperfine interactions.**

A very effective method for increasing spin coherence times consists in engineering a particular spin transition so that its frequency  $\nu$  is insensitive to magnetic fluctuations—that is,  $\partial\nu / \partial\mathbf{B} = 0$  up to first order. Such transitions are known as clock transitions in atomic physics, and were pioneered for nuclear spin systems in solid-state materials<sup>18</sup>, where they are called ZEFOZ (ZEro First Order Zeeman) transitions. The ZEFOZ technique is based on the application of a magnetic bias field in a particular ‘magic’ direction, where  $\partial\nu / \partial\mathbf{B} = 0$  simultaneously for all three spatial coordinates. The existence of such a direction depends entirely on the spin Hamiltonian of the system. Recently ZEFOZ transitions were also observed for electronic spins in silicon<sup>9,11</sup>, showing its general appeal for spin coherence enhancement.

In rare-earth (RE) ion doped crystals, engineered ZEFOZ transitions have been very effective in extending nuclear spin coherence times, by orders of magnitude, for REs without electronic spin ( $S=0$ )<sup>18–20</sup>. However, ZEFOZ transitions have not yet been achieved in RE ions having both electronic and nuclear spin degrees of freedom—so-called Kramers RE ions (containing an odd number of electrons)<sup>21–23</sup>. These often have shorter coherence lifetimes due to the large electronic spin coupling to the spin bath of the crystal,

which is composed of nuclear spins and the RE spins themselves, unless large magnetic fields are applied<sup>23</sup>. In terms of optical coherence times, RE ions are unique solid-state centres, as optical coherences can reach milliseconds<sup>24</sup>. In short this is due to the shielding of the 4f electrons by the 5s, 5p orbitals, which reduces the coupling to phonons in RE materials. However, also in the optical domain one needs to apply large magnetic fields to reach long optical coherence times for Kramers ions<sup>25</sup>. Yet, electronic spins are highly promising for broadband optical quantum memories<sup>4,14</sup>, microwave-to-optical quantum transduction, and coupling to superconducting qubits<sup>15,16</sup>. There is thus a general interest in simultaneously enhancing the spin and optical coherence times of Kramers ions, to profit from their distinct advantages. In addition, to interface with superconducting resonators and qubits, ZEFOZ transitions under low or zero magnetic fields are of particular interest.

In this study we use <sup>171</sup>Yb<sup>3+</sup>, a Kramers ion that has recently received interest for quantum information processing owing to its simple hyperfine structure. Basic optical<sup>26–28</sup> and spin<sup>27,28</sup> properties have been studied, and recent electron spin resonance measurements have shown promising spin coherence times at high magnetic fields<sup>29</sup> (73 μs at around 1 T). The <sup>171</sup>Yb<sup>3+</sup> ion is indeed unique among RE Kramers ions, as it has the lowest possible, non-zero, electronic  $S = \frac{1}{2}$  and nuclear  $I = \frac{1}{2}$  spin, resulting in the simplest possible hyperfine manifold of four states, as shown in Fig. 1a. This fact greatly simplifies both the optical and spin spectra, and makes optical manipulation of the hyperfine levels possible, an important feature of this work.

In this system, the electronic spin  $\mathbf{S}$  of the ytterbium ion is coupled with its nuclear spin  $\mathbf{I}$  through the hyperfine interaction tensor  $A$ , and the effective spin Hamiltonian involving the interaction with an external magnetic field  $\mathbf{B}$  can be written as

$$\mathcal{H} = \mathbf{S} \cdot A \cdot \mathbf{I} + \mu_B \mathbf{B} \cdot g \cdot \mathbf{S} - \mu_n \mathbf{B} \cdot g_n \cdot \mathbf{I} \quad (1)$$

Here,  $g$  and  $g_n$  are coupling tensors related to the electronic and nuclear Zeeman interactions of <sup>171</sup>Yb<sup>3+</sup>, respectively, and  $\mu_B$  and  $\mu_n$  are the electronic and nuclear magnetons. In the Y<sub>2</sub>SiO<sub>5</sub> crystal the <sup>171</sup>Yb<sup>3+</sup> ions replace Y<sup>3+</sup> ions in sites of low ( $C_1$ ) point symmetry, which makes the hyperfine  $A$  and Zeeman  $g$  tensors highly anisotropic for both the ground and excited states<sup>27</sup>. In general, for a highly anisotropic  $A$  tensor (with non-zero eigenvalues  $A_x \neq A_y \neq A_z$ ), the hyperfine coupling completely removes the degeneracy at zero magnetic field. It gives rise to the four eigenstates

<sup>1</sup>Groupe de Physique Appliquée, Université de Genève, Genève, Switzerland. <sup>2</sup>Chimie ParisTech, PSL University, CNRS, Institut de Recherche de Chimie Paris, Paris, France. <sup>3</sup>Faculté des Sciences et Ingénierie, Sorbonne Université, Paris, France. <sup>4</sup>These authors contributed equally: Antonio Ortu, Alexey Tiranov. \*e-mail: [mikael.afzelius@unige.ch](mailto:mikael.afzelius@unige.ch)

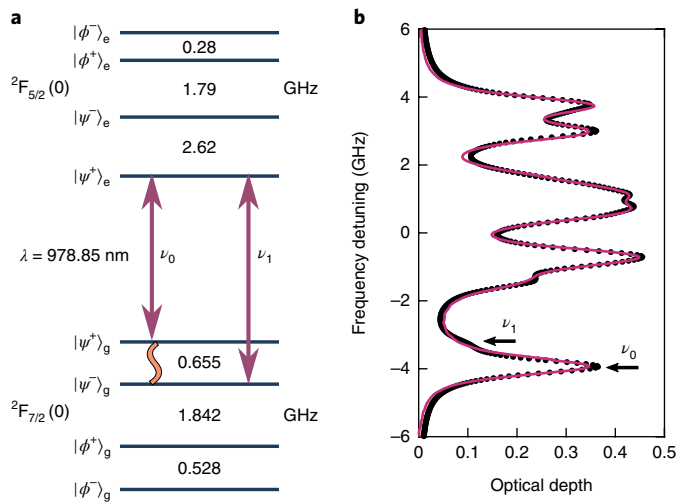


**Fig. 1 | Energy levels and absorption profile.** **a**, Energy level diagram for the optical transitions of  $^{171}\text{Yb}^{3+}:\text{Y}_2\text{SiO}_5$  under study and frequencies of the hyperfine transitions for the ground and excited states. Optical transitions identified with  $\nu_0$  and  $\nu_1$ , are used to study the spin and optical coherences. **b**, Absorption spectrum at zero magnetic field. Data are shown in black, while the pink line represents the result from the fitting based on the zero-field energy structure<sup>28</sup>. The black arrows indicate the optical transitions at  $\nu_0$  and  $\nu_1$  used in this work.

$|\psi^\pm\rangle = \frac{1}{\sqrt{2}}(|\uparrow\downarrow\rangle \pm |\downarrow\uparrow\rangle)$  and  $|\phi^\pm\rangle = \frac{1}{\sqrt{2}}(|\uparrow\uparrow\rangle \pm |\downarrow\downarrow\rangle)$ , where we decompose electronic  $|\uparrow\rangle \equiv |S_z = \frac{1}{2}\rangle$ ,  $|\downarrow\rangle \equiv |S_z = -\frac{1}{2}\rangle$  and nuclear  $|\uparrow\rangle \equiv |I_z = \frac{1}{2}\rangle$ ,  $|\downarrow\rangle \equiv |I_z = -\frac{1}{2}\rangle$  spin components. Their energies are expressed as  $E_{\psi^\pm} = \frac{1}{4}[A_z \pm (A_x - A_y)]$  and  $E_{\phi^\pm} = \frac{1}{4}[-A_z \pm (A_x + A_y)]$ .

By tracing out the electronic (nuclear) spin one can easily see that the resulting density matrix corresponds to the complete mixture of two orthogonal components  $\rho_e = \frac{1}{2}|\uparrow\rangle\langle\uparrow| + \frac{1}{2}|\downarrow\rangle\langle\downarrow| = 1/2$  ( $\rho_n = \frac{1}{2}|\uparrow\rangle\langle\uparrow| + \frac{1}{2}|\downarrow\rangle\langle\downarrow| = 1/2$ ), which is true for any eigenstate. This inherently gives a zero total spin vector for the electronic ( $\langle S \rangle = 0$ ) (nuclear ( $\langle I \rangle = 0$ )) spin polarization. Hence any first-order perturbation of the energy levels by the Zeeman terms of equation (1) is strictly zero for both the electronic and nuclear Zeeman components. More explicitly, for any state  $|\xi\rangle = |\psi^\pm\rangle$ ,  $|\phi^\pm\rangle$  the following is true:  $\langle \xi | \mathbf{B}_p \cdot \mathbf{g} \cdot \mathbf{S} | \xi \rangle = \langle \xi | \mathbf{B}_p \cdot \mathbf{g}_n \cdot \mathbf{I} | \xi \rangle = 0$  for any perturbing magnetic field  $\mathbf{B}_p$ . These results apply to any electronic state, hence the zero-field ZEFOZ condition occurs for any spin transition in the ground and excited states, and for any optical transition connecting the two electronic states. A similar effect has been observed in the hyperfine ground state in nitrogen vacancy centres in diamond<sup>30,31</sup>, but only for a reduced number of states due to the higher symmetry of the interaction tensor and, in particular, not for any optical transition.

To probe the zero-field spin and optical coherences in  $^{171}\text{Yb}^{3+}:\text{Y}_2\text{SiO}_5$  we use the transitions  $|\psi^+\rangle_g \leftrightarrow |\psi^-\rangle_g$  and  $|\psi^+\rangle_g \leftrightarrow |\psi^+\rangle_e$ , the latter being clearly resolved in the absorption spectrum in Fig. 1b. By means of optical pumping on the optical transition, the population difference between two spin states is created. A Hahn sequence on the spin transition follows, inducing an echo pulse in the microwave range, which is optically detected using Raman heterodyne scattering<sup>18</sup> (see Methods for details). The coherence lifetime  $T_2^{(s)}$  is thus measured as a function of the external magnetic field applied in various directions. The optical coherence lifetime  $T_2^{(o)}$  is instead measured through a standard photon echo technique using the same optical absorption line (Fig. 1b).

Figure 2b shows measurement results for the  $T_2^{(s)}$  lifetime as the magnetic field is varied close to the expected zero-field ZEFOZ

point along the crystal **b** axis. The coherence increases as the magnetic field is reduced, exceeding 1 ms lifetime for a few tens of microtesla. A similar behaviour is observed for the optical coherence  $T_2^{(o)}$ , which approaches 200  $\mu\text{s}$  close to zero field (Fig. 2a). These results clearly demonstrate the effectiveness of the zero-field ZEFOZ point for decoupling the  $^{171}\text{Yb}$  spins from the perturbing spin bath. Remarkably these spin and optical coherence times are similar to those found in non-Kramers RE ions (with  $S=0$ ) at zero field<sup>24</sup>.

The decoherence due to a given magnetic field noise  $\Delta\mathbf{B}$  can be modelled as<sup>20</sup>  $(\pi T_2)^{-1} = \mathbf{S}_1 \cdot \Delta\mathbf{B} + \Delta\mathbf{B} \cdot \mathbf{S}_2 \cdot \Delta\mathbf{B}$ , where  $\mathbf{S}_1$  and  $\mathbf{S}_2$  are the linear (gradient) and quadratic (curvature) Zeeman contributions to a transition energy. In a ZEFOZ point the linear term ideally vanishes and the limitation comes from the quadratic term. Here we use the known hyperfine<sup>28</sup>  $A$  and Zeeman<sup>27</sup>  $g$  tensors to calculate  $\mathbf{S}_1$  and  $\mathbf{S}_2$ , and fit the noise term  $\Delta\mathbf{B}$  for fields away from the ZEFOZ point, using both spin and optical data (see Fig. 2a,b). This results in  $|\Delta\mathbf{B}| \sim 3 \mu\text{T}$ , consistent with previous measurements in  $\text{Y}_2\text{SiO}_5$ , and is due to spin flip-flops of yttrium ions in this crystal<sup>19,20</sup>. At zero field, however, the model predicts up to  $\sim 10$  ms spin coherence time. The lower experimental value (a maximum of 1.5 ms was measured) could possibly be attributed to the presence of a bias magnetic field, which a separate measurement estimated to be  $\lesssim 15 \mu\text{T}$ .

We also explore a second ZEFOZ-like regime, using the low-field-assisted coherence enhancement technique, as shown on Fig. 3. It is based on the fact that the direction of an extremely small magnetic bias field can strongly reduce the linear term  $\mathbf{S}_1$ . This is due to the high anisotropy of the  $g$  tensor for the ground state, which has the strongest component  $g_z = 6.06$  close to the **b** axis of the crystal<sup>27</sup>, while its perpendicular components are up to fifty times lower and vary between  $g_x = 0.13$  and  $g_y = 1.50$ . In addition, the  $A$  tensor is almost parallel to the  $g$  tensor and the two have a similar anisotropy<sup>28</sup>. For a bias small field applied in the  $x$  direction, the gradient is  $|\mathbf{S}_1| \approx 2B\mu_B^2 g_x^2 A_y / A_z^2$ . For  $^{171}\text{Yb}^{3+}:\text{Y}_2\text{SiO}_5$  this results in  $|\mathbf{S}_1| \sim 0.001 \mu_B$  for bias fields of a few millitesla along the  $x$  axis (see Methods for details). In fact, any field in the  $xy$  plane results in a strongly reduced gradient, of the order of the nuclear spin sensitivity.

Figure 3a shows the numerically calculated  $\mathbf{S}_1$  gradient for a range of orientations of the bias field  $|\mathbf{B}| = 5$  mT. We here work in the (**D**<sub>1</sub>, **D**<sub>2</sub>, **b**) crystal frame commonly used in optics<sup>27</sup>, in which the  $xy$  plane is slightly tilted. The calculated gradient varies over four orders of magnitude in the narrow range shown in Fig. 3a, with minimum gradients lower than  $10 \text{ MHz T}^{-1}$  close to the  $xy$  plane. Such gradients are typical of nuclear spins, while electronic spins have gradients of  $10 \text{ GHz T}^{-1}$  or more. The calculations also indicate that a high precision of the bias field alignment is required to reach the minimum region of gradients, as explained below.

Although magnetic sensitivities of the energy levels are of the order of the nuclear moment, the dipole moments of the addressed transitions remain as high as for electronic ones. Explicitly,  $\langle \xi^\pm | \mathbf{B}_{ac} \cdot \mathbf{g} \cdot \mathbf{S} | \xi^\pm \rangle \propto g\mu_B$  with  $|\xi\rangle = |\psi\rangle$ ,  $|\phi\rangle$  and  $g$  being a constant arising from the elements of the electronic  $\mathbf{g}$  tensor in the  $z$  direction. By aligning  $\mathbf{B}_{ac}$  along the strongest component of the  $\mathbf{g}$  tensor we achieve Rabi frequencies of around 1 MHz for a weak excitation field of around  $30 \mu\text{T}$  (see Methods for details).

An example of a spin coherence lifetime measurement taken with a small scan of  $\theta$  at  $\varphi = -70^\circ$  is shown in Fig. 3c, together with the theoretical model using the calculated gradient and a magnetic noise of  $|\Delta\mathbf{B}| \sim 3 \mu\text{T}$ . The peak coherence time is 4 ms, and less than a degree misalignment significantly reduces the coherence time. This confirms that even extremely small bias fields can have a strong effect on the coherence properties in electronic spin systems characterized by a strongly anisotropic  $g$  tensor. Measurements made at different  $\varphi$  angles displayed the same behaviour, and the maximum coherence lifetimes are shown at their corresponding angular coordinates in Fig. 3a. In the entire plane of minimum gradients we achieve coherence times above 1 ms for a bias field of 5 mT.

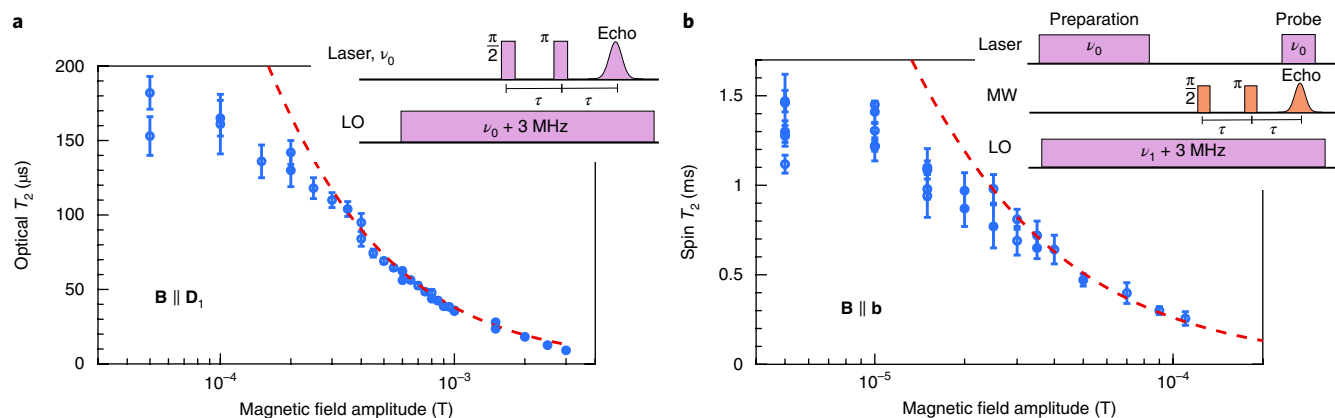


**Fig. 2 | Coherence enhancement under zero magnetic field.** **a**, Experimental photon echo sequence and coherence lifetime  $T_2^{(o)}$  measurements as a function of the external magnetic field. **b**, Experimental pulse sequence used to study spin coherence on 655 MHz hyperfine transition. The preparation step produces a population difference between states  $|\psi_g^+\rangle$  and  $|\psi_g^-\rangle$  before applying a series of microwave (MW) pulses to create the spin echo sequence. The echo signal is measured using Raman heterodyne scattering by detecting the beating between the coherently scattered emission at  $\nu_1$  and the local oscillator (LO). The results for the spin coherence lifetime  $T_2^{(s)}$  as a function of the external magnetic field are shown on the left. Dashed lines represent theoretical curves based on the decoherence model (see text for details). The error bars correspond to 95% confidence intervals on the fitted decay of the echoes (see Methods). Note that for some magnetic fields, particularly at extremely low fields, multiple data points are shown in **a** and **b**. These were measured during different days and generally show a good repeatability of the experiment. The relatively larger data spread for the lowest fields we attribute to small day-to-day variations of the bias field of the lab.

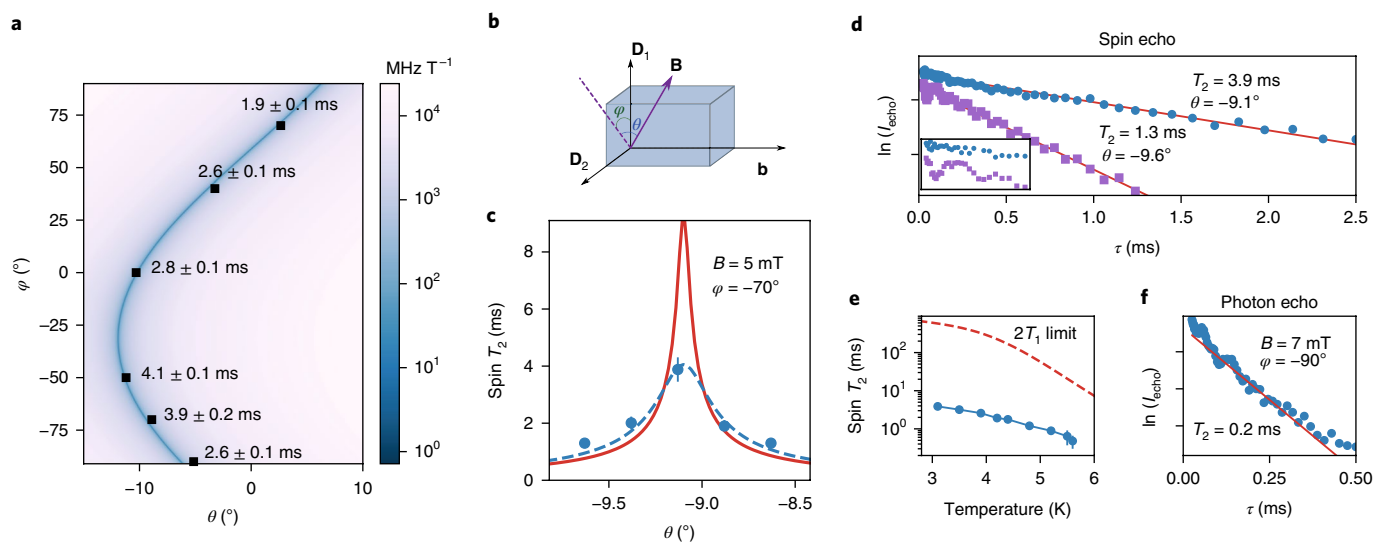


**Fig. 3 | Low-magnetic-field-assisted spin coherence enhancement.** **a**, Gradient of the spin transition for the ground state of  $^{171}\text{Yb}^{3+}:\text{Y}_2\text{SiO}_5$  for an external magnetic field of 5 mT applied in different directions.  $(\theta, \varphi)$  are spherical angular coordinates in the  $(\mathbf{D}_1, \mathbf{D}_2, \mathbf{b})$  frame. The dark region represents the directions where the gradient  $\mathbf{S}_i$  is minimal. Some examples of the measured values of  $T_2^{(s)}$  are shown at their respective coordinates. **b**, Scheme showing the direction of the magnetic field with respect to the axes  $\mathbf{D}_1, \mathbf{D}_2$  and  $\mathbf{b}$  of the  $\text{Y}_2\text{SiO}_5$  crystal. **c**, Spin coherence lifetime measured for  $\varphi = -70^\circ$  as a function of  $\theta$  near the region with minimal decoherence (points). Although the theoretical calculation (solid line) predicts longer coherence lifetimes, the results can be explained by the magnetic field inhomogeneity inside the crystal (see discussion in the text). **d**, Two-pulse spin echo intensity plotted against the delay between the microwave excitation pulses. Circles show the decay corresponding to the optimal point in **c**. Squares show the decay with the magnetic field tilted by  $0.5^\circ$  from the optimum. The inset shows a zoom of the first 300  $\mu\text{s}$ , where the decay displays oscillations due to coupling to nuclear spins in the host crystal. **e**, The optimized spin coherence lifetime  $T_2^{(s)}$  measured as a function of the crystal temperature. The dashed line shows the limit  $2T_1^{(s)}$  due to the spin-lattice relaxation lifetime  $T_1^{(s)}$  measured in ref.<sup>29</sup> **f**, An example of a photon echo decay measurement for a magnetic field of 7 mT. The error bars on  $T_2$  in all figures (most of the time smaller than the symbol representing the data point) correspond to 95% confidence intervals on the fitted decay of the echoes (see Methods).

The main limitation in the achieved spin coherence times using the bias field method probably stems from the inhomogeneity of the applied field. As seen in Fig. 3c, the field has to be precise to within 1/10th of a degree to reach the theoretical maximum. Our numerical calculations show that field inhomogeneities of approximately

0.5% in a volume of  $1 \text{ cm}^3$  are enough to explain the experimental data (Fig. 3c). Other possible limitations are discussed below.

Optical coherence times of up to 200  $\mu\text{s}$  were also measured with magnetic fields applied in the same directions where spin coherence times are maximum. An example of a photon echo decay



measurement is shown in Fig. 3f. The angular dependence was much less pronounced with respect to the spin coherence measurement, as a few degrees misalignment did not significantly reduce the coherence time. This is probably due to the dependence of the optical gradient on the  $g$  tensors in both the ground and excited states, which are not completely aligned<sup>27</sup>. Generally this helps one to simultaneously reach long optical and spin coherence times.

Another possible limitation to the achieved coherence times, both in the zero- and low-field regimes, comes from the superhyperfine interaction taking place between the electronic  $\text{Yb}^{3+}$  spin and nuclear spins of the environment. In the  $\text{Y}_2\text{SiO}_5$  host, nearest-neighbour nuclear spins of  $^{89}\text{Y}$  (100% with  $I = \frac{1}{2}$ ) and  $^{29}\text{Si}$  (5% with  $I = \frac{1}{2}$ ) interact strongly with  $\text{Yb}^{3+}$ , and we expect this interaction to modify the transition gradients. Further analysis is required to estimate these contributions to the observed spin coherence times. In addition, these interactions cause splitting of the microwave transitions when a magnetic bias field is applied, which causes characteristic oscillations on the spin echo decay curves. Such oscillations were seen at short time scales in the measurements with a small bias field, as shown in Fig. 3d. The period of the oscillations is consistent with coupling to  $^{89}\text{Y}$  ions. Surprisingly, these oscillations were systematically quenched in amplitude as the field was tuned to the optimal angle. Although this effect is not yet fully understood, this is a useful feature of these optimal points for applications such as quantum memories.

Finally, we studied the spin coherence lifetime as a function of temperature, with a magnetic field applied in the optimum point for  $\varphi = -70^\circ$ . As shown in Fig. 3e, the coherence time remains above 100  $\mu\text{s}$  for temperatures up to 5.6 K. Also, it remains well below the limit given by the spin-lattice relaxation lifetime as measured in ref.<sup>29</sup>. However, cross-relaxation between  $^{171}\text{Yb}^{3+}$  ions is likely to reduce the  $T_1$  lifetime of the hyperfine states<sup>32</sup>, in addition to causing spectral diffusion<sup>24</sup>. Further studies should measure and quantify these contributions to the measured spin coherence lifetimes, for instance by varying the  $^{171}\text{Yb}^{3+}$  doping concentration and/or applying a magnetic field gradient, as shown with naturally doped silicon samples<sup>8</sup>.

The spin coherence times we measured are similar to those found in naturally doped silicon, where the nuclear spin of  $^{29}\text{Si}$  causes magnetic noise. In silicon, coherence times of 10 s have been reached by isotope purification (pure  $^{28}\text{Si}$  samples)<sup>8</sup>. In contrast, yttrium has the unique isotope  $^{89}\text{Y}$  which has a nuclear spin, making such an approach impossible for  $\text{Y}_2\text{SiO}_5$ . A possible solution is to use isotopically enriched versions of tungsten oxide crystals (for example  $\text{CaWO}_4$ ), whose naturally doped version has been studied with various rare-earth dopants in the past<sup>21,33</sup>.

The described coherence enhancement techniques can generally be applied to any system having anisotropic Zeeman and hyperfine interactions. Particularly, they can be extended to higher odd nuclear spins ( $I = \frac{3}{2}, \frac{5}{2}, \frac{7}{2}$ ) coupled with half electronic spin ( $S = \frac{1}{2}$ ) (see Methods for details). Our approach in this case is directly applicable to other isotopes of Kramers ions with non-zero nuclear spin—in particular to  $^{167}\text{Er}^{3+}$ , which is of high interest for quantum communication owing to its optical transition in the telecommunications band<sup>23</sup>. Recent experiments<sup>34</sup> in  $^{167}\text{Er}^{3+}$  have reached promising hyperfine coherence times (up to 300  $\mu\text{s}$ ) by also using the mixing of electronic and nuclear spins at zero magnetic field, but without fully exploiting a ZEFOZ point. Hence, with ZEFOZ points or the low-field-assisted enhancement techniques used in our work, the spin coherence time could potentially be increased further. Other systems of interest include single molecular electron magnets incorporating rare-earth ions<sup>35,36</sup>.

In conclusion, we have shown that simultaneous enhancement of both optical and spin coherence times is possible, by using induced clock transitions at zero field or by minimizing the transition gradients using extremely low magnetic bias fields. These techniques are

applicable to any electronic spin system having anisotropic Zeeman and hyperfine interactions. The  $^{171}\text{Yb}^{3+}:\text{Y}_2\text{SiO}_5$  material studied here features a set of unique properties, such as a simple hyperfine manifold, optically resolved optical-hyperfine transitions, and long coherence times, making it a great resource for quantum information applications. This system will be highly interesting for applications in broadband optical quantum memories<sup>4,14</sup> and coupling to superconducting resonators/qubits in the microwave regime<sup>15,17</sup>.

## Methods

Methods, including statements of data availability and any associated accession codes and references, are available at <https://doi.org/10.1038/s41563-018-0138-x>.

Received: 24 January 2018; Accepted: 22 June 2018;

Published online: 23 July 2018

## References

- Wesenberg, J. H. et al. Quantum computing with an electron spin ensemble. *Phys. Rev. Lett.* **103**, 070502 (2009).
- Togan, E. et al. Quantum entanglement between an optical photon and a solid-state spin qubit. *Nature* **466**, 730–734 (2010).
- Gao, W. B. et al. Quantum teleportation from a propagating photon to a solid-state spin qubit. *Nat. Commun.* **4**, 2744 (2013).
- Bussi eres, F. et al. Quantum teleportation from a telecom-wavelength photon to a solid-state quantum memory. *Nat. Photon.* **8**, 775–778 (2014).
- Grinolds, M. S. et al. Subnanometre resolution in three-dimensional magnetic resonance imaging of individual dark spins. *Nat. Nanotech.* **9**, 279–284 (2014).
- Bluhm, H. et al. Dephasing time of GaAs electron-spin qubits coupled to a nuclear bath exceeding 200  $\mu\text{s}$ . *Nat. Phys.* **7**, 109–113 (2011).
- George, R. E. et al. Electron spin coherence and electron nuclear double resonance of Bi donors in natural Si. *Phys. Rev. Lett.* **105**, 067601 (2010).
- Tyryshkin, A. M. et al. Electron spin coherence exceeding seconds in high-purity silicon. *Nat. Mater.* **11**, 143–147 (2012).
- Wolfowicz, G. et al. Atomic clock transitions in silicon-based spin qubits. *Nat. Nanotech.* **8**, 561–564 (2013).
- Lo, C. C. et al. Hybrid optical–electrical detection of donor electron spins with bound excitons in silicon. *Nat. Mater.* **14**, 490–494 (2015).
- Morse, K. J. et al. A photonic platform for donor spin qubits in silicon. *Sci. Adv.* **3**, e1700930 (2017).
- Balasubramanian, G. et al. Ultralong spin coherence time in isotopically engineered diamond. *Nat. Mater.* **8**, 383–387 (2009).
- Sukachev, D. D. et al. Silicon-vacancy spin qubit in diamond: A quantum memory exceeding 10 ms with single-shot state readout. *Phys. Rev. Lett.* **119**, 223602 (2017).
- Saglamyurek, E. et al. Quantum storage of entangled telecom-wavelength photons in an erbium-doped optical fibre. *Nat. Photon.* **9**, 83–87 (2015).
- Probst, S. et al. Anisotropic rare-earth spin ensemble strongly coupled to a superconducting resonator. *Phys. Rev. Lett.* **110**, 157001 (2013).
- Fernandez-Gonzalvo, X., Chen, Y.-H., Yin, C., Rogge, S. & Longdell, J. J. Coherent frequency up-conversion of microwaves to the optical telecommunications band in Er:YSO crystal. *Phys. Rev. A* **92**, 062313 (2015).
- Bienfait, A. et al. Reaching the quantum limit of sensitivity in electron spin resonance. *Nat. Nanotech.* **11**, 253–257 (2016).
- Fraval, E., Sellars, M. J. & Longdell, J. J. Method of extending hyperfine coherence times in  $\text{Pr}^{3+}:\text{Y}_2\text{SiO}_5$ . *Phys. Rev. Lett.* **92**, 077601 (2004).
- Lovri c, M. et al. Hyperfine characterization and spin coherence lifetime extension in  $\text{Pr}^{3+}:\text{La}_2(\text{WO}_4)_3$ . *Phys. Rev. B* **84**, 104417 (2011).
- Zhong, M. et al. Optically addressable nuclear spins in a solid with a six-hour coherence time. *Nature* **517**, 177–180 (2015).
- Bertaina, S. et al. Rare-earth solid-state qubits. *Nat. Nanotech.* **2**, 39–42 (2007).
- Wolfowicz, G. et al. Coherent storage of microwave excitations in rare-earth nuclear spins. *Phys. Rev. Lett.* **114**, 170503 (2015).
- Ran ci c, M., Hedges, M. P., Ahlefeldt, R. L. & Sellars, M. J. Coherence time of over a second in a telecom-compatible quantum memory storage material. *Nat. Phys.* **14**, 50–54 (2018).
- Thiel, C., B ttger, T. & Cone, R. Rare-earth-doped materials for applications in quantum information storage and signal processing. *J. Lumin.* **131**, 353–361 (2011).
- Sun, Y., Thiel, C. W., Cone, R. L., Equall, R. W. & Hutcheson, R. L. Recent progress in developing new rare earth materials for hole burning and coherent transient applications. *J. Lumin.* **98**, 281–287 (2002).
- B ttger, T., Thiel, C. W., Cone, R. L., Sun, Y. & Faraon, A. Optical spectroscopy and decoherence studies of  $\text{Yb}^{3+}:\text{YAG}$  at 968 nm. *Phys. Rev. B* **94**, 045134 (2016).

27. Welinski, S., Ferrier, A., Afzelius, M. & Goldner, P. High-resolution optical spectroscopy and magnetic properties of Yb<sup>3+</sup> in Y<sub>2</sub>SiO<sub>5</sub>. *Phys. Rev. B* **94**, 155116 (2016).
28. Tiranov, A. et al. Spectroscopic study of hyperfine properties in <sup>171</sup>Yb<sup>3+</sup>:Y<sub>2</sub>SiO<sub>5</sub>. Preprint at <https://arXiv.org/abs/1712.08616> (2017).
29. Lim, H.-J., Welinski, S., Ferrier, A., Goldner, P. & Morton, J. J. L. Coherent spin dynamics of ytterbium ions in yttrium orthosilicate. *Phys. Rev. B* **97**, 064409 (2018).
30. Dolde, F. et al. Electric-field sensing using single diamond spins. *Nat. Phys.* **7**, 459–463 (2011).
31. Jamonneau, P. et al. Competition between electric field and magnetic field noise in the decoherence of a single spin in diamond. *Phys. Rev. B* **93**, 024305 (2016).
32. Cruzeiro, E. Z. et al. Spectral hole lifetimes and spin population relaxation dynamics in neodymium-doped yttrium orthosilicate. *Phys. Rev. B* **95**, 205119 (2017).
33. Rakhmatullin, R. M. et al. Coherent spin manipulations in Yb<sup>3+</sup>:CaWO<sub>4</sub> at X- and W-band EPR frequencies. *Phys. Rev. B* **79**, 172408 (2009).
34. Rakonjac, J. V., Chen, Y.-H., Horvath, S. P. & Longdell, J. J. Spin echoes in the ground and an optically excited state of <sup>167</sup>Er<sup>3+</sup>:Y<sub>2</sub>SO<sub>5</sub> at near-zero magnetic fields using Raman heterodyne spectroscopy. Preprint at <https://arXiv.org/abs/1802.03862> (2018).
35. Zadrozny, J. M., Niklas, J., Poluektov, O. G., & Freedman, D. E. Millisecond coherence time in a tunable molecular electronic spin qubit. *ACS Cent. Sci.* **1**, 488–492 (2015).
36. Shiddiq, M. et al. Enhancing coherence in molecular spin qubits via atomic clock transitions. *Nature* **531**, 348–351 (2016).

## Acknowledgements

We acknowledge funding from the Swiss FNS NCCR programme Quantum Science Technology (QSIT) and FNS research project no. 172590, EUs H2020 programme under the Marie Skłodowska-Curie project QCALL (GA 675662), EUs FP7 programme under the ERC AdG project MEC (GA 339198), ANR under grant agreement no. 145-CE26-0037-01 (DISCRYS) and NanoK project RECTUS and the IMTO Cancer AVIESAN (Cancer Plan, C16027HS, MALT).

## Author contributions

S.W., A.F. and P.G. grew the crystal sample, measured and analysed the absorption spectrum. A.T. and M.A. conceived and planned the optical and spin echo experiments, which were mainly carried out by A.O. and A.T. with contributions from S.W. and M.A. The theoretical model was developed by F.F., A.T., S.W., P.G. and M.A. The manuscript was mainly written by A.O., A.T. and M.A., with contributions from all the authors. N.G. and M.A. provided overall oversight of the project.

## Competing interests

The authors declare no competing interests.

## Additional information

**Supplementary information** is available for this paper at <https://doi.org/10.1038/s41563-018-0138-x>.

**Reprints and permissions information** is available at [www.nature.com/reprints](http://www.nature.com/reprints).

**Correspondence and requests for materials** should be addressed to M.A.

**Publisher's note:** Springer Nature remains neutral with regard to jurisdictional claims in published maps and institutional affiliations.

## Methods

**Crystal.** Our sample is a  $^{171}\text{Yb}^{3+}:\text{Y}_2\text{SiO}_5$  crystal with 10 ppm doping concentration and with an  $\text{Yb}^{3+}$  isotope purity of 95%, grown via the Czochralski method and cut along the  $\mathbf{D}_1$ ,  $\mathbf{D}_2$  and  $\mathbf{b}$  extinction axes. The sides parallel to these axes have lengths, respectively, of 5.7, 5.6 and 9.5 mm, and the faces parallel to the  $\mathbf{D}_1$ – $\mathbf{D}_2$  plane were polished so to reduce the scattering of the input light. Another crystal grown from the same bulk but with dimensions 10.0, 4.6 and 4.5 mm, respectively, was polished along the  $\mathbf{D}_2$ – $\mathbf{b}$  faces and used only for coherence lifetime measurements on site I (see the section ‘Optically detected spin echo’).  $\text{Y}_2\text{SiO}_5$  has a monoclinic structure of the  $C_{2h}^6$  space group.  $\text{Yb}^{3+}$  can replace  $\text{Y}^{3+}$  ions in two different crystallographic sites of  $C_1$  point symmetry (referred to as sites I and II), which in turn include two magnetically inequivalent sub-sites each. All results presented in the main text were obtained from site II. The hyperfine transitions of the two magnetic sites coincided when no static magnetic field was applied, but they could be addressed separately when we introduced a field of a few millitesla in directions neither orthogonal nor parallel to  $\mathbf{b}$ . The optical transitions had a full-width at half-maximum (FWHM) of about 500 MHz, while for the hyperfine transitions the FWHM was about 1 MHz.

**Experimental set-up.** The crystal was placed in a cryostat at about 3.5 K. A small coil of copper wire, connected to a generator and a 2 W amplifier, surrounded the crystal along the  $\mathbf{b}$  axis and allowed us to address the microwave transitions by inducing a.c. magnetic fields. The inductance of the coil was estimated to be 0.2  $\mu\text{H}$ , which gives approximately 0.5% of input microwave power to be transmitted to the crystal for a 655 MHz excitation frequency. The induced a.c. magnetic field amplitude in this case could go up to approximately 30  $\mu\text{T}$ .

A larger superconducting coil was placed along either  $\mathbf{D}_1$  or  $\mathbf{D}_2$  axes, and was used to create a component of the external static magnetic field up to 2 T. Placed outside the cryostat along the remaining crystal axes, two pairs of copper coils in a Helmholtz configuration completed the static field generation set-up, with a maximum of a few millitesla each. This solution proved to be enough to generate the required field along the directions of maximal suppression of decoherence presented in the main text. A 980 nm external cavity diode laser generated the optical beams, which were manipulated in amplitude and frequency by acousto-optical modulators so as to precisely define the pulse sequences we needed. The laser was split in two main paths, namely the pump/probe sent on the crystal and a local oscillator used in the heterodyne detection scheme. A nonlinear-crystal-based phase modulator controlled the frequency of the local oscillator.

**Optically detected spin echo.** We measure the spin coherence lifetime  $T_2^{(s)}$  through optical detection of a spin echo in a Hahn sequence using the Raman heterodyne scattering (RHS) technique<sup>18–20</sup>. All spin echo measurements reported in this paper were carried out on the  $|\psi_g^-\rangle \rightarrow |\psi_g^+\rangle$  transition (655 MHz) of optical site II. We also obtained similar results ( $T_2^{(s)} = 2.4$  ms) for the transition  $|\phi_g^-\rangle \rightarrow |\phi_g^+\rangle$  (528 MHz) for a small scan of magnetic field along  $\mathbf{D}_2$  in the range 0–1 mT. When addressing these two transitions, the excitation coil needed to be oriented with its main axis along  $\mathbf{b}$ , in agreement with our model (see main text). The linear polarization of the input light was aligned to be parallel to  $\mathbf{D}_2$ , so to maximize the absorption. Our predictions were also confirmed by  $T_2^{(s)}$  measurements on site I at 339 MHz and 823 MHz, respectively. Similarly to site II, values of  $T_2^{(s)}$  above a millisecond were found, with a field orientation along  $\mathbf{b}$  at 10 mT. Spectral hole lifetimes above 300 ms for temperatures below 4 K assured us that the coherence was not limited by the population lifetime.

The ensemble was first prepared by optical pumping at frequency  $\nu_0$  in 250 ms with a power of a few milliwatts. The duration of the  $\pi$  pulse in our echo sequence was 1.2  $\mu\text{s}$  and a Rabi frequency up to 2.5 MHz was measured by driving the spin transition at 655 MHz and simultaneously probing the transmitted intensity of light on the detector. The signal generated on the detector was analysed with a fast Fourier transform and the area of the peak corresponding to the beat at  $|\nu_{LO} - \nu_R|$  was acquired at various time delays  $\tau$ . The coherence lifetime  $T_2^{(s)}$  was then extracted by fitting the peak area decays as  $I_{\text{echo}}(\tau) = I_0 \exp(-4\tau/T_2^{(s)})$ .

The maxima of coherence lifetimes at non-zero magnetic field were found by optimizing the intensity of the echo at increasingly long delays  $\tau$  and correcting accordingly the magnetic field orientation. Similarly, we looked for the highest intensity of the echo when compensating the bias field of the lab while applying small intensities of an external field.

The error bars are obtained as follows: the amplitude and width of the echo signal are extracted from a Gaussian fit with 95% confidence intervals. The corresponding residuals are propagated to find the error on the area of the echo. The latter is in turn propagated on the natural logarithm of the area. For each value of magnetic field, the logarithms of the areas are fitted as a linear function of  $\tau$  to find  $T_2$ . The error on  $T_2$  corresponds to a 95% confidence interval on this last linear fit.

**Photon echo.** The optical coherence lifetime  $T_2^{(o)}$  is measured in an analogous way by preparing a photon echo sequence on a transition between a ground and an excited state. In this case, no preparation of population is needed, since the excited state is empty at the temperature considered, and the echo is readily detectable from the photodiode without RHS. However, we chose to measure an RHS signal at  $|\nu_{LO} - \nu_0|$  since, in our case, the technique leads to increased sensitivity to the echo amplitude. The duration of the  $\pi$  pulse was about 3  $\mu\text{s}$ . The errors on the coherence lifetimes are obtained as explained in the spin-echo section.

**Generalization of zero-field ZEFOZ for higher nuclear spins.** We find that the ZEFOZ behaviour is generic for all transitions at zero magnetic field under the following sufficient conditions:

1. The hyperfine coupling is fully anisotropic (that is, all three eigenvalues of the coupling tensor  $A$  are different and nonzero) to avoid degeneracies in the Hamiltonian;
2. The electronic spin is  $\frac{1}{2}$  and the nuclear spin is half integer.

This situation leads to a symmetry in the hyperfine coupling and maximally entangled eigenstates. The latter implies a vanishing polarization of the electronic spin and hence a vanishing first-order sensitivity to external magnetic fields. Also the polarization of the nuclear spin vanishes due to this symmetry. The ZEFOZ behaviour in general disappears when the symmetry is broken—that is, when eigenvalues degenerate, when the nuclear spin is an integer or when the electronic spin is not  $\frac{1}{2}$ .

Let us consider the situation with higher nuclear spin  $I = \frac{3}{2}$ , coupled with electronic spin one half. The hyperfine interaction alone leads to eigenstates of the form  $|\xi\rangle = \alpha \left| \uparrow, \frac{3}{2} \right\rangle + \beta \left| \uparrow, -\frac{1}{2} \right\rangle - \beta \left| \downarrow, \frac{1}{2} \right\rangle - \alpha \left| \downarrow, -\frac{3}{2} \right\rangle$ , where  $\alpha, \beta$  are coefficients defined by the eigenvalues of the  $A$  tensor. The average electronic polarization ( $\mathbf{S}$ ) is zero since the wavefunction can be rewritten as  $|\xi\rangle = |\uparrow\rangle \otimes \left( \alpha \left| \frac{3}{2} \right\rangle + \beta \left| -\frac{1}{2} \right\rangle \right) + |\downarrow\rangle \otimes \left( -\beta \left| \frac{1}{2} \right\rangle - \alpha \left| -\frac{3}{2} \right\rangle \right)$ , where the weights for  $|\uparrow\rangle$  and  $|\downarrow\rangle$  components are the same and  $|\alpha|^2 + |\beta|^2 = 1/2$ . The nuclear polarization ( $\mathbf{I}$ ) appears to be zero as well, since the projections with the opposite signs appear to have the same probabilities, giving  $\langle \mathbf{I} \rangle = |\alpha|^2 \frac{3}{2} - |\beta|^2 \frac{1}{2} + |\beta|^2 \frac{1}{2} - |\alpha|^2 \frac{3}{2} = 0$ . Vanishing  $\langle \mathbf{S} \rangle$  and  $\langle \mathbf{I} \rangle$  are also found for higher half-integer nuclear spins ( $\frac{5}{2}, \frac{7}{2}$  and so on).

For the full description one has to consider the quadrupolar tensor  $Q$ , which also contributes to the zero-field splittings. However, the quadrupole interaction  $\mathbf{I} \cdot \mathbf{Q} \cdot \mathbf{I}$  does not disturb the symmetry of the wavefunction for half-integer  $I$ . Hence, the ZEFOZ condition persists even in the presence of the quadrupole interaction. In contrast, if  $A$  and  $Q$  are not aligned and  $I$  is an integer, the quadrupolar  $\mathbf{I} \cdot \mathbf{Q} \cdot \mathbf{I}$  term seems to make the eigenstates even more susceptible to fluctuations in the  $xy$  plane (in the eigenbasis of  $A$ ).

**Low-magnetic-field-assisted coherence enhancement.** In the presence of a relatively small magnetic field (few millitesla) it is still possible to find an orientation which preserves the coherence. In ref.<sup>28</sup>, it was found that the  $g$  and  $A$  tensors are highly anisotropic ( $g_x \neq g_y \neq g_z$  together with  $A_x \neq A_y \neq A_z$ ) with their strongest component along very close directions. The following calculations can thus be simplified by assuming that the two tensors diagonalize in the same basis, while keeping the  $z$  direction as the one along which their components are strongest. Using equation (1), we can see how the transition sensitivities change with an external static magnetic field  $\mathbf{B}$  with  $(B_x, B_y, B_z)$  components by computing the magnitude of the gradient  $\mathbf{S}_1$  for one of the transitions:

$$|\mathbf{S}_1| = 2\mu_B^2 \sqrt{\frac{B_z^2 g_z^4}{(A_x + A_y)^2} + \frac{B_y^2 g_y^4 A_x^2}{(A_x - A_z)^2} + \frac{B_x^2 g_x^4 A_y^2}{(A_y - A_z)^2}} \quad (2)$$

Considering  $A_z \gg A_x, A_y$  and  $g_z \gg g_x, g_y$ , the presence of the product  $B_z g_z$  on the numerator of the first term and  $A_z$  in the denominator of the other terms tells us that to minimize the transition gradient it is convenient to choose a magnetic field orthogonal to the  $z$  axis. The expression above can thus be simplified:

$$|\mathbf{S}_1| = 2\mu_B^2 \frac{B}{A_z} \sqrt{g_y^4 A_x^2 \sin^2 \varphi + g_x^4 A_y^2 \cos^2 \varphi} \quad (3)$$

where  $\varphi$  is the angle on the plane orthogonal to  $z$ . Minimizing this expression leads us to a non-zero minimum of the gradient, similarly to a ZEFOZ, with a consequent suppression of decoherence.

**Data availability.** The data sets generated and/or analysed during the current study are available from the corresponding authors upon reasonable request.

In the format provided by the authors and unedited.

# Simultaneous coherence enhancement of optical and microwave transitions in solid-state electronic spins

Antonio Ortu<sup>1,4</sup>, Alexey Tiranov<sup>1,4</sup>, Sacha Welinski<sup>2</sup>, Florian Fröwis<sup>1</sup>, Nicolas Gisin<sup>1</sup>, Alban Ferrier<sup>2,3</sup>, Philippe Goldner<sup>2</sup> and Mikael Afzelius<sup>1\*</sup>

---

<sup>1</sup>Groupe de Physique Appliquée, Université de Genève, Genève, Switzerland. <sup>2</sup>Chimie ParisTech, PSL University, CNRS, Institut de Recherche de Chimie Paris, Paris, France. <sup>3</sup>Faculté des Sciences et Ingénierie, Sorbonne Université, Paris, France. <sup>4</sup>These authors contributed equally: Antonio Ortu, Alexey Tiranov. \*e-mail: [mikael.afzelius@unige.ch](mailto:mikael.afzelius@unige.ch)

# Supplementary materials: Simultaneous coherence enhancement of optical and microwave transitions in solid-state electronic spins

Antonio Ortu,<sup>1,\*</sup> Alexey Tiranov,<sup>1,\*</sup> Sacha Welinski,<sup>2</sup> Florian Fröwis,<sup>1</sup>  
Nicolas Gisin,<sup>1</sup> Alban Ferrier,<sup>2,3</sup> Philippe Goldner,<sup>2</sup> and Mikael Afzelius<sup>1,†</sup>

<sup>1</sup>*Groupe de Physique Appliquée, Université de Genève, CH-1211 Genève, Switzerland*

<sup>2</sup>*Chimie ParisTech, PSL University, CNRS, Institut de Recherche de Chimie Paris, 75005 Paris, France*

<sup>3</sup>*Sorbonne Université, 75005 Paris, France*

(Dated: June 8, 2018)

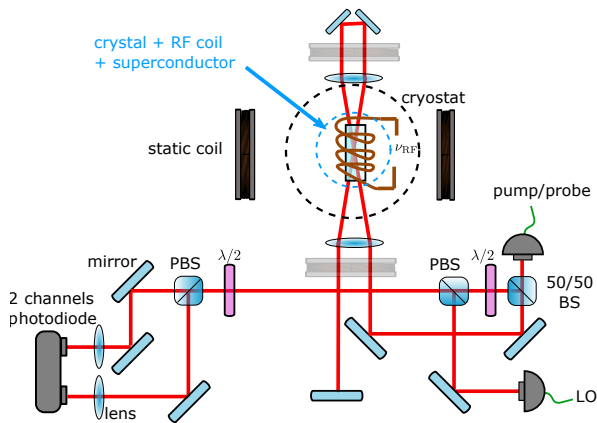


FIG. 1. Experiment setup

## I. SETUP

Our setup (excluding beams preparation) is shown in FIG. 1. The pump/probe beams traverse the crystal in a quadruple pass path, to increase the absorption and thus the final signal to noise ratio. The detection part is composed of a balanced heterodyne arrangement, so that we can detect interference with a local oscillator with zero offset. The combination of PBSs and waveplates allows for the alignment of light polarization according to the orientation of the extinction axes of the crystal.

## II. RAMAN HETERODYNE SCATTERING FOR OPTICAL DETECTION OF SPIN ECHO

The first step consists of the creation of a population difference between the two ground states through optical pumping via the  $|\phi^-\rangle_e$  state at frequency  $\nu_0$ . After a time longer than the excited state lifetime, a  $\pi/2$  RF pulse at frequency  $\nu_{\text{RF}}$  is sent to the excitation coil so to create a collective coherent superposition of two hyperfine states in an allowed transition, for example  $|\psi^-\rangle_g$  and  $|\psi^+\rangle_g$  of optical site II. The inhomogeneous broadening typical of RE doped crystals induces a dephasing of the atomic ensemble, a process that we reverse by a  $\pi$  pulse after a time  $\tau$  from the  $\pi/2$  pulse. Following the rephasing, a

collective coherent emission (echo) will take place on the hyperfine transition after another time interval  $\tau$ . We read out optically the echo by sending at the same time a probe pulse again at  $\nu_0$ , stimulating a Raman emission on the  $|\phi^-\rangle_e \rightarrow |\psi^+\rangle_g$  transition at frequency  $\nu_{\text{R}}$ . The Raman light is then combined on a beam splitter with a reference beam (local oscillator, LO) from the same laser, but with a frequency  $\nu_{\text{LO}}$  shifted with respect to the pump/probe beam by a chosen value through a phase modulator. The interference between Raman and LO is detected as a beat at the frequency  $|\nu_{\text{LO}} - \nu_{\text{R}}|$  in the Fourier spectrum of the signal obtained from a silicon photodiode. A particular strength of this technique is that microwave photons can be detected optically at any frequency without being limited by the bandwidth of the detector, provided that the phase modulator is able to produce at least one sideband on the LO of frequency close enough to the splitting of the hyperfine states  $\nu_{\text{RF}}$ .

The area of the beat signal so acquired, fitted as a function of the delay  $\tau$  of the echo sequence, provides the coherence lifetime  $T_2$  according to [cite]

$$I_{\text{echo}}(\tau) = I_0 e^{-4\tau/T_2}. \quad (1)$$

Some examples of measurements for  $T_2$  from spin echo decays are represented in FIG. 2 and FIG. 3.

## III. RHS FOR OPTICAL DETECTION OF SPIN RESONANCES

After a pumping pulse as in the previous section, if we address at the same time the optical and a hyperfine transition, an RHS signal can be detected showing the presence of a microwave resonance. By scanning the frequency  $\nu_{\text{RF}}$ , we can study the variation of the transition frequencies as we change the external magnetic field. FIG. 4a shows an example of scan for the 655 MHz transition of site II and small magnetic field values along  $\mathbf{D}_2$ . We can distinguish the two magnetic sub-sites as they split in frequency when few millitesla are applied, while they are equivalent at zero field. FIG. 4b represents a similar scan around an angle of decoherence suppression on the  $\mathbf{D}_2 - \mathbf{b}$  plane. The transition frequency has a minimum at this angle, consistently with our prediction that the components of the gradient orthogonal to the applied magnetic field should vanish. The two magnetic

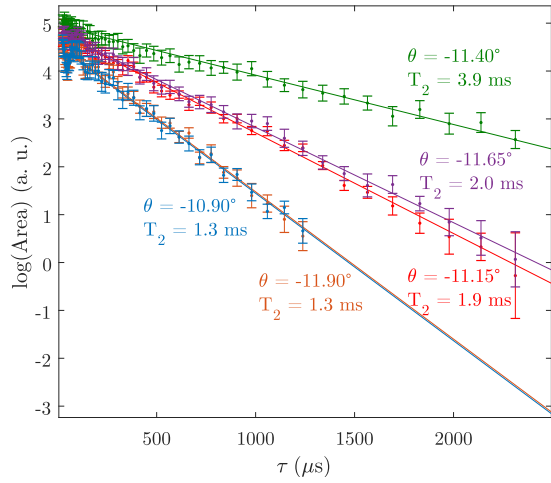


FIG. 2. **Spin echo decay, site II.** Examples of spin echo area measurements for varying delay  $\tau$ , at different values of  $\theta$  around a direction of magnetic field of maximum decoherence suppression for  $\varphi = -70^\circ$  and  $|B| = 5$  mT.

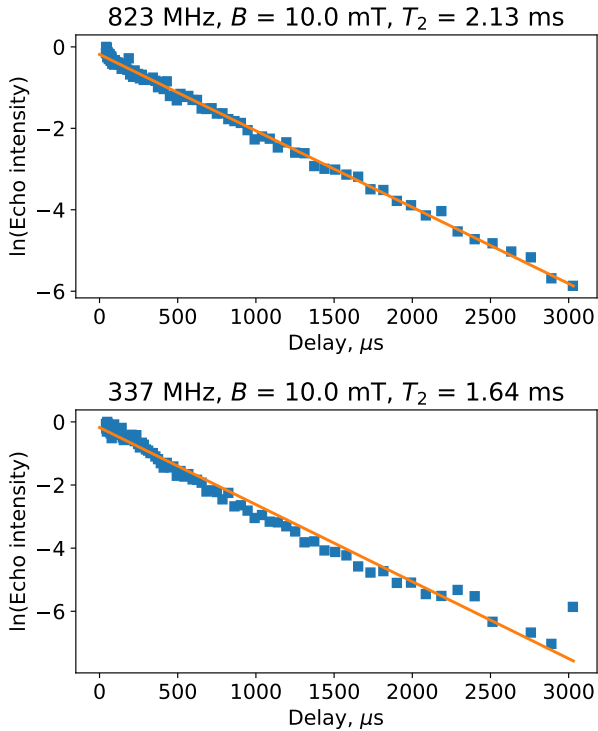


FIG. 3. **Spin echo decay, site I.** Example of spin echo decay measurement with related fit for  $T_2$ , showing compatible result with data from site II.

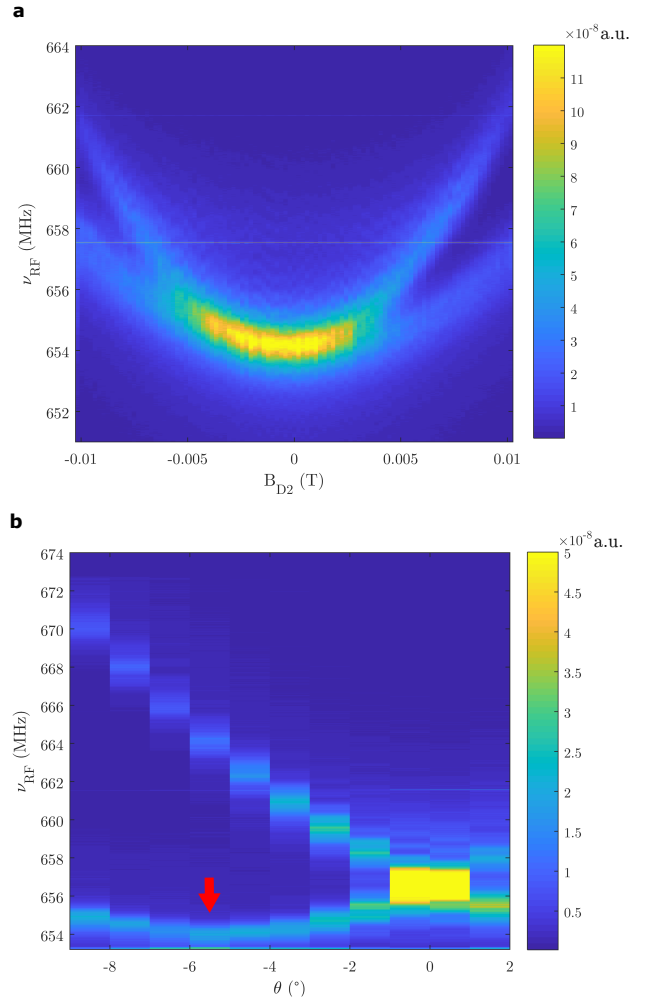



FIG. 4. **RHS spin resonance detection.** **a** RHS signal for a scan of the microwave excitation frequency  $\nu_{0\text{RF}}$  and magnetic field along  $D_2$ . **b** RHS signal around the angle of decoherence suppression, the corresponding transition is indicated by the red arrow. The magnetic field amplitude of 7 mT applied on the  $D_2 - \mathbf{b}$  plane was used.

sub-sites appear well separated in frequency for most of the scanned range, but become again equivalent when the applied field is orthogonal to  $\mathbf{b}$  ( $\theta = 0^\circ$ ).

**A.2 Paper II: Spectroscopic study of hyperfine properties in  $^{171}\text{Yb}^{3+}:\text{Y}_2\text{SiO}_5$**

Spectroscopic study of hyperfine properties in  $^{171}\text{Yb}^{3+}:\text{Y}_2\text{SiO}_5$ Alexey Tiranov,<sup>1</sup> Antonio Ortu,<sup>1</sup> Sacha Welinski,<sup>2</sup> Alban Ferrier,<sup>2,3</sup> Philippe Goldner,<sup>2</sup> Nicolas Gisin,<sup>1</sup> and Mikael Afzelius<sup>1,\*</sup><sup>1</sup>*Groupe de Physique Appliquée, Université de Genève, CH-1211 Genève, Switzerland*<sup>2</sup>*Chimie ParisTech, PSL University, CNRS, Institut de Recherche de Chimie Paris, 75005 Paris, France*<sup>3</sup>*Sorbonne Université, Faculté des Sciences et Ingénierie, UFR 933, Paris, France* (Received 1 March 2018; revised manuscript received 16 October 2018; published 8 November 2018)

Rare-earth ion-doped crystals are promising systems for quantum communication and quantum information processing. In particular, paramagnetic rare-earth centers can be utilized to realize quantum coherent interfaces simultaneously for optical and microwave photons. In this paper, we study hyperfine and magnetic properties of a  $\text{Y}_2\text{SiO}_5$  crystal doped with  $^{171}\text{Yb}^{3+}$  ions. This isotope is particularly interesting since it is the only rare-earth ion having electronic spin  $S = \frac{1}{2}$  and nuclear spin  $I = \frac{1}{2}$ , which results in the simplest possible hyperfine level structure. In this work, we determine the hyperfine tensors for the ground and excited states on the optical  $^2F_{7/2}(0) \longleftrightarrow ^2F_{5/2}(0)$  transition by combining spectral hole burning and optically detected magnetic resonance techniques. The resulting spin Hamiltonians correctly predict the magnetic-field dependence of all observed optical-hyperfine transitions, from zero applied field up to fields where the Zeeman interaction is dominating the hyperfine interaction. Using the optical absorption spectrum, we can also determine the order of the hyperfine levels in both states. These results pave the way for realizing solid-state optical and microwave quantum memories based on a  $^{171}\text{Yb}^{3+}:\text{Y}_2\text{SiO}_5$  crystal.

DOI: [10.1103/PhysRevB.98.195110](https://doi.org/10.1103/PhysRevB.98.195110)

## I. INTRODUCTION

Rare-earth ion-doped crystals (REIC) are of particular interest in domains of quantum information processing and quantum communication [1–5]. Thanks to their long optical and spin coherence times at low temperatures [6,7] and wide optical inhomogeneous linewidths (in the GHz range), they have been actively studied to realize optical quantum memories [1,3] and quantum processors [8,9]. In this context, the optically addressable hyperfine transitions of  $\text{Eu}^{3+}:\text{Y}_2\text{SiO}_5$  showed coherence lifetimes up to six hours [10,11]. Recent progress of optical memory experiments includes spin-wave storage [12–14], as well as memories with high efficiency [15,16] and long storage time [17]. Quantum applications of REIC involve photonic entanglement storage [18,19] of different types [20,21] and light-matter teleportation at a telecom wavelength [22]. The interface between single RE ions have also been demonstrated [23,24], which opens the way to quantum processing, using these systems.

RE ions with an odd number of electrons such as  $\text{Nd}^{3+}$ ,  $\text{Er}^{3+}$ , and  $\text{Yb}^{3+}$  are known to form paramagnetic  $S = \frac{1}{2}$  centers (Kramers doublets) when doped into low-symmetry crystal sites [25], with magnetic moments of the order of the electronic Bohr magneton  $\mu_B \approx 14$  GHz/T. Due to this fact, they can be interfaced with microwave photons through a superconducting resonator [26–28]. This approach gives additional tools for hybrid quantum technologies, since the nuclear hyperfine transitions for some isotopes can also provide long coherence time, as, for instance, more than one second in  $^{167}\text{Er}^{3+}:\text{Y}_2\text{SiO}_5$  [29]. The transfer of coherence

between the electronic and nuclear spins with high fidelity was achieved for  $^{145}\text{Nd}^{3+}:\text{Y}_2\text{SiO}_5$  with nuclear coherence times up to 9 ms [27].

Ytterbium has a number of advantages compared to other rare earths. The  $[\text{Xe}]4f^{13}$  electronic configuration of  $\text{Yb}^{3+}$  results in a simple energy-level structure consisting of only two electronic multiplets:  $^2F_{7/2}$  and  $^2F_{5/2}$  for ground and excited states, respectively. The optical line between the lowest energy levels of the ground and excited multiplets (around 980 nm) is easily accessible by standard diode lasers, while commercial single photon sources based on InGaAs quantum dots also cover these optical energies [30]. The favorable optical branching ratio connecting lowest crystal field levels, in comparison to other REIC systems, gives additional advantages for single ion detection using optical cavity enhancement [31,32]. Another advantage comes from the specific isotope  $^{171}\text{Yb}$ , which has the lowest non-zero nuclear spin ( $I = \frac{1}{2}$ ). This fact greatly simplifies the energy-level structure facilitating the spectral tailoring and the spectroscopic study using standard methods, as, for instance, it limits the number of different transition lines observed in absorption spectra, making them easier to identify.

The basic spectroscopic properties of a naturally doped  $\text{Yb}^{3+}:\text{Y}_2\text{SiO}_5$  crystal were presented in Ref. [33]. These included absorption coefficients as a function of polarization, characterization of radiative lifetimes and branching ratios, as well as magnetic properties of the ground and excited state. In this paper, we present a detailed spectroscopic study of the particular isotope  $^{171}\text{Yb}^{3+}$  in the same  $\text{Y}_2\text{SiO}_5$  host, using spectral hole burning (SHB) and optically detected magnetic resonance (ODMR) techniques. We find that the  $^{171}\text{Yb}^{3+}$  hyperfine tensor, deduced from standard electron paramagnetic resonance (EPR) measurements in Ref. [33], does not

\*mikael.afzelius@unige.ch



correctly predict the zero-field ODMR resonances, nor their magnetic field dependence in the intermediate nonlinear field regime where the hyperfine and Zeeman interactions have similar strength. We attribute this to the problem of properly determining the hyperfine tensor from EPR data when the tensor is anisotropic and the doping site has low symmetry ( $C_1$  in this case).

For the same reason, the spin Hamiltonian of  $^{167}\text{Er}^{3+}:\text{Y}_2\text{SiO}_5$  crystal was recently refined by combining the EPR measurements at low and high fields [34]. Using our SHB and ODMR data together with previous EPR measurements [33] allows us to determine the spin Hamiltonian for both the ground and excited states of  $^{171}\text{Yb}^{3+}:\text{Y}_2\text{SiO}_5$ . The predictions of the new spin Hamiltonians were compared with experimental data in a large range of magnetic fields, yielding an excellent agreement. Using the absorption profile measurements and selective ODMR, we also determine the order of the energy levels on the optical  $^2F_{7/2}(0) \longleftrightarrow ^2F_{5/2}(0)$  transition.

Note that throughout this paper, we call the *low-field regime*, where the hyperfine energy is larger than the hyperfine interaction, the *intermediate regime* where they have similar energy, and the *high-field regime* where the Zeeman energy is larger than the hyperfine energy. In any case, we do not consider the regime where the Zeeman interaction is nonlinear due to perturbations from higher-lying crystal field levels [35].

We additionally observe peculiar transformations of holes to antiholes in the SHB spectra, and vice versa, as the field intensity is varied across a nonlinear field regime. We interpret this as a change in spin cross-relaxation rates due to a transformation of the wave functions in the studied magnetic field region.

The paper is organized as follows. In Sec. II, we briefly describe the spin Hamiltonian utilized for spin  $\frac{1}{2}$  systems and our  $^{171}\text{Yb}^{3+}:\text{Y}_2\text{SiO}_5$  crystal. In Sec. III, we describe the setup and methods of SHB and ODMR. Section IV shows the main results: the measurement of ground state and excited state hyperfine splittings as a function of the external magnetic field and the refined spin Hamiltonian parameters. In Sec. V, we discuss the observed exchange of wave functions under an avoided crossing condition. We finally discuss the implications of our findings and give an outlook in Sec. VI.

## II. BASIC PROPERTIES OF $^{171}\text{Yb}^{3+}:\text{Y}_2\text{SiO}_5$

### A. Spin Hamiltonian

Let us consider a system with both electronic and nuclear spin  $1/2$  ( $S = 1/2$  and  $I = 1/2$ ). In this case, the electronic spin  $\mathbf{S}$  is coupled with its nuclear spin  $\mathbf{I}$  through the hyperfine interaction tensor  $\mathbf{A}$ , and the effective spin Hamiltonian involving the interaction with an external magnetic field  $\mathbf{B}$  can be written as [36]

$$\mathcal{H} = \mathbf{I} \cdot \mathbf{A} \cdot \mathbf{S} + \mu_B \mathbf{B} \cdot \mathbf{g} \cdot \mathbf{S} - \mu_n \mathbf{B} \cdot \mathbf{g}_n \cdot \mathbf{I}. \quad (1)$$

Here,  $\mathbf{g}$  and  $\mathbf{g}_n$  are the coupling tensors of the electronic and nuclear Zeeman interactions, respectively, while  $\mu_B$  and  $\mu_n$  are the electronic and nuclear magnetons. The quadrupolar interaction term  $\mathbf{I} \cdot \mathbf{Q} \cdot \mathbf{I}$ , present only for spin number  $I \geq 1$  systems, does not appear for the  $I = 1/2$  of  $^{171}\text{Yb}$ . This strongly simplifies the spectroscopic analysis of crystalline

systems doped with this isotope if compared to, for instance,  $^{167}\text{Er}^{3+}:\text{Y}_2\text{SiO}_5$ , which has  $I = 7/2$ . The nuclear Zeeman interaction is considered to be isotropic with  $g_n = 0.987$ . It is included for completeness, but it gives too small energy shifts to be detected for the range of magnetic fields used in this work.

If there is no applied magnetic field ( $\mathbf{B} = 0$ ), then the spin Hamiltonian can be diagonalized analytically, resulting in four states with energies

$$\frac{1}{4}[-A_3 \pm (A_1 + A_2)], \quad \frac{1}{4}[A_3 \pm (A_1 - A_2)], \quad (2)$$

where  $A_1$ ,  $A_2$ , and  $A_3$  are the eigenvalues of the  $\mathbf{A}$  tensor. In the  $\text{Y}_2\text{SiO}_5$  crystal,  $^{171}\text{Yb}^{3+}$  ions substitute  $\text{Y}^{3+}$  ions in sites with  $C_1$  point symmetry (see Sec. II B). For this low symmetry, the  $\mathbf{A}$  tensor has three independent eigenvalues  $A_1 \neq A_2 \neq A_3$ , such that the zero-field hyperfine structure consists of four nondegenerate energy levels. If these are known, then the  $\mathbf{A}$  tensor eigenvalues can be calculated analytically using Eq. (2). In Sec. IV, we use ODMR and SHB measurements to determine the zero-field energy level splittings, from which the tensor elements are calculated.

In  $C_1$  point symmetry, the orientation of the hyperfine tensor with respect to the crystal axes is not given by the symmetry. Hence, to fully characterize the hyperfine tensor, one also needs to determine three orientation angles. This can be done by applying a magnetic field ( $\mathbf{B} \neq 0$ ), and studying the energy levels as a function of the field vector  $\mathbf{B}$  (by varying its angle and/or strength). In this work, we were also aided by the fact that the electronic Zeeman tensors  $\mathbf{g}$  were fully known [33], both for the ground and excited states. Therefore, only the three orientation angles of the  $\mathbf{A}$  were free parameters when fitting the field measurement data to the spin Hamiltonian, as we discuss in detail in Sec. IV.

In conventional EPR spectroscopy, all six independent elements of the  $\mathbf{A}$  tensor (for  $C_1$  site symmetry) are deduced from measurements with applied magnetic fields. When using EPR at the common 9.7 GHz X band, the energy splittings are mostly given by the electronic Zeeman interaction part in Eq. (1), while the hyperfine interaction often has much less impact in this energy range. There is thus a question if X-band EPR data is sufficient to accurately fit all six elements in a  $C_1$  symmetry. It should be emphasized that a hyperfine tensor  $\mathbf{A}$  fitted using EPR data will generally be accurate in the range of fields where it was measured, as was the case in Ref. [33]. However, as shown in this work, the accuracy of those hyperfine elements can be insufficient to predict the energy levels outside this measurement region. Particularly in the low-field regime, where the hyperfine interaction dominates, or in the intermediate field region where both the Zeeman and hyperfine interactions have similar strengths.

### B. Crystal properties and optical spectra

Our crystal is a  $\text{Y}_2\text{SiO}_5$  host doped with 10 ppm  $^{171}\text{Yb}^{3+}$  with 95% isotope purity. It was grown via the Czochralski method and cut along the  $\mathbf{D}_1$ ,  $\mathbf{D}_2$ , and  $\mathbf{b}$  polarization extinction axes [37]. The sides parallel to these axes have lengths 5.7, 5.6, and 9.5 mm, and the faces corresponding to the  $\mathbf{D}_1$ – $\mathbf{D}_2$  plane were polished to reduce light scattering.  $\text{Y}_2\text{SiO}_5$  is a common crystal in the rare-earth community [11,38–40], as it

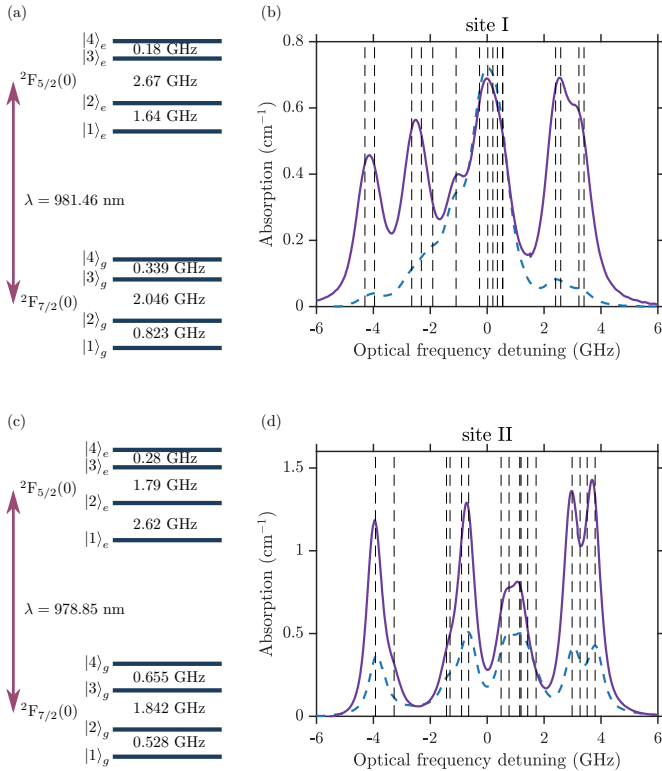


FIG. 1. Energy-level diagram of  $^{171}\text{Yb}^{3+}:\text{Y}_2\text{SiO}_5$  showing the zero-field hyperfine level structures of the lowest crystal-field levels of the ground  $^2F_{7/2}(0)$  and excited  $^2F_{5/2}(0)$  states, both for site I (a) and site II (c). The ground-state hyperfine level structures were determined from the zero-field ODMR measurements, while the excited-state structure was determined using SHB measurements (see Sec. IV). In (b) and (d), we show high-resolution optical absorption spectra of the  $^2F_{7/2}(0) \leftrightarrow ^2F_{5/2}(0)$  transition for site I and site II, respectively. These were recorded at low temperature (3 K) for light polarized along  $\mathbf{D}_2$  (solid line) and  $\mathbf{D}_1$  (dashed line) crystal axis. The position of all optical-hyperfine transitions have been calculated using the hyperfine  $\mathbf{A}$  tensors measured in this work (dashed vertical lines). Zero optical detuning refers to the central transition wavelength given in Sec. II B.

allows RE dopant ions to reach long coherence times due to the low nuclear spin density of the crystal. It has a monoclinic structure and it belongs to the  $C_{2h}^6$  space group.

$\text{Yb}^{3+}$  ions can replace  $\text{Y}^{3+}$  in the host crystal in two different sites of  $C_1$  point symmetry, usually called site I and site II [41]. Furthermore, each crystallographic site consists of two magnetic subsites which are related to each other via the  $C_2$  symmetry axis (this axis coincide with the  $\mathbf{b}$  axis).

The optical transition  $^2F_{7/2}(0) \leftrightarrow ^2F_{5/2}(0)$  under study here couples the lowest crystal field levels of the two electronic multiplets, with a vacuum wavelength of  $\lambda = 981.463$  nm for site I and  $\lambda = 978.854$  nm for site II [33]. The optical absorption spectra of this transition are shown in Fig. 1, which were recorded at zero magnetic field. Since both the ground and excited states have four nondegenerate energy levels, each spectrum consists of 16 optical-hyperfine transitions that are inhomogeneously broadened. The inhomogeneous profile was measured to be Lorentzian, with a full-width at half-maximum of 800 MHz for site I and 560 MHz

for site II. Although the spectra are partly resolved, one cannot accurately measure the hyperfine splittings using the inhomogeneous absorption spectra. For this purpose, we employ the SHB measurement technique.

### III. EXPERIMENTAL METHODS

#### A. Spectral hole burning

The SHB technique is commonly used to investigate transitions in systems with strong inhomogeneous broadening [42]. In solid state crystals, inhomogeneous broadening is often due to uneven strains in different positions of the crystal [43], so each ion can have a different detuning compared to the center of the frequency distribution of a certain transition.

In this context, SHB consists in irradiating the sample with laser light at a specific frequency inside the broadened spectrum (the burn pulse), so to pump atoms away into other energy levels via an excited state. A scan of a weaker probe around the pump frequency will then reveal a series of holes and antiholes corresponding to transitions from states with decreased or increased population, respectively (Fig. 2).

If the inhomogeneous broadening is much larger than the ground and excited state splittings, then a burn pulse at a fixed frequency can resonantly excite atoms in different *classes*, where for each class the burn pulse excites a different optical-hyperfine transition [42,44]. Each class will produce a pattern of holes and antiholes, see Fig. 2, and the resulting spectrum can be hard to interpret. Since for this system the inhomogeneous broadening is smaller than some of the hyperfine splittings, the number of contributing classes will depend on the exact burn frequency. It also causes an asymmetric hole/antihole pattern, with respect to the burn frequency. The hole/antihole structures can be studied as a function of the time between the pump and the probe pulses to reveal population lifetimes [44], and as a function of other external parameters such as magnetic field and temperature [45].

In this paper, we focus on the dependence of the position of spectral holes/antiholes on an external magnetic field, which induces shifts in frequency of the holes/antiholes as the energy level splittings are varied by Zeeman interaction [46].

As will be explained in Sec. IV, we can also observe *hole*  $\leftrightarrow$  *antihole* transformations as the magnetic field is varied across a critical value [Fig. 2(c)]. This phenomenon marks the passage from a low field regime with highly nonlinear energy shifts due mostly to the hyperfine interaction, to a high field, linear regime dominated by Zeeman interactions. Hole/antihole transformations have been observed in different contexts including modification of the cross-relaxation [47] or temperature-dependant phononic relaxation [48], or as a result of superhyperfine resonances between a thulium dopant and aluminium ions in a  $\text{Tm}^{3+}:\text{YAG}$  crystal [49].

#### B. Optically detected magnetic resonance

Magnetic resonance techniques can be combined with SHB to study transitions in domains different than the optical one [11,50–52]. Hyperfine and Zeeman interactions often induce splittings in the microwave range in atomic ensembles, and these splittings can be varied by using an external magnetic field in a broad range between MHz and GHz

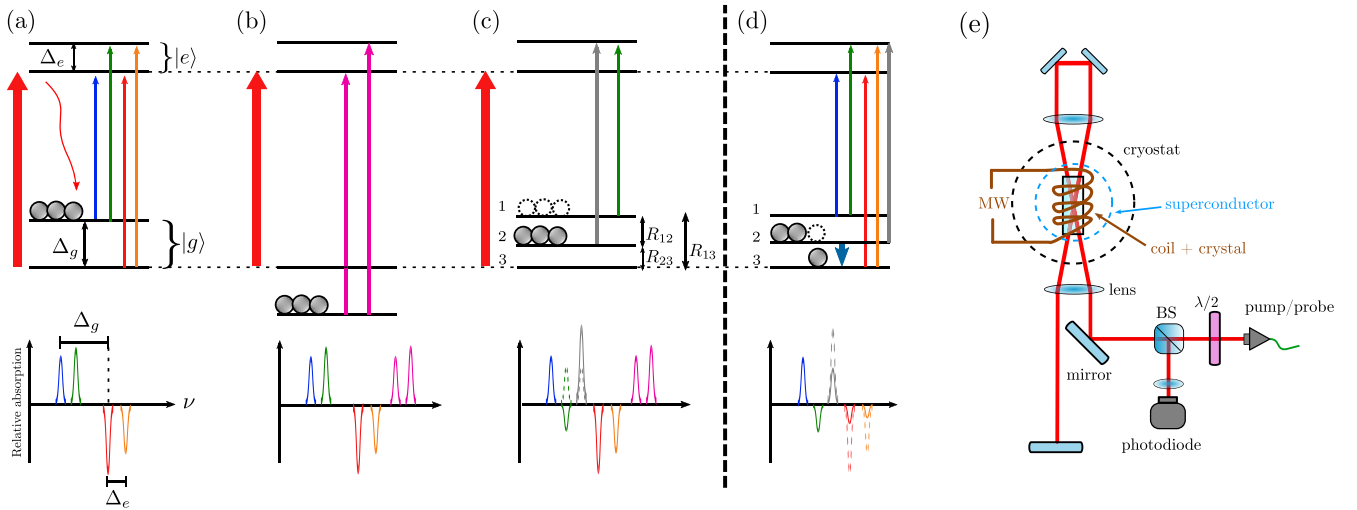


FIG. 2. Examples of the SHB and ODMR techniques and experimental setup. (a) During a burning pulse (large red arrow), the pumped atoms are redistributed among the ground levels (wavy arrow). A weaker probe pulse is then sent on the system while the frequency is scanned, making holes and antiholes visible in the absorption spectrum (bottom). The splitting between two excited states  $\Delta_e$  can be deduced from the difference in frequency between two holes with a common ground state. Similarly, ground splittings  $\Delta_g$  can be found from the difference of frequencies related to antiholes with a common excited state. (b) Example of additional antiholes due to a different class of atoms resonant with the burn pulse in (a). (c) Example of transformation from antihole to hole when the ground state is made of more than two levels. If the decay rates connecting each upper ground level with the burned level ( $R_{13}$  and  $R_{23}$ ) are much lower than the rate connecting themselves  $R_{12}$ , the probe will produce antiholes when scanned over levels 1 and 2, which is the usual situation. However, population on level 1 can be depleted during burning if  $R_{13} \gg R_{12}, R_{23}$ . Thus, a hole appears instead of the antihole seen in the previous case. (d) Schematic explanation of ODMR for a microwave transition. If after the burning pulse, all the pumped ions are in 2, by applying microwave radiation resonant with the  $2 \leftrightarrow 3$  transition (thick dark blue arrow), the population will redistribute among the levels involved, leading to a decrease of the related holes/antihole structure. (e) The experimental setup. See Sec. III C for details.

frequencies, requiring a broadband investigation technique. We thus rely on ODMR to study transitions between spin states for various conditions of external magnetic field. The technique consists of burning a spectral hole and observing its variation as a microwave transition is addressed at the same time as an optical probe beam is on at a constant frequency [Fig. 2(d)] [25]. When the microwave radiation is in resonance with the spin transition, the latter will be detected as a population change, which in turn reduces the amplitude of the spectral hole.

To find the spin resonance and obtain information such as its central frequency and linewidth, we measure the hole amplitude while scanning the microwave frequency. The measurements can be repeated at various external magnetic field values so to obtain information about its influence on the transition.

### C. Experimental setup

Our setup is shown schematically in Fig. 2(e). The crystal is placed inside a cryostat in vacuum and at temperature of about 3 K. A copper coil surrounds the crystal with its longitudinal axis coincident with the crystal  $\mathbf{b}$  axis, and it is used in the ODMR technique to address the spin transitions by generating a microwave field (up to 4 GHz in frequency, fed with power up to  $\sim 2$  W). A superconductor coil surrounds the crystal and copper coil, and allows us to apply static fields up to 2 T in directions orthogonal to  $\mathbf{b}$ . In the experiments presented here, we use a pulsed laser beam (through an acousto-optic modulator, not shown), generated by a tunable

$\sim 980$  nm external cavity diode laser and injected into a single mode polarization maintaining fibre. A half-waveplate right after the fiber output allows the adjustment of polarization according to the orientation of the crystal extinction axis of maximal absorption ( $\mathbf{D}_2$  axis). The light is then focused on the sample in a spot with a diameter of  $\sim 100 \mu\text{m}$  and traverses it in four passes to further increase the amount of light absorbed. Finally, a beam splitter redirects the output light on a silicon photodiode.

## IV. EXPERIMENTAL RESULTS

In principle, the SHB measurement can provide all required information about energy splittings for the ground and excited states. However, the interpretation of the SHB data is difficult as most antiholes depend on both the ground and excited state splittings. Moreover, as explained in Fig. 2(c), one can observe so-called pseudoholes, where one would expect to see an antihole, further complicating the interpretation.

To facilitate the analysis, we first detect the hyperfine splittings of the ground state at zero magnetic field, using the ODMR technique explained previously (see Sec. III B). For this purpose, the laser producing the burn and probe pulses was tuned to the middle of the absorption structure (Fig. 1) to address a maximum number of classes and to produce a population difference for a high number of spin transitions.

For optical site I, we detected four ODMR lines at [2046, 2385, 2869, 3208] MHz [Fig. 3(a)], while for site II five ODMR lines were found at [528, 655, 2370, 2496, 3025] MHz (see Appendix, Fig. 6). The ODMR linewidths varied between

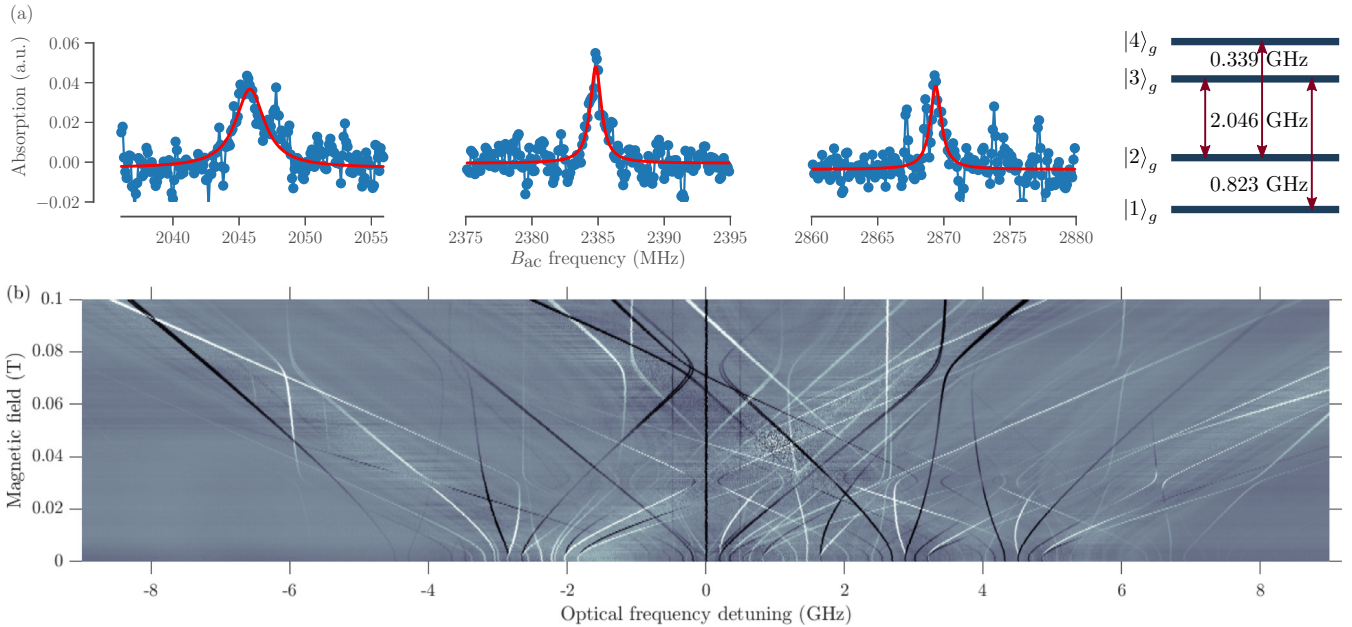


FIG. 3. Experimental results. (a) Optically detected magnetic resonance (ODMR) lines at zero magnetic field for site I of  $^{171}\text{Yb}^{3+}:\text{Y}_2\text{SiO}_5$ . The oscillating magnetic field  $B_{ac}$  was applied in **b** direction. Three different transitions are shown and their corresponding levels are depicted on the right. The variation of the measured spin linewidths could be attributed to the power broadening effect. (b) Recorded optical spectral hole burning (SHB) spectra of site I of  $^{171}\text{Yb}^{3+}:\text{Y}_2\text{SiO}_5$  crystal measured for different magnetic field amplitudes applied in the direction close to  $\mathbf{D}_1$  axis. Zero frequency detuning corresponds to the central frequency at which spectral hole burning is performed. Black regions correspond to lower absorption (holes), while white lines correspond to lower transmission (antiholes) regions. The bending of some of the holes and antiholes at around 30 mT of magnetic field is a result of avoided crossings of the associated ground-state levels. Many of these also show an unusual hole-antihole transformation in this field region (see also Fig. 5 and Sec. V).

0.5 and 1.2 MHz. These were limited by the inhomogeneous linewidths and possibly by additional power broadening.

Using the detected ODMR resonances and Eq. (2), one can easily calculate the eigenvalues of the ground-state hyperfine  $\mathbf{A}$  tensor. These are listed in Table I and the corresponding

TABLE I. Hyperfine properties of  $^{171}\text{Yb}^{3+}:\text{Y}_2\text{SiO}_5$  on optical  ${}^2F_{7/2}(0) \leftrightarrow {}^2F_{5/2}(0)$  transition. Principal values of the  $\mathbf{A}$  tensors (in GHz) and Euler angles (in degrees), defining the orientations of tensor's principal axes ( $z,x,z$  convention) in the crystal frame ( $\mathbf{D}_1$ ,  $\mathbf{D}_2$ , **b**). The information about Zeeman interaction  $\mathbf{g}$  tensors is taken from Ref. [33].

	Site I		Site II	
	Ground	Excited	Ground	Excited
$A_1$ (GHz)	0.481	1.44	-0.1259	2.34
$A_2$ (GHz)	1.159	1.82	1.1835	2.90
$A_3$ (GHz)	5.251	7.20	4.8668	6.49
$\alpha_A$ ( $^\circ$ )	72.25	73.88	45.86	51.07
$\beta_A$ ( $^\circ$ )	92.11	84.76	11.13	14.11
$\gamma_A$ ( $^\circ$ )	63.92	90.13	2.97	-0.67
$ g_1 $	0.31	0.8	0.13	1.0
$ g_2 $	1.60	1.0	1.50	1.4
$ g_3 $	6.53	3.4	6.06	3.3
$\alpha_g$ ( $^\circ$ )	72.8	77	59.10	54
$\beta_g$ ( $^\circ$ )	88.7	84	11.8	23
$\gamma_g$ ( $^\circ$ )	66.2	-7	-12.6	-10

energy level diagrams are reported in Fig. 3(a) and Fig. 1. These eigenvalues of the ground-state hyperfine tensor differ considerably from the ones obtained from high field EPR measurements [33]. This clearly demonstrates the problem of standard X-band EPR for characterizing a highly anisotropic magnetic interaction in the case of low site symmetry. The strength of using zero-field ODMR is that we can determine the eigenvalues of the hyperfine tensors, independently of their orientation with respect to the crystal axes and without using any nonlinear fitting algorithm. In EPR measurements, the eigenvalues and orientation angles (six parameters) are fitted simultaneously to the experimental data, which can introduce errors.

The ODMR technique can also be used to measure hyperfine splittings of the excited state. However, due to the limited excited state lifetime (order of  $\approx 1$  ms for both sites [33]), excited-state ODMR resonances were not observed in these experiments. The SHB technique was thus used for this purpose. To clearly identify the SHB features stemming from the zero-field hyperfine splittings in the excited state, we found it necessary to also study the SHB spectra as a function of applied magnetic field, as explained in the following.

The SHB pattern appearing inside the absorption profile was recorded at different external magnetic fields in various directions. For each measurement, the normalization signal—that is, the absorption profile without hole burning—was subtracted from the acquired trace to leave only the hole/antihole structure visible [Fig. 3(b)] (also see Appendix, Fig. 6). An example of such a measurement, for site I and magnetic field

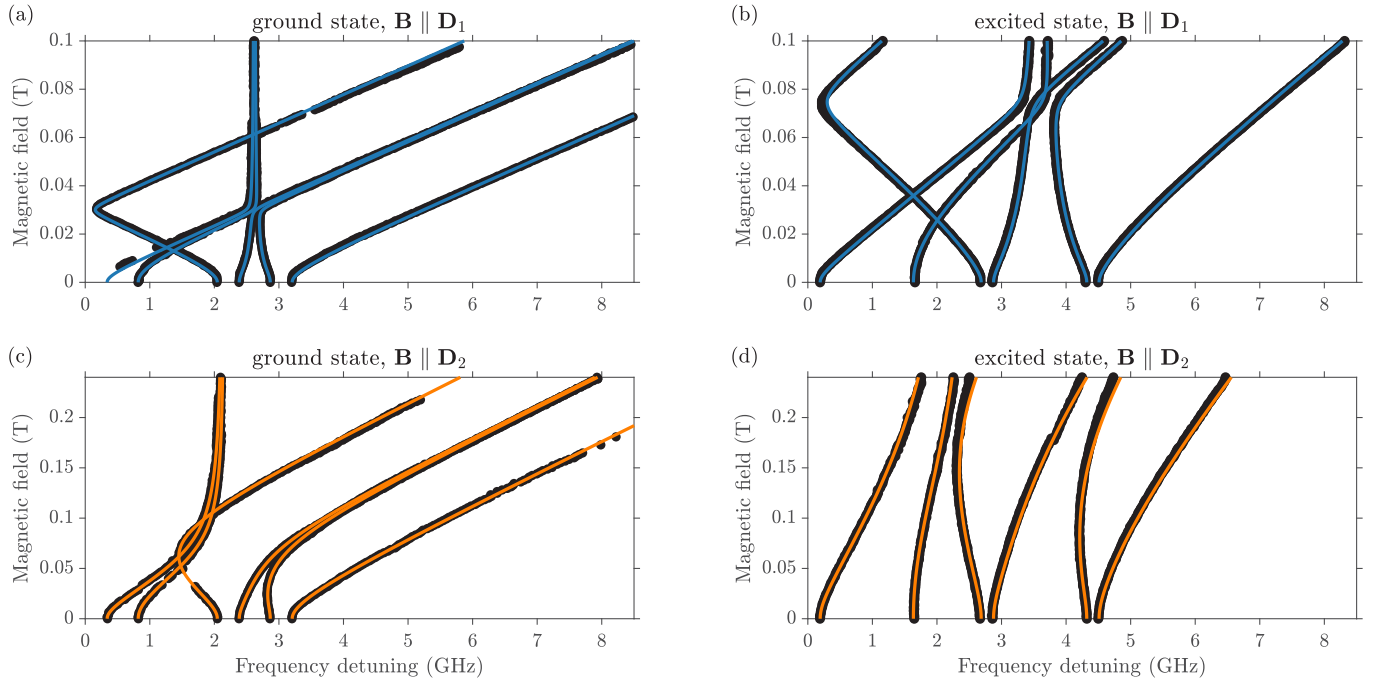


FIG. 4. Energies for different spin transitions and fitting results of the hyperfine interaction tensors. Transition frequencies for ground (left) and excited (right) states for site I as a function of magnetic field amplitudes applied in two different directions ( $\mathbf{D}_1$  on the top and  $\mathbf{D}_2$  for bottom). Experimental points were extracted from SHB measurements (the example is depicted in Fig. 3) and used to fit hyperfine  $\mathbf{A}$  tensor parameters (its orientation) given in Table I. Calculated transition frequencies are plotted with solid lines.

parallel to  $\mathbf{D}_1$  axis, is shown in Fig. 3(b). It clearly shows a series of lines which shift linearly at high magnetic fields and go into a nonlinear regime at lower magnetic fields. The holes and antiholes appear as darker and brighter lines, respectively. By following these lines, one can precisely characterize the nonlinear behavior for various magnetic field regimes. The widths of the observed spectral holes were of a few MHz, which were mainly limited by the laser linewidth.

In conventional SHB methods, the side holes usually correspond to the structure of the excited state (see Fig. 2). Therefore, one expects to observe six holes on each side of the main hole, corresponding to the six possible spin transitions of the excited state. However, in our case, we detect a much higher number of side holes, with some of them corresponding to the ground-state energy levels. This happens due to the relatively fast relaxation rate on the spin transitions, which is comparable to the burning time used in our experiment (hundreds of milliseconds). In this situation, the optical pumping process effectively empties not only the addressed level but also the ones which are connected to it by fast relaxation processes. This leads to the emergence of pseudoholes at the positions expected for the antiholes, as also explained in Fig. 2(c), and it complicates the interpretation of the spectra, in particular the identification of the zero-field hyperfine resonances in the excited state.

In a first step, we use the zero-field ground state structure determined from the ODMR data to identify, without ambiguity, several SHB resonances that only depend on the ground state splitting. We use this information to extract the field dependence of the corresponding transitions in a large range of magnetic field amplitudes from the recorded

SHB spectra (Fig. 3). The extracted data for site I is shown in Fig. 4.

In a second step, we determine the excited state structure, which requires distinguishing between pseudoholes and holes. To this end, we use the fact that we generally observe two distinct regions of nonlinear Zeeman effects in the SHB data. For the particular case of site I and  $\mathbf{B}$  parallel to the  $\mathbf{D}_1$  axis, these appear at around 30 and 80 mT, see Fig. 3(b). The one at 30 mT is due to a nonlinear Zeeman effect in the ground state, as seen in the already identified transition energies of the ground state shown in Fig. 4(a). The one at 80 mT is then due to the excited state Zeeman effect, which is consistent with the fact that the effective  $g$ -factor is twice as low in the excited state [33]. Hence, SHB holes that display nonlinear behavior in both the 30 and 80 mT region are pseudoholes that can be disregarded from the excited state analysis.

In a third step, we identify strong SHB side holes, particularly at higher fields, which only display the nonlinearity at around 80 mT, as shown in Fig. 4(b). To further confirm that these are indeed true holes depending on the excited state hyperfine splits, we use the complete set of resonances from both ground and excited states to calculate the position of all expected antiholes. Many of these are seen in the SHB spectra (see Appendix, Fig. 9), and most importantly none of these predicted lines are in contradiction with the observed SHB spectra. The same approach was also used to analyze the SHB spectra recorded with  $\mathbf{B}$  parallel to the  $\mathbf{D}_2$  axis for site I, see Figs. 4(c)–4(d). We also fully measured and analyzed the SHB spectra along the  $\mathbf{D}_1$  and  $\mathbf{D}_2$  axes for site II (see Appendix, Fig. 7).

The analysis presented above allows us to clearly identify excited-state hyperfine resonances at zero magnetic field,

from which the eigenvalues of the excited state hyperfine tensor are calculated. These are listed in Table I and the corresponding energy-level diagrams are reported in Fig. 1, both for sites I and II.

It remains to determine the orientation of the hyperfine  $\mathbf{A}$  tensors with respect to the crystal axes. To this end, we use the fact that accurate Zeeman  $\mathbf{g}$  tensors were already determined [33] for  $\text{Yb}^{3+}$  ions having no hyperfine states ( $I = 0$ ). The hyperfine tensors are thus fitted with respect to the  $\mathbf{g}$  tensors, both for the ground and excited states. In the fit, we use the hyperfine splittings as a function of magnetic field, measured using the SHB technique. In addition, for the ground state we can use the X-band EPR data from Ref. [33] (see Appendix, Fig. 8), which was recorded at higher fields in between 100 mT and 1 T. The fitting procedure and the definition of all rotation matrices are given in the Appendix. The fitted rotation angles for all  $\mathbf{A}$  tensors are listed in Table I. To determine the order of the energy splittings, we fit the absorption profiles measured at zero magnetic field (Fig. 1). Only the central frequency offset is used as a free parameter while all the differences between absorption lines are fixed using a certain order of the energy splittings. From the four different possibilities, we find that only one gives a spectrum in a good agreement with the experiment. The order found for both sites is depicted in Fig. 1. This result is further confirmed using separate ODMR measurements by selective optical excitation at the outermost absorption lines. We note that the order is given by the relative signs between the  $\mathbf{A}$  tensor eigenvalues, while the simultaneous sign change of two elements does not alter the order. The signs combination corresponding to the determined order is given in Table I for sites I and II.

## V. DISCUSSION

A close look at the spectral hole map on Fig. 3 (especially in the nonlinear regime around 30 mT) reveals many positions of the antiholes with peculiar behavior. As an example, in Fig. 5(a) we show the variation in hole amplitude of the 2046 MHz transition (at zero magnetic field). As seen, it features the expected antihole behavior below and above 30 mT, while at around 30 mT it features a pseudohole. Similar behavior can be seen also for other lines corresponding to various optical classes (Fig. 3).

We believe this is due to the strong admixing of the corresponding wave functions which appear for this magnetic field region. Indeed, from the decomposition of the eigenstates involved in this spin transition [Fig. 5(b)], one can see the strong nonlinear dependence and flip of the electronic wave functions associated with the avoided crossing. This can lead to an enhanced relaxation process on this transition, which leads to the observed transformation of the antihole into a pseudohole. We note that a similar hole-antihole transformation was reported in ruby [47], and the given explanation was also based on the modified cross-relaxation under external magnetic fields.

The phenomenon of pseudoholes is also observed at zero magnetic field, where the antiholes corresponding to  $|1\rangle_g \leftrightarrow |2\rangle_g$  and  $|3\rangle_g \leftrightarrow |4\rangle_g$  transitions (823 MHz and 339 MHz, respectively) appear as pseudoholes. To explain this, we

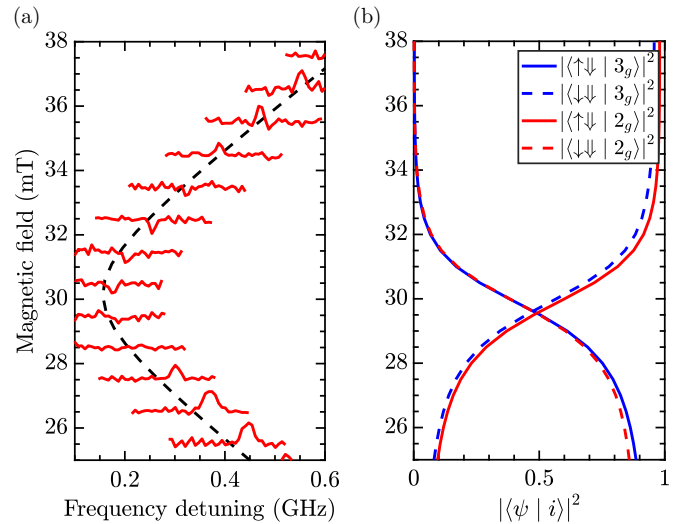


FIG. 5. Example of the hole-antihole transformation. (a) Shown is the transformation of the  $e |2_g\rangle \leftrightarrow |3_g\rangle$  ground-state transition (at 2046 MHz for zero field). The data is taken from Fig. 3 for magnetic field amplitudes around 30 mT. We believe this transformation to be due to an increased relaxation rate of this transition, which in turn is caused by the rapid change in wave functions in this field region [see (b)]. The dashed line represents the predicted spectral position of the antihole. The discrepancy between the measured and calculated values can be attributed to the accuracy of the calibration of the laser scan. (b) The change in wave function of states  $|2_g\rangle$  and  $|3_g\rangle$  can be visualized by plotting their overlap with the separable states  $|\uparrow\downarrow\rangle$  and  $|\downarrow\downarrow\rangle$ , where  $|\uparrow, \downarrow\rangle \equiv |S_z = \frac{1}{2}, -\frac{1}{2}\rangle$  and  $|\downarrow, \uparrow\rangle \equiv |S_z = \frac{1}{2}, -\frac{1}{2}\rangle$ . Note that the negligible overlap with the remaining basis states  $|\uparrow\uparrow\rangle$  and  $|\downarrow\uparrow\rangle$  are not shown. All calculations were based on diagonalizing the spin Hamiltonian for the ground state.

assume that the relaxation process at these transitions is faster than for other spin transitions, which makes the optical pumping to be efficient for both of the connected levels [see Fig. 2(c)]. The flip-flop relaxation process between different  $\text{Yb}^{3+}$  ions could be dominant for low magnetic field in this material, as observed in  $\text{Nd}^{3+}$  doped  $\text{Y}_2\text{SiO}_5$  [45]; however, further studies of the relaxation rates are required to conclude about the nature of the observed phenomena.

The same behavior is also present for other antiholes on this map, whose energy splittings involve the excited state spin transition, and can be found in many parts of the spectrum. Although this effect complicates the reading of the hole-burning spectra, as discussed above, it potentially can also give additional information about the relative relaxation dynamics between particular sets of spin transitions.

Finally, we briefly discuss the relative orientations of the  $\mathbf{g}$  and  $\mathbf{A}$  tensors, and their anisotropy in the ground and excited states. By evaluating the values for hyperfine tensors from Table I one can see that the orientations of the  $\mathbf{g}$  and  $\mathbf{A}$  tensors for each state are almost parallel. For site I, the orientation of the maximum  $g$ -factor is close to  $\mathbf{D}_1$ , while for site II it is close to  $\mathbf{b}$ . The ratio between the tensor elements  $A_i/g_i$  is nearly constant for each component. This indicates that each

state on the optical  ${}^2F_{7/2}(0) \longleftrightarrow {}^2F_{5/2}(0)$  transition is close to a pure  $J$  multiplet [33].

## VI. CONCLUSION AND OUTLOOK

In conclusion, we have characterized the hyperfine interaction of the  ${}^{171}\text{Yb}^{3+}:\text{Y}_2\text{SiO}_5$  crystal on the optical  ${}^2F_{7/2}(0) \longleftrightarrow {}^2F_{5/2}(0)$  transition. We refined the hyperfine tensor of the ground state and determined its parameters for the excited state. The largest principal values of these tensors are oriented along similar directions for the ground and excited states, which are close to  $\mathbf{D}_1$  axis for site I and close to  $\mathbf{b}$  axis for site II. The hyperfine tensors are also

similarly oriented as the corresponding Zeeman tensors [33]. This simplifies the description of the spin Hamiltonians of  ${}^{171}\text{Yb}^{3+}:\text{Y}_2\text{SiO}_5$  crystal.

Our characterization of  ${}^{171}\text{Yb}^{3+}:\text{Y}_2\text{SiO}_5$  is in good agreement with previously obtained results for the Zeeman tensors of both the ground and excited states. However, for the hyperfine tensors of the ground states, the eigenvalues are very different as compared to those obtained through conventional EPR measurements in the high-field regime [33]. While both hyperfine tensors accurately predict the high-field regime (within experimental errors), only the hyperfine tensors given here work well at low fields. We believe this to be due to the difficulty to accurately determine all eigenvalues in the high-

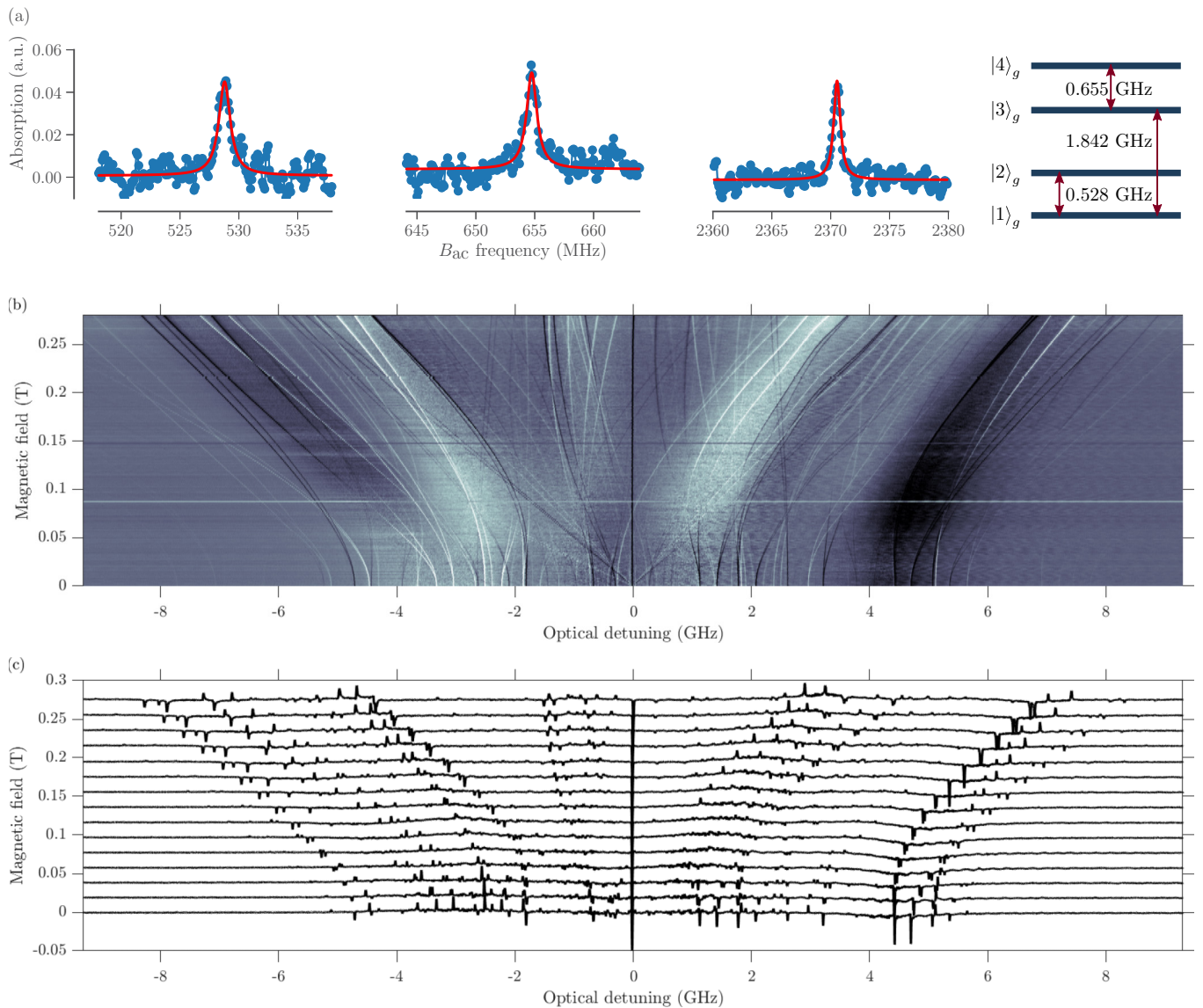


FIG. 6. Experimental results. (a) Optically detected magnetic resonance (ODMR) signals measured for site II and the reconstructed energy-level structure of the ground state. The oscillating magnetic field  $B_{ac}$  was applied in  $\mathbf{b}$  direction. Three different transitions are shown and their corresponding levels are depicted on the right. (b) Recorded optical spectral hole burning (SHB) spectra for site II of  ${}^{171}\text{Yb}^{3+}:\text{Y}_2\text{SiO}_5$  crystal measured for different magnetic field amplitudes applied in the direction close to  $\mathbf{D}_2$  axis. Zero frequency detuning corresponds to the central frequency at which spectral hole burning is performed. Black regions correspond to lower absorption (holes), while white lines correspond to lower transmission (antihole) regions. White and black dashed lines indicate energy-level splittings of ground and excited states, respectively. (c) The examples of SHB spectra taken from (b) with lower for magnetic field resolution.

field regime, where the hyperfine interaction is a perturbation to the Zeeman interaction. This problem was also recently encountered in a  $^{167}\text{Er}^{3+}:\text{Y}_2\text{SiO}_5$  crystal [34], hence it appears to be a general problem that has not yet been studied in EPR studies.

We also observed pseudoholes in the SHB spectra, at positions where antiholes were expected. We attribute this to cross-relaxation processes that efficiently couple certain hyperfine states. Further studies of the hole lifetimes at different magnetic fields, particularly for the highly nonlinear regime, can give information about relaxation rates and can help to attribute the observed effects to the particular relaxation process.

The spin Hamiltonian presented here allows the calculation of transition frequencies in the spin and optical domain under arbitrarily orientated external magnetic fields, over a wide range of magnetic fields. We note, however, that the effective spin Hamiltonian will break down for very high magnetic fields (for fields significantly higher than 1 tesla), where perturbations from the nearest crystal-field level cannot be neglected. In particular, the Hamiltonian can be used to accurately predict so-called ZEFOZ (ZEro First-Order Zeeman) points, where the sensitivity of transitions to magnetic field perturbations are highly suppressed [39]. In a parallel work, the Hamiltonian was used to predict ZEFOZ and near ZEFOZ points in  $^{171}\text{Yb}^{3+}:\text{Y}_2\text{SiO}_5$ , at zero and low external magnetic fields, respectively [53]. Furthermore, it was experimentally demonstrated that a strong enhancement of both optical and spin coherence times appears in these points, with optical coherence times reaching up to  $200\ \mu\text{s}$  and spin coherence times reaching up to 4 ms [53]. Based on these results, we

believe the  $^{171}\text{Yb}^{3+}:\text{Y}_2\text{SiO}_5$  crystal is very promising for optical quantum memories [1,3], microwave-to-optical transducers [51], and coupling to superconducting qubits in the microwave range [26].

### ACKNOWLEDGMENTS

The authors thank F. Fröwis and E. Z. Cruzeiro for useful discussions, as well as Claudio Barreiro for technical support. We acknowledge funding from EUs H2020 Program under the Marie Skłodowska-Curie Project QCALL (GA 675662), ANR under Grant Agreement No. 145-CE26-0037-01 (DISCRYS), Nano'K Project RECTUS, and the IMTO Cancer AVIESAN (Cancer Plan C16027HS, MALT).

### APPENDIX: HAMILTONIAN DEFINITION

The tensors  $\mathbf{A}$  and  $\mathbf{g}$  for the ground and excited states can be diagonalized in their respective principle axis systems. To express them in the crystal frame, we define a rotation with the usual Euler angle convention:

$$\mathbf{A} = R(\alpha_A, \beta_A, \gamma_A) \cdot \begin{bmatrix} A_1 & 0 & 0 \\ 0 & A_2 & 0 \\ 0 & 0 & A_3 \end{bmatrix} \cdot R(\alpha_A, \beta_A, \gamma_A)^T, \quad (\text{A1})$$

$$\mathbf{g} = R(\alpha_g, \beta_g, \gamma_g) \cdot \begin{bmatrix} g_1 & 0 & 0 \\ 0 & g_2 & 0 \\ 0 & 0 & g_3 \end{bmatrix} \cdot R(\alpha_g, \beta_g, \gamma_g)^T, \quad (\text{A2})$$

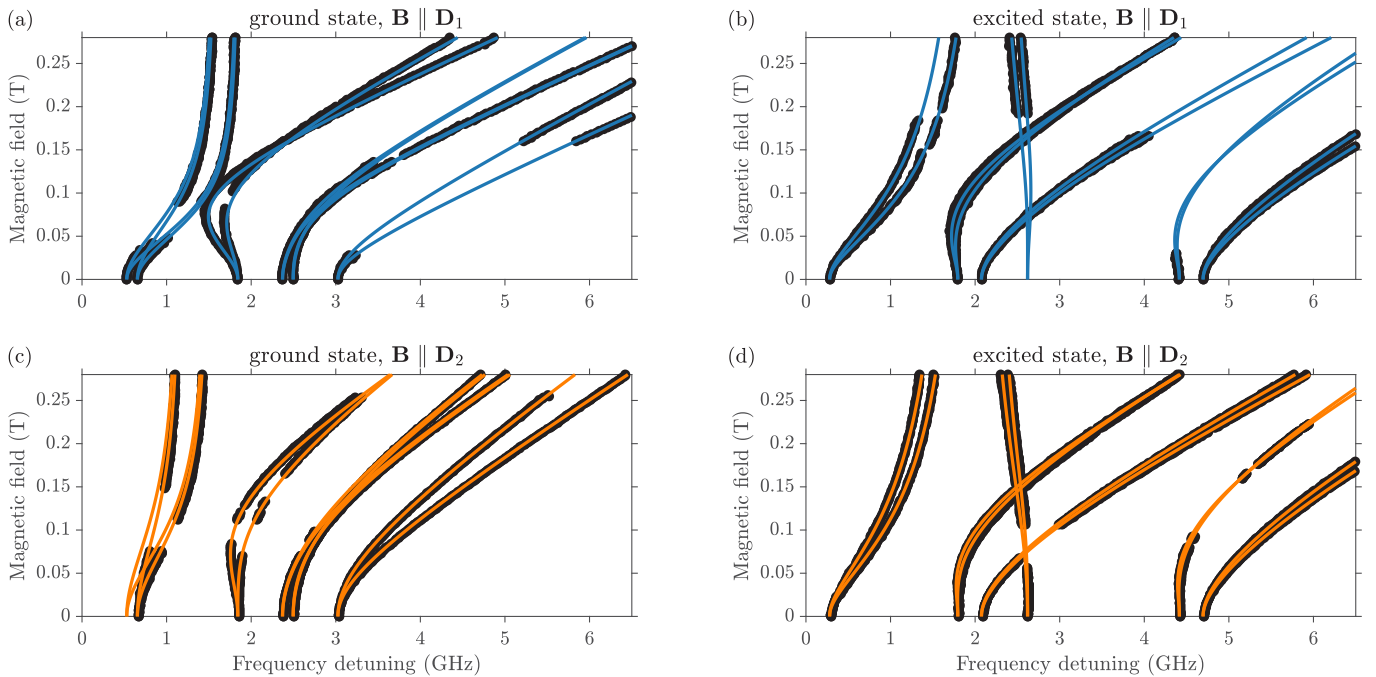


FIG. 7. Transition frequencies for ground (left) and excited (right) states for site II as a function of magnetic field amplitudes applied in two different directions ( $D_1$  on the top and  $D_2$  for bottom). Experimental points were extracted from SHB measurements (for example, Fig. 3) and used to fit hyperfine  $\mathbf{A}$  tensor parameters given in Table I. Calculated transition frequencies are plotted with solid lines.



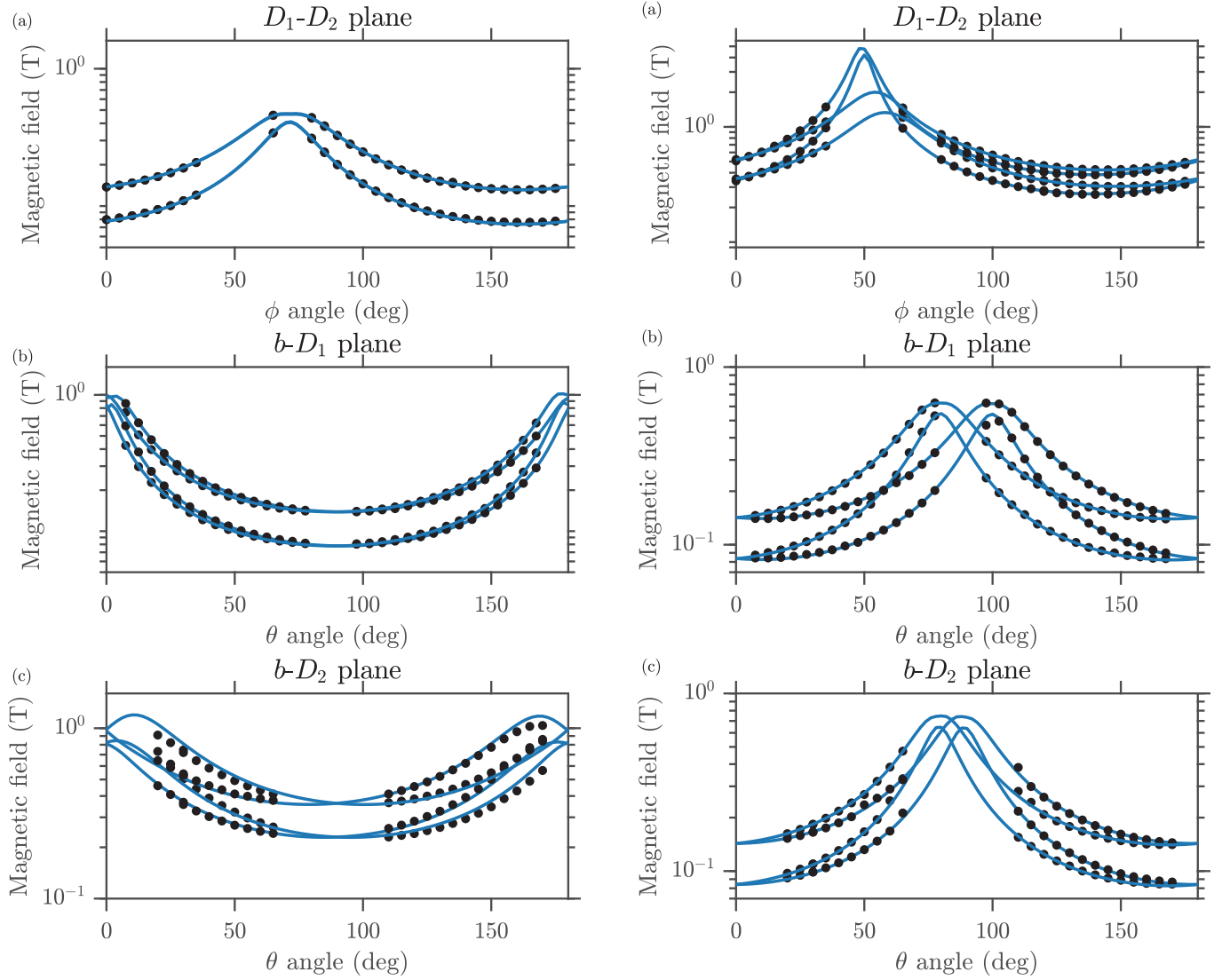


FIG. 8. Angular variations of the EPR transitions of  $^{171}\text{Yb}^{3+}:\text{Y}_2\text{SiO}_5$  ground state for site I (left) and site II (right) in the three perpendicular crystallographic planes ( $D_1-D_2$ ,  $b-D_1$ , and  $b-D_2$ ). Experimental data (points) are well described by the model based on previously measured  $\mathbf{g}$ -tensors [33] and fitted hyperfine  $\mathbf{A}$  tensors in this work (solid lines).

where  $R(\alpha, \beta, \gamma)$  is the rotation matrix with Euler angles  $(\alpha, \beta, \gamma)$  for  $zxz$  convention

$$R(\alpha, \beta, \gamma) = R_z(\alpha) \cdot R_x(\beta) \cdot R_z(\gamma),$$

where

$$R_z(\alpha) = \begin{bmatrix} \cos(\alpha) & -\sin(\alpha) & 0 \\ \sin(\alpha) & \cos(\alpha) & 0 \\ 0 & 0 & 1 \end{bmatrix}, \quad (\text{A3})$$

$$R_x(\beta) = \begin{bmatrix} 1 & 0 & 0 \\ 0 & \cos(\beta) & -\sin(\beta) \\ 0 & \sin(\beta) & \cos(\beta) \end{bmatrix}. \quad (\text{A4})$$

The interaction tensors for the second magnetic subsite are defined using an additional  $\pi$ -rotation around the symmetry  $b$  axis of the crystal and given by

$$R_z(\pi) \cdot \mathbf{g} \cdot R_z(\pi)^T, \quad (\text{A5})$$

$$R_z(\pi) \cdot \mathbf{A} \cdot R_z(\pi)^T. \quad (\text{A6})$$

Additional rotation is applied to go from the crystal  $(D_1, D_2, b)$  frame to the laboratory  $(X, Y, Z)$  frame and was found to contain the angles lower than  $5^\circ$ . The orientation of the  $\mathbf{D}_1$  and  $\mathbf{D}_2$  axes was checked using the polarization dependent absorption measurement. The expected error in their determination could reach  $10^\circ$ . The interaction tensors in  $(D_1, D_2, b)$  crystal frame for the ground and excited state are found to be (in GHz)

$$\mathbf{A}_I^{(g)} = \begin{pmatrix} 4.847 & -1.232 & -0.244 \\ -1.232 & 1.425 & -0.203 \\ -0.244 & -0.203 & 0.618 \end{pmatrix}_{D_1 D_2 b},$$

$$\mathbf{A}_I^{(e)} = \begin{pmatrix} 6.715 & -1.413 & 0.499 \\ -1.413 & 2.233 & -0.143 \\ 0.499 & -0.143 & 1.513 \end{pmatrix}_{D_1 D_2 b},$$

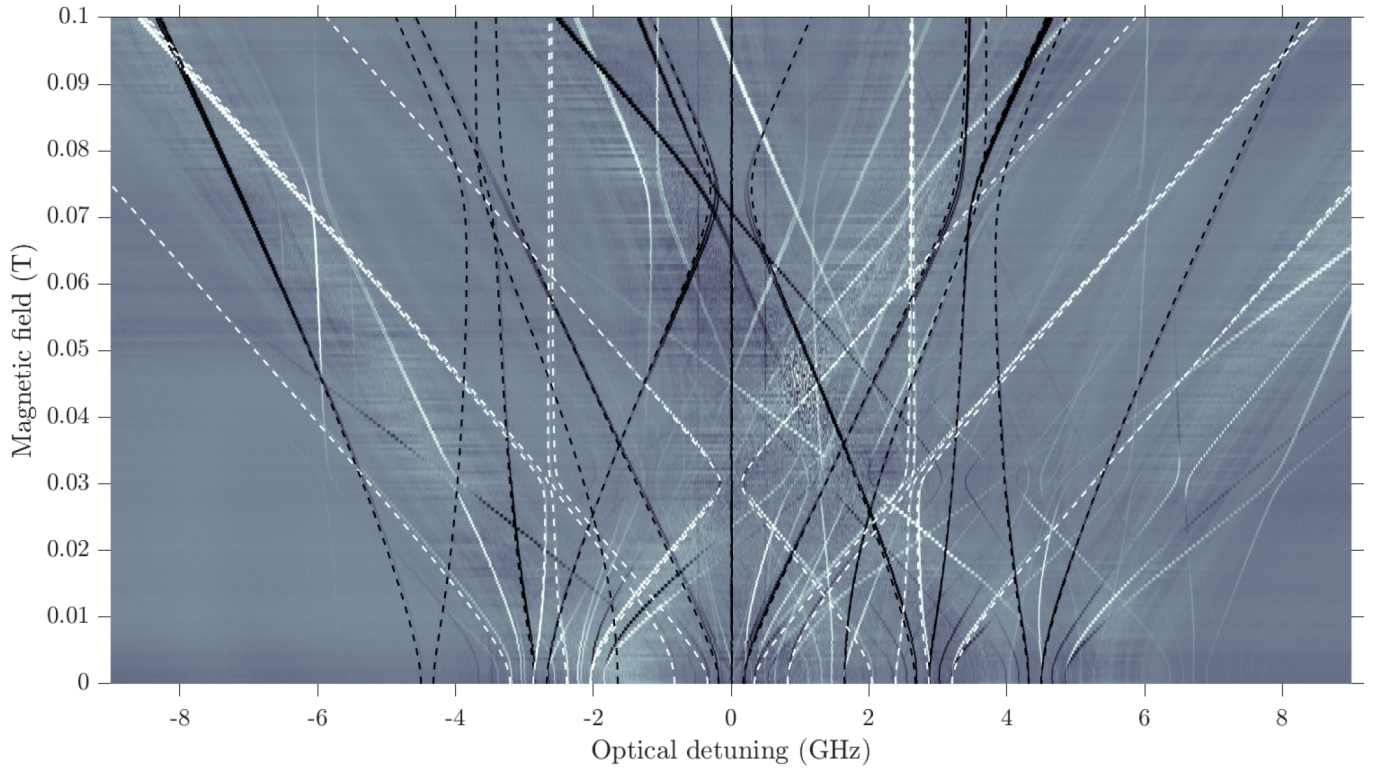


FIG. 9. Recorded optical spectral hole burning spectra for site II of  $^{171}\text{Yb}^{3+}:\text{Y}_2\text{SiO}_5$  crystal measured for different magnetic field amplitudes applied in the direction close to  $\mathbf{D}_2$  axis. Zero frequency detuning corresponds to the central frequency at which spectral hole burning is performed. Black regions correspond to lower absorption (holes), while white lines correspond to lower transmission (antihole) regions. White and black dashed lines indicate energy-level splittings of ground and excited states, respectively. The deviation from the data is attributed to the imperfect calibration of the laser scan.

$$\mathbf{A}_{\text{II}}^{(g)} = \begin{pmatrix} 0.686 & -0.718 & 0.492 \\ -0.718 & 0.509 & -0.496 \\ 0.492 & -0.496 & 4.729 \end{pmatrix}_{D_1 D_2 b},$$

$$\mathbf{A}_{\text{II}}^{(e)} = \begin{pmatrix} 2.802 & -0.379 & 0.661 \\ -0.379 & 2.652 & -0.532 \\ 0.661 & -0.532 & 6.277 \end{pmatrix}_{D_1 D_2 b}.$$

The corresponding  $\mathbf{g}$ -tensors used for the fitting are

$$\mathbf{g}_{\text{I}}^{(g)} = \begin{pmatrix} 6.072 & -1.460 & -0.271 \\ -1.460 & 1.845 & -0.415 \\ -0.271 & -0.415 & 0.523 \end{pmatrix}_{D_1 D_2 b},$$

$$\mathbf{g}_{\text{I}}^{(e)} = \begin{pmatrix} 3.242 & -0.566 & 0.249 \\ -0.566 & 0.934 & -0.033 \\ 0.249 & -0.033 & 1.023 \end{pmatrix}_{D_1 D_2 b},$$

$$\mathbf{g}_{\text{II}}^{(g)} = \begin{pmatrix} 0.999 & -0.766 & 0.825 \\ -0.766 & 0.825 & -0.424 \\ 0.825 & -0.424 & 5.867 \end{pmatrix}_{D_1 D_2 b},$$

$$\mathbf{g}_{\text{II}}^{(e)} = \begin{pmatrix} 1.389 & -0.337 & 0.572 \\ -0.337 & 1.308 & -0.383 \\ 0.572 & -0.383 & 3.008 \end{pmatrix}_{D_1 D_2 b}.$$

- [1] W. Tittel, M. Afzelius, T. Chanelière, R. Cone, S. Kröll, S. Moiseev, and M. Sellars, *Laser Photonics Rev.* **4**, 244 (2010).  
 [2] C. Thiel, T. Böttger, and R. Cone, *J. Lumin.* **131**, 353 (2011).  
 [3] F. Bussièrès, N. Sangouard, M. Afzelius, H. de Riedmatten, C. Simon, and W. Tittel, *J. Mod. Opt.* **60**, 1519 (2013).  
 [4] H. de Riedmatten and M. Afzelius, Quantum light storage in solid state atomic ensembles, in *Engineering the Atom-Photon Interaction: Controlling Fundamental Processes with Photons, Atoms and Solids*, edited by A. Predojević and M. W. Mitchell,

Nano-Optics and Nanophotonics (Springer International Publishing, Switzerland, 2015), Chap. 9, pp. 241–268.

- [5] P. Goldner, A. Ferrier, and O. Guillot-Nöel, Rare earth-doped crystals for quantum information processing, in *Handbook on the Physics and Chemistry of Rare Earths*, edited by J.-C. G. Bünzli and V. K. Pecharsky (Elsevier Science Publishers, North Holland, Amsterdam, 2015), Vol. 46, Chap. 267, pp. 1–78.  
 [6] R. M. Macfarlane, *J. Lumin.* **100**, 1 (2002).  
 [7] T. Böttger, C. W. Thiel, R. L. Cone, and Y. Sun, *Phys. Rev. B* **79**, 115104 (2009).

- [8] J. J. Longdell and M. J. Sellars, *Phys. Rev. A* **69**, 032307 (2004).
- [9] R. L. Ahlefeldt, D. L. McAuslan, J. J. Longdell, N. B. Manson, and M. J. Sellars, *Phys. Rev. Lett.* **111**, 240501 (2013).
- [10] A. Arcangeli, M. Lovrić, B. Tumino, A. Ferrier, and P. Goldner, *Phys. Rev. B* **89**, 184305 (2014).
- [11] M. Zhong, M. P. Hedges, R. L. Ahlefeldt, J. G. Bartholomew, S. E. Beavan, S. M. Wittig, J. J. Longdell, and M. J. Sellars, *Nature* **517**, 177 (2015).
- [12] P. Jobez, C. Laplane, N. Timoney, N. Gisin, A. Ferrier, P. Goldner, and M. Afzelius, *Phys. Rev. Lett.* **114**, 230502 (2015).
- [13] M. Gündoğan, P. M. Ledingham, K. Kutluer, M. Mazzerà, and H. de Riedmatten, *Phys. Rev. Lett.* **114**, 230501 (2015).
- [14] A. Seri, A. Lenhard, D. Rieländer, M. Gündoğan, P. M. Ledingham, M. Mazzerà, and H. de Riedmatten, *Phys. Rev. X* **7**, 021028 (2017).
- [15] M. Sabooni, Q. Li, S. Kröll, and L. Rippe, *Phys. Rev. Lett.* **110**, 133604 (2013).
- [16] P. Jobez, I. Usmani, N. Timoney, C. Laplane, N. Gisin, and M. Afzelius, *New J. Phys.* **16**, 083005 (2014).
- [17] G. Heinze, C. Hubrich, and T. Halfmann, *Phys. Rev. Lett.* **111**, 033601 (2013).
- [18] E. Saglamyurek, N. Sinclair, J. Jin, J. A. Slater, D. Oblak, F. Bussièrès, M. George, R. Ricken, W. Sohler, and W. Tittel, *Nature* **469**, 512 (2011).
- [19] C. Clausen, I. Usmani, F. Bussièrès, N. Sangouard, M. Afzelius, H. de Riedmatten, and N. Gisin, *Nature* **469**, 508 (2011).
- [20] A. Tiranov, J. Lavoie, A. Ferrier, P. Goldner, V. B. Verma, S. W. Nam, R. P. Mirin, A. E. Lita, F. Marsili, H. Herrmann, C. Silberhorn, N. Gisin, M. Afzelius, and F. Bussièrès, *Optica* **2**, 279 (2015).
- [21] A. Tiranov, P. C. Strassmann, J. Lavoie, N. Brunner, M. Huber, V. B. Verma, S. W. Nam, R. P. Mirin, A. E. Lita, F. Marsili, M. Afzelius, F. Bussièrès, and N. Gisin, *Phys. Rev. Lett.* **117**, 240506 (2016).
- [22] F. Bussièrès, C. Clausen, A. Tiranov, B. Korzh, V. B. Verma, S. W. Nam, F. Marsili, A. Ferrier, P. Goldner, H. Herrmann, C. Silberhorn, W. Sohler, M. Afzelius, and N. Gisin, *Nat. Photon.* **8**, 775 (2014).
- [23] R. Kolesov, K. Xia, R. Reuter, R. Stöhr, A. Zappe, J. Meijer, P. Hemmer, and J. Wrachtrup, *Nat. Commun.* **3**, 1029 (2012).
- [24] T. Utikal, E. Eichhammer, L. Petersen, A. Renn, S. Götzinger, and V. Sandoghdar, *Nat. Commun.* **5**, 3627 (2014).
- [25] R. Macfarlane and R. Shelby, in *Spectroscopy of Crystals Containing Rare Earth Ions*, Modern Problems in Condensed Matter Sciences, edited by A. Kaplyankii and R. Macfarlane (Elsevier Science Publishers, North Holland, Amsterdam, 1987), Vol. 21, Chap. 4, pp. 51–184.
- [26] S. Probst, H. Rotzinger, S. Wünsch, P. Jung, M. Jerger, M. Siegel, A. V. Ustinov, and P. A. Bushev, *Phys. Rev. Lett.* **110**, 157001 (2013).
- [27] G. Wolfowicz, H. Maier-Flaig, R. Marino, A. Ferrier, H. Vezin, J. J. L. Morton, and P. Goldner, *Phys. Rev. Lett.* **114**, 170503 (2015).
- [28] Y.-H. Chen, X. Fernandez-Gonzalvo, and J. J. Longdell, *Phys. Rev. B* **94**, 075117 (2016).
- [29] M. Rančić, M. P. Hedges, R. L. Ahlefeldt, and M. J. Sellars, *Nat. Phys.* **14**, 50 (2018).
- [30] J. C. Loredó, N. A. Zakaria, N. Somaschi, C. Anton, L. de Santis, V. Giesz, T. Grange, M. A. Broome, O. Gazzano, G. Coppola, I. Sagnes, A. Lemaitre, A. Auffèves, P. Senellart, M. P. Almeida, and A. G. White, *Optica* **3**, 433 (2016).
- [31] D. Ding, L. M. C. Pereira, J. F. Bauters, M. J. R. Heck, G. Welker, A. Vantomme, J. E. Bowers, M. J. A. de Dood, and D. Bouwmeester, *Nat. Photon.* **10**, 385 (2016).
- [32] E. Miyazono, T. Zhong, I. Craiciu, J. M. Kindem, and A. Faraon, *Appl. Phys. Lett.* **108**, 011111 (2016).
- [33] S. Welinski, A. Ferrier, M. Afzelius, and P. Goldner, *Phys. Rev. B* **94**, 155116 (2016).
- [34] Y.-H. Chen, X. Fernandez-Gonzalvo, S. P. Horvath, J. V. Rakonjac, and J. J. Longdell, *Phys. Rev. B* **97**, 024419 (2018).
- [35] V. Mehta, O. Guillot-Noel, D. Gourier, Z. Ichalalene, M. Castonguay, and S. Jandl, *J. Phys.: Condens. Matter* **12**, 7149 (2000).
- [36] A. Abragam and B. Bleaney, *Electronic Paramagnetic Resonance of Transition Ions* (Clarendon Press, Oxford UK, 1970).
- [37] C. Li, C. Wyon, and R. Moncorge, *IEEE J. Quantum Electron.* **28**, 1209 (1992).
- [38] R. W. Equall, Y. Sun, R. L. Cone, and R. M. Macfarlane, *Phys. Rev. Lett.* **72**, 2179 (1994).
- [39] E. Fraval, M. J. Sellars, and J. J. Longdell, *Phys. Rev. Lett.* **92**, 077601 (2004).
- [40] T. Böttger, C. W. Thiel, Y. Sun, and R. L. Cone, *Phys. Rev. B* **73**, 075101 (2006).
- [41] I. Kurkin and K. Chernov, *Physica B+C* **101**, 233 (1980).
- [42] R. M. Macfarlane and R. M. Shelby, *Opt. Lett.* **6**, 96 (1981).
- [43] A. M. Stoneham, *Rev. Mod. Phys.* **41**, 82 (1969).
- [44] S. R. Hastings-Simon, M. Afzelius, J. Minář, M. U. Staudt, B. Lauritzen, H. de Riedmatten, N. Gisin, A. Amari, A. Walther, S. Kröll, E. Cavalli, and M. Bettinelli, *Phys. Rev. B* **77**, 125111 (2008).
- [45] E. Z. Cruzeiro, A. Tiranov, I. Usmani, C. Laplane, J. Lavoie, A. Ferrier, P. Goldner, N. Gisin, and M. Afzelius, *Phys. Rev. B* **95**, 205119 (2017).
- [46] H. Riesen and A. Szabo, *Phys. Proc.* **3**, 1577 (2010).
- [47] H. Riesen, B. F. Hayward, and A. Szabo, *J. Lumin.* **127**, 655 (2007).
- [48] S. R. Hastings-Simon, B. Lauritzen, M. U. Staudt, J. L. M. van Mechelen, C. Simon, H. de Riedmatten, M. Afzelius, and N. Gisin, *Phys. Rev. B* **78**, 085410 (2008).
- [49] R. L. Ahlefeldt, M. F. Pascual-Winter, A. Louchet-Chauvet, T. Chanelière, and J.-L. Le Gouët, *Phys. Rev. B* **92**, 094305 (2015).
- [50] C. Laplane, E. Zambrini Cruzeiro, F. Fröwis, P. Goldner, and M. Afzelius, *Phys. Rev. Lett.* **117**, 037203 (2016).
- [51] X. Fernandez-Gonzalvo, Y.-H. Chen, C. Yin, S. Rogge, and J. J. Longdell, *Phys. Rev. A* **92**, 062313 (2015).
- [52] R. M. Macfarlane, A. Arcangeli, A. Ferrier, and P. Goldner, *Phys. Rev. Lett.* **113**, 157603 (2014).
- [53] A. Ortu, A. Tiranov, S. Welinski, F. Fröwis, N. Gisin, A. Ferrier, P. Goldner, and M. Afzelius, *Nat. Mater.* **17**, 671 (2018).

**A.3 Paper III: Optical and spin manipulation of non-Kramers rare-earth ions in a weak magnetic field for quantum memory applications**

# Optical and spin manipulation of non-Kramers rare-earth ions in a weak magnetic field for quantum memory applications

J. Etesse<sup>1,\*</sup>, A. Holzäpfel<sup>2</sup>, A. Ortu<sup>2</sup> and M. Afzelius<sup>2</sup>

<sup>1</sup>Université côte d'Azur, CNRS, Institut de Physique de Nice (INPHYNI), UMR 7010, Parc Valrose, Nice Cedex 2, France

<sup>2</sup>Department of Applied Physics, University of Geneva, CH-1211 Geneva 4, Switzerland



(Received 12 November 2020; accepted 29 January 2021; published 26 February 2021)

Rare-earth ion doped crystals have proven to be solid platforms for implementing quantum memories. Their potential use for integrated photonics with large multiplexing capability and unprecedented coherence times is at the core of their attractiveness. The best performances of these ions are, however, usually obtained when subjected to a DC magnetic field, but consequences of such fields on the quantum memory protocols have only received little attention. In this paper, we focus on the effect of a DC bias magnetic field on the population manipulation of non-Kramers ions with nuclear quadrupole states, both in the spin and optical domains, by developing a simple theoretical model. We apply this model to explain experimental observations in a  $^{151}\text{Eu}:\text{Y}_2\text{SiO}_5$  crystal, and highlight specific consequences on the atomic frequency comb spin-wave protocol. The developed analysis should allow predicting optimal magnetic field configurations for various protocols.

DOI: [10.1103/PhysRevA.103.022618](https://doi.org/10.1103/PhysRevA.103.022618)

## I. INTRODUCTION

Processing and distribution of quantum information has seen tremendous progress in recent years, thanks to the development of architectures for quantum computing [1] and deployment of photonics-based large-scale quantum networks [2,3]. A crucial ingredient is, however, still missing to fully synchronize the elementary photonic links in the networks and implement, for instance, quantum repeaters [4]: the quantum memories [5]. Different platforms exist for implementing these devices [6–10] but a particularly interesting one has emerged over the last decade for this purpose: rare-earth ion doped crystals (REIDCs) [11–17]. Together with the spin-wave atomic frequency comb (AFC) protocol [18], state-of-the-art performances have been demonstrated with these elements in terms of storage duration [13,17,19], multiplexing capacity [12,20], ability to store single photons [14–16], and potential for high-efficiency storage [21,22]. A fully favorable regime for operating REIDCs is usually at magnetic fields that allows reaching a point where the magnetic sensitivity to environmental fluctuations is minimal (so-called zero first-order Zeeman points) [13,23,24]. However, this situation requires a higher degree of control: magnetic field amplitudes could be high and their direction has to be precisely adjusted [19]. On the other hand, working with intermediate amplitude magnetic fields ( $\sim 10$  to  $100$  mT) also results in larger effective coherence times [25] and allowed reaching storage times of the order of a second [17]. So far, only a few studies have been conducted to identify side-effects of such a field on the protocol at these field intensities and experimental requirements are still widely unknown. In this paper, we identify phenomena affecting the performance of population manipulations both

in the optical and spin domains for REIDCs and identify consequences on the spin-wave AFC protocol in this regime.

The paper is organized as follows: In Sec. II, we recall the principle of the spin-wave AFC protocol and its application to REIDC, and describe the different experimental setups used for the experiments of this paper. In Sec. III, we focus on the influence of an external bias field on the spin-level manipulations. The studies are conducted in the case of a  $3/2$  nuclear spin, governed by an effective quadrupole Hamiltonian, and theoretical findings are confronted to experimental observations. In Sec. IV, the influence of the field on the population preparation necessary for the AFC protocol is addressed, and the temporal dependence of the AFC spin-wave efficiency under such a field is closely studied. In particular, we identify frequencies that appear in the efficiency curve and associate them with beatings between different quantum paths linked to the lift of the Zeeman degeneracy.

## II. SPIN-WAVE AFC IN REIDC

### A. The AFC protocol

Let us recall the principles of the spin-wave AFC protocol. The protocol, as described in Ref. [18] and represented on the left part of Fig. 1, relies on the shaping of the absorption profile of an ensemble of  $N$  absorbers as a series of periodic teeth (period  $\Delta_{\text{AFC}}$ ) on a  $|g\rangle \leftrightarrow |e\rangle$  transition.

The absorption of an input photon by this structure then brings the ensemble in a so-called Dicke state,

$$|\psi\rangle \propto \sum_{j=1}^N e^{-i2\pi n_j t \Delta_{\text{AFC}}} |g_1, \dots, e_j, \dots, g_N\rangle, \quad (1)$$

where  $n_j$  is the number of the tooth to which the  $j$ th atom belongs. According to this expression, the excitation will rephase after a time  $\tau_{\text{AFC}} = 1/\Delta_{\text{AFC}}$ , leading to the

\*Corresponding author: [jean.ettesse@inphyni.cnrs.fr](mailto:jean.ettesse@inphyni.cnrs.fr)

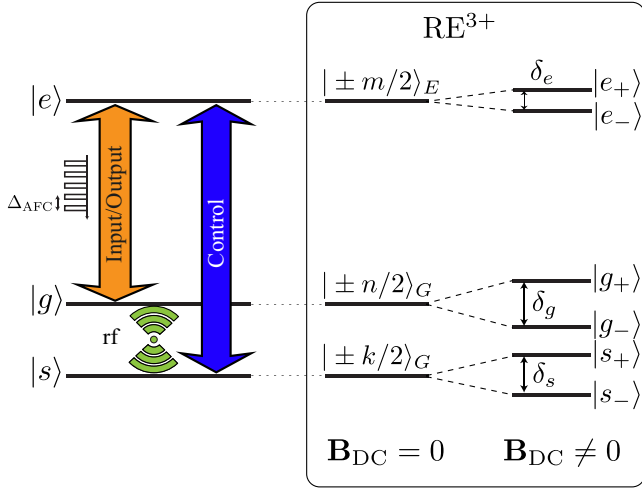


FIG. 1. The AFC protocol (left) and its application to nuclear spin levels of rare-earth ion doped crystals (right). Under the application of an external magnetic field  $\mathbf{B}_{DC}$ , the different Zeeman levels split.

re-emission of the input photon under the form of an echo. We will refer to this echo as the AFC echo. In forward emission, i.e., when the echo is emitted with the same  $\mathbf{k}$  vector as the input pulse, the efficiency of retrieval can be written in a general form [26]:

$$\eta_{\text{AFC}} = \eta_{\text{deph}} \tilde{d}^2 e^{-\tilde{d}} e^{-4/(T_2^{\text{opt}} \Delta_{\text{AFC}})}. \quad (2)$$

In this expression,  $\eta_{\text{deph}}$  accounts for the remaining dephasing process due to the finite width and shape of the teeth of the comb,  $\tilde{d}$  is the effective optical depth of the ensemble, and  $T_2^{\text{opt}}$  is the optical coherence time. One can show that the optimal shape for the comb is square [27], in which case  $\tilde{d} = d/F$  ( $d$  the optical depth,  $F$  the comb finesse) and  $\eta_{\text{deph}} = \text{sinc}^2(\pi/F)$  [26]. The finesse that maximizes the efficiency is then  $F = \pi/\text{atan}(2\pi/d)$  [27].

To make this protocol on-demand, a third shelving level  $|s\rangle$  can be used for the transfer of the optical coherence (1) into a long-lived spin coherence. The efficiency of the full AFC spin-wave memory protocol is

$$\eta_{\text{sw}} = \eta_{\text{AFC}} \eta_T^2 e^{-2T_s/T_2^{\text{spin}}}, \quad (3)$$

where  $\eta_T$  is the transfer efficiency from the optical to the spin transition,  $T_s$  is the storage time, and  $T_2^{\text{spin}}$  is the spin coherence time [26]. Optical pumping techniques can be used to shape the frequency comb in the absorption profile [26] and, in this case, a third ground state (that we will denote  $|\text{aux}\rangle$ , not shown in Fig. 1) has to be involved to store the removed population. These pumping techniques are impacted by the presence of a bias magnetic field, as we will see in Sec. IV. Additionally, spin manipulation may have to be performed between states  $|g\rangle$  and  $|s\rangle$  during the storage procedure to dynamically decouple the ions of interest from external fluctuations [17] or simply to rephase them efficiently due to the spin inhomogeneous linewidth [28]. These manipulations are at the core of the study conducted in Sec. IV of the present paper.

## B. Case of the REIDC

Two main systems have demonstrated high performances regarding the AFC spin-wave protocol, europium ( $\text{Eu}^{3+}$ ) and praseodymium ( $\text{Pr}^{3+}$ ), by using the optical electronic  $4f \leftrightarrow 4f$  transition together with the nuclear quadrupole spin states. To be more explicit, the nuclear spin Hamiltonian of both electronic ground (noted  $G$ ) and excited (noted  $E$ ) states can be written in the form [24,29–31]

$$H_E = \mathbf{I} Q_E \mathbf{I} + \mathbf{B}(t) M_E \mathbf{I}, \quad (4a)$$

$$H_G = \mathbf{I} Q_G \mathbf{I} + \mathbf{B}(t) M_G \mathbf{I}, \quad (4b)$$

where  $\mathbf{I}$  is the nuclear spin vector,  $Q_X$  are the effective pseudo quadrupole interaction tensors,  $M_X$  the Zeeman tensors, and  $X$  stands for  $E$  or  $G$ .  $\mathbf{B}(t)$  is the applied magnetic field vector that can be decomposed into a constant component and an oscillatory component that drives the transitions between the states:  $\mathbf{B}(t) = \mathbf{B}_{DC} + \mathbf{B}_{AC}(t)$ . Then, the Hamiltonians (4) can be decomposed as the sum of a time-independent and a time-dependent interaction Hamiltonian, respectively,

$$H_X = H_X^0 + H_X^{\text{int}}(t), \quad (5a)$$

with

$$H_X^0 = \mathbf{I} Q_X \mathbf{I} + \mathbf{B}_{DC} M_X \mathbf{I}, \quad (5b)$$

$$H_X^{\text{int}}(t) = \mathbf{B}_{AC}(t) M_X \mathbf{I}. \quad (5c)$$

In the case where  $\mathbf{B}_{DC} = 0$ , the two Hamiltonians (5b) give rise to  $n = (2I + 1)/2$  doubly degenerate states that can be used for the AFC protocol. This is shown in the central part of Fig. 1, where two of these doubly degenerate states have been represented for the ground state ( $|\pm k/2\rangle_G$  and  $|\pm n/2\rangle_G$ ), and one for the excited state ( $|\pm m/2\rangle_E$ ). For rare-earth ions with nuclear spin  $I$  above or equal to  $5/2$ , the spin-wave AFC protocol can be implemented by using the three doubly degenerate ground states as  $|g\rangle$ ,  $|s\rangle$ , and the auxiliary level  $|\text{aux}\rangle$ . Then, given the typical order of magnitude of the nuclear spin splittings, the spin manipulations can be performed by using radiofrequency (rf) pulses for inversion on the  $|g\rangle \leftrightarrow |s\rangle$  transition. Interestingly, the application of a magnetic field of the order of  $\sim 10$  mT to the ensemble leads to an increase in the coherence times [25] and allowed us to demonstrate spin-wave storage of classical optical pulses for about a second [17]. The focus of the paper will be to understand how the spin and optical manipulation necessary for the memory protocols are affected by this external field by only relying on the structure (4) of the Hamiltonians, with a particular glimpse at the spin-wave AFC protocol. It has to be noted that most of the derivations that are performed throughout this paper are not restricted to a specific ion in a given host crystal, but are valid for each system described by Hamiltonians of the form (4), with  $I \geq 3/2$ . Experimental verifications of the theoretical results have been conducted with a setup that we will now describe.

## C. Experimental setup

Our system is sketched in Fig. 2. We use a 1000 ppm doped isotopically pure  $^{151}\text{Eu} : \text{Y}_2\text{SiO}_5$  crystal, whose energy

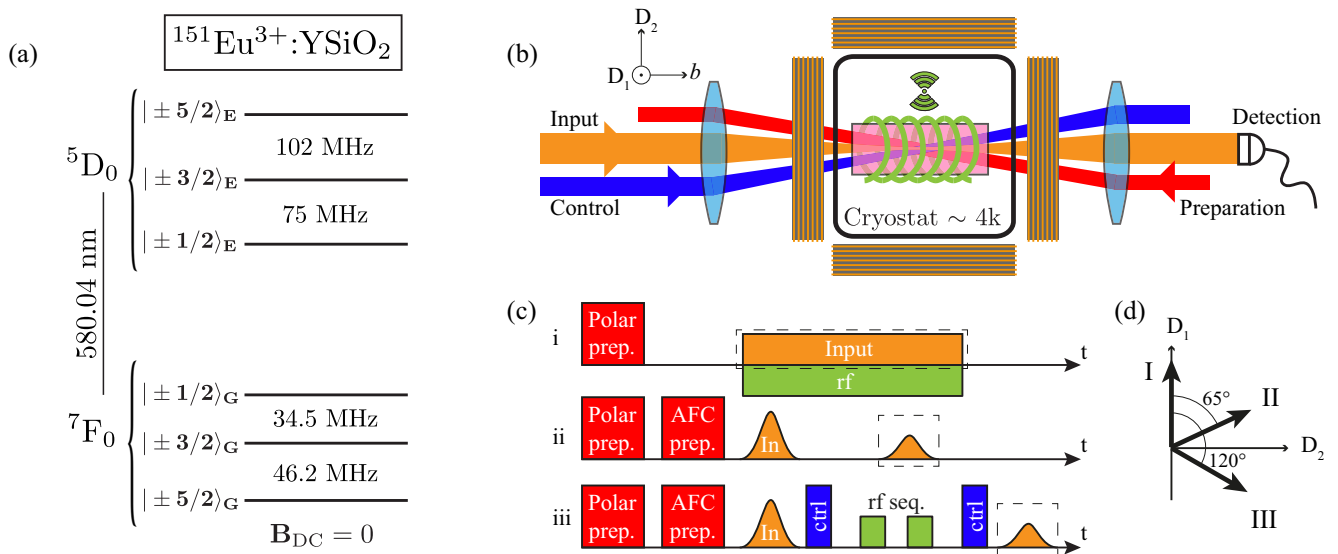


FIG. 2. Experimental system. (a) Energetic structure of  $^{151}\text{Eu} : \text{Y}_2\text{SiO}_5$  at zero field. Application of a DC bias field will lift the degeneracy of the states, as shown on the right part of Fig. 1. (b) Experimental apparatus. The  $b$ -cut  $^{151}\text{Eu} : \text{Y}_2\text{SiO}_5$  crystal is placed in a cryostat at 4K, and optically addressed with three beams: preparation (red), input (orange), and control (blue). The rf coil (green) allows us to apply the required rf fields. Three pairs of coils then allow us to apply the required DC bias field to the crystal (the coils in the  $D_1$  direction have not been represented here for clarity). The optical signal is detected with a variable gain photodiode in the input path. (c) Experimental sequences used throughout the paper. The measured optical signal is surrounded with a dashed box. (i) Optically detected nuclear magnetic resonance: The spins are polarized in one of the ground states and spin flops are performed with a constant amplitude rf field applied with the coil. Oscillations are detected with a simple absorption measurement with the input beam. (ii) Simple AFC echo experiment: After preparation by optical pumping, an input pulse with a Gaussian temporal shape is sent to the ensemble and the intensity of the echo is measured. (iii) Full spin-wave AFC protocol: Same as in (ii) but with a transfer of the optical coherence in the spin domain, using the control fields (ctrl, in blue). rf pulses are applied during the spin-wave storage for rephasing of the inhomogeneous ensemble. (d) Definition of the three DC bias magnetic field directions I, II, and III.

structure at zero field is shown in Fig. 2(a). The host matrix  $\text{Y}_2\text{SiO}_5$  is a biaxial crystal with polarization eigenaxes  $D_1$ ,  $D_2$ ,  $b$  [32]. The crystal is cut along these axes, and all optical beams are sent along the  $b$  axis, with their polarization along  $D_1$  to maximize the absorption coefficient ( $\alpha = 2.6 \text{ cm}^{-1}$ ). It is then placed on a homebuilt low-vibration mount in a closed-cycle helium cryostat at 4 K. The  $4f\text{-}4f$   ${}^7\text{F}_0 \leftrightarrow {}^5\text{D}_0$  atomic transition is addressed with a laser at 580.04 nm.

The setup around the cryostat is shown in Fig. 2(b). Thanks to acousto-optic modulators, the laser is split into three optical beams with arbitrary amplitude and phase control: the preparation, the input and the control. The preparation beam allows us to shape the ensemble thanks to optical pumping techniques and to prepare pits of absorption or complex structures like AFCs [26,33]. In particular, we use it prior to all our experiments to apply a class cleaning sequence, which allows us to pump away all the atoms that are resonant on an unwanted transition. Therefore, after application of this sequence, individual  $|\pm k\rangle_G \leftrightarrow |\pm l\rangle_E$  optical transitions can be addressed. Details of this procedure are given in Refs. [26,33] and shall not be discussed here. Then, the input beam is used either to probe the absorption of the ensemble or to send input pulses to be stored in it. Finally, the control beam allows us to apply the optical transfer pulses that are required in the spin-wave AFC protocol. A six-turn coil wrapped around the crystal then allows us to apply the radio-frequency AC field along the  $b$  axis for spin manipulation. To enhance the generated AC field,

a resonator outside of the cryostat consisting in one capacitor in parallel and one in series is used [16,17,34].

An external magnetic field can then be applied with three pairs of coils in Helmholtz configuration around the cryostat. With our setup, a maximum field amplitude of  $\sim 15$  mT can be achieved. We label the direction of the field with the two angles  $\theta_{\text{DC}}$  and  $\varphi_{\text{DC}}$ , such that  $\mathbf{B}_{\text{DC}} = B_{\text{DC}}[\cos(\theta_{\text{DC}})\cos(\varphi_{\text{DC}}), \cos(\theta_{\text{DC}})\sin(\varphi_{\text{DC}}), \sin(\theta_{\text{DC}})]$  in the  $D_1, D_2, b$  basis. A particularity of the  $\text{Y}_2\text{SiO}_5$  matrix subject to such a field is that there exists two magnetically inequivalent subsites for the ions, such that in general applying a DC bias field does involve four times as many levels as in the zero field case. However, due to the symmetries of the crystal, if  $\mathbf{B}_{\text{DC}}$  is applied along  $b$  or in the  $(D_1, D_2)$  plane, the two sites behave equivalently and the system is simpler to handle [31]. In the rest of the paper, three particularly interesting field configurations within the  $(D_1, D_2)$  plane ( $\theta_{\text{DC}} = 0$ ) are explored, and shown in Fig. 2(d):

- (1) Direction I, for which  $\varphi_{\text{DC}} = 0$  (field aligned along  $D_1$ ), where the effective gyromagnetic ratio of the ground state  $|\pm 1/2\rangle_G$  is minimal ( $\sim 4$  kHz/mT)
- (2) Direction II, for which  $\varphi_{\text{DC}} = 65^\circ$ , where the effective gyromagnetic ratios of the ground states  $|\pm 1/2\rangle_G$  and  $|\pm 3/2\rangle_G$  are equal ( $\sim 14$  kHz/mT)
- (3) Direction III, for which  $\varphi_{\text{DC}} = 120^\circ$ , where the effective gyromagnetic ratio of the excited state  $|\pm 5/2\rangle_E$  is minimal ( $\sim 2.5$  kHz/mT)

### III. EFFICIENT POPULATION INVERSIONS IN FOUR-LEVEL SYSTEMS

To perform spin echo sequences with high retrieval efficiency, high-quality rephasing sequences must be used. A common way to implement these sequences is to apply a series of inverting  $\pi$  – pulses. Among other parameters, the quality of inversion directly impacts the quality of the rephasing [35]. In this section, we are interested in understanding how one can perform efficient spin inversions between the  $|g\rangle$  and  $|s\rangle$  states. We will first answer this question for the zero-field case and generalize it for the presence of a field. To simplify the calculation, we will only consider the restriction of the spin Hamiltonian  $H_G$  given in Eq. (4b) to the subspace of dimension 4 spanned by  $\{|-k/2\rangle_G, |k/2\rangle_G, |-n/2\rangle_G, |n/2\rangle_G\}$ , eigenvectors of  $H_G^0$ . In the following, and as shown in Fig. 1, this basis will now be noted as  $\{|s_-\rangle, |s_+\rangle, |g_-\rangle, |g_+\rangle\}$  for simplicity. We will note the restriction of all operators to this subspace via an exponent  $\{4\}$ . This restriction is equivalent to assuming that the population is constrained within the considered subspace and that there is no leakage, by spontaneous emission, crosstalk, or any other process.

#### A. Case $B_{DC}=0$

##### 1. Hamiltonian

When no external bias field is applied to the ions, the time-independent Hamiltonian  $[H_G^0]^{(4)}$  reads

$$[H_G^0]^{(4)} = [\mathbf{I}Q_G\mathbf{I}]^{(4)} = -\frac{\hbar}{2} \left[ \omega_0 \begin{pmatrix} \mathbb{1} & 0 \\ 0 & -\mathbb{1} \end{pmatrix} \right], \quad (6)$$

where  $\hbar\omega_0$  is simply the energy gap between the two doubly degenerate states  $|s_{\pm}\rangle$  and  $|g_{\pm}\rangle$  depicted in Fig. 1 and  $\mathbb{1}$  is the  $2 \times 2$  identity matrix. As  $B_{DC} = 0$ , the magnetic field only consists of the driving radiofrequency field of the form

$$\mathbf{B}(t) = \mathbf{B}_{AC}(t) = B_{AC} \cos(\omega_{\text{rot}}t + \varphi) \mathbf{e}_{AC}, \quad (7)$$

where  $B_{AC}$ ,  $\omega_{\text{rot}}$ ,  $\varphi$ , and  $\mathbf{e}_{AC}$  are, respectively, the field amplitude, frequency, phase, and direction ( $|\mathbf{e}_{AC}| = 1$ ). One can show that in the same basis as in (6),  $[\mathbf{B}(t)M_G\mathbf{I}]^{(4)}$  takes the form (see Appendix A)

$$[\mathbf{B}_{AC}(t)M_G\mathbf{I}]^{(4)} = -B_{AC} \cos(\omega_{\text{rot}}t + \varphi) \begin{pmatrix} G_{ss} & G_{sg} \\ G_{gs}^\dagger & G_{gg} \end{pmatrix}, \quad (8)$$

where  $G_{xy} = \frac{\mu_{xy}}{2} U_{xy}$ . In this expression,  $\mu_{sg} = 2\sqrt{|\det(G_{sg})|}$  is the effective magnetic transition moment of the  $s \leftrightarrow g$  transition and  $U_{xy}$  are unitary matrices. Up to unitary transformations in the subsequent  $2 \times 2$  subspaces, one can choose  $U_{sg} \in \text{SU}(2)$  (see Appendix A). For simplicity, we will now use the notation  $U_{sg} := U$  and  $\mu_{sg} := \mu$ .

##### 2. Solution to the Schrödinger equation

To understand the dynamics of the spin manipulation, we simply have to solve the Schrödinger equation

$$i\hbar \frac{d|\psi_{\text{spin}}(t)\rangle}{dt} = H_G^{(4)} |\psi_{\text{spin}}(t)\rangle, \quad (9)$$

with  $H_G^{(4)} = [\mathbf{I}Q_G\mathbf{I}]^{(4)} + [\mathbf{B}_{AC}(t)M_G\mathbf{I}]^{(4)}$ . Then, in the rotating frame,

$$|\psi_{\text{spin}}(t)\rangle = \begin{pmatrix} e^{i\frac{\omega_{\text{rot}}t}{2}} \mathbb{1} & 0 \\ 0 & e^{-i\frac{\omega_{\text{rot}}t}{2}} \mathbb{1} \end{pmatrix} |\psi'_{\text{spin}}(t)\rangle, \quad (10)$$

and after doing the rotating wave approximation, (9) becomes

$$\frac{d|\psi'_{\text{spin}}(t)\rangle}{dt} = \frac{i}{2} A |\psi'_{\text{spin}}(t)\rangle, \quad (11)$$

where

$$A = \Delta \begin{pmatrix} \mathbb{1} & 0 \\ 0 & -\mathbb{1} \end{pmatrix} + \Omega_0 \begin{pmatrix} 0 & e^{i\varphi} U \\ e^{-i\varphi} U^\dagger & 0 \end{pmatrix}, \quad (12)$$

$\Delta = \omega_{\text{rot}} - \omega_0$  and  $\Omega_0 = \mu B_{AC}/(2\hbar)$ . In the case  $\Delta = 0$ , the propagator associated with Eq. (11) is (see Appendix C)

$$U_0(t) = \cos\left(\frac{\Omega_0 t}{2}\right) \mathbb{1} + i \sin\left(\frac{\Omega_0 t}{2}\right) \begin{pmatrix} 0 & e^{i\varphi} U \\ e^{-i\varphi} U^\dagger & 0 \end{pmatrix}. \quad (13)$$

This propagator is similar to the case of a two-level drive, except each level is replaced by a doubly degenerate one. Consequently, perfect Rabi flops can be performed and ideal spin rephasing sequences can be applied. This means that the ground state depicted in Fig. 1 for  $B_{DC} = 0$  can indeed be treated as a two-level system regarding the population behavior during driving.

##### 3. Optical transitions

Interestingly, a similar reasoning can be applied for the optical transition. Indeed, given the very different orders of magnitudes of the interactions, the nuclear spin contribution can be considered as a perturbation of the electronic part [36], which in turn allows us to write the wave function of the ion as a tensor product between the electronic and the spin parts:

$$|\psi\rangle = |\psi_{\text{opt}}\rangle \otimes |\psi_{\text{spin}}\rangle. \quad (14)$$

This allows us to write the electric dipole interaction Hamiltonian for the optical fields following the notations in Fig. 1 in the reduced basis  $\{|s_-\rangle, |s_+\rangle, |g_-\rangle, |g_+\rangle, |e_-\rangle, |e_+\rangle\}$ ,

$$H_{\text{opt}}^{(6)} = dE_{\text{opt}} \cos(\omega_{\text{rot}}^{\text{opt}} + \varphi^{\text{opt}}) \begin{pmatrix} 0 & 0 & G_{se} \\ 0 & 0 & G_{ge} \\ G_{se}^\dagger & G_{ge}^\dagger & 0 \end{pmatrix}, \quad (15)$$

where  $G_{ke}$  ( $k$  standing for  $g$  or  $s$ ) are  $2 \times 2$  matrices that we write of the form  $G_{ke} = b_{ke} V_{ke}$ . As for the magnetic transition,  $b_{ke}^2 = |\det G_{ke}|$  is the branching ratio of transition  $k \leftrightarrow e$ , and  $V_{ke}$  are unitary matrices, of the form

$$V_{se} = \frac{1}{b_{se}} \begin{pmatrix} \langle s_- | e_- \rangle & \langle s_- | e_+ \rangle \\ \langle s_+ | e_- \rangle & \langle s_+ | e_+ \rangle \end{pmatrix}, \quad (16a)$$

$$V_{ge} = \frac{1}{b_{ge}} \begin{pmatrix} \langle g_- | e_- \rangle & \langle g_- | e_+ \rangle \\ \langle g_+ | e_- \rangle & \langle g_+ | e_+ \rangle \end{pmatrix}. \quad (16b)$$

The dynamics of the atom on the optical transition is then the one of a two-level system, as in (13). Notice that in the present example, only one excited state and two ground states are considered, even if  $n = (2I + 1)/2$  nuclear states in each electronic state are present. In practice, all eigenstates are then vectors with  $2n$  components.



## B. Case $B_{DC} \neq 0$

### 1. Hamiltonian

When subject to a constant DC magnetic field, the degeneracy of the doubly degenerate nuclear spin states is lifted. In the linear Zeeman regime, i.e., when first-order perturbation theory applies to the system (regime  $\delta_x \ll \omega_0$ ), the Hamiltonian (5b) in the basis  $\{|s_-\rangle, |s_+\rangle, |g_-\rangle, |g_+\rangle\}$  reads (see Appendix A)

$$[H_G^0]^{(4)} = -\frac{\hbar}{2} \left[ \omega_0 \begin{pmatrix} \mathbb{1} & 0 \\ 0 & -\mathbb{1} \end{pmatrix} + \delta_s \begin{pmatrix} \sigma_z & 0 \\ 0 & 0 \end{pmatrix} + \delta_g \begin{pmatrix} 0 & 0 \\ 0 & \sigma_z \end{pmatrix} \right], \quad (17)$$

where  $\mathbb{1}$  is the  $2 \times 2$  identity matrix and  $\sigma_z$  is the usual Pauli matrix. Notice that we choose an increasing order in the eigenvalues, such that  $\delta_s$  and  $\delta_g$  are always positive. In the linear Zeeman regime, these splittings linearly depend on the field as  $\delta_x = g_x |B_{DC}|$  (see Appendix A).

Then, following the same reasoning as in the previous paragraph, we have to solve the same Eq. (11) with

$$A = \Delta \begin{pmatrix} \mathbb{1} & 0 \\ 0 & -\mathbb{1} \end{pmatrix} + \delta_s \begin{pmatrix} \sigma_z & 0 \\ 0 & 0 \end{pmatrix} + \delta_g \begin{pmatrix} 0 & 0 \\ 0 & \sigma_z \end{pmatrix} + \Omega_0 \begin{pmatrix} 0 & e^{i\varphi} U \\ e^{-i\varphi} U^\dagger & 0 \end{pmatrix} \quad (18)$$

and  $\Omega_0 = \mu B_{AC}/(2\hbar)$ .  $U$  can be chosen in  $SU(2)$ , similarly as in paragraph III A (see Appendix A). It can then be written in the general form

$$U = \begin{pmatrix} u_1 & u_2 \\ -u_2^* & u_1^* \end{pmatrix}, \quad (19)$$

with  $|u_1|^2 + |u_2|^2 = 1$ .

### 2. Solution to the Schrödinger equation

The solution of (11) is found by determining the four eigenvalues of  $A$ , which in the general case is a nontrivial problem. Fortunately, as shown in Appendix B, we can derive their approximate expression under the assumption  $(g_s - g_g)^2/|g_s g_g| \ll 1$ , where  $g_g$  (respectively  $g_s$ ) is the effective gyromagnetic ratio of the  $|g\rangle$  (respectively  $|s\rangle$ ) state. This condition is fulfilled as soon as all gyromagnetic ratios are of the same order of magnitude, which is the case in most of the experimental situations for europium and praseodymium. In the case  $\Delta = 0$ , a good approximation of the eigenvalues is given by

$$\zeta_1 = \sqrt{\frac{\delta_g^2 + \delta_s^2}{2} + \Omega_0^2 + (\delta_g + \delta_s) \sqrt{\left(\frac{\delta_g - \delta_s}{2}\right)^2 + |\Omega_1|^2}}, \quad (20a)$$

$$\zeta_2 = \sqrt{\frac{\delta_g^2 + \delta_s^2}{2} + \Omega_0^2 - (\delta_g + \delta_s) \sqrt{\left(\frac{\delta_g - \delta_s}{2}\right)^2 + |\Omega_1|^2}}, \quad (20b)$$

$$\zeta_3 = -\zeta_2, \quad (20c)$$

$$\zeta_4 = -\zeta_1, \quad (20d)$$

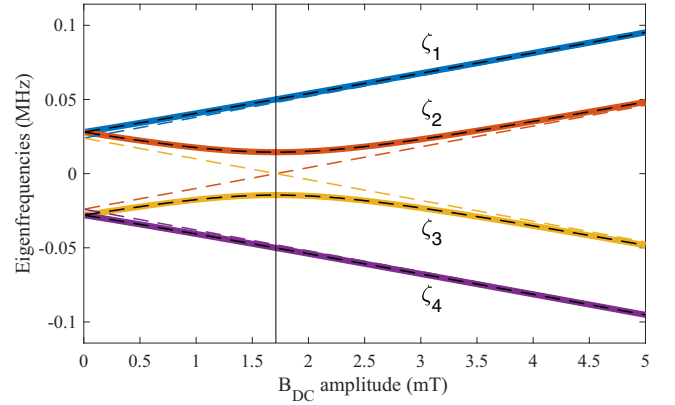


FIG. 3. Eigenvalues of the  $A$  matrix given in Eq. (18) as a function of the applied static magnetic field applied along direction II. A driving rf field, resonant with the spin transition and with 3 mT amplitude is applied along the  $b$  axis. Solid lines are numerical solutions, black dashed lines are analytical approximations, given by Eq. (20). Colored dashed lines are uncoupled eigenvalues ( $|u_2| = 0$ , see Appendix B).

where  $\Omega_1 = u_1 \Omega_0$ . The approximate values in the case  $\Delta \neq 0$  are given in Appendix B by Eqs. (B13).

If we apply this formula to our system with  $|s\rangle = |\pm 3/2\rangle_G$  and  $|g\rangle = |\pm 1/2\rangle_G$ , we find the magnetic-field dependency of the  $\zeta_i$  shown in Fig. 3. In the case chosen here, the  $B_{DC}$  field is applied along direction II ( $\theta_{DC} = 0$ ,  $\varphi_{DC} = 65^\circ$ ), the angle for which  $g_g = g_s = 14$  kHz/mT, and the radio-frequency field is applied on resonance along the  $b$  axis of the crystal (where  $\mu/(2\hbar) = 10$  kHz/mT), with an amplitude of 3 mT, leading to a zero-field Rabi frequency of  $\Omega_0 = 2\pi \times 30$  kHz. For this field direction, the coupling terms are  $|u_1| = 0.856$  and  $|u_2| = 0.517$ .

This behavior reveals an anticrossing of amplitude  $2|\Omega_2|$ , where  $\Omega_2 = u_2 \Omega_0$ , at a magnetic field  $B_{\text{cross}}$  for which  $|\Omega_1| = \sqrt{\delta_g \delta_s}$  (namely,  $B_{\text{cross}} = B_{AC} |u_1| \mu / \sqrt{g_g g_s}$ ). Intuitively, this new regime is entered when the system cannot be considered as a two-level system anymore: the Rabi frequency becomes comparable with the geometrical average of the splittings. The exact eigenvalues are represented in solid lines, while the approximations given by Eqs. (20) are represented with dashed black lines, revealing the validity of the approximation. This figure also allows us to define three regions for the field amplitude that we will denote as

- (1)  $B_{DC} \ll B_{\text{cross}}$ : weak field regime
- (2)  $B_{DC} \gg B_{\text{cross}}$ : strong field regime
- (3)  $B_{DC} \sim B_{\text{cross}}$ : intermediate field regime.

As we will see later, the behavior of the atoms in these three regions will be very different when attempting to perform population inversions.

Finally, the solution for Eq. (11) can be written in general as

$$|\psi_{\text{spin}}(t)\rangle = \alpha_{s_-}(t)|s_-\rangle + \alpha_{s_+}(t)|s_+\rangle + \alpha_{g_-}(t)|g_-\rangle + \alpha_{g_+}(t)|g_+\rangle, \quad (21)$$

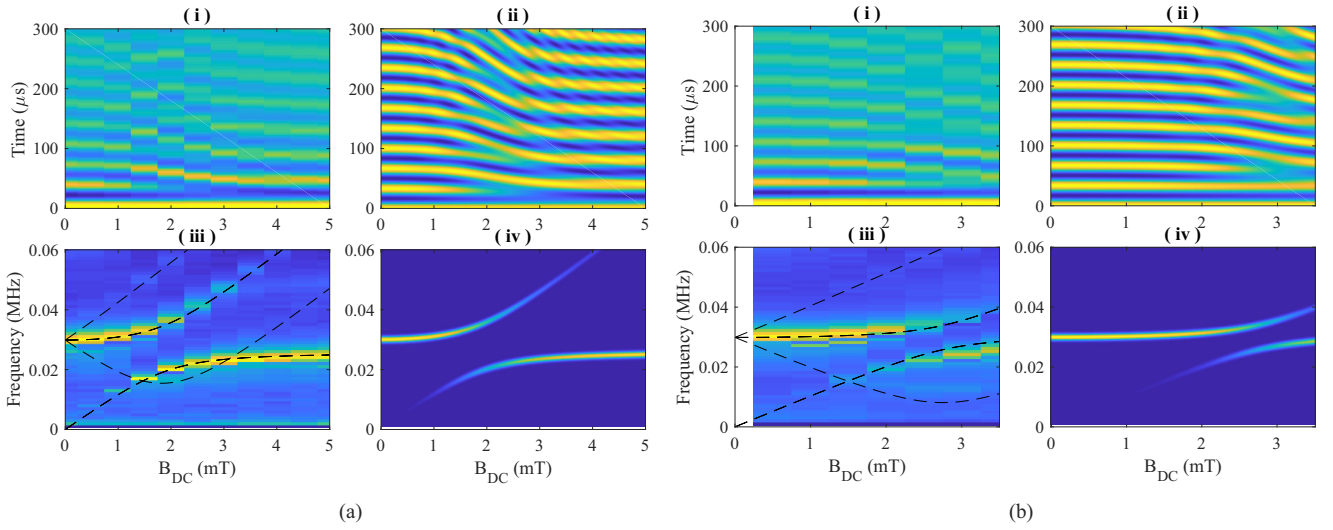


FIG. 4. ODNMR traces for a DC bias magnetic field at (a) point II and (b) point III. In each case, (i) gives the experimental temporal traces as a function of the bias field and (iii) its Fourier transform, (ii) gives the expected analytical time trace as predicted by Eq. (23), and (iv) gives the Fourier transform of the theoretical curve. The experimental frequency trace is also overlapped with dashed lines, which indicate the expected positions of the frequency components.

where

$$\alpha_x(t) = \sum_{k=1}^4 B_x^{(k)} e^{i\frac{\omega_k}{2}t}. \quad (22)$$

In this expression, the  $B_x^{(k)}$  coefficients are uniquely determined by the initial conditions.

### 3. ODNMR

To measure experimentally the previous parameters and validate the model, a simple method is to perform a drive of the spin population and follow the population dynamics by applying a constant amplitude rf field to the atoms. A common optically detected nuclear magnetic resonance (ODNMR) technique for this purpose consists of driving the spin transition ( $|s\rangle \leftrightarrow |g\rangle$ ) in Fig. 1) while monitoring the absorption on an optical transition (e.g.,  $|g\rangle \leftrightarrow |e\rangle$ ) in Fig. 1). Oscillations in the optical transmission directly give access to the spin population in the probed level and thus allows determining the population dynamics.

Referring to the previous analysis, the optical measurement will turn into measuring one population term  $|\alpha_x(t)|^2$  from Eq. (22) or a sum of these populations when they cannot be discriminated. It directly becomes apparent that all the angular frequencies  $\omega_{kl} = |\zeta_k - \zeta_l|$  could in principle appear in the observed oscillations. In the general case, this gives the possibility to observe up to six frequencies in the spin dynamics ( $\omega_{12}, \omega_{13}, \omega_{14}, \omega_{23}, \omega_{24}, \omega_{34}$ ), which reduces to four in the case  $\Delta = 0$  [ $\omega_{12} = \omega_{34}$  and  $\omega_{13} = \omega_{24}$ , see Eqs. (20)].

We have performed the ODNMR protocol with our setup, of which the time sequence is shown in Fig. 2(c)(i). After the class-cleaning procedure, the population was polarized into the  $|g\rangle = |\pm 1/2\rangle_G$  state with the preparation beam, and the coil generated a rf field at 34.54 MHz, resonant with the  $|g\rangle \leftrightarrow |s\rangle = |\pm 3/2\rangle_G$  transition ( $\Delta = 0$ ) at  $B_{DC} = 0$ . With our setup, a Rabi frequency at zero DC bias magnetic field of

$\Omega_0 = 2\pi \times 30$  kHz could be achieved. The optical input beam was then set to be resonant with the  $|g\rangle \leftrightarrow |e\rangle = |\pm 5/2\rangle_E$  transition. Notice that here, class cleaning is not performed at the Zeeman level, and thus the optical input beam simultaneously addresses four classes of atoms, each resonant with a different Zeeman transition. The two directions II and III were explored here. In particular, for direction III, the  $|u_2|$  parameter in Eq. (19) is minimal, such that the avoided crossing has the smallest gap  $2|\Omega_2|$  for a given AC field amplitude.

Figures 4(a)(i) and 4(b)(i) show the time traces of the ODNMR experiments as a function of the applied magnetic field  $B_{DC}$ . The expected anticrossing is made visible by performing the Fourier transform of the time traces, as shown in the Figs. 4(a)(iii) and 4(b)(iii). Over these experimental curves, the four previously mentioned frequencies  $\omega_{kl}$  are represented by black dashed lines, revealing a very good match with the measurement. However, it clearly appears that only two of them ( $\omega_{12}$  and  $\omega_{13}$ ) have a nonzero contribution. To understand this, we have used the analytical model developed in the previous paragraph [Eqs. (21) and (22)] and made two hypotheses. The first one is that, as no class cleaning is performed for the Zeeman levels, we suppose that the input beam simultaneously probes a class of atoms in  $|g_- \rangle$  (noted  $C_-$ ) and a class of atoms in  $|g_+ \rangle$  (noted  $C_+$ ), such that the intensity of the transmitted input is proportional to

$$I(t) \propto |\alpha_{C_-,g_-}(t)|^2 + |\alpha_{C_+,g_+}(t)|^2, \quad (23)$$

the sum of the populations in the two states of the two classes, given by Eq. (22). The second hypothesis concerns the initial state of the spins: Even if optical pumping is performed prior to the experiment to polarize the spins in  $|g\rangle$ , it does not discriminate between the Zeeman sublevels, such that we start with an initially mixed state between  $|g_- \rangle$  and  $|g_+ \rangle$  for both classes  $C_-$  and  $C_+$ :

$$\rho_{C_-}(t=0) = \rho_{C_+}(t=0) = \frac{1}{2}(|g_- \rangle \langle g_-| + |g_+ \rangle \langle g_+|). \quad (24)$$

The corresponding theoretical time traces are shown in Figs. 4(a)(ii) and 4(b)(ii) and show good agreement with the experimental ones, Figs. 4(a)(i) and 4(b)(i). The theoretical Fourier components are displayed in Figs. 4(a)(iv) and 4(b)(iv) and reveal indeed that the contributions for frequencies  $\omega_{14}$  and  $\omega_{23}$  of both classes of atoms annihilate,

$$B_{C_{-,g_-}}^{(1)} (B_{C_{-,g_-}}^{(4)})^* + B_{C_{+,g_+}}^{(1)} (B_{C_{+,g_+}}^{(4)})^* = 0, \quad (25a)$$

$$B_{C_{-,g_-}}^{(2)} (B_{C_{-,g_-}}^{(3)})^* + B_{C_{+,g_+}}^{(2)} (B_{C_{+,g_+}}^{(3)})^* = 0, \quad (25b)$$

even if they are nonzero for each class. We note that this is true for  $\Delta = 0$  only.

It should finally be noted that in the experimental trace, the oscillations fade after  $\sim 100 \mu\text{s}$  while they don't in the theoretical trace. Indeed, the spin manipulations are performed on an inhomogeneously broadened ensemble, such that each spin oscillates with its own Rabi frequency. Therefore, this decay depends both on the inhomogeneous broadening of the spin transition and on applied AC field (the spin homogeneous broadening contribution can be neglected at  $\sim 100 \mu\text{s}$  timescales). This decay gives the width of the frequency traces (iii) in Figs. 4(a) and 4(b). However, in the theoretical model, the spin transition is considered to be perfectly homogeneously broadened and the theoretical frequency traces should consequently be infinitely thin. To make them visible, we have simply enlarged them with a Gaussian profile with 700 Hz standard deviation width.

An important conclusion of this model is that if no care is taken about the magnetic field direction, amplitude, and

rf field detuning, up to 12 frequencies (six per magnetic subsite) can simultaneously coexist in the population dynamics, clearly lowering the transfer efficiency of the rf pulses and altering their rephasing capabilities. In the two next paragraphs, we will address two possible strategies to circumvent this problem: one can either diminish the amplitude of the DC bias field to neglect its influence or one can use complex adiabatic pulses that manage to drive the population efficiently.

#### 4. Efficient inversions in the weak field regime

According to our previous considerations, if one applies a field  $B_{\text{DC}} \ll B_{\text{cross}}$ , perfect inversions between the two states can be performed. This is what we observe experimentally from Figs. 4(a)(i) and 4(b)(i): At low fields, the population oscillates between  $|g\rangle$  and  $|s\rangle$  with a single frequency and with a very good transfer efficiency. Let us prove mathematically this observation. In the weak field regime, we can derive an analogous formula to Eq. (13) for the propagator (see Appendix C),

$$U_{\text{prop}}(t) \simeq \cos\left(\frac{\epsilon|\Omega_1|t}{2}\right)U_0(t) + \sin\left(\frac{\epsilon|\Omega_1|t}{2}\right)U_{\text{pert}}(t), \quad (26)$$

where  $\epsilon = \frac{\delta_x + \delta_y}{2\Omega_0} \ll 1$ ,  $U_0(t)$  is the propagator at zero field, given in Eq. (13),

$$U_{\text{pert}}(t) = i \cos\left(\frac{\Omega_0 t}{2}\right) \begin{pmatrix} |u_1| & -u_2 e^{i\phi_1} & 0 & 0 \\ -u_2^* e^{-i\phi_1} & 0 & |u_1| & u_2 e^{-i\phi_1} \\ 0 & 0 & u_2^* e^{i\phi_1} & -|u_1| \\ 0 & 0 & 0 & 0 \end{pmatrix} + \sin\left(\frac{\Omega_0 t}{2}\right) \begin{pmatrix} 0 & 0 & -e^{i(\varphi+\phi_1)} & 0 \\ 0 & 0 & 0 & e^{i(\varphi-\phi_1)} \\ -e^{-i(\varphi+\phi_1)} & 0 & 0 & 0 \\ 0 & e^{-i(\varphi-\phi_1)} & 0 & 0 \end{pmatrix}, \quad (27)$$

and  $e^{i\phi_1} = u_1/|u_1|$ . By choosing a pulse duration of  $\tau_l = (2l + 1)\pi/\Omega_0$ , the  $2 \times 2$  diagonal blocks of  $U_{\text{prop}}$  vanish:

$$U_{\text{prop}}(\tau_l) \simeq i(-1)^l \begin{pmatrix} 0 & e^{i\varphi}(c_l U - is_l V) \\ e^{-i\varphi}(c_l U^\dagger - is_l V^\dagger) & 0 \end{pmatrix}, \quad (28)$$

with  $c_l = \cos(\frac{\epsilon|\Omega_1|\tau_l}{2})$  and  $s_l = \sin(\frac{\epsilon|\Omega_1|\tau_l}{2})$  and

$$V = \begin{pmatrix} -e^{i\phi_1} & 0 \\ 0 & e^{-i\phi_1} \end{pmatrix}. \quad (29)$$

This form proves the aforementioned experimental observation, as no population remains in the initial state. It is also worth noticing that at first order the field does not induce an error on the quality of the inversion (the error is not equivalent to an imperfect rotation of angle  $\pi + \delta\theta$ ) [35]. However, this expression also reveals that the inversion induces some intermixing in both  $|g_\pm\rangle$  and  $|s_\pm\rangle$  doublets. To be more explicit, up

to a global phase and in the case  $\varphi = 0$ , the top antidiagonal term reads

$$c_l U - is_l V = (\mathcal{R}(u_1)c_l - \sin\phi_1 s_l)\mathbb{1} + i\mathcal{I}(u_2)c_l\sigma_x + i\mathcal{R}(u_2)c_l\sigma_y + i(\mathcal{I}(u_1)c_l + \cos\phi_1 s_l)\sigma_z. \quad (30)$$

This matrix, also writable in the form

$$\exp(i\alpha\mathbf{n} \cdot \hat{\sigma}/2) = \cos\frac{\alpha}{2}\mathbb{1} + i\mathbf{n} \cdot \hat{\sigma} \sin\frac{\alpha}{2}, \quad (31)$$

corresponds to a rotation on the Zeeman Bloch sphere with an angle  $-\alpha$

$$\sin\frac{\alpha}{2} = \sqrt{|u_2|^2 c_l^2 + (\mathcal{I}(u_1)c_l + \cos\phi_1 s_l)^2}, \quad (32a)$$

$$\cos\frac{\alpha}{2} = \mathcal{R}(u_1)c_l - \sin\phi_1 s_l, \quad (32b)$$

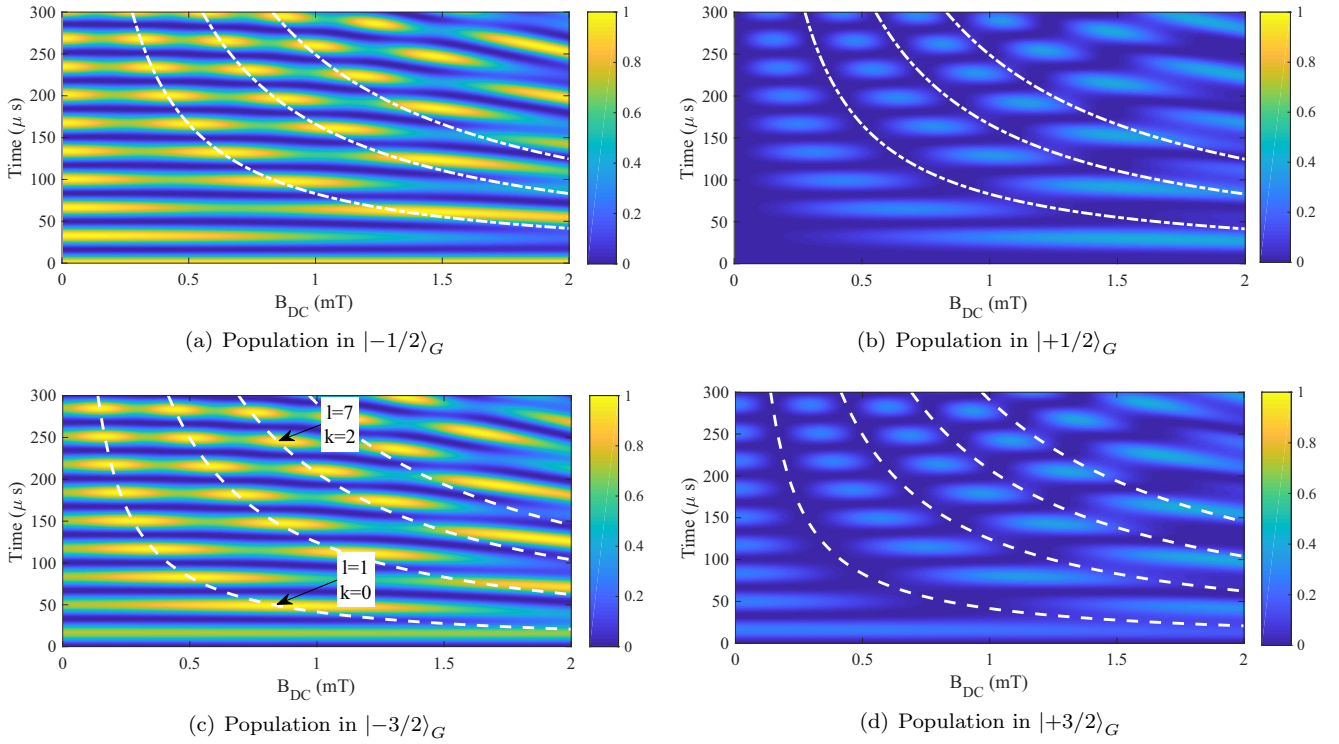


FIG. 5. Numerical simulations of temporal spin population dynamics for a continuously driven transition, as a function of applied DC bias magnetic field. Note that Fig. 4(a)(ii) is simply a sum of plots (a) and (b) here. The white dashed lines in (c) and (d) represent the condition at which the crosstalk between Zeeman sublevels vanishes as in Eq. (34) for  $k$  between 0 and 3, highlighting regions where high quality inversions can be performed. The dashed-dotted lines in (a) and (b) represent twice the duration of the previous condition, highlighting regions where high-quality identity operation can be performed.

around the vector

$$\mathbf{n} = \frac{1}{\sin \frac{\alpha}{2}} \begin{pmatrix} \mathcal{I}(u_2)c_l \\ \mathcal{R}(u_2)c_l \\ \mathcal{I}(u_1)c_l + \cos \phi_1 s_l \end{pmatrix}. \quad (33)$$

In the general case ( $|u_2| \neq 0$ ), this expression clearly indicates that a  $(2l + 1)\pi$ -pulse also mixes the population of the Zeeman doublet: the rotation in the Bloch sphere does not occur around the  $z$  axis. This is quite intuitive, as  $|u_2|$  in the  $U$  matrix is a coupling term between the two Zeeman states. To illustrate our mathematical finding, we plot in Fig. 5 the population evolution of an ion initially prepared in the  $|-1/2\rangle_G$  state as a function of time and applied magnetic field, for  $|-1/2\rangle_G$ ,  $|+1/2\rangle_G$ ,  $|-3/2\rangle_G$ , and  $|+3/2\rangle_G$ . In this simulation, all parameters are identical to those of Fig. 4(a), and note that Fig. 4(a)(ii) is simply the sum of Figs. 5(a) and 5(b). A striking fact that appears here is that opposed to Fig. 4(a)(ii), the visibility of the Rabi oscillations is strongly affected by the field. Therefore, perfect transfer from  $|-1/2\rangle_G$  to  $|-3/2\rangle_G$  cannot be realized with a basic  $\pi$  pulse at low field (see the first temporal population maximum in  $|-3/2\rangle_G$  in Fig. 5(c), which is not 1).

The consequence of such a phenomenon is that the application of an even number of  $\pi$  pulses together with free evolutions does not bring the spins back into their initial state in general, which is of crucial importance for rephasing sequences like spin-echo techniques [28] or dynamical decoupling sequences [17,35]. Fortunately, Fig. 5 also reveals

that under specific conditions, near-perfect inversions without crosstalk can be performed in the weak field regime (regions simultaneously at maximal population for  $|-3/2\rangle_G$  and minimal population for  $|+3/2\rangle_G$ ). This is confirmed by Eqs. (28) and (33): If  $c_l = 0$ , the cross terms in the  $c_l U - i s_l V$  matrix vanish. This condition reads

$$\frac{\epsilon |\Omega_1| \tau_l}{2} = (2k + 1) \frac{\pi}{2}, \quad k \in \mathbb{Z}. \quad (34)$$

and is plotted in Figs. 5(c) and 5(d) with dashed lines for  $k$  between 0 and 3. In a way, the grid of peaks in the transfer efficiency is identified with an index  $(l, k)$ , where  $l$  is the line number (from bottom to top), and  $k$  is the column number (from left to right). Two points have, for instance, been highlighted in Fig. 5(c), one at  $l = 1, k = 0$  and one at  $l = 7, k = 2$ . As expected, the model leads to a good prediction accuracy in the upper left corner of the plot, where

$$\epsilon = \frac{(2k + 1)\pi}{|\Omega_1| \tau_l} = \frac{2k + 1}{|u_1|(2l + 1)} \ll 1, \quad (35)$$

where  $k$  is small and  $l$  is large. However, experimentally there will obviously be a tradeoff between quality of the theoretical inversion and duration of the pulse, due to the finite coherence time. As an illustration, we see that our experimental curves have a contrast in the oscillations that vanish after  $\sim 2$  complete population inversions [see Figs. 4(a)(i) and 4(b)(i)], limiting  $l$  in practice to 1 or 2. In summary, to perform inversions without crosstalk, we simply have to set the pulse

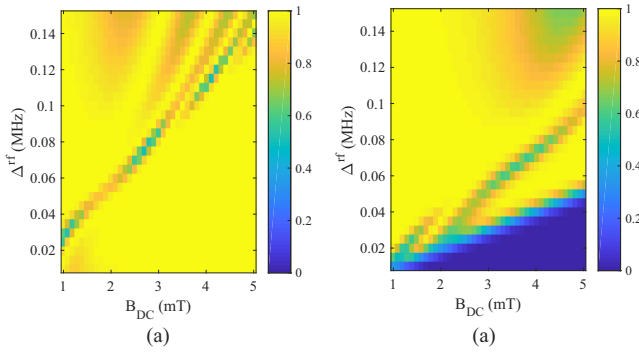


FIG. 6. Numerical simulations of the population in  $|g\rangle$  after adiabatic transfer from  $|s\rangle$ , with a secant hyperbolic profile (37) where  $\text{FWHM} = 120 \mu\text{s}$ , as a function of  $\Delta^{\text{rf}}$  and the applied magnetic field along (a) direction II ( $\varphi_{\text{DC}} = 65^\circ$ ) and (b) direction I ( $\varphi_{\text{DC}} = 0^\circ$ ).

duration to  $\tau_l = (2l + 1)\pi/\Omega_0$  and to adjust the DC bias field to

$$B_{\text{DC}} = \frac{2(2k + 1)\Omega_0}{(2l + 1)(g_g + g_s)|u_1|}. \quad (36)$$

For validation of our reasoning, we also plot in Figs. 5(a) and 5(b) the expected position of the population after two optimal pulses, for  $k = 0$  to 2 with dash-dotted lines, and see that the population can be brought back with very high efficiency in  $|-1/2\rangle_G$ .

##### 5. Adiabatic transfer of population: Transfers in all the regimes

If we now release the constraint on the magnitude of the DC bias magnetic field, Figs. 4(a)(ii) and 4(b)(ii) show that the pulse duration should be chosen very carefully to perform good quality inversions due to the particularly messy transfer pattern around the anticrossing point. Performing high quality inversions and rephasing [37] is, however, usually possible by using adiabatic pulses and we have numerically studied their application to an ion subject to a DC bias field. As before, we have focused on the simulation of our system, with the spin transition  $|g\rangle = |\pm 1/2\rangle_G \leftrightarrow |s\rangle = |\pm 3/2\rangle_G$  at 34.54 MHz. The adiabatic pulses were chosen of the form [26,38,39]

$$B_{\text{AC}}(t) = \text{sech}(\beta t) \cos \left[ \omega_{\text{rot}} t + \frac{\pi \Delta^{\text{rf}}}{2\beta} \ln(\cosh(\beta t)) \right], \quad (37)$$

where  $\beta$  relates to the pulse full width at half maximum (FWHM) like  $\beta = 2 \text{ arch}(2)/\text{FWHM}$ ,  $\Delta^{\text{rf}}$  is the pulse bandwidth (in Hz), and  $\omega_{\text{rot}}$  is the central angular frequency.

Figure 6 shows the transfer map that can be achieved with such an adiabatic pulse of  $120 \mu\text{s}$  FWHM and various chirps  $\Delta^{\text{rf}}$  as a function of the applied DC bias field. In the simulation, the population was initially set to an equal statistical mixture between  $|s_-\rangle$  and  $|s_+\rangle$ , and we plot  $|\alpha_{g_+}(\infty)|^2 + |\alpha_{g_-}(\infty)|^2$ , the sum of the populations long after the pulse in  $|g_-\rangle$  and  $|g_+\rangle$ . A first striking fact is that imperfect inversion cannot simply be linked with the position of the previously described avoided crossing. Indeed, for a field oriented along direction II [Fig. 6(a)], imperfect inversion does not only occur for a magnetic field amplitude of  $B_{\text{DC}} \sim 1.7 \text{ mT}$  as predicted in Fig. 3, but instead forms a complex pattern, which

depends on the total pulse chirp  $\Delta^{\text{rf}}$ . We recall, however, that along direction II,  $g_g = g_s$  such that perfect inversion can be performed if the field amplitude is high enough: both parallel transitions ( $|s_-\rangle \leftrightarrow |g_-\rangle$  and  $|s_+\rangle \leftrightarrow |g_+\rangle$ ) remain resonant, independently of the field intensity. However, if one goes out of this configuration, for instance, with a DC bias field applied along direction I (along  $D_1$ ,  $\varphi_{\text{DC}} = 0^\circ$ ), one finds the pattern shown in Fig. 6(b), for which transfer efficiency drops to zero if the applied DC field is too high, while still following a complex shape for higher chirp. In this case, the splitting is such that the applied field separates all the transitions too much, making it impossible to address all of them simultaneously with good efficiency.

It then clearly appears that to perform good quality population inversion with adiabatic pulses, one has to carefully adjust the different pulse parameters. Fortunately, it seems that in the regime of field explored here, there is always a set of parameters that allows performing arbitrarily good population inversions.

#### IV. AFC PROTOCOL AT $B_{\text{DC}} \neq 0$

In this section, we will focus on the influence of the field on the AFC protocol efficiency by studying the preparation sequence and the spin-wave decay curves for a system subject to an external field.

##### A. Comb shaping

As a reminder of what was briefly said in Sec. II A, the preparation of an AFC relies, in general, on two steps: First, the ensemble is polarized in the  $|g\rangle$  state using optical pumping techniques and, second, spectral hole burning is used to burn the transparency regions of the AFC [26]. To this extent, ions at the corresponding frequencies are repeatedly excited to  $|e\rangle$  until all of the unwanted population has relaxed to  $|aux\rangle$ . If the degeneracy of  $|g\rangle$  and  $|e\rangle$  is lifted by an external magnetic field, the preparation of an AFC becomes more involved. To understand why, let us first consider the simple case of hole burning in an inhomogeneously broadened ensemble, as sketched in Fig. 7. We will first assume that the ensemble is only subject to an excited state splitting  $\delta_e$ . In this ensemble, any atom that is absorbing at frequency  $f_0$  will also be absorbing either at frequency  $f_0 + \delta_e$  or at frequency  $f_0 - \delta_e$ . Consequently, optical pumping at frequency  $f_0$  will not only generate a transparency region at frequency  $f_0$  (dark blue in Fig. 7), but also at frequencies  $f_0 \pm \delta_e$  (light blue) [31]. These additional transparency regions are usually referred to as side holes. If the bandwidth of the frequency comb is larger than  $\delta_e$ , then the side holes of the transparency regions of the AFC may overlap with the absorptive regions of the AFC. In this case, the optical depth of the comb is reduced and, consequently, its efficiency is decreased [see Eq. (2)]. However, if the excited state splitting is a multiple of the periodicity  $\Delta_{\text{AFC}}$  of the frequency comb

$$\delta_e = n \Delta_{\text{AFC}} \iff \Delta_{\text{AFC}} = \frac{B_{\text{DC}} g_e}{n} \quad n \in \mathbb{N}, \quad (38)$$

where  $g_e$  is the effective gyromagnetic ratio of the excited state, then every side hole will coincide with a transparency

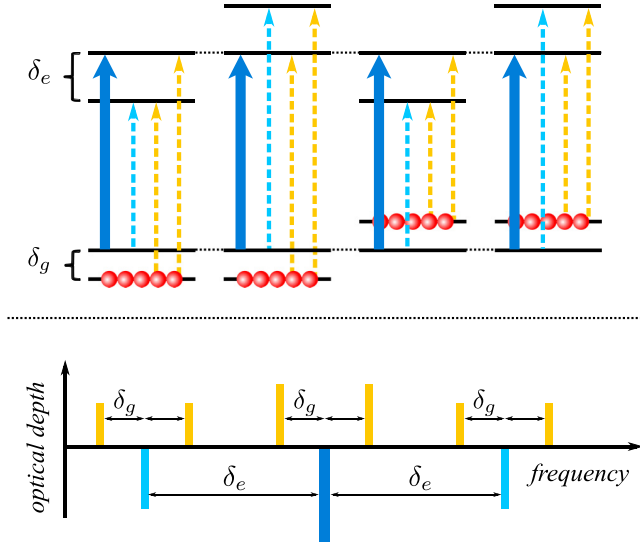


FIG. 7. Hole burning in a four-level system. Pumping with a single frequency (wide dark blue arrow) creates a central transparency peak (large blue) as well as side transparency peaks at  $\delta_e$  (thin blue, associated with blue dashed arrows). The pumped ions then lead to an increased absorption at frequencies  $\delta_g$  around transparency peaks (orange, associated with orange dashed arrows).

region of the comb. In this case, we expect no decrease of the memory efficiency compared to the degenerate case.

Let us second consider the effect of a split ground state with splitting  $\delta_g$ . Population that is excited can then relax into the other ground state instead of  $|aux\rangle$  (see Fig. 7). Consequently, hole burning at frequency  $f_0$  will result in additional absorption at the frequencies  $f_0 \pm \delta_g$  (two orange central peaks in Fig. 7). One usually refers to these regions as antiholes. Analogous to the scenario with a split excited state, one might expect that the efficiency of the comb is reduced if these antiholes coincide with the transparent regions of the frequency comb. Consequently, an efficient comb can only be prepared if the antiholes coincide with absorptive regions of the comb, leading to the condition

$$\delta_g = \left(n - \frac{1}{2}\right) \Delta_{\text{AFC}} \Leftrightarrow \Delta_{\text{AFC}} = \frac{B_{\text{DC}} g_g}{n - \frac{1}{2}} \quad n \in \mathbb{N}, \quad (39)$$

where  $g_g$  is the effective gyromagnetic ratio of the ground state.

Unlike the effect of side holes, this does not necessarily pose a fundamental limitation. The comb preparation consists of many repeated cycles of excitation and relaxation, such that a population that has relaxed back to  $|g\rangle$  instead of  $|aux\rangle$  will be excited in the following cycles until it finally reaches  $|aux\rangle$ . In this fashion, the effect of antiholes can be completely negated by repeating the preparation sequence sufficiently often, provided that  $|aux\rangle$  is long-lived enough that reflux from  $|aux\rangle$  to  $|g\rangle$  can be neglected. In contrast to this, side holes share the ground state with their respective central hole, such that transparency at the central hole position inevitably comes with increased transparency at the side-hole positions with a ratio between the two given purely by branching ratios, independently of the particulars of the preparation procedure.

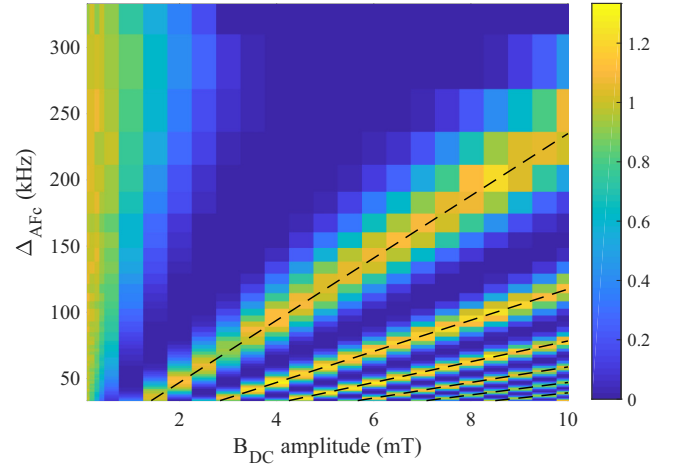


FIG. 8. Experimental efficiency ratio of AFCs prepared with and without an external field along direction I ( $D_1$  direction,  $\varphi_{\text{DC}} = 0^\circ$ ). We mark with dashed lines conditions (38) for  $n = 1, \dots, 6$  using an effective gyromagnetic ratio of  $g_e = 24$  kHz/mT, as determined in Ref. [31].

Finally, if one considers a system with both a split ground as well as excited state, additional absorption occurs at the frequencies  $f_0 \pm |\delta_g + \delta_e|$  and  $f_0 \pm |\delta_g - \delta_e|$  (four orange satellite peaks in Fig. 7). These anti-holes correspond to the transitions for which neither the ground state nor the excited state is shared with the central hole. Conditions similar to Eq. (39) may be formulated for these features but, for the same reason as mentioned previously, we do not expect to be fundamentally limited by these antiholes.

To validate the previous prediction, we have performed simple optical AFC echo experiments under magnetic field with our system, by choosing  $|g\rangle = |\pm 1/2\rangle_G$  and  $|e\rangle = |\pm 5/2\rangle_E$ . We have run the experiments with a field along direction I, where  $g_e = 24$  kHz/mT  $\gg g_g = 4$  kHz/mT, allowing us to test the validity of relation (38), and with a field along direction III, where  $g_g = 12$  kHz/mT  $\gg g_e = 2$  kHz/mT, allowing us to test the validity of relation (39). The experimental time sequence that we use is shown in Fig. 2(c) at line (ii), and simply consists in the preparation of an AFC and measurement of the two-level echo intensity for different values of the field applied during the whole sequence. To understand the relative effect of this field, we recorded the ratio between the AFC efficiency with and without it.

The data recorded along direction I are shown in Fig. 8 and reveal a very clear modulation of the efficiency: For some regions, the efficiency is close to zero, while in other regions no decrease of the efficiency as compared to without bias field is observed. If we superimpose on the plot the condition that we have found for minimizing the disturbance of the preparation process (38), we find that there is a very good agreement between the data and our expectation. Additionally, there is a region for low fields where the efficiency remains mainly unchanged. In this regime  $\delta_e \ll \Delta_{\text{AFC}}$ , such that the side hole is sufficiently close to the central hole and its detrimental effect can be neglected. It finally has to be noted that as  $g_g$  is very small for direction I, condition (39) is never met within the measured region.

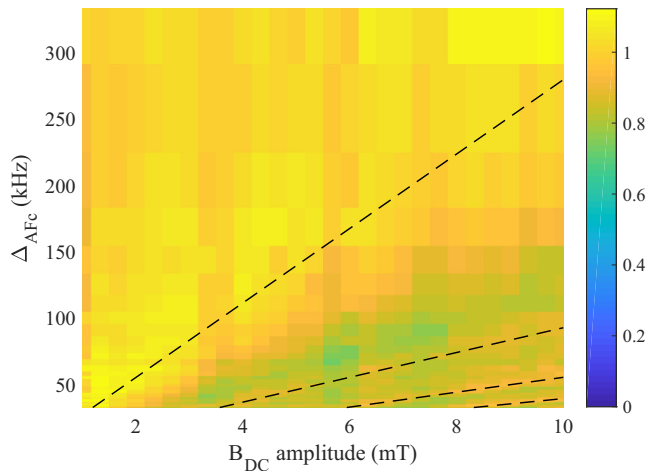


FIG. 9. Experimental efficiency ratio of AFCs prepared with and without an external field along direction III ( $\varphi_{\text{DC}} = 120^\circ$ ). Compared to the previous case,  $g_e < g_g$  such that the detrimental side holes are pushed away from the figure. A slight modulation is still visible that we attribute to side antiholes at  $f_0 \pm \delta_g$ . The dashed lines indicate their expected positions, according to Eq. (39), for  $n = 1, \dots, 4$  with  $g_g = 12 \text{ kHz/mT}$ , as determined in Ref. [31].

Along direction III, the measured ratios are shown in Fig. 9 and clearly indicate a strongly reduced sensitivity of the efficiency on the magnetic field compared to point I, for all comb spacings. While the modulations that we expect from Eq. (38) are outside of the observed parameter space, we notice another, much more faint modulation: Comparing with the prediction from Eq. (39) seems to indicate that these modulations might be connected to the antihole at  $f = f_0 \pm \delta_g$ , as depicted by the dashed lines. However, the strongly reduced strength of the modulation clearly corroborates our intuition that the side antiholes do not play a role that is as detrimental as side holes.

A simple way to link the two plots is that at point III, we remain in the zone  $\delta_e \ll \Delta_{\text{AFC}}$  for all fields under consideration, whereas the corresponding region was limited to the left part of the plot at point I. Following these observations, we note that efficient AFCs can be prepared in the presence of an external bias field even if their bandwidth is exceeding the Zeeman splitting that is induced by the field, provided that the periodicity of the comb is matched with the excited state splitting. The AFC preparation is therefore not fundamentally limiting the viability of AFC memories at low field in the REID systems that we consider.

### B. Spin-wave storage under weak magnetic field

Now that we have identified a favorable regime for the amplitude of the magnetic field regarding AFC preparation, let us focus on its influence on the full AFC spin-wave storage efficiency. Remember from Fig. 2(c)(iii) the principle of the experiment: In addition to the two-level AFC protocol, optical control fields are used to store the coherence in a long-lived spin state.

### 1. Optical transfer pulses

A question that arises is the influence of the field on the optical transfer pulse efficiency. Indeed, given the form of the optical interaction Hamiltonian (15), one should observe exactly the same phenomena as described in Sec. III for the spin inversions. Fortunately, we can derive the same kind of condition as defined in previous section: For an optical drive on the  $|g\rangle \leftrightarrow |e\rangle$  transition, the anticrossing occurs at  $\Omega_1^{\text{opt}} = \sqrt{\delta_g \delta_e}$ , where  $\Omega_1^{\text{opt}} = \langle g_- | e_- \rangle dE^{\text{opt}} / \hbar$ . Notice the similarity with the writing  $\Omega_1 = u_1 \mu B_{\text{AC}} / \hbar$  for the spin transition, where  $\mu = \mu_{sg}$  can be identified to  $b_{ge} d$  and  $u_1$  [first diagonal element of  $U = U_{sg}$  in Eq. (19)] can be identified to  $\langle g_- | e_- \rangle / b_{ge}$  [first diagonal element of  $V_{ge}$  in Eq. (16)]. Experimentally verifying this behavior in the optical domain is, however, more involved than in the spin domain as we have performed in Sec. III due to the much more limited coherence times: Spin coherence times are, for instance, around three orders of magnitude larger than optical ones, whereas the Rabi frequencies are at best one order of magnitude better in the optical domain. We then only expect to see a decrease in the efficiency when approaching the avoided crossing point.

To be far from this region, one simply has to consider  $\langle g_- | e_- \rangle dE^{\text{opt}} \gg \sqrt{g_g g_e} B_{\text{DC}}$ , which is easily realized with optical field powers of  $\sim 100 \text{ mW}$  focused on  $\sim 10 \mu\text{m}$ , leading for instance to optical Rabi frequencies of the order of  $\sim 100 \text{ kHz}$  for europium. Then, one has to limit the  $B_{\text{DC}}$  field to get splittings smaller than this value or use guided designs to confine the optical field more and push the Rabi frequency even higher [40]. With this in mind, we investigated the shape of the decays of AFC spin-wave echoes.

### 2. AFC spin-wave echoes

Motivated by our recent study of dynamical decoupling under small magnetic field in the AFC spin-wave storage protocol [17], we have investigated the shape of the measured decay more deeply. For this purpose, we have used our europium sample in a slightly different experimental apparatus and selected  $|\pm 5/2\rangle_G$  as  $|g\rangle$ ,  $|\pm 3/2\rangle_G$  as  $|s\rangle$ , and  $|\pm 1/2\rangle_E$  as  $|e\rangle$  to implement the protocol (see Figs. 1 and 2 for notations). The spin manipulation now occurs at a rf frequency of  $46.2 \text{ MHz}$  and is performed in the same way as depicted in the previous part. Due to technical reasons, we had to use a different experimental apparatus as compared with previous section, and the field could only be applied along  $D_1$  (direction I), and with a maximal amplitude of  $1.4 \text{ mT}$ . The AFC parameter for this experiment is  $1/\Delta_{\text{AFC}} = 20 \mu\text{s}$ , and adiabatic optical transfer pulses were used [26].

The time sequence that we have used in our protocol is shown in insets of Figs. 10(a) and 10(b). The overall efficiency (3) of the protocol is  $\eta_{\text{sw}} \simeq 5 \%$  in both cases, explained as follows. With our experimental parameters, the AFC echo efficiency (2) is  $\eta_{\text{AFC}} = 16\%$ . Then, in the AFC spin-wave memory efficiency formula (3), two additional efficiency terms enter into play: the transfer efficiency  $\eta_T$  and the spin dephasing term. In Figs. 10(a) and 10(b), we plot the efficiency of the spin-wave AFC echo as a function of the total storage time  $T_s$  under a magnetic field of  $B_{\text{DC}} = 1.4 \text{ mT}$ , and it clearly appears that the monotonically decreasing dephasing term does not play a role at the timescales we are

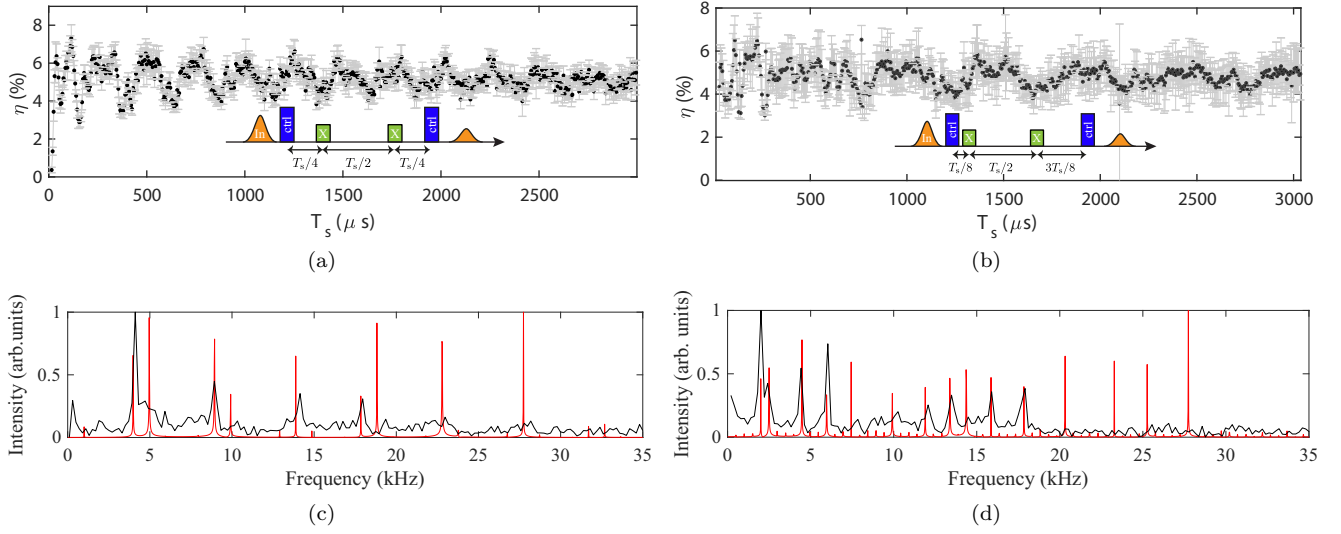


FIG. 10. AFC spin wave echo modulations. (a), (b) Echo efficiency as a function of the spin-wave storage time  $T_s$  under 1.4 mT bias magnetic field along direction I with a XX rf sequence that is (a) centered and (b) shifted by  $T_s/8$ . (c), (d) Fourier transforms of (a) and (b), respectively. Numerical simulations are shown in red.

considering here. Therefore, the remaining contribution should come from the transfer efficiency, which would be estimated to be  $\eta_T = \sqrt{\eta_{sw}/\eta_{AFC}} \simeq 56\%$  according to Eq.(3). However, the transfer pulses manage to reduce the amplitude of the AFC echo by 90%. Even if this value only gives an upper bound for its efficiency, the discrepancy between these two values is still unexplained and requires further investigations. Two scenarios are envisaged for the rf rephasing pulse configurations: In both cases, a XX rf sequence is used (two  $\pi$  pulses with the same phase [28]), but in Fig. 10(a) it is centered around  $T_s/2$  whereas in Fig. 10(b) it is shifted by  $T_s/8$ . It clearly appears that the echo decays contain a complex oscillatory pattern, whose richness is made visible by their respective Fourier transforms in Figs. 10(c) and 10(d) in black. We propose here a simple numerical analysis to partially explain this shape based on the study that we have performed in Sec. III. We have considered a single initial spin in the  $| -5/2 \rangle_G$  initial state, and have applied to it a series of operators linked with Hamiltonian (15) for optical transfers, (28) for spin transfers, and free evolution operators in between to simulate the whole spin-storage sequence. Namely, we simulate the output state as

$$|\psi_{out}\rangle = U_{opt2}^\pi U_{spin}^{free}(t_3) U_{prop}(\tau_0) U_{spin}^{free}(t_2) U_{prop}(\tau_0) U_{spin}^{free}(t_1) \times U_{opt2}^\pi U_{opt1}^{\pi/2} |\psi_{in}\rangle. \quad (40)$$

The initial coherence is simulated by a  $\pi/2$  pulse for simplicity. Finally, the echo will be emitted with an amplitude proportional to the coherences weighted by their branching ratios.

We have plotted the numerical results in red for  $2t_1 = t_2 = t_3 = T_s/2$  in Fig. 10(c) and for  $t_1 = T_s/8$ ,  $t_2 = T_s/2$  and  $t_3 = 3T_s/8$  in Fig. 10(d). We see with these plots that each experimentally observed peak can be associated with a numerically predicted one, and that the numerical simulation accounts for the difference between the two rf rephasing sequences. Given that the only difference between the two sequences is a phase

accumulation difference, this clearly gives a solid hint that the oscillations originate from interferences between different quantum paths during spin storage. Similar oscillations observed in stopped-light experiments in Pr:Y<sub>2</sub>SiO<sub>5</sub> have also been interpreted as being due to nuclear Zeeman states split by small applied magnetic fields [41].

The data presented in Fig. 10 shows that the weights of the different frequency components are not well reproduced by the numerical model, even if actual branching ratios both in the optical and the spin domain have been taken into account. Also, unobserved additional high frequency components are predicted by the model. These discrepancies could be due to specificities of the AFC protocol and dephasing during optical evolutions. The model also considers that the whole ion coherence contributes to the emission of the echo, which is not strictly true for the AFC protocol, as the echo emission consists of the interference of the field emitted by many ions with different detunings: the single ion model is probably too simplistic here. Also, the optical control pulses that are actually used in the experimental setup are adiabatic pulses (see Sec. III B 5), and the inversion dynamics is more complex than the one of a  $\pi$  pulse as used in the numerical model. Despite these discrepancies, our simple toy model shows that the modulations in the echo have components that mostly originate from interferences between different Zeeman paths of a single ion.

These echo modulations originate from different phenomena as the ones witnessed with Kramers ions mostly originating from superhyperfine splitting [42]. Indeed, as europium does not possess an electronic spin, we expect this coupling to be of much smaller amplitude. However, oscillations due to superhyperfine interaction between Pr and Y ions have been observed in spin-echo measurements in Pr:Y<sub>2</sub>SiO<sub>5</sub> [43]. We note that Pr ions have larger nuclear magnetic moment than Eu ions in Y<sub>2</sub>SiO<sub>5</sub>. As the gyromagnetic ratio of Yttrium is  $\gamma_Y = 209$  Hz/G [43], if observable the associated oscillations should appear around 2 kHz in our case. In



Fig. 10(c), we indeed see a weak amplitude peak at 2 kHz that is not explained by the previous numerical model, but in Fig. 10(d) other peaks linked with the numerical model hide its possible presence. To confirm this, we have also performed measurements with the same experimental apparatus as the one used in Sec. IV A for a DC bias magnetic field of 1 mT magnitude oriented along directions I and III and in each measurement a peak at  $\sim 2$  kHz was indeed present.

As a remark, this study also highlights the fact that minimal crosstalk both in the spin and in the optical transitions has to be investigated together to find a fully favorable configuration: Condition (36) exhibited for the spin should hold simultaneously for the optical transition.

## V. CONCLUSION

We have investigated the effect of a DC bias magnetic field on different aspects of the manipulation of rare-earth ions, both in the optical and in the spin domain. After reminding the Hamiltonian of the considered category of ions, we have derived the solution of the Schrödinger equation for a four-level driven system and have identified three field regimes (weak, strong, intermediate) that lead to different population dynamics. The theoretical model was compared to experimental realizations and allowed us to predict specific regimes in which perfect inversions could be performed. The effects of a DC bias magnetic field on the particular case of the spin-wave AFC protocol were then tackled both for the preparation of the structure as well as for the explanation of complex oscillatory patterns in spin-wave echoes experiments. The developed model should help to identify optimal field configuration in protocols involving optical or spin manipulation under magnetic field.

## ACKNOWLEDGMENTS

We would like to thank Alexey Tiranov for fruitful discussions at the early stage of the developments presented here, as well as Claudio Barreiro for technical support. This work was financially supported by the European Union Horizon 2020 research and innovation program within the Flagship on Quantum Technologies through GA 820445 (QIA), by the Marie Skłodowska-Curie program through GA 675662 (QCALL), and by the Swiss FNS NCCR programme Quantum Science Technology (QSIT).

## APPENDIX A: FORM OF THE INTERACTION MATRIX

In this Appendix, we prove the form of the  $2 \times 2$  block matrices that appear in the interaction matrix  $\mathbf{B}M_X\mathbf{I}$  [see Eq. (8)], once written in the eigenspace of  $\mathbf{I}Q_X\mathbf{I}$ .

Notice that the demonstration performed here does not require us to assume the restriction to the space of dimension 4, but is valid for all half-integer spins. From now on, we also drop the index  $X$  to simplify the writing.

Let us place ourselves in the eigenbase of  $Q$  such that it can be written [31]

$$Q = \begin{pmatrix} -E & 0 & 0 \\ 0 & E & 0 \\ 0 & 0 & D \end{pmatrix}. \quad (\text{A1})$$

Then,  $\mathbf{I}Q\mathbf{I}$  takes the simple form

$$\mathbf{I}Q\mathbf{I} = -EI_x^2 + EI_y^2 + DI_z^2, \quad (\text{A2})$$

where the  $I_i$  are the usual spin matrices, for a spin of value  $I = n - 1/2$ ,  $n \in \mathbb{N}^*$ .

### 1. Rewriting of the spin matrices

The first and most important step of this calculation is to group the spin  $z$  - projections  $2 \times 2$ , thanks to the transformation

$$F = \begin{pmatrix} 1 & & & & & & & & & & & & 0 \\ & 0 & & & & & & & & & & & 1 \\ & & 1 & & & & & & & & 0 & & \\ & & & \ddots & & & & & & & 1 & & \\ & & & & \ddots & & & & & & & & \\ & & & & & 1 & & & & & 0 & & \\ & & & & & & 1 & & & & & & \\ 0 & 1 & & & & & & & & & 1 & & \\ & & & & & & & & & & & & 0 \end{pmatrix}. \quad (\text{A3})$$

Intuitively, this transformation exchanges the even indexes with respect to the end indexes (index 2 is exchanged with index  $2n$ , index 4 is exchanged with index  $2n - 2$ , etc.) while leaving the odd indexes untouched. In this way, the eigenvalues of the spin  $z$  projection are grouped  $2 \times 2$ , and we can find similarities of the spin matrices with the  $1/2$ -spin Pauli matrices. To illustrate the effect of this transform, let us focus on the spin- $3/2$  case. Here, the transformation reads

$$F = \begin{pmatrix} 1 & 0 & 0 & 0 \\ 0 & 0 & 0 & 1 \\ 0 & 0 & 1 & 0 \\ 0 & 1 & 0 & 0 \end{pmatrix}, \quad (\text{A4})$$

such that the spin matrices are modified according to (remember that  $F^{-1} = F$ )

$$\begin{aligned} FI_xF &= \frac{1}{2} \begin{pmatrix} 0 & 0 & 0 & \sqrt{3} \\ 0 & 0 & \sqrt{3} & 0 \\ 0 & \sqrt{3} & 0 & 2 \\ \sqrt{3} & 0 & 2 & 0 \end{pmatrix}, \\ &= \frac{1}{2} \begin{pmatrix} 0 & \sqrt{3} \\ \sqrt{3} & 2 \end{pmatrix} \otimes \sigma_x, \end{aligned} \quad (\text{A5a})$$

$$\begin{aligned} FI_yF &= \frac{1}{2} \begin{pmatrix} 0 & 0 & 0 & -i\sqrt{3} \\ 0 & 0 & i\sqrt{3} & 0 \\ 0 & -i\sqrt{3} & 0 & 2i \\ i\sqrt{3} & 0 & -2i & 0 \end{pmatrix}, \\ &= \frac{1}{2} \begin{pmatrix} 0 & \sqrt{3} \\ \sqrt{3} & -2 \end{pmatrix} \otimes \sigma_y, \end{aligned} \quad (\text{A5b})$$

$$\begin{aligned} FI_zF &= \frac{1}{2} \begin{pmatrix} 3 & 0 & 0 & 0 \\ 0 & -3 & 0 & 0 \\ 0 & 0 & -1 & 0 \\ 0 & 0 & 0 & 1 \end{pmatrix}, \\ &= \frac{1}{2} \begin{pmatrix} 3 & 0 \\ 0 & -1 \end{pmatrix} \otimes \sigma_z. \end{aligned} \quad (\text{A5c})$$

This clearly shows that after the transform  $F$ , each spin matrix is composed of blocks of  $2 \times 2$  matrices that are simply multiples of Pauli matrices. This writing can then easily be generalized to arbitrary spin  $I = n - 1/2$ ,

$$FI_x F = \frac{1}{2} \begin{pmatrix} 0 & & a_{2n-3} & a_{2n-1} \\ & \ddots & \ddots & a_{2n-2} \\ a_3 & a_4 & & 0 \\ a_1 & a_2 & & \end{pmatrix} \otimes \sigma_x := A_x \otimes \sigma_x, \quad (\text{A6a})$$

$$FI_y F = \frac{1}{2} \begin{pmatrix} 0 & & a_{2n-3} & -a_{2n-1} \\ & \ddots & \ddots & -a_{2n-2} \\ a_3 & -a_4 & & 0 \\ a_1 & -a_2 & & \end{pmatrix} \otimes \sigma_y := A_y \otimes \sigma_y, \quad (\text{A6b})$$

$$FI_z F = \frac{1}{2} \begin{pmatrix} c_1 & & & \\ c_3 & & & 0 \\ & \ddots & & \\ 0 & & c_{2n-3} & \\ & & & c_{2n-1} \end{pmatrix} \otimes \sigma_z := A_z \otimes \sigma_z, \quad (\text{A6c})$$

where

$$a_k = \sqrt{k(2n - k)} = a_{2n-k}, \quad (\text{A7a})$$

$$c_k = 2(n - k) + 1, \quad (\text{A7b})$$

and where the  $\sigma_i$  are the Pauli matrices.

## 2. Diagonalization of the quadrupole Hamiltonian

Once written under the previous form, the squared spin matrices that appear in Eq. (A2) simply read

$$FI_x^2 F = A_x^2 \otimes \mathbb{1}, \quad (\text{A8a})$$

$$FI_y^2 F = A_y^2 \otimes \mathbb{1}, \quad (\text{A8b})$$

$$FI_z^2 F = A_z^2 \otimes \mathbb{1}, \quad (\text{A8c})$$

which gives the simple expression for the quadrupole component in the new basis:

$$FIQIF = (-EA_x^2 + EA_y^2 + DA_z^2) \otimes \mathbb{1}. \quad (\text{A9})$$

Then, to find the eigenvalues of this Hamiltonian, one just has to find the eigenvalues of the real symmetric matrix  $-EA_x^2 + EA_y^2 + DA_z^2$ . In other words, the matrix that will diagonalize  $FIQIF$  will only act on the left part of the tensor product and can be written of the form  $P \otimes \mathbb{1}$ , where  $P$  is a real orthogonal matrix of size  $n$ . This means that

$$P^{-1}(-EA_x^2 + EA_y^2 + DA_z^2)P \otimes \mathbb{1} \quad (\text{A10})$$

is diagonal, with  $n$  doubly degenerate eigenvalues. This is the result that we expect, as plotted in Figs. 1(right) and 2(a) for the case of europium.

## 3. Rewriting of the interaction Hamiltonian in the case $B_{DC} = 0$

Let us now see the effect of these transforms on the interaction Hamiltonian  $\mathbf{B}_{AC}(t)M\mathbf{I}$ . According to the general writing of  $\mathbf{B}_{AC}(t)$  of Eq. (7), the interaction matrix form will be determined by the direction of the magnetic field  $\mathbf{e}_{AC}$ .

Mathematically, it can always be written as

$$\mathbf{e}_{AC}M\mathbf{I} = \alpha_x^{\text{AC}}I_x + \alpha_y^{\text{AC}}I_y + \alpha_z^{\text{AC}}I_z, \quad (\text{A11})$$

where  $\alpha_i$  are real coefficients. Then, the transformation  $F$  will simply affect the spin operators according to the (A6) equations:

$$F\mathbf{e}_{AC}M\mathbf{I}F = \alpha_x^{\text{AC}}A_x \otimes \sigma_x + \alpha_y^{\text{AC}}A_y \otimes \sigma_y + \alpha_z^{\text{AC}}A_z \otimes \sigma_z. \quad (\text{A12})$$

Then, the transformation  $P \otimes \mathbb{1}$  which diagonalizes  $FIQIF$  acts on  $F\mathbf{e}_{AC}M\mathbf{I}F$  according to

$$\begin{aligned} (P^{-1} \otimes \mathbb{1})F\mathbf{e}_{AC}M\mathbf{I}F(P \otimes \mathbb{1}) \\ = \alpha_x^{\text{AC}}P^{-1}A_xP \otimes \sigma_x + \alpha_y^{\text{AC}}P^{-1}A_yP \otimes \sigma_y + \alpha_z^{\text{AC}}P^{-1}A_zP \otimes \sigma_z \\ := \mathcal{A}_x^{\text{AC}} \otimes \sigma_x + \mathcal{A}_y^{\text{AC}} \otimes \sigma_y + \mathcal{A}_z^{\text{AC}} \otimes \sigma_z. \end{aligned} \quad (\text{A13})$$

Formally speaking, the generic form of each  $2 \times 2$  submatrix in Eq. (A13) is then simply

$$G_{kl}^{\text{AC}} = (\mathcal{A}_x^{\text{AC}})_{kl} \sigma_x + (\mathcal{A}_y^{\text{AC}})_{kl} \sigma_y + (\mathcal{A}_z^{\text{AC}})_{kl} \sigma_z \quad (\text{A14a})$$

$$= \frac{\mu_{kl}}{2} U_{kl}^{\text{AC}}, \quad (\text{A14b})$$

with

$$\begin{aligned} \mu_{kl} &= 2\sqrt{-\det(G_{kl}^{\text{AC}})} \\ &= 2\sqrt{(\mathcal{A}_x^{\text{AC}})_{kl}^2 + (\mathcal{A}_y^{\text{AC}})_{kl}^2 + (\mathcal{A}_z^{\text{AC}})_{kl}^2} \end{aligned} \quad (\text{A15})$$

the effective magnetic moment of the transition,

$$U_{kl}^{\text{AC}} = (C_x^{\text{AC}})_{kl} \sigma_x + (C_y^{\text{AC}})_{kl} \sigma_y + (C_z^{\text{AC}})_{kl} \sigma_z, \quad (\text{A16})$$

and  $(C_i^{\text{AC}})_{kl} = 2(\mathcal{A}_i^{\text{AC}})_{kl}/\mu_{kl}$  such that  $U_{kl}$  is a unitary matrix with determinant  $-1$ .

It is worth noticing that one can also perform arbitrary unitary transforms  $\mathfrak{U}_i$  in each of the  $2 \times 2$  subspaces, resulting in the redefinition of the  $U_{kl}^{\text{AC}}$  matrices:

$$(U_{kl}^{\text{AC}})' = \mathfrak{U}_k^\dagger U_{kl}^{\text{AC}} \mathfrak{U}_l. \quad (\text{A17})$$

In particular, in the body of the paper, we chose  $U_{sg}$  ( $k = 1$  and  $l = 2$  in the spin 3/2 case) such that  $U_{sg} \in SU(2)$ . This can be done from Eqs. (A16) and (A17) by using  $\mathfrak{U}_k = \mathbb{1}$  and  $\mathfrak{L}_l = \sigma_z$  such that

$$(U_{kl}^{AC})' = -i(c_x^{AC})_{kl}\sigma_y + i(c_y^{AC})_{kl}\sigma_x + (c_z^{AC})_{kl}\mathbb{1}, \quad (\text{A18})$$

which clearly has a determinant +1.

#### 4. Influence of a magnetic field

The application of an external magnetic field  $\mathbf{B}_{DC} = B_{DC}\mathbf{e}_{DC}$  on our system modifies the Hamiltonian according to Eq. (5b):

$$H^0 = \mathbf{IQI} + B_{DC}\mathbf{e}_{DC}\mathbf{MI}. \quad (\text{A19})$$

If we suppose that the applied magnetic field is sufficiently small, i.e., that the Zeeman splittings are all small compared to the quadrupolar splittings, then one can perform first-order perturbation theory to estimate the effect of the field on the eigenlevels as well as eigenstates. To this extent, we simply have to diagonalize the  $2 \times 2$  submatrices of  $\mathbf{B}_{DC}\mathbf{MI}$  corresponding to the eigenspaces of  $\mathbf{IQI}$ , found in the previous paragraphs. We recall that the diagonal matrix that we found is  $(P^{-1} \otimes \mathbb{1})\mathbf{FIQIF}(P \otimes \mathbb{1})$ .

In the same way as what was derived in the previous paragraph, each diagonal  $2 \times 2$  matrix of  $(P^{-1} \otimes \mathbb{1})\mathbf{F}\mathbf{e}_{DC}\mathbf{MIF}(P \otimes \mathbb{1})$  can be written as

$$G_{kk}^{DC} = \frac{g_k}{2}V_k, \quad (\text{A20})$$

with

$$g_k = 2\sqrt{-\det(G_{kk}^{DC})}, \quad (\text{A21})$$

and

$$V_k = (c_x^{DC})_k\sigma_x + (c_y^{DC})_k\sigma_y + (c_z^{DC})_k\sigma_z, \quad (\text{A22})$$

such that  $V_k^{DC}$  is unitary with determinant  $-1$ . Now the diagonalization of this matrix gives the modification of the eigenvalues of  $\mathbf{IQI}$  and gives a preferential direction for its eigenvectors due to the lift of degeneracy. If  $(c_z^{DC})_k = 1$ , then  $V_k = \sigma_z$  is diagonal; if not, all the unitary matrices of the form

$$\mathfrak{P}_k^{DC} = \frac{V_k - \sigma_z}{[2 - 2(c_z^{DC})_k]^{1/2}} e^{i\varphi_k^{DC}} \quad (\text{A23})$$

then allow us to diagonalize  $V_k$ , with eigenvalues  $-1$  and  $+1$ , where  $\varphi_k^{DC}$  can be chosen arbitrarily.

Eigenvectors: Formally speaking, this means that the perturbation matrices of the eigenenergies are simply given by

$$B_{DC}\mathfrak{P}_k^\dagger G_{kk}^{DC} \mathfrak{P}_k = -\frac{g_k}{2}B_{DC}\sigma_z. \quad (\text{A24})$$

In the body of the text, we have simply noted  $|g_k B_{DC}| = \hbar\delta_k$ , such that  $g_k = 2\sqrt{-\det(G_{kk}^{DC})}$  is the effective gyromagnetic ratio of level  $k$ .

Eigenvectors: This new basis now allows us to rewrite the interaction  $2 \times 2$  submatrices  $U_{kl}^{AC}$  such that

$$(U_{kl}^{AC})' = \mathfrak{P}_k^\dagger U_{kl}^{AC} \mathfrak{P}_l, \quad (\text{A25})$$

where we recall that  $U_{kl}^{AC}$  is given by Eq. (A16).

Even if now only a restricted set of unitary transforms are allowed, they still allow us to bring the determinant equal to 1. Indeed, as  $\det(U_{kl}^{AC}) = -1$ , we only have to choose the phases  $\varphi_k = -\varphi_l = \pi/2$  [in (A23)] such that  $\det[(U_{kl}^{AC})'] = 1$ .

#### APPENDIX B: DIAGONALIZATION OF THE A MATRIX

In this Appendix, we prove the approximate form of the eigenvalues of the  $A$  matrix in the regime  $(g_s - g_g)^2 / |g_s g_g| \ll 1$  given in Eq. (20).

To this extent, let us rewrite the  $A$  matrix given by expression (18) in a more suitable basis, that makes it explicit that  $u_1$  couples spins of the same sign and  $u_2$  couples spins of opposite sign. For that, let us simply swap vectors 2 and 3 to define a new matrix  $A'$ ,

$$A' = \begin{pmatrix} \Delta + \delta_s & e^{i\varphi}\Omega_1 & 0 & e^{i\varphi}\Omega_2 \\ e^{-i\varphi}\Omega_1^* & -\Delta + \delta_g & -e^{-i\varphi}\Omega_2 & 0 \\ 0 & -e^{i\varphi}\Omega_2^* & \Delta - \delta_s & e^{i\varphi}\Omega_1^* \\ e^{-i\varphi}\Omega_2^* & 0 & e^{-i\varphi}\Omega_1 & -\Delta - \delta_g \end{pmatrix}, \quad (\text{B1})$$

where  $\Omega_1 = u_1\Omega_0$  and  $\Omega_2 = u_2\Omega_0$ , following the notations of Eq. (19).

We then decompose this matrix in three terms:

$$A' = A_{\text{free}} + A_{\text{par}} + A_{\text{cross}}, \quad (\text{B2a})$$

with

$$A_{\text{free}} = \begin{pmatrix} \Delta + \delta_s & 0 & 0 & 0 \\ 0 & -\Delta + \delta_g & 0 & 0 \\ 0 & 0 & \Delta - \delta_s & 0 \\ 0 & 0 & 0 & -\Delta - \delta_g \end{pmatrix}, \quad (\text{B2b})$$

$$A_{\text{par}} = \begin{pmatrix} 0 & e^{i\varphi}\Omega_1 & 0 & 0 \\ e^{-i\varphi}\Omega_1^* & 0 & 0 & 0 \\ 0 & 0 & 0 & e^{i\varphi}\Omega_1^* \\ 0 & 0 & e^{-i\varphi}\Omega_1 & 0 \end{pmatrix}, \quad (\text{B2c})$$

$$A_{\text{cross}} = \begin{pmatrix} 0 & 0 & 0 & e^{i\varphi}\Omega_2 \\ 0 & 0 & -e^{-i\varphi}\Omega_2 & 0 \\ 0 & -e^{i\varphi}\Omega_2^* & 0 & 0 \\ e^{-i\varphi}\Omega_2^* & 0 & 0 & 0 \end{pmatrix}. \quad (\text{B2d})$$

The interpretation of these matrices is simple:  $A_{\text{free}}$  characterizes the ion level without interaction,  $A_{\text{par}}$  the coupling of the levels with no spin flip, and  $A_{\text{cross}}$  the interaction with a spin flip. To conduct our study, we will first diagonalize the sum  $A_{\text{free}} + A_{\text{par}}$  alone and see in which regime  $A_{\text{cross}}$  remains unchanged by this diagonalization process.

It is straightforward to see that

$$A_{\text{free}} + A_{\text{par}} = \begin{pmatrix} \Delta + \delta_s & e^{i\varphi}\Omega_1 & 0 & 0 \\ e^{-i\varphi}\Omega_1^* & -\Delta + \delta_g & 0 & 0 \\ 0 & 0 & \Delta - \delta_s & e^{i\varphi}\Omega_1^* \\ 0 & 0 & e^{-i\varphi}\Omega_1 & -\Delta - \delta_g \end{pmatrix} \quad (\text{B3})$$

has the eigenvalues

$$\zeta_1^0 = \frac{1}{2} \left( \delta_s + \delta_g + \sqrt{(2\Delta + \delta_s - \delta_g)^2 + 4|\Omega_1|^2} \right), \quad (\text{B4a})$$

$$\zeta_2^0 = \frac{1}{2} \left( \delta_s + \delta_g - \sqrt{(2\Delta + \delta_s - \delta_g)^2 + 4|\Omega_1|^2} \right), \quad (\text{B4b})$$

$$\zeta_3^0 = -\frac{1}{2} \left( \delta_s + \delta_g - \sqrt{(2\Delta + \delta_g - \delta_s)^2 + 4|\Omega_1|^2} \right), \quad (\text{B4c})$$

$$\zeta_4^0 = -\frac{1}{2} \left( \delta_s + \delta_g + \sqrt{(2\Delta + \delta_g - \delta_s)^2 + 4|\Omega_1|^2} \right), \quad (\text{B4d})$$

and corresponding eigenvectors

$$\mathcal{P}_1 = \begin{pmatrix} \cos \theta_1 & -e^{i(\varphi+\phi_1)} \sin \theta_1 & 0 & 0 \\ e^{-i(\varphi+\phi_1)} \sin \theta_1 & \cos \theta_1 & 0 & 0 \\ 0 & 0 & \cos \theta_2 & -e^{i(\varphi-\phi_1)} \sin \theta_2 \\ 0 & 0 & e^{-i(\varphi-\phi_1)} \sin \theta_2 & \cos \theta_2 \end{pmatrix}, \quad (\text{B5})$$

where

$$\cos \theta_1 = \frac{2\Delta + \delta_s - \delta_g + \sqrt{(2\Delta + \delta_s - \delta_g)^2 + 4|\Omega_1|^2}}{N_1}, \quad (\text{B6a})$$

$$\sin \theta_1 = \frac{2|\Omega_1|}{N_1}, \quad (\text{B6b})$$

$$\cos \theta_2 = \frac{2\Delta + \delta_g - \delta_s + \sqrt{(2\Delta + \delta_g - \delta_s)^2 + 4|\Omega_1|^2}}{N_2}, \quad (\text{B6c})$$

$$\sin \theta_2 = \frac{2|\Omega_1|}{N_2}, \quad (\text{B6d})$$

$e^{i\phi_1} = u_1/|u_1|$ ,  $N_1$ , and  $N_2$  are real normalization factors. As an indication, these four eigenvalues are represented with colored dashed lines in Fig. 3 in the main text. An important point is that the two eigenvalues  $\zeta_2^0$  and  $\zeta_3^0$  have the possibility to cross at the point where

$$|\Omega_1|^2 + 4\Delta^2 \frac{\delta_s \delta_g}{(\delta_s + \delta_g)^2} = \delta_s \delta_g. \quad (\text{B7})$$

Another way of formulating (B7) is that the two eigenvalues cross for a magnetic field of amplitude

$$B_{\text{DC}} = \sqrt{\frac{|\Omega_1|^2}{g_s g_g} + \frac{4\Delta^2}{(g_s + g_g)^2}}, \quad (\text{B8})$$

where  $g_i$  is the effective gyromagnetic ratio of state  $i$ .

If we now add the cross-interaction term  $A_{\text{cross}}$ , the eigenvalues will be modified. This modification will be noticeable only at the point where the  $\zeta_i^0$  values cross, that is, at zero field and at the crossing point. In general,  $A_{\text{cross}}$  is modified according to

$$\mathcal{P}_1^{-1} A_{\text{cross}} \mathcal{P}_1 = \begin{pmatrix} 0 & R \\ R^\dagger & 0 \end{pmatrix}, \quad (\text{B9})$$

where

$$R = \Omega_2 \begin{pmatrix} e^{i\phi_1} \sin(\theta_2 - \theta_1) & e^{i\varphi} \cos(\theta_2 - \theta_1) \\ -e^{-i\varphi} \cos(\theta_2 - \theta_1) & e^{-i\phi_1} \sin(\theta_2 - \theta_1) \end{pmatrix}. \quad (\text{B10})$$

The cross-interaction matrix  $A_{\text{cross}}$  can then be considered as unchanged by the transformation  $\mathcal{P}_1$  in the condition where the ratio between the diagonal terms and the antidiagonal ones in  $R$  is  $\ll 1$ . This can simply be rewritten as  $|\tan(\theta_1 - \theta_2)| \ll$

1, which translates as

$$\frac{|\Omega_1| |\delta_s - \delta_g|}{\delta_s \delta_g} \ll 1, \quad (\text{B11})$$

which at the crossing point can be rewritten, thanks to (B8) like

$$Q = \frac{(g_s - g_g)^2}{g_s g_g + \frac{4\Delta^2 g_s^2 g_g^2}{|\Omega_1|^2 (g_s + g_g)^2}} \ll 1. \quad (\text{B12})$$

This condition is the one given in the body of the text, with  $\Delta = 0$ . When  $A_{\text{cross}}$  can be considered as unchanged by the  $\mathcal{P}_1$  matrix, the eigenvalues of  $A'$  are simple to calculate and can be approximated by

$$\zeta_1 = \frac{1}{2} \left( \zeta_1^0 + \zeta_4^0 + \sqrt{(\zeta_1^0 - \zeta_4^0)^2 + 4|\Omega_2|^2} \right), \quad (\text{B13a})$$

$$\zeta_2 = \frac{1}{2} \left( \zeta_2^0 + \zeta_3^0 + \sqrt{(\zeta_2^0 - \zeta_3^0)^2 + 4|\Omega_2|^2} \right), \quad (\text{B13b})$$

$$\zeta_3 = \frac{1}{2} \left( \zeta_2^0 + \zeta_3^0 - \sqrt{(\zeta_2^0 - \zeta_3^0)^2 + 4|\Omega_2|^2} \right), \quad (\text{B13c})$$

$$\zeta_4 = \frac{1}{2} \left( \zeta_1^0 + \zeta_4^0 - \sqrt{(\zeta_1^0 - \zeta_4^0)^2 + 4|\Omega_2|^2} \right). \quad (\text{B13d})$$

Notice that we have not performed perturbation theory on  $\Omega_2$ : the results presented here hold for arbitrary values of  $\Omega_2$ . However, the reasoning that we have applied here is not symmetric in  $\Omega_1$  and  $\Omega_2$  as seen with Eqs. (B13): the reason for this is that condition (B12) introduces some asymmetry in the role of  $\Omega_1$  and  $\Omega_2$ . Namely, if one first diagonalizes  $A_{\text{free}} + A_{\text{cross}}$ ,  $A_{\text{par}}$  will be strongly affected by the transformation.

As a sanity check, let us ensure that condition (B12) is relevant for the approximation of the eigenvalues of  $A'$ . The most sensitive eigenvalues are the one that are the most affected by the avoided crossing, namely,  $\zeta_2$  and  $\zeta_3$ . Following this remark, Fig. 11(a) shows the relative distance between  $\zeta_2$  given by (B13b) with the actual second eigenvalue of  $A'$ :  $|\zeta_2 - \text{eig}_2(A')|/\zeta_2$  as a function of  $\varphi_{\text{DC}}$  and  $\theta_{\text{DC}}$ , angles of the  $\mathbf{B}_{\text{DC}}$  field, in the same practical case as in Sec. III, for site I of  $^{151}\text{Eu}^{3+}$ :  $\text{Y}_2\text{SiO}_5$  for the  $^7\text{F}_0 | \pm 3/2 \rangle_G \leftrightarrow | \pm 1/2 \rangle_G$  nuclear spin transition. On the other hand, if one plots the  $Q$  parameter given by Eq. (B12), one obtains the dependency shown in Fig. 11(b). The similarity of the two plots clearly validates the condition that we have found.

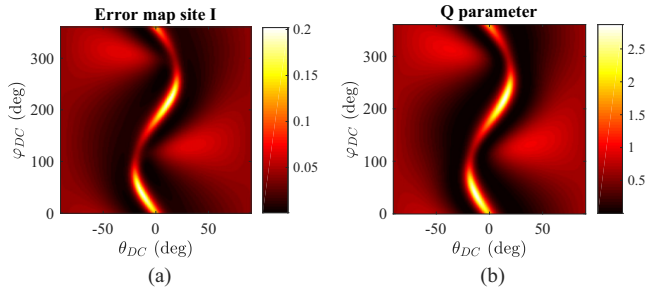


FIG. 11. Validity of condition (B12) for site I [44] of our system. (a) Relative error  $|\zeta_2 - \text{eig}_2(A')|/\zeta_2$  between estimated [ $\zeta_2$ , given by Eq. (B13b)] and actual [ $\text{eig}_2(A')$ ] second eigenvalue. A maximal relative error of  $\sim 20\%$  can be seen. (b) Q parameter (B12). As expected, when the condition is not well satisfied (large  $Q$ ), the relative error on the eigenvalue is maximal.

### APPENDIX C: EXPRESSION OF THE PROPAGATOR AT LOW FIELD

In this Appendix, we derive the expression of the propagator at low field. To simplify the calculations, we place ourselves in the resonant case ( $\Delta = 0$ ).

$$\mathcal{P}_2 = \begin{pmatrix} \cos \theta_4 & 0 & 0 & -e^{i(\phi_2+\varphi)} \sin \theta_4 \\ 0 & \cos \theta_3 & -e^{i(\phi_2-\varphi)} \sin \theta_3 & 0 \\ 0 & e^{-i(\phi_2-\varphi)} \sin \theta_3 & \cos \theta_3 & 0 \\ e^{-i(\phi_2+\varphi)} \sin \theta_4 & 0 & 0 & \cos \theta_4 \end{pmatrix}, \quad (\text{C4})$$

where

$$\cos \theta_3 = \frac{-\zeta_2^0 + \sqrt{(\zeta_2^0)^2 + |\Omega_2|^2}}{N_3}, \quad (\text{C5a})$$

$$\sin \theta_3 = \frac{|\Omega_2|}{N_3}, \quad (\text{C5b})$$

$$\cos \theta_4 = \frac{\zeta_1^0 + \sqrt{(\zeta_1^0)^2 + |\Omega_2|^2}}{N_4}, \quad (\text{C5c})$$

$$\sin \theta_4 = \frac{|\Omega_2|}{N_4}, \quad (\text{C5d})$$

and  $e^{i\phi_2} = u_2/|u_2|$ . Now that we have the explicit expression of the matrices, we can write the propagator. However, its general expression without approximation is not so trivial.

$$P \simeq \frac{1}{\sqrt{2}} \begin{pmatrix} c_0 & -c_0 e^{i(\phi_1+\varphi)} & s_0 e^{i(\phi_1+\phi_2)} & -s_0 e^{i(\phi_2+\varphi)} \\ -s_0 e^{-i(\phi_1+\phi_2)} & s_0 e^{-i(\phi_2-\varphi)} & c_0 & -c_0 e^{-i(\phi_1-\varphi)} \\ c_0 e^{-i(\phi_1+\varphi)} & c_0 & -s_0 e^{i(\phi_2-\varphi)} & -s_0 e^{i(\phi_2-\phi_1)} \\ s_0 e^{-i(\phi_2+\varphi)} & s_0 e^{-i(\phi_2-\phi_1)} & c_0 e^{i(\phi_1-\varphi)} & c_0 \end{pmatrix} \quad (\text{C8})$$

and

$$\exp\left(\frac{i}{2}Dt\right) \simeq \begin{pmatrix} e^{\frac{i}{2}\Omega_0 t} e^{\frac{i}{2}\epsilon|\Omega_1|t} & 0 & 0 & 0 \\ 0 & e^{-\frac{i}{2}\Omega_0 t} e^{\frac{i}{2}\epsilon|\Omega_1|t} & 0 & 0 \\ 0 & 0 & e^{\frac{i}{2}\Omega_0 t} e^{-\frac{i}{2}\epsilon|\Omega_1|t} & 0 \\ 0 & 0 & 0 & e^{-\frac{i}{2}\Omega_0 t} e^{-\frac{i}{2}\epsilon|\Omega_1|t} \end{pmatrix}. \quad (\text{C9})$$

Given that the Schrödinger equation simply reduces to (11), the propagator reads

$$U_{\text{prop}} = e^{iAt/2} = P \cdot e^{iDt/2} \cdot P^{-1}, \quad (\text{C1})$$

where  $P$  is the transfer matrix that diagonalizes  $A$  to  $D$ :

$$D = \begin{pmatrix} \zeta_1 & 0 & 0 & 0 \\ 0 & \zeta_3 & 0 & 0 \\ 0 & 0 & \zeta_2 & 0 \\ 0 & 0 & 0 & \zeta_4 \end{pmatrix} = \begin{pmatrix} \zeta_1 & 0 & 0 & 0 \\ 0 & \zeta_3 & 0 & 0 \\ 0 & 0 & -\zeta_3 & 0 \\ 0 & 0 & 0 & -\zeta_1 \end{pmatrix}. \quad (\text{C2})$$

Remember that the eigenvalues obtained in Appendix B are the ones of  $A'$ , for which vectors 2 and 3 were exchanged (we note the corresponding flip matrix  $\mathcal{P}_{23}$ ), hence a change in the indexes of the eigenvalues in  $D$ . Then, at zero detuning, we simply have  $\zeta_2 = -\zeta_3$  and  $\zeta_4 = -\zeta_1$ . The transfer matrix is then given by

$$P = \mathcal{P}_{23}\mathcal{P}_1\mathcal{P}_2, \quad (\text{C3})$$

where  $\mathcal{P}_1$  is given in Eq. (B5) and  $\mathcal{P}_2$  is the transfer matrix from the base in which  $A_{\text{free}} + A_{\text{par}}$  is diagonal to the base where  $A'$  is diagonal. In the case  $\Delta = 0$ , it simply reads

As we are interested in its expression at low fields, we can consider that  $\epsilon = \frac{\delta_g + \delta_c}{2\Omega_0} \ll 1$ . Under this approximation,

$$\zeta_1 \simeq \Omega_0 + \epsilon|\Omega_1|, \quad (\text{C6a})$$

$$\zeta_3 \simeq -\Omega_0 + \epsilon|\Omega_1|, \quad (\text{C6b})$$

$$\cos \theta_1 \simeq \cos \theta_2 \simeq \sin \theta_1 \simeq \sin \theta_2 \simeq 1/\sqrt{2}, \quad (\text{C7a})$$

$$\cos \theta_3 \simeq \cos \theta_4 \simeq \frac{\Omega_0 + |\Omega_1|}{\sqrt{2\Omega_0(\Omega_0 + |\Omega_1|)}} := c_0 = \sqrt{\frac{1}{2}}\sqrt{1 + |u_1|}, \quad (\text{C7b})$$

$$\sin \theta_3 \simeq \sin \theta_4 \simeq \frac{|\Omega_2|}{\sqrt{2\Omega_0(\Omega_0 + |\Omega_1|)}} := s_0 = \sqrt{\frac{1}{2}}\sqrt{1 - |u_1|}. \quad (\text{C7c})$$

The transfer matrix then simply reads

Injecting (C8) and (C9) into (C3) and (C1), we get the expression of the propagator,

$$U_{\text{prop}}(t) \simeq \cos\left(\frac{\epsilon|\Omega_1|t}{2}\right)U_0(t) + \sin\left(\frac{\epsilon|\Omega_1|t}{2}\right)U_{\text{pert}}(t), \quad (\text{C10})$$

with  $U_0(t)$  the propagator at zero field:

$$U_0(t) = \cos\left(\frac{\Omega_0 t}{2}\right)\mathbb{1} + i \sin\left(\frac{\Omega_0 t}{2}\right)\begin{pmatrix} 0 & e^{i\varphi}U \\ e^{-i\varphi}U^\dagger & 0 \end{pmatrix} \quad (\text{C11})$$

and

$$U_{\text{pert}}(t) = i \cos\left(\frac{\Omega_0 t}{2}\right)\begin{pmatrix} |u_1| & -u_2 e^{i\phi_1} & 0 & 0 \\ -u_2^* e^{-i\phi_1} & -|u_1| & 0 & 0 \\ 0 & 0 & |u_1| & u_2 e^{-i\phi_1} \\ 0 & 0 & u_2^* e^{i\phi_1} & -|u_1| \end{pmatrix},$$

$$+ \sin\left(\frac{\Omega_0 t}{2}\right)\begin{pmatrix} 0 & 0 & -e^{i(\varphi+\phi_1)} & 0 \\ 0 & 0 & 0 & e^{i(\varphi-\phi_1)} \\ -e^{-i(\varphi+\phi_1)} & 0 & 0 & 0 \\ 0 & e^{-i(\varphi-\phi_1)} & 0 & 0 \end{pmatrix}. \quad (\text{C12})$$

- 
- [1] F. Arute, K. Arya, R. Babbush, D. Bacon, J. C. Bardin, R. Bardens, R. Biswas, S. Boixo, F. G. S. L. Brandao, D. A. Burkett *et al.*, *Nature* **574**, 505 (2019).
- [2] A. Boaron, G. Boso, D. Rusca, C. Vulliez, C. Autebert, M. Caloz, M. Perrenoud, G. Gras, F. Bussi eres, M.-J. Li, D. Nolan, A. Martin, and H. Zbinden, *Phys. Rev. Lett.* **121**, 190502 (2018).
- [3] S.-K. Liao, W.-Q. Cai, W.-Y. Liu, L. Zhang, Y. Li, J.-G. Ren, J. Yiu, Q. Shen, Y. Cao, Z.-P. Li *et al.*, *Nature* **549**, 43 (2017).
- [4] N. Sangouard, C. Simon, H. de Riedmatten, and N. Gisin, *Rev. Mod. Phys.* **83**, 33 (2011).
- [5] K. Heshami, D. G. England, P. C. Humphreys, P. J. Bustard, V. M. Acosta, J. Nunn, and B. J. Sussman, *J. Mod. Opt.* **63**, 2005 (2016).
- [6] A. G. Radnaev, Y. O. Dudin, R. Zhao, H. H. Jen, S. D. Jenkins, A. Kuzmich, and T. A. B. Kennedy, *Nat. Phys.* **6**, 894 (2010).
- [7] A. Nicolas, L. Veissier, L. Giner, E. Giacobino, D. Maxein, and J. Laurat, *Nat. Photonics* **8**, 234 (2014).
- [8] S.-J. Yang, X.-J. Wang, X.-H. Bao, and J.-W. Pan, *Nat. Photonics* **10**, 381 (2016).
- [9] Y.-F. Pu, N. Jiang, W. Chang, H.-X. Yang, C. Li, and L.-M. Duan, *Nat. Commun.* **8**, 15359 (2017).
- [10] L. Tian, Z. Xu, L. Chen, W. Ge, H. Yuan, Y. Wen, S. Wang, S. Li, and H. Wang, *Phys. Rev. Lett.* **119**, 130505 (2017).
- [11] J. J. Longdell, E. Fraval, M. J. Sellars, and N. B. Manson, *Phys. Rev. Lett.* **95**, 063601 (2005).
- [12] I. Usmani, M. Afzelius, H. de Riedmatten, and N. Gisin, *Nat. Commun.* **1**, 12 (2010).
- [13] G. Heinze, C. Hubrich, and T. Halfmann, *Phys. Rev. Lett.* **111**, 033601 (2013).
- [14] K. R. Ferguson, S. E. Beavan, J. J. Longdell, and M. J. Sellars, *Phys. Rev. Lett.* **117**, 020501 (2016).
- [15] A. Seri, A. Lenhard, D. Riel ander, M. G undoĝan, P. M. Ledingham, M. Mazzera, and H. de Riedmatten, *Phys. Rev. X* **7**, 021028 (2017).
- [16] C. Laplane, P. Jobez, J. Etesse, N. Gisin, and M. Afzelius, *Phys. Rev. Lett.* **118**, 210501 (2017).
- [17] A. Holz apfel, J. Etesse, K. T. Kaczmarek, A. Tiranov, N. Gisin, and M. Afzelius, *New J. Phys.* **22**, 063009 (2020).
- [18] M. Afzelius, C. Simon, H. de Riedmatten, and N. Gisin, *Phys. Rev. A* **79**, 052329 (2009).
- [19] M. Zhong, M. P. Hedges, R. L. Ahlefeldt, J. G. Bartholomew, S. E. Beavan, S. M. Wittig, J. J. Longdell, and M. J. Sellars, *Nature* **517**, 177 (2015).
- [20] N. Sinclair, E. Saglamyurek, H. Mallahzadeh, J. A. Slater, M. George, R. Ricken, M. P. Hedges, D. Oblak, C. Simon, W. Sohler, and W. Tittel, *Phys. Rev. Lett.* **113**, 053603 (2014).
- [21] M. Sabooni, Q. Li, S. Kr oll, and L. Rippe, *Phys. Rev. Lett.* **110**, 133604 (2013).
- [22] P. Jobez, I. Usmani, N. Timoney, C. Laplane, N. Gisin, and M. Afzelius, *New J. Phys.* **16**, 083005 (2014).
- [23] E. Fraval, M. J. Sellars, and J. J. Longdell, *Phys. Rev. Lett.* **92**, 077601 (2004).
- [24] J. J. Longdell, A. L. Alexander, and M. J. Sellars, *Phys. Rev. B* **74**, 195101 (2006).
- [25] R. W. Equall, Y. Sun, R. L. Cone, and R. M. Macfarlane, *Phys. Rev. Lett.* **72**, 2179 (1994).
- [26] P. Jobez, N. Timoney, C. Laplane, J. Etesse, A. Ferrier, P. Goldner, N. Gisin, and M. Afzelius, *Phys. Rev. A* **93**, 032327 (2016).
- [27] M. Bonarota, J. Ruggiero, J.-L. Le Gou et, and T. Chanli ere, *Phys. Rev. A* **81**, 033803 (2010).
- [28] P. Jobez, C. Laplane, N. Timoney, N. Gisin, A. Ferrier, P. Goldner, and M. Afzelius, *Phys. Rev. Lett.* **114**, 230502 (2015).
- [29] M. A. Teplov, *Sov. Phys. JETP* **26**, 872 (1968).
- [30] M. Lovri c, P. Glasenapp, and D. Suter, *Phys. Rev. B* **85**, 014429 (2012).
- [31] E. Z. Cruzeiro, J. Etesse, A. Tiranov, P.-A. Bourdel, F. Fr owis, P. Goldner, N. Gisin, and M. Afzelius, *Phys. Rev. B* **97**, 094416 (2018).
- [32] C. Li, C. Wyon, and R. Moncorge, *IEEE J. Quantum Electron.* **28**, 1209 (1992).

- [33] B. Lauritzen, N. Timoney, N. Gisin, M. Afzelius, H. de Riedmatten, Y. Sun, R. M. Macfarlane, and R. L. Cone, *Phys. Rev. B* **85**, 115111 (2012).
- [34] C. Laplane, P. Jobez, J. Etesse, N. Timoney, N. Gisin, and M. Afzelius, *New J. Phys.* **18**, 013006 (2016).
- [35] E. Z. Cruzeiro, F. Fröwis, N. Timoney, and M. Afzelius, *J. Mod. Opt.* **63**, 2101 (2016).
- [36] J. G. Bartholomew, R. L. Ahlefeldt, and M. J. Sellars, *Phys. Rev. B* **93**, 014401 (2016).
- [37] R. Lauro, T. Chanelière, and J.-L. Le Gouët, *Phys. Rev. B* **83**, 035124 (2011).
- [38] L. Rippe, M. Nilsson, S. Kröll, R. Klieber, and D. Suter, *Phys. Rev. A* **71**, 062328 (2005).
- [39] F. de Seze, F. Dahes, V. Crozatier, I. Lorgeré, F. Bretenaker, and J.-L. L. Gouët, *Eur. Phys. J. D* **33**, 343 (2005).
- [40] A. Seri, G. Corrielli, D. Lago-Rivera, A. Lenhard, H. de Riedmatten, R. Osellame, and M. Mazzer, *Optica* **5**, 934 (2018).
- [41] G. Heinze, S. Mieth, and T. Halfmann, *Phys. Rev. A* **84**, 013827 (2011).
- [42] B. Car, J.-L. Le Gouët, and T. Chanelière, *Phys. Rev. B* **102**, 115119 (2020).
- [43] E. Fraval, M. Sellars, A. Morrison, and A. Ferris, *J. Lumin.* **107**, 347 (2004).
- [44] R. Yano, M. Mitsunaga, and N. Uesugi, *Opt. Lett.* **16**, 1884 (1991).

## **A.4 Paper IV: Storage of photonic time bin qubits up to 20 ms in a rare-earth doped crystal**



# Storage of photonic time-bin qubits for up to 20 ms in a rare-earth doped crystal

Antonio Ortu,<sup>1</sup> Adrian Holzäpfel,<sup>1</sup> Jean Etesse,<sup>2</sup> and Mikael Afzelius<sup>1</sup>

<sup>1</sup>*Département de Physique Appliquée, Université de Genève, CH-1211 Genève, Switzerland*

<sup>2</sup>*Université côte d'Azur, CNRS, Institut de Physique de Nice (INPHYNI), UMR 7010, Parc Valrose, Nice Cedex 2, France*

(Dated: September 15, 2021)

Long-duration quantum memories for photonic qubits are essential components for achieving long-distance quantum networks and repeaters. The mapping of optical states onto coherent spin-waves in rare earth ensembles is a particularly promising approach to quantum storage. However, it remains challenging to achieve long-duration storage at the quantum level due to read-out noise caused by the required spin-wave manipulation. In this work, we apply dynamical decoupling techniques and a small magnetic field to achieve the storage of six temporal modes for 20, 50 and 100 ms in a  $^{151}\text{Eu}^{3+}:\text{Y}_2\text{SiO}_5$  crystal, based on an atomic frequency comb memory, where each temporal mode contains around one photon on average. The quantum coherence of the memory is verified by storing two time-bin qubits for 20 ms, with an average memory output fidelity of  $F = (85 \pm 3)\%$  for an average number of photons per qubit of  $\mu = 0.92 \pm 0.04$ . The qubit analysis is done at the read-out of the memory, using a novel composite adiabatic read-out pulse.

## INTRODUCTION

The realization of quantum repeaters<sup>1-3</sup>, and more generally quantum networks, is a long-standing goal in quantum communication. It will enable long-range quantum entanglement distribution, long-distance quantum key distribution (QKD), distributed quantum computation and quantum simulation<sup>4</sup>. Many schemes of quantum repeaters rely on the heralding of entanglement between quantum nodes in elementary links<sup>2,5</sup>, followed by local swapping gates<sup>1</sup> to extend the entanglement. The introduction of atomic ensembles as repeater nodes, and the use of linear optics for the entanglement swapping, stems from the seminal DLCZ proposal<sup>2</sup>. A key advantage of atomic ensembles is their ability to store qubits in many modes through multiplexing<sup>6-12</sup>, which is crucial for distributing entanglement efficiently and with practical rates<sup>13</sup>.

Rare-earth-ion (RE) doped crystals provide a solid-state approach for ensemble-based quantum nodes. RE doped crystals can provide multiplexing in different degrees of freedom<sup>8,9,11,14-16</sup>, efficient storage<sup>17,18</sup>, and long coherence time of hyperfine states, allowing<sup>19-22</sup> long-duration and on-demand storage of optical quantum states. The longest reported storage time of optical states with mean photon number of around 1 in RE doped solids is about 1 ms in  $^{151}\text{Eu}^{3+}:\text{Y}_2\text{SiO}_5$ <sup>23</sup>. However, even near-term quantum repeaters spanning distances of 100 km or above would certainly require storage times of at least 10 ms, and more likely of hundreds of ms<sup>24</sup>. A particular challenge of long duration quantum storage in RE systems is noise introduced by the application of the dynamical decoupling (DD) sequences that are required to overcome the inhomogeneous spin dephasing<sup>23</sup> and the spectral diffusion<sup>20,22</sup>. To reduce the noise one can apply error-compensating DD sequences<sup>25</sup>, or increase the spin coherence time by applying magnetic fields to reduce the required number of pulses<sup>20,26,27</sup>.

In this article we report on an atomic frequency comb (AFC) spin-wave memory in  $^{151}\text{Eu}^{3+}:\text{Y}_2\text{SiO}_5$ , in which

we demonstrate storage of 6 temporal modes with mean photon occupation number  $\mu = 0.711 \pm 0.006$ /mode for a duration of 20 ms using a XY-4 DD sequence with 4 pulses. The output signal-to-noise (SNR) ratio is  $7.4 \pm 0.5$ , for a storage efficiency of  $\eta_s = 7\%$ . To reach this result we applied a small magnetic field of 1.35 mT in a specific direction, which increases the spin coherence time from a few ms to 70 ms. By applying a longer DD sequence of 16 pulses (XY-16) we demonstrate storage with  $\mu = 1.062 \pm 0.007$ /mode for a duration of 100 ms, with a SNR of  $2.5 \pm 0.2$  and an efficiency of  $\eta_s = (2.60 \pm 0.02)\%$ . In addition we stored two time-bin qubits for 20 ms and performed a quantum state tomography of the output state, showing a fidelity of  $F = (84 \pm 3)\%$  for  $\mu = 0.92 \pm 0.04$  photons per qubit. To analyse the qubit we propose a composite adiabatic control pulse that projects the output qubit on superposition states of the time-bin modes. The current limit in storage time is technical, due to heating effects in the cryo cooler caused by the high peak power of the DD pulses. The measured spin coherence time as a function of the DD pulse number  $n_p$  follows closely the expected  $n_p^{2/3}$  dependence, which suggests that considerably longer storage times are within reach with some engineering efforts.

## RESULTS

The platform for our quantum memory is a  $^{151}\text{Eu}^{3+}:\text{Y}_2\text{SiO}_5$  crystal with an energy structure at zero magnetic field as in figure 1a. The excited and ground states can be connected via optical transitions at about 580 nm<sup>28</sup>. The quadrupolar interaction due to the effective nuclear spin  $I = 5/2$  of the  $\text{Eu}^{3+}$  ions generates three doublets in both the ground and excited states, separated by tens of MHz. This structure allows to choose a  $\Lambda$ -system with a first ground state  $|g\rangle$  into which the population is initialized, connected to an excited state  $|e\rangle$  for optical absorption of the input light, and a second

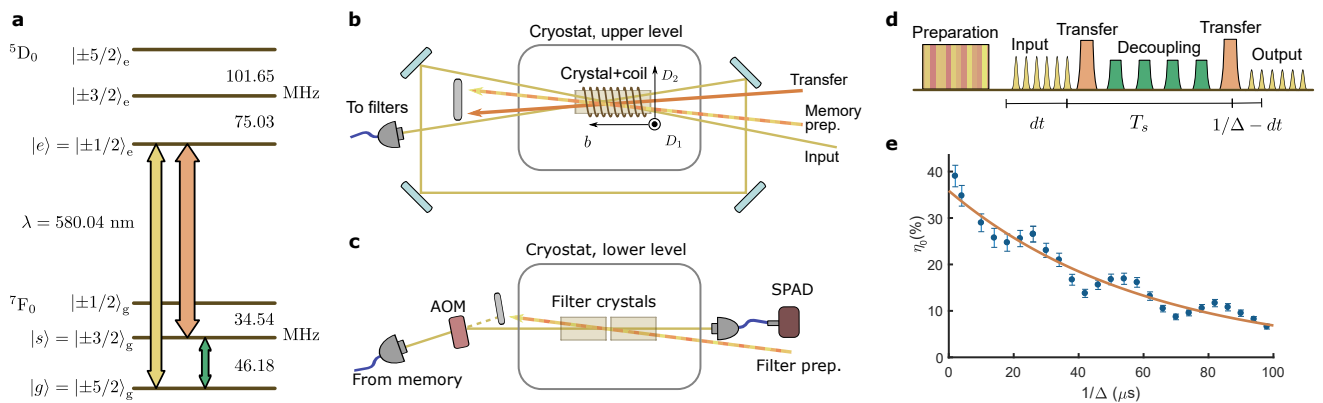


FIG. 1. **System and setup** (a) Atomic energy structure of  $^{151}\text{Eu}^{3+}:\text{Y}_2\text{SiO}_5$  and transitions used in the memory protocol. (b) and (c), sketches of the experimental setup around the memory and filter crystals, respectively. The crystals are glued on a custom mount with two levels at different heights, in the same cryostat. The memory crystal is at the center of a small coil used to generate the RF signal. A larger coil (not shown) on top of the cryostat generates a static magnetic field along the  $D_1$  axis of the  $\text{Y}_2\text{SiO}_5$  crystal. Optical beams are depicted with exaggerated angles for clarity. AOM: acousto-optic modulator; SPAD: single photon avalanche diode (d) Sketch of the time sequence of pulses used for multimode spin-storage. (e) AFC efficiency measured as a function of AFC time  $1/\Delta$ , with bright input pulses and magnetic field of 1.35 mT along  $D_1$ . The solid line indicates the exponential fit resulting in zero-time efficiency  $\eta_0 = (36 \pm 3)\%$  and effective coherence time  $T_2^{\text{AFC}} = (240 \pm 30) \mu\text{s}$  (see text for details).

ground state  $|s\rangle$  for on-demand long-time storage.

The full AFC-spin wave protocol<sup>7,29</sup>, sketched in figure 1d, begins by initializing the memory so to have a comb-like structure in the frequency domain with periodicity  $\Delta$  on  $|g\rangle$  and an empty  $|s\rangle$  state, via an optical preparation beam (see figure 1b). The initialization step closely follows the procedure outlined by Jobez et al.<sup>30</sup>. The photons to be stored are sent along the input path and are absorbed by the AFC on the  $|g\rangle \leftrightarrow |e\rangle$  transition, leading to a coherent superposition in the atomic ensemble. The AFC results in a rephasing of the atoms after a duration  $1/\Delta$ , while normally they would dephase quickly due to the inhomogeneous broadening. Before the AFC echo emission, the excitation is transferred to the storage state  $|s\rangle$  via a strong transfer pulse. The radio-frequency (RF) field at 46.18 MHz then dynamically decouples the spin coherence from external perturbations and compensates for the spin dephasing induced by the inhomogeneous broadening of the spin transition  $|g\rangle \leftrightarrow |s\rangle$ . In our particular crystal, the shape of the spin transition absorption line is estimated to be Gaussian with a width of about 60 kHz (see supplementary materials for details). A second strong optical pulse transfers the coherent atoms back into the  $|e\rangle$  state, after which the AFC phase evolution concludes with an output emission along  $|e\rangle \rightarrow |g\rangle$ .

To implement the memory scheme, a coherent and powerful laser (1.8 W) at 580 nm is generated by amplifying and frequency doubling a 1160 nm laser that is locked on a high-finesse optical cavity<sup>31</sup>. The 580 nm beam traverses a cascade of bulk acousto-optic modulators (AOM), each controlling an optical channel of the experiment, namely optical transfer, memory prepara-

tion, filter preparation and input. The optical beams and the main elements of the setup are represented in figure 1b, c. A memory and two filtering crystals are cooled down in the same closed-cycle helium cryostat to  $\sim 4\text{K}$ , placed on two levels of a single custom mount. The 1.2 cm long memory crystal is enveloped by a coil of the same length to generate the RF field. Another larger coil is placed outside the cold chamber and used to generate a static magnetic field. After the cryostat, the light in the input path can be detected either by a linear Si photodiode for experiments with bright pulses, or by a Si single photon avalanche diode (SPAD) detector for weak pulses at the single photon-level. For photon counting it is necessary to use a filtering setup (figure 1c) to block any scattered light and noise generated by the second transfer pulse. Another AOM acts as a temporal gate, before passing the beam through two filtering crystals that are optically pumped so to have a transmission window around the input photon frequency and maximum absorption corresponding to the transfer pulse transition.

The  $^{151}\text{Eu}^{3+}:\text{Y}_2\text{SiO}_5$  crystals are exposed to a small static magnetic field along the crystal  $D_1$  axis<sup>32</sup>. At zero magnetic field, the protocol enabled to achieve storage of multiple coherent single photon-level pulses up to about 1 ms<sup>23</sup>. However, it has been shown that even a weak magnetic field can increase the coherence lifetime<sup>22,33–35</sup>, which motivated us to use a  $\sim 1.35\text{ mT}$  field along the  $D_1$  axis<sup>27</sup>.

The AFC spin-wave memory consists of three distinct processes: the AFC echo, the transfer pulses and the RF sequence, and each process introduces a set of parameters that will need to be optimized globally in order to achieve

the best possible SNR, multimode capacity and storage time. Below we briefly describe some of the constraints leading to the particular choice of parameters used in these experiments.

The maximum AFC spin-wave efficiency is limited by the AFC echo efficiency for a certain  $1/\Delta$ , which typically decreases exponentially as a function of  $1/\Delta$ . We can define an effective AFC coherence lifetime  $T_2^{\text{AFC}}$  and efficiency  $\eta_{\text{AFC}}$  as  $\eta_{\text{AFC}} = \eta_0 \exp(-4/(\Delta T_2^{\text{AFC}}))$ <sup>30</sup>, where  $\eta_0$  depends on the optical depth and the AFC parameters. With an external magnetic field of 1.35 mT  $\parallel D_1$ , we obtained  $T_2^{\text{AFC}} = (240 \pm 30) \mu\text{s}$  with an extrapolated zero-time efficiency of  $\eta_0 = (36 \pm 3) \%$ , see figure 1e. The  $\eta_0$  efficiency is consistent with the initial optical depth of 6 in our double-pass input configuration (each pass provides an optical depth of about 3). The data also shows a modulation of the efficiency dependent on the external magnetic field, which is an effect of the Zeeman splitting onto the AFC preparation process<sup>27</sup>. Whenever the comb periodicity is a multiple of the excited state splitting, the optical depth of the prepared AFC is reduced. The inverse of the observed modulation period of approximately 25  $\mu\text{s}$  matches well the expected Zeeman splitting of  $|e\rangle - 30.64 \text{ MHz/T} \cdot 1.35 \text{ mT} \approx 41.4 \text{ kHz}$ <sup>36</sup>. The exponential decay implies that there is a trade-off between the memory efficiency (favoring short  $1/\Delta$ ) and temporal multimode capacity (favoring long  $1/\Delta$ ). In addition we must consider the shortest input duration that can be stored, which is limited by the effective memory bandwidth.

The optical transfer pulses should ideally perform a perfect coherent population inversion between states  $|e\rangle$  and  $|s\rangle$ , uniformly over the entire bandwidth of the input pulse. Efficient inversion with a uniform transfer probability in frequency space can be achieved by adiabatic, chirped pulses<sup>37</sup>. Here we employ two HSH pulses proposed by Tian et al.<sup>38</sup>, which are particularly efficient given a limitation in pulse duration. For a fixed Rabi frequency the bandwidth of the pulse can be increased by increasing the pulse duration<sup>37</sup>, which however reduces the multimode capacity of the AFC spin-wave memory.

Considering as a priority to preserve the storage efficiency while still being able to store several time modes, we set  $1/\Delta = 25 \mu\text{s}$ , corresponding to the first maximum (with efficiency 28%) on the AFC echo decay curve in figure 1e. Given the  $1/\Delta$  delay, we optimized the HSH control pulse duration, leading to a bandwidth of 1.5 MHz for a HSH pulse duration of 15  $\mu\text{s}$ . The remaining 10  $\mu\text{s}$  were used to encode 6 temporal modes, giving a mode duration of  $T_m = 1.65 \mu\text{s}$ . Each mode contained a Gaussian pulse with a full-width at half-maximum of about 700 ns.

The RF sequence compensates for the inhomogeneous spin dephasing and should ideally reduce the spectral diffusion due to spin-spin interactions through dynamical decoupling (DD)<sup>22,39-41</sup>. However, effective dynamical decoupling requires many pulses, with pulse separations less than the characteristic time of the spin fluctuations. Pulse errors can then introduce noise at the

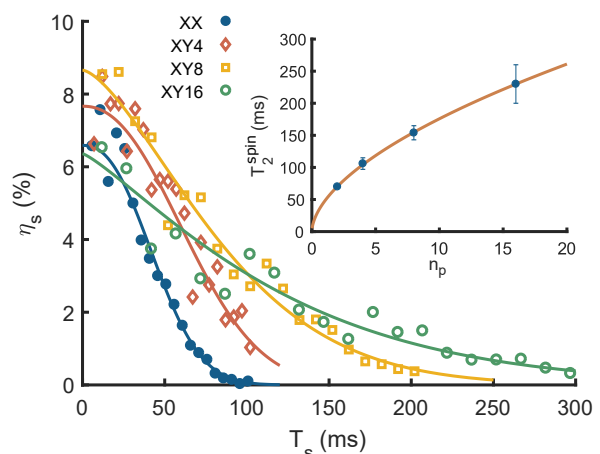


FIG. 2. **Spin storage coherence time.** Spin storage efficiency as a function of storage time for four different dynamical decoupling sequences. The solid lines are fits of the Mims model with  $\eta_s(0)$ ,  $T_2^{\text{spin}}$  and  $m$  as free parameters (see text for details). Inset: spin effective coherence time as a function of the number of pulses  $n_p$  in the DD sequence. The solid line is a fit to a power law as described in the main text.

memory output<sup>23</sup>, which in principle can be reduced by using error-compensating DD sequences<sup>25</sup>. In practice, however, other factors such as heating of the crystal due to the intense RF pulses limit the effectiveness of such sequences, and noise induced by the RF sequence is the main limitation in SNR of long-duration AFC spin-wave memories<sup>9,23,42</sup>.

We first present a characterization of the memory using bright input pulses and a linear Si photodiode, implementing four decoupling sequences with a number of pulses ranging from a minimum of 2 to a maximum of 16. Figure 2 displays the resulting efficiency decay curves as a function of the time  $T_s$  spent by the atoms in the spin transition, which corresponds to the time difference between the two optical transfer pulses. The solid lines show fits obtained from a Mims model, which takes into account the effect of spectral diffusion<sup>43</sup> according to the relation  $\eta_s(T_s) = \eta_s(0) \exp[-2(T_s/T_2^{\text{spin}})^m]$ , where  $T_2^{\text{spin}}$  is the effective spin coherence time, and  $m$  the Mims factor.

We extracted effective coherence times of  $70 \pm 2$ ,  $106 \pm 9$ ,  $154 \pm 11$  and  $(230 \pm 30) \text{ ms}$  respectively for XX, XY-4, XY-8 and XY-16 sequences, which show a clear decoupling effect as more pulses are added. This is also confirmed by the expected change of  $T_2^{\text{spin}}$  as a function of  $n_p$  visible in the inset of figure 2, which closely follows a power-law relation  $T_2^{\text{spin}}(n_p) = T_2^{\text{spin}}(1) n_p^{\gamma_p}$  with  $\gamma_p = 0.57 \pm 0.03$  and  $T_2^{\text{spin}}(1) = (47 \pm 2) \text{ ms}$ , as expected for a Ornstein-Uhlenbeck spectral diffusion process<sup>40,41,44</sup>. A similar scaling was obtained in Holzäpfel et al.<sup>22</sup>, using a slightly different experimental setup, magnetic field and  $\Lambda$ -system, which indicates that much

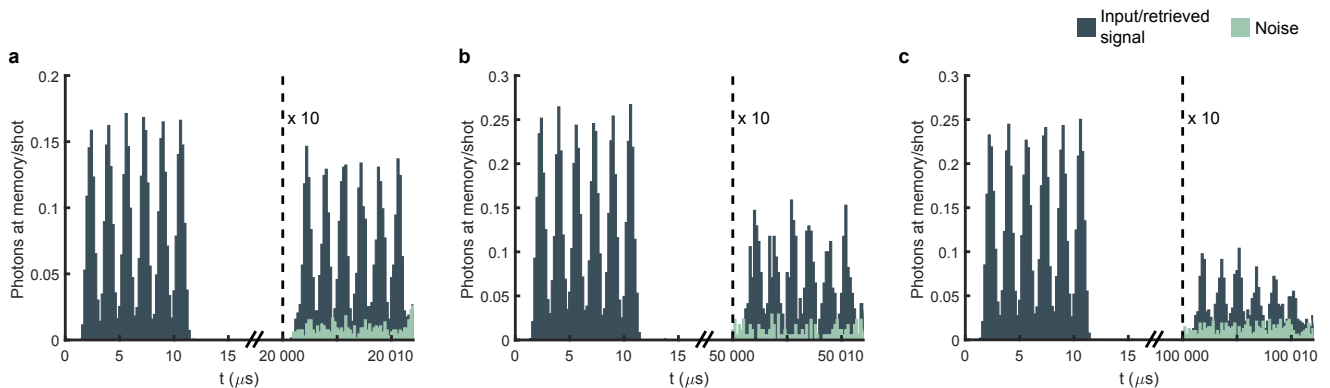


FIG. 3. **Single photon-level spin storage.** Examples of spin storage at 20 ms (a), 50 ms (b) and 100 ms (c). The dark blue histogram shows the input pulses (left of each figure) and the retrieved signal. Light orange histograms display the noise floor. Each signal peak is at the center of a  $1.65 \mu\text{s}$  time mode. The average sum of the counts in one input mode is close to 1 (see table I and the supplementary materials for details).

$T_s$ (ms)	$\mu_{\text{in}}$	$p_N$	$\eta$ (%)	SNR	$\mu_1$
20	$0.711 \pm 0.006$	$0.0073 \pm 0.0012$	$7.39 \pm 0.04$	$7.4 \pm 0.5$	$0.098 \pm 0.002$
50	$1.21 \pm 0.01$	$0.009 \pm 0.002$	$4.37 \pm 0.04$	$5.6 \pm 0.7$	$0.218 \pm 0.008$
100	$1.062 \pm 0.007$	$0.0110 \pm 0.0015$	$2.60 \pm 0.02$	$2.5 \pm 0.2$	$0.445 \pm 0.008$

TABLE I. **Summary of single photon-level storage.** Values of input mean photon number  $\mu_{\text{in}}$ , storage efficiency  $\eta$ , signal-to-noise ratio SNR and the equivalent mean input photon number for SNR=1,  $\mu_1$ , for different spin-wave storage times  $T_s$ . The reported values are averages over the 6 temporal modes, and the value for each mode stems from the summed counts over the mode size  $T_m$ . See also methods for details.

longer storage times could be achieved. However, adding more pulses for the same storage times introduces additional heating, causing temperature-dependent frequency shifts of the optical transition<sup>28,45</sup>. This technical issue could be addressed in the future by optimizing the heat dissipation in proximity of the crystal. The extrapolated zero-time efficiencies vary between 6 and 9%, and the data appears relatively scattered around the fitted curves for the longer decoupling sequences. These two observations might be a sign of the presence of beats originating in the different phase paths available to the atoms during storage, due to the small Zeeman splitting of the ground state doublets in this regime of weak magnetic field. Similar effects have been shown in a more detailed model of interaction between a system with splittings smaller than the RF pulses chirp<sup>27</sup>.

We now discuss the memory performance at the single photon level. The dark histograms in figure 3 show three examples of spin storage outputs with their respective input modes for reference. The lighter histograms show the noise background, measured while executing the complete memory scheme without any input light (see methods section for details). This noise floor, when integrated over the mode size  $T_m$ , gives us the noise probability  $p_N$ . When compared to the sum of the counts in the retrieved signal in the mode, the summed noise count is well below the retrieved signal for all the storage times here reported. We used an XY-4 type of RF

sequence for storage at 20 ms, XY-8 for 50 ms and XY-16 for 100 ms. Table I summarizes the relevant results, in particular with SNR values ranging from 7.4 to 2.5 for 20 ms and 100 ms respectively. The average input photon number per time mode  $\mu_{\text{in}}$  is close to 1 in all cases, although it varies slightly. To account for this, an independent figure of merit is the parameter  $\mu_1 = p_N/\eta$ , which corresponds to the average input photon number that would give an SNR of 1 in output<sup>46</sup>. Since it scales as the inverse of the efficiency<sup>23</sup>, it increases with storage time, but for all cases studied here it is well below 1.

The noise probability  $p_N$  varied from  $7 \cdot 10^{-3}$  to  $11 \cdot 10^{-3}$ , see Table I, similar to previous experiments<sup>23</sup>. An independent noise measurement at 20 ms showed that the XX, XY-4 and XY-8 resulted in almost identical noise values of  $p_N = 7.4 \cdot 10^{-3}$ ,  $8.1 \cdot 10^{-3}$  and  $8.6 \cdot 10^{-3}$  (error  $\pm 0.3 \cdot 10^{-3}$ ), respectively. This shows that pulse area errors are effectively suppressed by the higher order DD sequences, and that the read-out noise is caused by other types of errors, which at this point are not well understood.

If compared with the efficiencies measured with bright pulses in figure 2, the storage efficiency measured at the single photon-level is noticeably lower for 50 and 100 ms. We believe this is due to the long measurement times required for accumulating the necessary statistics, which exposes the experiment to long-term fluctuations affecting optical alignment in general and specifically fiber cou-

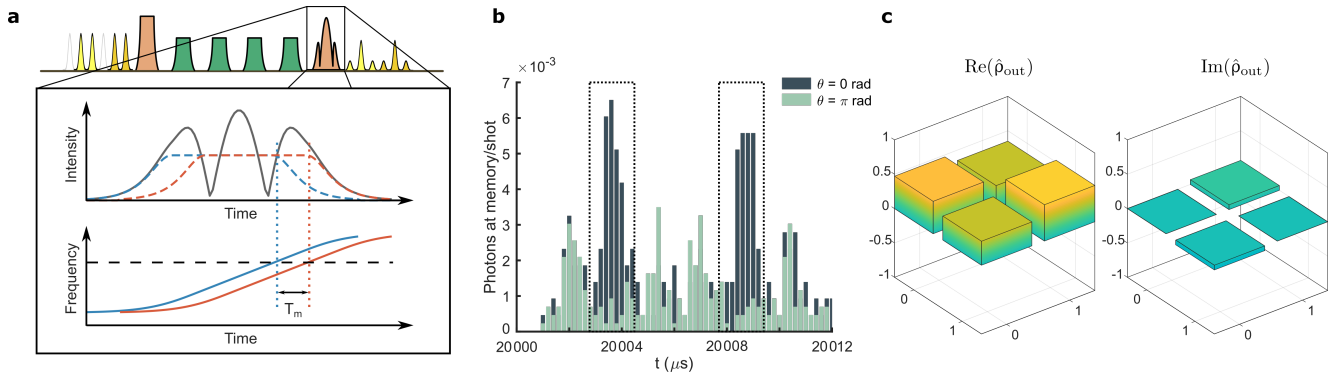


FIG. 4. **Qubit tomography** (a) Projections for the tomography are implemented by choosing the appropriate pulse profile for the second transfer pulse in the storage sequence. For projections in  $\sigma_x$  and  $\sigma_y$  the second transfer pulse takes the form of a composite HSH, obtained from the sum of the fields of two chirped pulses that are temporally shifted by the width of one time bin ( $T_m$ ) relative to each other. In the top figure, the envelopes of the two partial pulses are shown with dashed lines and the resulting composite pulse with a solid line. As a consequence, each specific frequency of the AFC (e.g. the dashed line in the bottom figure) is addressed at two different times separated by  $T_m$ , as indicated by the crossings with the two solid lines (b) Two examples of projection of the output state onto  $|+\rangle$  (dark histogram) and  $|-\rangle$  (light histogram) eigenstates of the  $\sigma_x$  operator. The overlap is proportional to the amplitude in the interference bins (dotted boxes). The input state  $\psi_{in}$  was prepared in the  $|+\rangle$  eigenstate of  $\sigma_x$  (c) Reconstructed density matrix  $\hat{\rho}_{out}$  of the output state.

pling efficiencies. Nonetheless, our results show that our memory is capable of storing successfully multiple time modes at the single photon level, with a SNR that is in principle compatible with storage of quantum states<sup>23</sup> for up to 100ms. More information on the memory parameter estimations from the data can be found in the supplementary materials.

To characterize the quantum fidelity of the memory, we analyzed the storage of time-bin-encoded qubits. Both qubits were prepared in the ideally pure superposition state  $\psi_{in} = 1/\sqrt{2}(|e\rangle + |l\rangle)$ , where  $|e\rangle$  and  $|l\rangle$  represent the early and late time modes of each qubit. Exploiting our 6-modes capacity, we encoded the components  $|e\rangle$  and  $|l\rangle$  of the first qubit into the temporal modes 2 and 3 respectively, and similarly for the second qubit in modes 5 and 6.

To perform a full quantum tomography of the memory output state, represented by the density matrix  $\rho_{out}$ , one needs to be able to perform measurements of the observables represented by the Pauli matrices  $\sigma_x$ ,  $\sigma_y$  and  $\sigma_z$ . The observable  $\sigma_z$  can simply be measured using histogram traces as shown in figure 3. The  $\sigma_x$  and  $\sigma_y$  observables can be measured by making two partial read-outs of the memory<sup>46–48</sup>, separated by the qubit mode spacing  $T_m$ , where each partial transfer pulse should ideally perform a 50% transfer. In the past, this has been achieved by using two distinct, shorter transfer pulses<sup>46,48,49</sup>, separated by  $T_m$ , which in practice can reduce the efficiency below the ideal 50% transfer<sup>46</sup>. This is particularly true for long adiabatic, chirped pulses, which would then need to be severely shortened to produce two distinct pulses separated by the mode spacing  $T_m$ . In addition the first control pulse would need to be reduced in duration as well, as the chirp rate of all the transfer pulses should be the same<sup>37</sup>.

To overcome the efficiency limitation for qubit analysis based on partial read-outs with adiabatic pulses, we propose a novel composite pulse that can achieve the ideal 50% partial transfer, independently of the pulse duration and mode separation. The composite HSH pulse (cHSH) is a linear sum of two identical adiabatic HSH pulses, with their centers separated in time by  $T_m$ . The cHSH has a characteristic amplitude oscillation due to the interference of the two chirps, see figure 4a. Intuitively, one can think of each specific frequency within the AFC bandwidth as being addressed twice by the cHSH, once by each component, at two distinct times separated exactly by  $T_m$ , despite the fact that the whole cHSH pulse itself is much longer than  $T_m$ . As a consequence, the addressed atomic population partially rephases after the pulse at two times separated by  $T_m$ . An alternative method for analysing qubits consists in using an AFC-based analyser in the filtering crystal<sup>50,51</sup>. However, we observed that the SNR was deteriorated when using the same crystal as both filtering and analysing device. The cHSH-based analyser resulted in a significantly better SNR after the filters, yielding a higher storage fidelity.

The phase difference  $\theta$  between the two cHSH components sets the measurement basis, where  $\theta = 0$  ( $\theta = \pi/2$ ) and  $\theta = \pi$  ( $\theta = 3\pi/2$ ) projects respectively on the  $|+\rangle$  and  $|-\rangle$  eigenstates of  $\sigma_x$  ( $\sigma_y$ ), encoded in the early-late time modes basis as  $1/\sqrt{2}(|e\rangle + e^{i\theta}|l\rangle)$ . Note that this type of analyser can only project onto one eigenstate of each basis, hence two measurements are required per Pauli operator. Figure 4b shows the histograms corresponding to the two  $\sigma_x$  projections.

After measuring the expectation value of all three Pauli operators, we can reconstruct the full quantum

state  $\hat{\rho}_{out}$  using direct inversion<sup>52</sup> and derive a fidelity of  $F = (85 \pm 3)\%$ , averaged over the two qubits. The average number of photons per qubit was  $\mu = 0.92 \pm 0.04$  and the reconstructed density matrix  $\hat{\rho}_{out}$  is shown in figure 4c. The purity of the reconstructed state is  $P = (76 \pm 3)\%$ , which limits the maximum achievable fidelity in absence of any unitary errors to 87%. This indicates that the fidelity is limited by white noise generated by the RF sequence at the memory read-out. Another element supporting this conclusion is given by the fidelity measured with bright pulses, so that the noise is negligible (see supplementary materials), yielding a value of 96%. We further note that the  $\sigma_z$  measurement yielded a SNR of  $3.48 \pm 0.15$ , which when scaled up to the single photon level in one time bin becomes about 7.0. This is compatible with the value reported in table I and would result in an upper bound on the fidelity of  $F = (\text{SNR} + 1)/(\text{SNR} + 2) = (88.9 \pm 0.04)\%$  assuming a white noise model<sup>23</sup>.

## DISCUSSION AND CONCLUSIONS

The results presented here demonstrate that long-duration quantum storage based on dynamical decoupling of spin-wave states in  $^{151}\text{Eu}^{3+}:\text{Y}_2\text{SiO}_5$  is a promising avenue. In terms of qubit storage, we observe a 40-fold increase in storage time with respect to the previous longest quantum storage of photonic qubits in a solid-state device<sup>9</sup>. Currently, the storage time in  $^{151}\text{Eu}^{3+}:\text{Y}_2\text{SiO}_5$  is limited by the heating observed when adding more pulses in the decoupling sequence, which is a technical limitation, but the classical storage experiments by Holzäpfel et al.<sup>22</sup> suggest that even longer storage times are within reach in  $^{151}\text{Eu}^{3+}:\text{Y}_2\text{SiO}_5$ . Our observation that DD sequences with more pulses did not generate more read-out noise is key to achieving longer storage times also at the quantum level. We also note that these techniques could be applied also to  $\text{Pr}^{3+}$  doped  $\text{Y}_2\text{SiO}_5$  crystals, where currently quantum entanglement storage experiments are limited to about  $50 \mu\text{s}$ <sup>53</sup>. Another interesting avenue is to apply these techniques to extend the storage time of spin-photon correlations experiments<sup>42,51</sup> in rare-earth-doped crystals.

## METHODS

### Expanded setup

The core of the setup consist of a closed-cycle pulsed helium cryostat with a sample chamber at a typical temperature of 3.5 K. In the sample chamber, a custom copper mount holds the memory crystal, with dimensions  $2.5 \text{ mm} \times 2.9 \text{ mm} \times 12.3 \text{ mm}$  along the  $(D_1, D_2, b)$  axes<sup>32</sup>, and a series of two filtering crystals with similar size. All these are  $^{151}\text{Eu}^{3+}:\text{Y}_2\text{SiO}_5$  crystals with a doping concentration of 1000 ppm<sup>23</sup>. Around the memory

crystal, a copper coil generates the RF field to manipulate the atoms on their spin transitions. The coil is coupled to a resonator circuit, with resonance tuned on the 46 MHz spin transition, which produces a Rabi frequency of 120 kHz, corresponding roughly to an AC field of amplitude 12 mT. Before the resonator, the RF signal is created by an arbitrary wave generator, and amplified with a 100 W amplifier coupled to a circulator to redirect unwanted reflection from the resonator system.

The input beam is used to create the optical pulses to be stored, and it goes through the memory crystal twice with a waist diameter of  $50 \mu\text{m}$ . The memory preparation beam is overlapped with the input path with a larger spot size around  $700 \mu\text{m}$ , to ensure homogeneity of the preparation along the crystal length, with an incident angle of about  $1^\circ$ . The transfer beam is overlapped in a similar way, with a beam diameter at the waist of  $250 \mu\text{m}$ .

### Photon counting and noise measurement

The quantities  $\mu_{in}$  and  $p_N$  in table I, correspond to average number of photons at the memory output for a single storage attempt. They are obtained by summing raw detections in modes of duration  $T_m = 1.65 \mu\text{s}$ , then dividing by the number of experiment repetitions, averaging over the 6 modes, and dividing by the detector efficiency  $\eta_D = 57\%$  and cryostat-to-detector path transmission (typically between 17 and 20%). The histograms in figures 3 and 4b are obtained in the same way for a binning resolution of 200 ns.

The noise parameter  $p_N$  indicates the probability of a noise photon being emitted by the memory during a time corresponding to the mode size  $T_m = 1.65 \mu\text{s}$ . For the spin storage data at  $T_s = 20 \text{ ms}$ , visible in figure 3a and table I, it is measured independently by blocking the input beam during the full storage sequence in the same time-modes in which the retrieved modes would be. A more detailed analysis per-mode and the exact number of repetitions for all experiments are reported in the supplementary materials.

To decrease the total acquisition time of the experiments at  $T_s = 50$  and  $100 \text{ ms}$ , we calculated the respective  $p_N$  values reported in table I from a  $\sim 225 \mu\text{s}$  time window centered at about  $190 \mu\text{s}$  after the first retrieved mode in the same dataset. By doing so, we exploited the fact that the noise floor is due to spontaneous emission with a decay time of  $1.9 \text{ ms}$ <sup>33</sup>, and can be considered uniform up to  $\sim 200 \mu\text{s}$  after readout. This is confirmed experimentally on the 20 ms datasets, as the difference in  $p_N$  calculated in the retrieved mode position of the data with input blocked correspond to the result of the procedure above within the Poissonian standard deviation. The histograms displaying noise in figure 3b and c are representative regions of the noise floor taken at about  $20 \mu\text{s}$  after the retrieved modes in the same dataset.

All errors are estimated from Poissonian standard deviations on the raw detector counts and propagated con-

sidering the memory temporal modes as independent.

## DATA AVAILABILITY

The data sets generated and/or analysed during the current study are available from the corresponding authors upon reasonable request.

## ACKNOWLEDGEMENTS

We acknowledge funding from the Swiss FNS NCCR programme Quantum Science Technology (QSIT), European Union Horizon 2020 research and innovation program within the Flagship on Quantum Technologies through GA 820445 (QIA) and under the Marie Skłodowska-Curie program through GA 675662 (QCALL).

We also thank Philippe Goldner and Alban Ferrier from Chimie ParisTech for fruitful discussions and for providing the crystals.

- 
- <sup>1</sup> H.-J. Briegel, W. Dür, J. I. Cirac, and P. Zoller, *Phys. Rev. Lett.* **81**, 5932 (1998).
- <sup>2</sup> L.-M. Duan, M. D. Lukin, J. I. Cirac, and P. Zoller, *Nature* **414**, 413 (2001).
- <sup>3</sup> N. Sangouard, C. Simon, H. de Riedmatten, and N. Gisin, *Rev. Mod. Phys.* **83**, 33 (2011).
- <sup>4</sup> H. J. Kimble, *Nature* **453**, 1023 (2008).
- <sup>5</sup> C. Cabrillo, J. I. Cirac, P. García-Fernández, and P. Zoller, *Phys. Rev. A* **59**, 1025 (1999).
- <sup>6</sup> J. Nunn, K. Reim, K. C. Lee, V. O. Lorenz, B. J. Sussman, I. A. Walmsley, and D. Jaksch, *Phys. Rev. Lett.* **101**, 260502 (2008).
- <sup>7</sup> M. Afzelius, C. Simon, H. de Riedmatten, and N. Gisin, *Phys. Rev. A* **79**, 052329 (2009).
- <sup>8</sup> N. Sinclair, E. Saglamyurek, H. Mallahzadeh, J. A. Slater, M. George, R. Ricken, M. P. Hedges, D. Oblak, C. Simon, W. Sohler, and W. Tittel, *Physical Review Letters* **113**, 053603 (2014).
- <sup>9</sup> C. Laplane, P. Jobez, J. Etesse, N. Timoney, N. Gisin, and M. Afzelius, *New Journal of Physics* **18**, 013006 (2015).
- <sup>10</sup> M. Parniak, M. Dabrowski, M. Mazelanik, A. Leszczyński, M. Lipka, and W. Wasilewski, *Nature Communications* **8** (2017), 10.1038/s41467-017-02366-7.
- <sup>11</sup> T.-S. Yang, Z.-Q. Zhou, Y.-L. Hua, X. Liu, Z.-F. Li, P.-Y. Li, Y. Ma, C. Liu, P.-J. Liang, X. Li, Y.-X. Xiao, J. Hu, C.-F. Li, and G.-C. Guo, *Nature Communications* **9** (2018), 10.1038/s41467-018-05669-5.
- <sup>12</sup> L. Heller, P. Farrera, G. Heinze, and H. de Riedmatten, *Physical Review Letters* **124**, 210504 (2020).
- <sup>13</sup> C. Simon, H. de Riedmatten, M. Afzelius, N. Sangouard, H. Zbinden, and N. Gisin, *Phys. Rev. Lett.* **98**, 190503 (2007).
- <sup>14</sup> I. Usmani, M. Afzelius, H. de Riedmatten, and N. Gisin, *Nat Commun* **1**, 12 (2010).
- <sup>15</sup> A. Seri, A. Lenhard, D. Rieländer, M. Gündoğan, P. M. Ledingham, M. Mazzer, and H. de Riedmatten, *Phys. Rev. X* **7**, 021028 (2017).
- <sup>16</sup> A. Seri, D. Lago-Rivera, A. Lenhard, G. Corrielli, R. Oselame, M. Mazzer, and H. de Riedmatten, *Phys. Rev. Lett.* **123**, 080502 (2019).
- <sup>17</sup> M. Sabooni, Q. Li, S. Kröll, S., and L. Rippe, *Phys. Rev. Lett.* **110**, 133604 (2013).
- <sup>18</sup> M. P. Hedges, J. J. Longdell, Y. Li, and M. J. Sellars, *Nature* **465**, 1052 (2010).
- <sup>19</sup> G. Heinze, C. Hubrich, and T. Halfmann, *Phys. Rev. Lett.* **111**, 033601 (2013).
- <sup>20</sup> M. Zhong, M. P. Hedges, R. L. Ahlefeldt, J. G. Bartholomew, S. E. Beavan, S. M. Wittig, J. J. Longdell, and M. J. Sellars, *Nature* **517**, 177 (2015).
- <sup>21</sup> M. Businge, A. Tiranov, K. Kaczmarek, S. Welinski, Z. Zhang, A. Ferrier, P. Goldner, and M. Afzelius, *Physical Review Letters* **124**, 053606 (2020).
- <sup>22</sup> A. Holzäpfel, J. Etesse, K. T. Kaczmarek, A. Tiranov, N. Gisin, and M. Afzelius, *New Journal of Physics* **22**, 063009 (2020).
- <sup>23</sup> P. Jobez, C. Laplane, N. Timoney, N. Gisin, A. Ferrier, P. Goldner, and M. Afzelius, *Physical Review Letters* **114**, 230502 (2015).
- <sup>24</sup> Y. Wu, J. Liu, and C. Simon, *Phys. Rev. A* **101**, 042301 (2020).
- <sup>25</sup> E. Z. Cruzeiro, F. Fröwis, N. Timoney, and M. Afzelius, *Journal of Modern Optics* **63**, 2101 (2016), <https://doi.org/10.1080/09500340.2016.1204472>.
- <sup>26</sup> E. Fraval, M. J. Sellars, and J. J. Longdell, *Phys. Rev. Lett.* **92**, 077601 (2004).
- <sup>27</sup> J. Etesse, A. Holzäpfel, A. Ortu, and M. Afzelius, *Physical Review A* **103**, 022618 (2021).
- <sup>28</sup> F. Könz, Y. Sun, C. W. Thiel, R. L. Cone, R. W. Equall, R. L. Hutcheson, and R. M. Macfarlane, *Phys. Rev. B* **68**, 085109 (2003).
- <sup>29</sup> M. Afzelius, I. Usmani, A. Amari, B. Lauritzen, A. Walther, C. Simon, N. Sangouard, J. Minar, H. de Riedmatten, N. Gisin, and S. Kröll, *Phys. Rev. Lett.* **104**, 040503 (2010).
- <sup>30</sup> P. Jobez, N. Timoney, C. Laplane, J. Etesse, A. Ferrier, P. Goldner, N. Gisin, and M. Afzelius, *Phys. Rev. A* **93**, 032327 (2016).
- <sup>31</sup> P. Jobez, I. Usmani, N. Timoney, C. Laplane, N. Gisin, and M. Afzelius, *New Journal of Physics* **16**, 083005 (2014).
- <sup>32</sup> C. Li, C. Wyon, and R. Moncorge, *IEEE Journal of Quantum Electronics* **28**, 1209 (1992).
- <sup>33</sup> R. W. Equall, Y. Sun, R. L. Cone, and R. M. Macfarlane, *Phys. Rev. Lett.* **72**, 2179 (1994).
- <sup>34</sup> A. L. Alexander, J. J. Longdell, and M. J. Sellars, *J. Opt. Soc. Am. B* **24**, 2479 (2007).
- <sup>35</sup> A. Arcangeli, M. Lovrić, B. Tumino, A. Ferrier, and P. Goldner, *Phys. Rev. B* **89**, 184305 (2014).
- <sup>36</sup> E. Z. Cruzeiro, J. Etesse, A. Tiranov, P.-A. Bourdel, F. Fröwis, P. Goldner, N. Gisin, and M. Afzelius, *Physical Review B* **97**, 094416 (2018).
- <sup>37</sup> J. Minář, N. Sangouard, M. Afzelius, H. de Riedmatten, and N. Gisin, *Phys. Rev. A* **82**, 042309 (2010).

- <sup>38</sup> M. Tian, T. Chang, K. D. Merkel, and W. Randall, *Appl. Opt.* **50**, 6548 (2011).
- <sup>39</sup> L. Viola and S. Lloyd, *Phys. Rev. A* **58**, 2733 (1998).
- <sup>40</sup> G. de Lange, Z. H. Wang, D. Ristè, V. V. Dobrovitski, and R. Hanson, *Science* **330**, 60 (2010).
- <sup>41</sup> J. Medford, L. Cywiński, C. Barthel, C. M. Marcus, M. P. Hanson, and A. C. Gossard, *Phys. Rev. Lett.* **108**, 086802 (2012).
- <sup>42</sup> C. Laplane, P. Jobez, J. Etesse, N. Gisin, and M. Afzelius, *Physical Review Letters* **118**, 210501 (2017).
- <sup>43</sup> W. B. Mims, *Phys. Rev.* **168**, 370 (1968).
- <sup>44</sup> J. R. Klauder and P. W. Anderson, *Phys. Rev.* **125**, 912 (1962).
- <sup>45</sup> M. J. Thorpe, D. R. Leibrandt, and T. Rosenband, *New Journal of Physics* **15**, 033006 (2013).
- <sup>46</sup> M. Gündoğan, P. M. Ledingham, K. Kutluer, M. Mazzerà, and H. de Riedmatten, *Physical Review Letters* **114**, 230501 (2015).
- <sup>47</sup> M. U. Staudt, S. R. Hastings-Simon, M. Nilsson, M. Afzelius, V. Scarani, R. Ricken, H. Suche, W. Sohler, W. Tittel, and N. Gisin, *Phys. Rev. Lett.* **98**, 113601 (2007).
- <sup>48</sup> M. Gündoğan, M. Mazzerà, P. M. Ledingham, M. Cristiani, and H. de Riedmatten, *New Journal of Physics* **15**, 045012 (2013).
- <sup>49</sup> Y.-Z. Ma, M. Jin, D.-L. Chen, Z.-Q. Zhou, C.-F. Li, and G.-C. Guo, *Nature Communications* **12** (2021), [10.1038/s41467-021-24679-4](https://doi.org/10.1038/s41467-021-24679-4).
- <sup>50</sup> P. Jobez, (2015), [10.13097/ARCHIVE-OUVERTE/UNIGE:83671](https://doi.org/10.13097/ARCHIVE-OUVERTE/UNIGE:83671).
- <sup>51</sup> K. Kutluer, E. Distantè, B. Casabone, S. Duranti, M. Mazzerà, and H. de Riedmatten, *Physical Review Letters* **123**, 030501 (2019).
- <sup>52</sup> R. Schmied, *Journal of Modern Optics* **63**, 1744 (2016), <https://doi.org/10.1080/09500340.2016.1142018>.
- <sup>53</sup> J. V. Rakonjac, D. Lago-Rivera, A. Seri, M. Mazzerà, S. Grandi, and H. de Riedmatten, (2021), [arXiv:2106.05079 \[quant-ph\]](https://arxiv.org/abs/2106.05079).



# Supplementary materials - Storage of photonic time-bin qubits for up to 20 ms in a rare-earth doped crystal

Antonio Ortu,<sup>1</sup> Adrian Holzäpfel,<sup>1</sup> Jean Etesse,<sup>2</sup> and Mikael Afzelius<sup>1</sup>

<sup>1</sup>*Département de Physique Appliquée, Université de Genève, CH-1211 Genève, Switzerland*

<sup>2</sup>*Université côte d'Azur, CNRS, Institut de Physique de Nice (INPHYNI), UMR 7010, Parc Valrose, Nice Cedex 2, France*

(Dated: September 14, 2021)

## Crystals optical initialization

The preparation procedure begins with a class cleaning sequence<sup>1</sup>. This first step ensures that each frequency corresponds to a transition between the same two states for all atoms involved, for both the optical and RF transitions we are interested in. The frequencies of the cleaning pulses are the one corresponding to the  $|g\rangle \leftrightarrow |e\rangle$  transition, on which the AFC is addressed, and four others with relative detuning of  $-46$  MHz,  $-6$  MHz,  $+46$  MHz and  $-92$  MHz, which correspond respectively to the spin transfer transition, the auxiliary transition for storing atoms not being part of the comb, and two additional transitions to empty states of other unwanted classes that might be addressed by the RF. The second step consists in polarizing the atomic population into the  $|g\rangle = |\pm 5/2\rangle$  state, by optically pumping the other two ground states  $|s\rangle = |\pm 3/2\rangle$  (the storage state) and  $|a\rangle = |\pm 1/2\rangle$  (the auxiliary state). The third step involves the preparation of the AFC with optical pulses specifically modulated to have the corresponding comb-like spectrum<sup>2</sup>, with defined maximum bandwidth  $\Gamma$ , teeth periodicity  $\Delta$  and tooth width  $\gamma$ . A sequence of repumping pulses ensures that the  $|s\rangle$  state stays empty in the process. All this steps are achieved by the memory preparation beam.

In parallel, via the filter preparation beam, the filtering crystals are initialized by a simpler optical pumping sequence which results in 2 MHz wide transparency and absorption windows, with central frequencies corresponding respectively to the  $|g\rangle \rightarrow |e\rangle$  and  $|s\rangle \rightarrow |e\rangle$  transitions. This way, ideally, only the photons emitted from the memory at the AFC transition will arrive at the detector, while the absorption profile blocks photons potentially emitted by atoms falling back along the  $|e\rangle \rightarrow |s\rangle$  transition and possible scattered components of the final transfer pulse into the input spatial mode.

## Spin resonance

The inhomogeneous broadening of the  $|g\rangle \leftrightarrow |s\rangle$  transition was characterized by probing the effect of spin dephasing on the retrieved signal in a modified spin storage sequence. A single input signal is stored in the memory and the amplitude of the retrieved signal is recorded while varying the temporal position  $\tau$  of the second optical transfer pulse with respect to its position in the optimal rephasing case, while all other optical and RF pulses

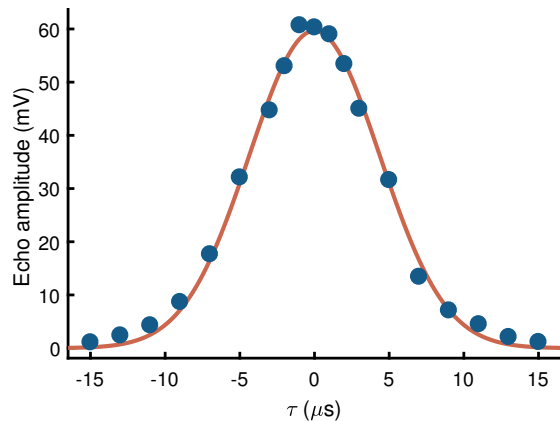


FIG. 1. **Spin resonance at 46 MHz.** Amplitude of retrieved signal after storage, as a function of the temporal shift  $\tau$  applied to the center of the second transfer pulse with respect to its normal position for optimal dephasing. The solid line indicates the Gaussian fit used to extract the linewidth.

are kept fixed. The signal amplitude thus decreases as a function of  $\tau$  according to a decay constant given by the inhomogeneous broadening. The data is shown in figure 1, with a fit to the equation

$$f(\tau) = a e^{-\frac{(\pi\Gamma_s\tau)^2}{2\ln(2)}}.$$

Here, the maximum amplitude  $a$  and transition linewidth (FWHM)  $\Gamma_s$  are free parameters. The resulting linewidth is  $\Gamma_s = (61 \pm 2)$  kHz, with an error corresponding to a 95% confidence interval.

## RF sequence

All dynamical decoupling sequences were composed of adiabatic pulses with a hyperbolic secant amplitude profile<sup>3</sup> with a total duration (at the edges of which the signal is completely cut off) of 200  $\mu\text{s}$ , a full width at half maximum of 50  $\mu\text{s}$  and a frequency chirp of 300 kHz (about 5 times the spin broadening). The field shape is programmed via Matlab into a digital arbitrary wave generator and sent to a 100 W amplifier with 50  $\Omega$  impedance. This is coupled in output to a RF circulator and a custom resonant circuit based on lumped elements. The circuit is needed to impedance-match the coil surrounding the crystal with the system generating the RF

signal at  $50 \Omega$ . With this setup, we could achieve a Rabi frequency on the  $|g\rangle \leftrightarrow |s\rangle$  transition of about 120 kHz, measured experimentally from the oscillation of population in the  $|g\rangle$  state while driving the system at 46 MHz and optically probing on  $|g\rangle \leftrightarrow |e\rangle$ .

### Optical transfer pulses

The optical transfer pulses on the optical transitions in the spin wave experiments are adiabatic HSH pulses<sup>4</sup>, with flat central part of duration  $10.7 \mu\text{s}$ , FWHM of the hyperbolic secant sides of  $1.65 \mu\text{s}$ , total duration of  $15 \mu\text{s}$  and frequency chirp of 1.5 MHz. The signal shape is programmed into an arbitrary wave generator with a central frequency of about 200 MHz, at the output of which the signal is amplified and fed to an acousto-optic modulator in double pass configuration.

### Spin storage with bright pulses

The memory efficiency data points of the spin storage with bright pulses displayed in figure 2 of the main text and used in the evaluation of the performance of the dynamical decoupling sequences are obtained from the time profile of the retrieved pulses by means of an oscilloscope. For each storage time and each DD sequence, the experiment is repeated 10 times. Each pulse profile is fitted with a Gaussian curve to extract the pulse area, which in turn is averaged over the 10 measurements, and divided by the area of a reference input pulse obtained analogously. The relative error (not shown in the figure) is dominated by shot-to-shot fluctuations and typically results in a standard deviation below 10%. The inverse of the error of each data point is used as weight in the fitting procedure of the efficiency curve.

DD type	$T_2^{\text{spin}}$ (ms)	$\eta_s(0)$ (%)	$m$
XX	$70 \pm 2$	$6.6 \pm 0.6$	$2.4 \pm 0.4$
XY-4	$106 \pm 9$	$7.7 \pm 1.6$	$2.2 \pm 0.9$
XY-8	$154 \pm 11$	$8.6 \pm 1.4$	$1.5 \pm 0.3$
XY-16	$230 \pm 30$	$6.4 \pm 1.7$	$1.2 \pm 0.3$

TABLE I. **Dynamical decoupling with bright input pulses.** Fitted parameters of the spin storage curves with bright pulses for different DD sequences, according to equation 1.  $T_2^{\text{spin}}$  = effective spin coherence time;  $\eta_s(0)$  = extrapolated zero-time efficiency;  $m$  = Mims factor.

Table I reports all free parameters obtained from the least-squares fits of the spin storage efficiency curves as a function of storage time  $T_s$ . The model follows Mims' equation<sup>5</sup>

$$\eta_s(T_s) = \eta_s(0) e^{-2(T_s/T_2^{\text{spin}})^m}, \quad (1)$$

which takes into account the deviation from a pure exponential behavior due to spectral diffusion via the parameter  $m$ . Errors correspond to 95% confidence intervals.

### Photon counting

Table II is an extension of table I of the main text, displaying the average results of the storage experiments at the single photon level. The results are obtained from averaging the raw counts over the 6 time modes of duration  $T_m = 1.65 \mu\text{s}$  each. Errors are obtained from the standard deviation of a Poissonian distribution of the raw counts and propagated on the average considering the 6 modes as independent. The quantities  $\mu_{\text{in}}$  and  $p_N$  correspond to average number of photons at the memory output. They are obtained from the raw counts by dividing by the number of experiment repetitions, averaging over the 6 modes, and dividing by the detector efficiency  $\eta_D = 57\%$  and cryostat-to-detector path transmission (typically between 17 and 20% depending on the specific experimental run). See also the Methods section of the main text.

Table III reports the same quantities obtained separately in each temporal mode for the case  $T_s = 20 \text{ ms}$ .

### Qubit tomography

Table IV displays additional details on the qubit storage. The raw counts in the interference temporal bins are used to calculate the visibility relative to each basis, from which a full tomography of the state can be derived. To increase the repetition rate of the experiment, two of the six temporal modes of the memory were used as for the interference of two different qubits respectively. The projection basis at readout is chosen by changing the relative phase  $\theta$  of the two HSH components of the cHSH pulse. For the trivial case of the  $Z$  basis, the readout pulse is the same single HSH used in the other multimode spin-wave storage experiments, and the output signal is simply the retrieved qubit after storage on the same base as the input. In this particular case, the average visibility is calculated from the counts in modes 2 and 5 (the retrieved early components of the two stored qubits) and the counts in modes 3 and 6 (the retrieved late components).

Figure 2 shows the oscilloscope traces collected at readout of a storage experiment of two bright input pulses in adjacent time modes, analogous to the qubit storage. The traces displays the transmitted component of the cHSH analyzer pulse followed by the retrieved modes, showing interference in a time bin of  $1.65 \mu\text{s}$ . The interference pattern depends on the cHSH phase  $\theta$  and corresponds to the case of two orthogonal projection on the x-basis in the qubit experiment. After eliminating the background level and integrating the area in the interference bin, we calculate a visibility of 92% and a fidelity

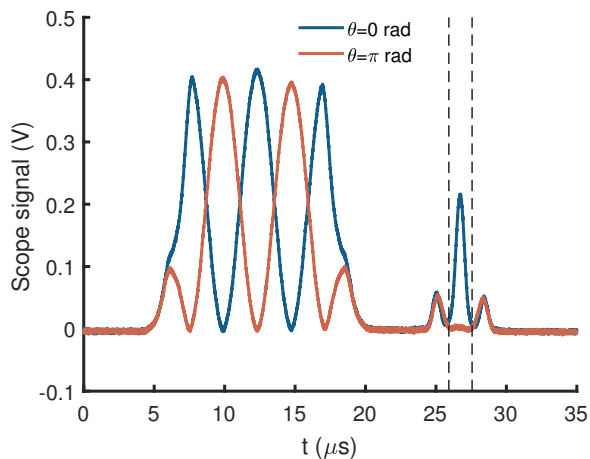


FIG. 2. **Analyzer readout with bright pulses.** Readout of a storage experiment of two bright input pulses in adjacent time modes, emulating a qubit experiment. The transmitted component of cHSH analyzer pulse and the retrieved modes are visible for two values of  $\theta$  corresponding to orthogonal projections on the x-basis of the qubit experiment. The dashed lines indicate the time bin from which the fidelity is measured.

of 96%. This further suggests that the fidelity at qubit-level is limited by the noise introduced by the RF pulses, which becomes negligible when we use bright pulses as input.

---

<sup>1</sup> B. Lauritzen, N. Timoney, N. Gisin, M. Afzelius, H. de Riedmatten, Y. Sun, R. M. Macfarlane, and R. L. Cone, *Phys. Rev. B* **85**, 115111 (2012).  
<sup>2</sup> P. Jobez, N. Timoney, C. Laplane, J. Etesse, A. Ferrier, P. Goldner, N. Gisin, and M. Afzelius, *Phys. Rev. A* **93**, 032327 (2016).

<sup>3</sup> M. S. Silver, R. I. Joseph, and D. I. Hault, *Phys. Rev. A* **31**, 2753 (1985).

<sup>4</sup> M. Tian, T. Chang, K. D. Merkel, and W. Randall, *Appl. Opt.* **50**, 6548 (2011).

<sup>5</sup> W. B. Mims, *Phys. Rev.* **168**, 370 (1968).

$T_s$ (ms)	$\mu_{\text{in}}$	$\mu_{\text{out}}$	$p_N$	$\eta$ (%)	SNR	$\mu_1$
20	$0.711 \pm 0.006$	$0.0525 \pm 0.0012$	$0.0073 \pm 0.0012$	$7.39 \pm 0.04$	$7.4 \pm 0.5$	$0.098 \pm 0.002$
50	$1.21 \pm 0.01$	$0.053 \pm 0.003$	$0.009 \pm 0.002$	$4.37 \pm 0.04$	$5.6 \pm 0.7$	$0.218 \pm 0.008$
100	$1.062 \pm 0.007$	$0.0276 \pm 0.0012$	$0.0110 \pm 0.0015$	$2.60 \pm 0.02$	$2.5 \pm 0.2$	$0.445 \pm 0.008$

TABLE II. **Extended table of single photon-level storage.** Relevant quantities averaged over all 6 modes for different spin-wave storage times  $T_s$ .  $\mu_{\text{in}}$  = input number of photons;  $\mu_{\text{out}}$  = retrieved number of photon after storage;  $p_N$  = number of noise photons;  $\eta$  = storage efficiency; SNR= signal-to-noise ratio;  $\mu_1$  = number of photons at input equivalent to SNR=1. All photon numbers are obtained from the detector counts by correcting for the detector efficiency and the path losses from the cryostat output to the detector.

Mode n.	$\mu_{\text{in}}$	$\mu_{\text{out}}$	$p_N$	$\eta$	SNR	$\mu_1$
1	$0.697 \pm 0.015$	$0.055 \pm 0.003$	$0.0078 \pm 0.0011$	$0.0797 \pm 0.0017$	$7.1 \pm 1.2$	$0.10 \pm 0.02$
2	$0.702 \pm 0.015$	$0.048 \pm 0.003$	$0.0078 \pm 0.0011$	$0.0685 \pm 0.0014$	$6.2 \pm 1.1$	$0.11 \pm 0.04$
3	$0.707 \pm 0.015$	$0.055 \pm 0.003$	$0.0084 \pm 0.0011$	$0.0781 \pm 0.0016$	$6.6 \pm 1.1$	$0.11 \pm 0.03$
4	$0.727 \pm 0.015$	$0.050 \pm 0.003$	$0.0067 \pm 0.0010$	$0.0692 \pm 0.0014$	$7.5 \pm 1.3$	$0.10 \pm 0.03$
5	$0.721 \pm 0.015$	$0.055 \pm 0.003$	$0.0078 \pm 0.0011$	$0.0763 \pm 0.0016$	$7.1 \pm 1.2$	$0.10 \pm 0.03$
6	$0.712 \pm 0.015$	$0.051 \pm 0.003$	$0.0052 \pm 0.0010$	$0.0714 \pm 0.0015$	$9.8 \pm 1.9$	$0.073 \pm 0.018$

TABLE III. **Time mode analysis for 20 ms spin storage.** Quantities as in table II, obtained separately for each storage mode.

Basis	$\theta$	Mode n.	Counts	$V$
X	0	3	64	$0.70 \pm 0.04$
		6	60	
	$\pi$	3	25	
		6	19	
Y	$-\pi/2$	3	48	$-0.14 \pm 0.07$
		6	36	
		3	58	
	$\pi/2$	6	52	
		2	248	
		3	218	
Z	5	197	$-0.06 \pm 0.03$	
	6	281		

TABLE IV. **Qubit storage results.** Raw counts obtained from the qubit storage experiment. Two of the six time modes of the memory were used at each storage attempt to double the acquisition rate. The readout pulse shape and relative cHSH phase  $\theta$  define the basis projection after storage.  $V$  indicates the average visibility obtained for each basis.

$T_s$ (ms)	Ref. reps.	Storage reps.	Noise reps.
20	27000	51799	53449
50	13673	15693	15693
100	31159	43500	43500

TABLE V. **Experiment repetitions, single photon level storage.** Number of repetitions of each experiment used to accumulate accurate statistics and errors for the single photon level storage datasets. The number of repetitions is indicated for the acquisition of the reference input signal, the retrieved signal after storage, and the noise background.

Basis/phase	Ref. reps.	Storage reps.
$X 0$	222578	19862
$X \pi$	222578	39600
$Y -\pi/2$	259576	33995
$Y \pi/2$	259576	33729
$Z 0$	277692	73076

TABLE VI. **Experiment repetitions, 20 ms qubit storage.** Number of repetitions of each experiment used to accumulate accurate statistics and errors for the qubit storage datasets. The number of repetitions is indicated for the acquisition of the reference input signal and the retrieved signal after storage with different projection bases and analyzer phases.

## **A.5 Paper V: Multimode capacity of atomic frequency comb quantum memories**

# Multimode capacity of atomic-frequency comb quantum memories

Antonio Ortu<sup>1</sup>, Jelena Rakonjac<sup>2</sup>, Adrian Holzäpfel<sup>1</sup>,  
Alessandro Seri<sup>2</sup>, Samuele Grandi<sup>2</sup>, Hugues de Riedmatten<sup>2,3</sup>,  
and Mikael Afzelius<sup>1</sup>

<sup>1</sup>Department of Applied Physics, University of Geneva, CH-1211 Geneva 4, Switzerland

<sup>2</sup> ICFO - Institut de Ciències Fòniques, The Barcelona Institute of Science and Technology, Castelldefels (Barcelona) 08860, Spain

<sup>3</sup> ICREA-Institució Catalana de Recerca i Estudis Avançats, 08015 Barcelona, Spain

E-mail: mikael.afzelius@unige.ch

December 2021

## Abstract.

Multimode quantum memories are key to developing ensemble-based quantum repeaters, to overcome the intrinsic rate limitation imposed by finite communication times over long distances. Rare-earth ion doped crystals are main candidates for highly multimode quantum memories, where time, frequency and spatial multiplexing can be exploited to store multiple modes. In this context the atomic frequency comb (AFC) quantum memory provides large temporal multimode capacity and it can readily be combined with multiplexing in frequency and space. In this article, we derive theoretical formulas for quantifying the temporal multimode capacity of AFC-based memories, both for optical memories with fixed storage time and spin-wave memories with longer storage times and on-demand read out. The temporal multimode capacity is expressed in key memory parameters, such as AFC bandwidth, fixed-delay storage time, memory efficiency, and control field Rabi frequency. Current experiments in europium and praeosodymium doped  $\text{Y}_2\text{SiO}_5$  are analyzed within the theory, and prospects for higher temporal capacity in these materials are considered. In addition we consider the possibility of spectral and spatial multiplexing to further increase the mode capacity, with examples given for praeosodymium doped  $\text{Y}_2\text{SiO}_5$ .

## 1. Introduction

The realization of quantum networks relies on the distribution of entanglement over remote quantum nodes using photons. As these need to travel between the nodes e.g. in optical fibers, the entanglement rate decreases exponentially with the distance, because of optical fiber attenuation, with practical distances limited to a few hundred km. To overcome this limitation, quantum repeaters have been proposed [1–5].

Near term quantum repeaters are based on creating heralded entanglement within elementary links. These are the individual segments in which the network branch is divided into. Each elementary link has two so-called “quantum nodes”, with the ability to generate entanglement and store a part of it in a quantum memory, while the other part is used to perform entanglement swapping operations with neighbouring links. Repeating this swapping operation through the whole chain of elementary links will eventually lead to entanglement between the two end nodes of the network branch. Heralding and storing the entanglement between remote quantum memories in an elementary link is the key to the sub-exponential scaling of entanglement rate with distance in quantum repeaters.

The generation of remote heralded entanglement usually relies on a measurement-induced process that requires the detection of photons, that were generated by the quantum nodes, at a central station located between the two nodes. These photonic modes, each entangled with the node that is storing the other portion of the entangled state, are mixed at a beam splitter (BS), which, if they are indistinguishable, erases the information about their origin: the detection of photons after the BS projects the two quantum nodes to an entangled state. The heralding of the entanglement then requires photonic modes traveling from the quantum nodes to the central station and the result of the photon detection traveling back to the nodes, i.e. a two-way communication. If the two quantum memories can store only one single mode and are separated by a distance  $L_0$ , an entanglement creation trial duration is bounded by the communication time  $\tau_{comm} = L_0/c$ , such that the overall repetition rate of the entanglement generation in one link is limited to  $R = 1/\tau_{comm}$  [3]. For long distances,  $R$  could decrease significantly. For example, for two single-mode quantum memories separated by 100 km the repetition rate of the entanglement generation trials is limited to  $R = 1/\tau_{comm} = 2$  kHz, therefore seriously constraining the achievable entanglement rate.

The entanglement heralding rate can be significantly increased by the use of so-called multimode memories, which allow multiplexing the entanglement generation. A multimode quantum memory allows the storage of various photonic modes in different degrees of freedom, e.g. temporal, frequency or spatial modes. Using a multimode memory that is able to store  $N$  modes it is possible to perform  $N$  entanglement creation trials during a communication time, therefore increasing the entanglement generation rate by a factor  $N$ , to first order [3]. Moreover, the increase of entanglement rate has the beneficial side effect of relaxing the requirement on the storage time of the quantum memories [6].

Quantum memories based on ensembles of atoms are well suited for developing multimode quantum memories. Cold atomic clouds have been so far mostly used to investigate spatially multimode memories [7–10], although a few experiments have demonstrated time multiplexing as well [11]. Rare-earth doped crystals are particularly promising for the realization of massively multiplexed quantum memories. Their static inhomogeneous broadening can be used as a resource for time and frequency multiplexing, a precious capability that could be combined with spatial multiplexing.



Among the many protocols that have been proposed to store photonic qubits in rare-earth doped crystals, the atomic frequency comb scheme [12] is naturally suited for temporal multiplexing [add citations]. Temporal multiplexing is attractive because it can be used in a simple manner in quantum repeater architecture, just by detecting the arrival time of the photon using a single detector. In contrast, spectral and spatial multiplexing, if they are used as parallel channels, require complex de-multiplexing manipulations using e.g. switches or narrow-band frequency filters as well as many detectors. An attractive possibility is to convert frequency and spatial multiplexing onto time multiplexing such that a single channel and single detector can be used.

Following the first demonstration of an AFC memory [13], several proof-of-principle demonstrations have been performed with photonic qubits and single photons enabling light-matter [14–16] and matter-matter entanglement [17,18]. AFC spin-wave memories with on-demand read-out have also been demonstrated for photonic qubits [19,20] and single photons [16,21]. Temporal multimodality has been shown in several experiments [22–25]. Spectral multiplexing has also been achieved by creating several AFCs at different frequencies within the inhomogeneous broadening [26,27].

In this paper, we analyze in detail the multimode capacity of AFC quantum memories in rare-earth (RE) doped crystals, taking into account realistic parameters. We develop a model to infer the maximum number of temporal modes for a given efficiency as a function of the coherence of the optical transition, the bandwidth of the AFC and the Rabi frequency of the control pulses in case of spin-wave storage. We also estimate the maximal number of spectral and spatial modes that could be stored using realistic parameters. In addition, we provide experimental demonstrations of multimode storage in  $\text{Eu}^{3+}:\text{Y}_2\text{SiO}_5$  and  $\text{Pr}^{3+}:\text{Y}_2\text{SiO}_5$ , where we report the largest number of temporal modes stored both in the the optical and spin transition to date.

## 2. Atomic frequency comb quantum memories

Atomic frequency comb (AFC) quantum memories [12] are based on a periodic atomic absorption profile in the form of a comb structure, with a given periodicity  $\Delta$  and total bandwidth  $\Gamma$ , see Figure 1(a). The comb can be created on an inhomogeneously broadened optical transition  $|g\rangle-|e\rangle$  through the use of spectral hole burning techniques, i.e. by frequency-selective optical pumping. RE-doped crystals are ideal systems in this respect, given their large, static inhomogeneous broadening, narrow homogeneous broadening and low spectral diffusion [28]. To efficiently burn the periodic structure while maintaining high spectral resolution one can use optimized optical pumping sequences based on multi-frequency adiabatic pulses [23].

Input pulses absorbed by the comb on the  $|g\rangle-|e\rangle$  transition results in AFC echoes after a fixed-delay storage time of  $1/\Delta$ , owing to the transient response of the medium, see Figure 1(b). If the minimum input pulse duration set by the AFC bandwidth is much shorter than the fixed storage time  $1/\Delta$ , then temporal multimode storage is possible. Let's consider that a smooth temporal mode occupies a truncated (cut-off) duration of

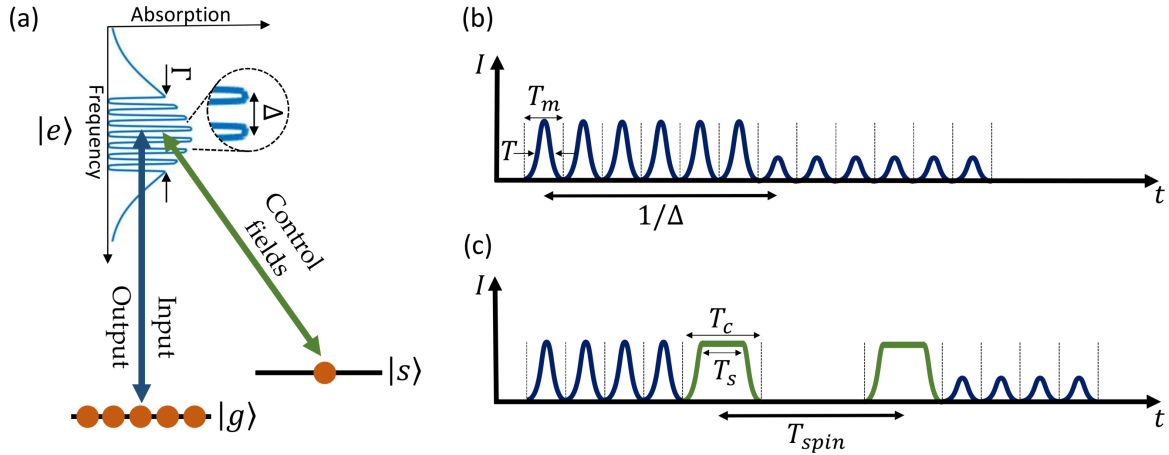


**Figure 1.** (a) The AFC fixed-delay memory is based on the absorption and re-emission of an echo by a comb structure of periodicity  $\Delta$  and bandwidth  $\Gamma$  written into an inhomogeneous absorption profile. The AFC spin-wave memory is based on a coherent and reversible transfer to a second ground state, allowing on-demand read out and long storage times. (b) Time sequence of an AFC echo memory with a fixed delay of  $1/\Delta$ . The input consists of a train of modes with mode duration  $T_m$ , each containing pulses with a FWHM of duration  $T$  in intensity. Note that the train can be a sequence of pulses with random intensities, but with otherwise identical properties. (c) In the case of an AFC spin-wave memory the control pulse occupies a bin size of  $T_c$ , such that the total duration in which input modes can be defined is now reduced to  $1/\Delta - T_c$ . In this illustration the control pulse consumes exactly two input mode bins. In this article smooth adiabatic pulses with a constant intensity duration of  $T_s$  are treated analytically, see text for details. The total spin-wave storage time is  $T_{spin}$ .

$T_m$ , then the temporal multimode capacity is given by  $N_t = 1/(\Delta T_m)^\ddagger$ . In this article we show that the multimode capacity is related to the mode size  $T_m$  and the bandwidth  $\Gamma$ , while the exact shape and full-width at half-maximum (FWHM) of the mode is of less importance provided its total energy is mostly contained within the cut-off duration  $T_m$ . A detailed analysis assuming Gaussian intensity mode profiles will be given. We will also consider the impact of the optical coherence time  $T_2$  (between  $|g\rangle$ - $|e\rangle$ ) on the temporal multimode capacity.

On-demand read-out and longer storage times can be achieved through the reversible transfer of the optical excitation to a second ground state  $|s\rangle$  using two control fields, see Figure 1(c). The storage time  $T_{spin}$  in the spin state is limited by dephasing due to inhomogeneous spin broadening and spectral diffusion. By applying a spin echo sequence the storage time can be extended to the regime of seconds, as demonstrated when storing strong laser pulses [29–31]. In the quantum regime one must deal with technical noise generated by the imperfect spin echo sequences, where up to 100 ms of

$\ddagger$  Formulas given throughout the article for calculating mode numbers  $N_t$  will generate non-integer numbers in general. Mathematically the maximum mode number should be the integer part  $\lfloor N_t \rfloor$ , while in practice if  $N_t$  is close to the next-highest integer another mode can be stored with negligible loss of efficiency.

spin-storage time has been achieved so far [32].

Efficient mapping to and from the  $|s\rangle$  state requires high transfer probability over the entire bandwidth  $\Gamma$  of the AFC. This is a challenge with RE ions due to their low optical oscillator strengths [28]. To circumvent this one can use adiabatic, frequency-chirped pulses [33–35] having a flat transfer profile over  $\Gamma$ . However, these pulses are much longer than the  $\pi$  pulse duration set by the optical Rabi frequency  $\Omega$ . If the cut-off duration assigned to a single control pulse is  $T_c$  (assuming two identical control pulses), then as a consequence the temporal multimode capacity is reduced to  $N_t^{sw} = (1/\Delta - T_c)/T_m$ . In this article we will calculate the required duration  $T_c$  assuming a specific adiabatic pulse proposed by Tian et al. [36], which is particularly efficient given a constraint of the total cut-off duration  $T_c$ .

### 3. Theoretical temporal multimode capacity

#### 3.1. Capacity limit of the AFC fixed-delay memory due to Nyquist-Shannon sampling theorem

The preservation of temporal information is closely related to the Nyquist-Shannon sampling theorem, which roughly states that a modulated signal can be supported by the system bandwidth  $\Gamma$  (in Hz), here the memory bandwidth, only if the frequency of modulation  $f_s$  (or sampling frequency) is less or equal to half the bandwidth, i.e.  $f_s \leq \Gamma/2$ . In our case the train of input pulses is modulated in amplitude at a frequency of  $f_s = 1/T_m$ , where  $T_m$  is the mode spacing, which results in the condition  $T_m \geq 2/\Gamma$ . Hence, there is a strict minimum mode size  $T_m$  imposed by the AFC bandwidth, independently of the exact temporal shape of the mode inside the mode  $T_m$ .

This point can be illustrated further by looking at the Fourier transform of a train of pulses of equal amplitude. In Fig. 2 the Fourier spectrum of a sequence of 5 modes with  $T_m = 1 \mu\text{s}$  is shown. The mode spacing of  $T_m$  results in the two Fourier peaks at  $\pm f_s = \pm 1 \text{ MHz}$ . To preserve the information encoded at the modulation frequency  $f_s$ , then clearly one must have a total bandwidth of at least  $2f_s$ , which encapsulates the Nyquist-Shannon sampling theorem. Note that a sequence of modes with random amplitude and phase modulation have its Fourier information encoded within the Nyquist limits.

To completely capture the Fourier peaks at  $\pm f_s$  and to minimize distortion due to the truncation in Fourier space, one requires a slightly larger bandwidth. We here propose the following relation between the AFC memory bandwidth  $\Gamma$  and the input mode size  $T_m$ ,

$$T_m = \frac{2.5}{\Gamma}. \quad (1)$$

The temporal multimode capacity  $N_t$  for a AFC fixed-delay memory is then

$$N_t = \frac{1/\Delta}{T_m} = \frac{\Gamma}{2.5\Delta}. \quad (2)$$

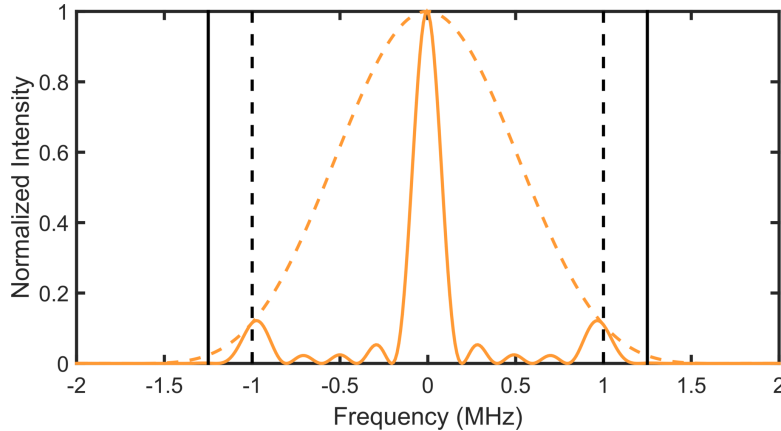


**Figure 2.** Fourier transform of a train of 5 Gaussian pulses of equal intensity with a FWHM of 410 ns (solid line), each truncated to a mode size of  $T_m = 1 \mu\text{s}$ . The Nyquist sampling limits at  $\pm 1/T_m = \pm 1 \text{ MHz}$  are indicated by dashed vertical lines. The proposed bandwidth limit corresponding to  $2.5/T_m$  is shown by the solid vertical lines. The Fourier transform of a single Gaussian mode is shown as a dashed line.

One can also rewrite the formula as  $N_t = N_{\text{tooth}}/2.5$ , where  $N_{\text{tooth}}$  is the number of teeth in the AFC, showing that each temporal mode requires about 2.5 additional peaks in the AFC.

The temporal mode capacity doesn't depend directly on the choice of pulse shape, nor on the FWHM of the pulse within the cut-off duration  $T_m$ . However, clearly one should also consider the pulse energy contained in the mode, given the mode profile. In general one can optimize the relation between the mode FWHM  $T$  and the mode size  $T_m$ , where we define  $T_m = \kappa T$ . In Appendix A the case of a Gaussian mode is treated in detail. It is shown that for  $\kappa \approx 2.38$  then 99.5% of the energy is contained both in the time cut-off  $T_m$  and in the power spectrum cut-off  $\Gamma$ . This choice is illustrated as the dashed line in Fig. 2. Other choices of  $\kappa$  might increase the energy content in either time or frequency domain, at the expense of less energy content in the reciprocal domain. In practice any choice in the range of  $\kappa = 2$  to  $\kappa = 2\sqrt{2}$  preserves at least 98.1% of the energy in either domain for Gaussian modes.

### 3.2. Effects of finite optical coherence time

The AFC echo memory efficiency is ultimately limited by the dephasing caused by decoherence on the optical transition. The optical coherence time, or equivalently the homogeneous linewidth, limits the AFC memory efficiency both in the optical pumping step (the AFC creation step), and during the actual storage time  $1/\Delta$ . State-of-the-art measurements of the AFC efficiency as a function of the fixed-delay  $1/\Delta$  storage time shows exponential decays [18,23,37]. In Ref. [23] it was argued, based on Maxwell-Bloch simulations of the AFC preparation step, that ultimately the AFC efficiency is limited by

$$\eta_{T_2} = \exp(-4/(\Delta T_2)), \quad (3)$$

where  $T_2$  is the optical coherence time of the transition [23]. Note that the relative  $\eta_{T_2}$  efficiency only accounts for the loss due to the optical  $T_2$  limitation, given the choice of optical storage time  $1/\Delta$ . See Ref. [23] for a more comprehensive discussion of the total AFC memory efficiency.

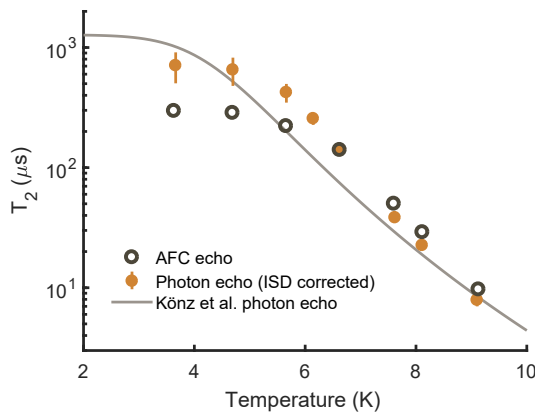


**Figure 3.** Coherence times obtained from AFC (open symbols) and PE (solid symbols) data in  $^{151}\text{Eu}:\text{Y}_2\text{SiO}_5$ , as a function of the sample temperature. The PE data has been corrected for instantaneous spectral diffusion in the conventional manner [38]. The PE data by Kőnz et al. [38] is shown for reference (solid line). The coherence times are also reported in Appendix B.

State-of-the-art AFC experiments [18, 23, 37] so far have not reached the  $T_2$  limit given by Eq. (3). To further investigate the effect of  $T_2$  we have performed both AFC efficiency decay measurements and photon echo (PE) measurements in  $^{151}\text{Eu}:\text{Y}_2\text{SiO}_5$ , as a function of temperature, see Appendix B for experimental details. The  $T_2$  data from the PE measurements are taken as the reference, which the effective  $T_2$  extracted from the AFC measurements should ideally reach. As shown in Figure 3, the PE and AFC coherence times do indeed converge at temperatures above 6.5 K, supporting the  $\eta_{T_2}$  limit introduced in Ref. [23]. The AFC coherence time of  $T_2 = 300 \pm 30 \mu\text{s}$  obtained at low temperatures is the longest reported AFC coherence time so far. Yet, the PE data results in  $T_2 = 707 \pm 204 \mu\text{s}$ , which is a significant difference that negatively affects the current temporal multimode capacity in  $^{151}\text{Eu}:\text{Y}_2\text{SiO}_5$ . We believe that the lower AFC  $T_2$  is due to technical issues, such as laser frequency drifts and/or dephasing induced by vibrations in the employed closed-cycle cryostats [39]. In Figure 3 the temperature dependence of the  $T_2$  measured by Kőnz et al. [38] in a Eu-doped  $\text{Y}_2\text{SiO}_5$  sample with natural isotopic abundance is shown as reference, where a slightly longer  $T_2$  of 1.27 ms was reached which we attribute to sample differences. It should also be noted that a coherence time up to 2.6 ms has been measured with PE in a Eu-doped  $\text{Y}_2\text{SiO}_5$  sample under a weak magnetic field [40]. Pr-doped  $\text{Y}_2\text{SiO}_5$  crystals generally have shorter

optical coherence times, reaching  $111 \mu\text{s}$  at 1.4 K at zero magnetic field and  $152 \mu\text{s}$  with a weak magnetic field [41]. The longest measured AFC  $T_2$  of  $92 \pm 6 \mu\text{s}$  is close to the PE coherence time (see Sec. 5.1), lending further support to Eq. (3).

In the following we assume that the loss of efficiency due to the optical coherence time can be modelled with Eq. (3), and we express  $\Delta$  as a function of  $\eta_{T_2}$  and insert the expression into Eq. (2), which gives a temporal multimode capacity of

$$N_t = \frac{\ln(1/\eta_{T_2})}{10} \Gamma T_2. \quad (4)$$

The factor  $\Gamma T_2$  is the ultimate upper limit of the mode capacity, as it represents the intrinsic time-bandwidth product of the memory. However, in practice only a small fraction of the memory can be exploited if an efficient storage is to be achieved. For  $\eta_{T_2} = 0.9$ , only about 1% of  $\Gamma T_2$  can be used, while for  $\eta_{T_2} = 0.5$  that factor goes up to 7% of  $\Gamma T_2$  but at the cost of significantly reduced efficiency. Furthermore, it should be pointed out that  $\Gamma$  is often limited by hyperfine and/or Zeeman splittings, which generally is much narrower than the entire optical inhomogeneous broadening.

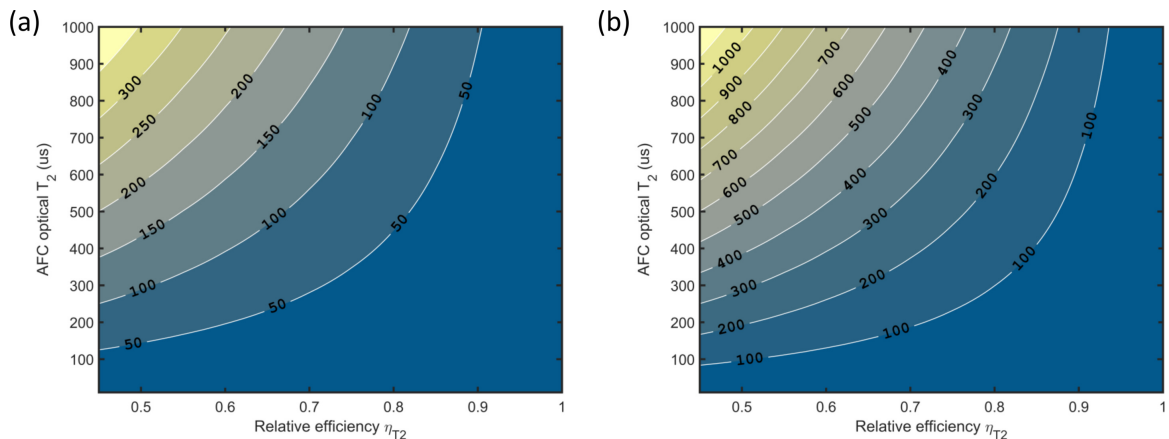


**Figure 4.** Contour plots of the temporal multimode capacity  $N_t$  of AFC fixed-delay memories as a function of the relative efficiency  $\eta_{T_2}$  and the AFC optical coherence time  $T_2$ , calculated using Eq. (4) for (a)  $\Gamma = 5 \text{ MHz}$  and (b)  $\Gamma = 15 \text{ MHz}$ .

It is illustrating to plot a contour map of the AFC echo multimode capacity as a function of optical  $T_2$  and relative efficiency  $\eta_{T_2}$ , as shown in Fig. 4(a) and (b) for a bandwidth of  $\Gamma = 5 \text{ MHz}$  and  $15 \text{ MHz}$ , respectively. These bandwidths are compatible with those achievable in the RE systems  $^{151}\text{Eu}:\text{Y}_2\text{SiO}_5$  and  $\text{Pr}:\text{Y}_2\text{SiO}_5$  (5 MHz), and  $^{153}\text{Eu}:\text{Y}_2\text{SiO}_5$  (15 MHz), respectively. The plots clearly show that achieving both high multimode capacity and high relative efficiency requires long optical coherence times, given the limitations in bandwidth.

### 3.3. Multimode capacity of the AFC spin-wave memory

AFC spin-wave memories require efficient transfer of the optical excitation over the entire bandwidth  $\Gamma$  of the AFC. This can be achieved by chirped adiabatic control pulses [35].

In NMR research, inversion pulses based on complex hyperbolic secant pulses, or sech pulses, were proposed for selective inversion of a flat frequency spectrum [33]. In the adiabatic regime the sech-pulse bandwidth is entirely determined by range of its frequency chirp width, which follows a smooth tanh function, with a flat transfer efficiency over that bandwidth that can approach 100% with the appropriate pulse parameters [34]. However, the sech pulse has a smooth almost Gaussian intensity profile, hence it doesn't make very efficient use of the cut-off duration  $T_c$  allocated to the control pulse. More recently Tian et al. [36] proposed an "extended" sech pulse, called a hyperbolic-square-hyperbolic (HSH) pulse, which has a flat intensity profile of duration  $T_s$  in the center and smoothed sech pulse edges, see Figure 1(c). The frequency chirp is still described by a tanh function, but with an extended linear regime in the center. As a result the HSH reaches significantly higher efficiency over the same bandwidth, given a cut-off duration  $T_c$ . The analysis here will be based on HSH control pulses, as efficient transfer using the shortest possible duration  $T_c$  is paramount for the temporal multimode capacity of AFC spin-wave memories.

For the analysis it is assumed that the HSH chirp width matches exactly the AFC bandwidth  $\Gamma$ . We further assume that the square part of the HSH pulse  $T_s$  is much longer than the edges of the HSH pulse, and that the chirp width  $\Gamma$  is significantly larger than the Rabi frequency  $\Omega$  of the pulse, the natural working regime for chirped, adiabatic pulses. Under these conditions the population transfer efficiency of the pulse can be written as (see Supplemental Material of Ref. [42])

$$\eta = 1 - \exp\left(-\pi^2 \frac{T_s \Omega^2}{\Gamma}\right). \quad (5)$$

Note that  $\Omega$  and  $\Gamma$  are defined in natural frequency (Hz) and not in angular frequency (rad/s) as in Ref. [42]. Now, by setting  $\pi^2 T_s \Omega^2 / \Gamma = 4$  it is assured that the transfer efficiency is at least 98%. In practice it will be slightly more efficient, as the smooth sech edges of the HSH pulse will also contribute to the transfer efficiency. If we introduce the relation  $T_c = \chi T_s$ , where  $\chi \gtrsim 1$ , it follows that the spin-wave multimode capacity  $N_t^{sw}$  can be expressed as

$$N_t^{sw} = \frac{1/\Delta - T_c}{T_m} = \frac{1}{2.5} \left( \frac{\Gamma}{\Delta} - \chi \frac{4}{\pi^2} \frac{\Gamma^2}{\Omega^2} \right), \quad (6)$$

where we have used Eq. (1). As it is assumed that  $\Gamma > \Omega$ , it follows that a certain number of modes will necessarily be consumed by the HSH pulse, where the exact number depends on the ratio  $\Gamma^2/\Omega^2$ . The AFC spin-wave multimode capacity can also be expressed as a function of  $\eta_{T_2}$  and  $T_2$  to account for the finite optical coherence time, by simply modifying the first term in Eq. (6) to yield

$$N_t^{sw} = \frac{1}{2.5} \left( \frac{\log(1/\eta_{T_2})}{4} \Gamma T_2 - \chi \frac{4}{\pi^2} \frac{\Gamma^2}{\Omega^2} \right) \quad (7)$$

#### 4. Temporal multimode storage experiments in $^{151}\text{Eu}:\text{Y}_2\text{SiO}_5$

##### 4.1. AFC fixed-delay multimode storage in $\text{Eu}:\text{Y}_2\text{SiO}_5$

Europium-doped  $\text{Y}_2\text{SiO}_5$  features long optical and spin coherence times, hence it is particularly favorable for temporal multimodality and long-duration spin storage. Storage experiments in the quantum regime have so far utilized the  $^{151}\text{Eu}$  isotope [20, 24, 32, 43]. Given the long AFC  $T_2$  obtained in the  $^{151}\text{Eu}:\text{Y}_2\text{SiO}_5$  system, it is particularly interesting to compare its experimental multimode storage capacity to the theoretical results obtained in Section 3.

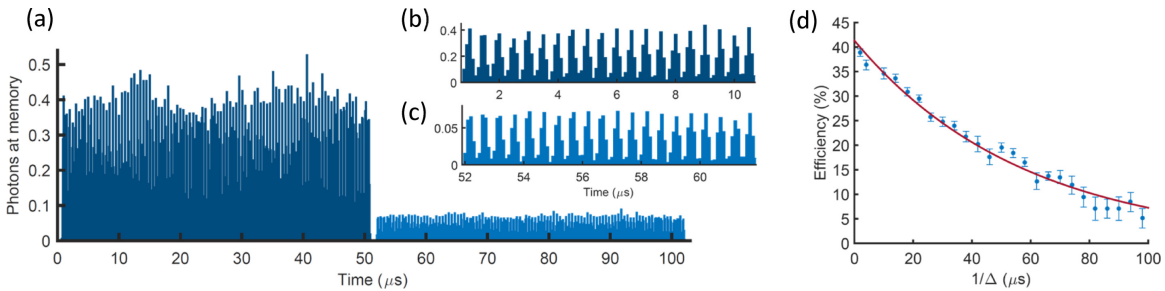


**Figure 5.** a) Storage of a train of 100 temporal modes in  $^{151}\text{Eu}:\text{Y}_2\text{SiO}_5$ , for a fixed duration of  $1/\Delta = 50.7 \mu\text{s}$  with a storage efficiency of 18%. Vertical axis shows average number of photons at the memory. The integrated average number of photons per pulse is about 1. Panels b) and c) shows a zoom on the first 20 input and output modes, respectively. d) The AFC echo efficiency as a function of storage time  $1/\Delta$ , resulting in a AFC coherence time of  $T_2 = 249 \pm 14 \mu\text{s}$  and a zero-time efficiency of  $41.3 \pm 1.7\%$ .

The bandwidth of  $^{151}\text{Eu}:\text{Y}_2\text{SiO}_5$  AFC memories are limited by overlapping optical-hyperfine transitions, which in turn depends on the choice of three-level system used for spin-wave storage. So far AFC experiments have used either the 35 MHz or 46 MHz spin transitions, which limits the bandwidth to less than 5.7 MHz. Here we set the memory bandwidth to  $\Gamma = 5$  MHz and the fixed storage time to  $1/\Delta = 50.7 \mu\text{s}$ , which results in a mode size of  $T_m = 500$  ns and a temporal multimode capacity of  $N_t = 100$  modes according to Eqs. (1) and (2), respectively. The intensity FWHM of the Gaussian modes were set to about 210 ns, giving a  $\kappa$  parameter close to the theoretical optimum of 2.38. The mean photon number in the input modes was  $\bar{n} = 0.99 \pm 0.05$ , integrated over the mode size  $T_m$ . The experimental photon counting histograms are displayed in Figure 5(a-c) and the zoom on the first 20 input/output modes shows clearly distinguishable modes with these mode settings. The average storage efficiency was  $18 \pm 2\%$ .

In Figure 5(d) the AFC echo efficiency for a single input mode is shown as a function of  $1/\Delta$ . The zero-time efficiency of 41.3% is the highest reported AFC echo efficiency without cavity enhancement. The AFC  $T_2 = 250 \mu\text{s}$  is slightly shorter than the value reported in Figure 3, which we attribute to larger sample vibrations in this experiment. The relative efficiency at  $1/\Delta = 50 \mu\text{s}$  is then  $\eta_{T_2} = 0.45$ . Given the bandwidth limitation of  $\Gamma = 5$  MHz, one can store  $N_t = 13$  modes at a relative efficiency of  $\eta_{T_2} = 0.9$ , and  $N_t = 28$  modes at  $\eta_{T_2} = 0.8$ , according to Eq. (4).



#### 4.2. Current and future spin-wave multimode capacity in $\text{Eu:Y}_2\text{SiO}_5$

Multimode AFC spin-wave storage experiments have been performed under different experimental conditions in  $^{151}\text{Eu:Y}_2\text{SiO}_5$  [20, 23, 32, 43]. Multimode storage of bright coherent input modes containing large numbers of photons has reached up to 50 modes [23]. The experiment used a long  $1/\Delta = 41 \mu\text{s}$ , and the AFC coherence time was relatively short at  $T_2 = 110 \mu\text{s}$ , as compared to the state-of-the-art values reported here and in [32]. In addition, the HSH was too short,  $T_c = 14 \mu\text{s}$ , for the memory bandwidth of  $\Gamma = 5 \text{ MHz}$ , resulting in a poor transfer efficiency of 55% per HSH pulse. These factors contributed to an efficiency of only 1.6%. The theoretical capacity with these values is 54 modes, according to  $N_t^{sw} = (1/\Delta - T_c)/T_m$  (see Eq. (6)) and Eq. (1), in close agreement with the experiment reported in [23].

Storage of weak coherent input pulses with a mean photon number of around 1 generally requires higher efficiencies given the read-out noise of the memory, particularly when spin-echo and dynamical decoupling techniques are employed to achieve long storage times [23, 32, 43]. Refs. [20, 43] showed storage of 5 temporal modes using the 35 MHz spin transition in  $^{151}\text{Eu:Y}_2\text{SiO}_5$ , with a spin-storage time of about 1 ms. Recently, storage of 6 temporal modes for a duration of  $T_{spin} = 20$  to 100 ms was demonstrated using the 46 MHz transition, based on dynamical decoupling (DD) of the spin transition. The main difficulty in combining spin-wave storage and DD of the spin transitions lies in the read-out noise generated by errors in the DD sequence [32, 43, 44]. To achieve high signal-to-noise ratio in this context requires a spin-wave storage efficiency in the range of 5-10%, which in turn reduces the multimode capacity.

The theoretical spin-wave capacity can be compared to the latest experiment in Ref. [32]. The AFC parameters were  $1/\Delta = 25 \mu\text{s}$  and  $\Gamma = 1.5 \text{ MHz}$ . The bandwidth was smaller than the maximum limit of 5 MHz, in order to optimize the HSH transfer pulse efficiency given the limited Rabi frequency of  $\Omega = 230 \text{ kHz}$ . The experimentally-optimized HSH pulse had parameters  $T_c = 15 \mu\text{s}$  and  $T_c = 11 \mu\text{s}$  (i.e.  $\chi = 1.36$ ). Using these values Eq. (6) predicts a storage capacity of  $N_t^{sw} = 5.6$  modes, in accordance with the experimentally optimized value of 6 modes. The small difference certainly lies in the strong dependence of  $N_t^{sw}$  on the Rabi frequency, which is the parameter with the largest experimental error. For example, with  $\Omega = 250 \text{ kHz}$  one finds  $N_t^{sw} = 7.1$  modes. The spin-wave storage efficiency at  $T_{spin} = 20 \text{ ms}$  was  $\eta_{sw} = (7.39 \pm 0.04)\%$ .

It is clear that the Rabi frequency seriously limits the currently achievable multimode capacity for AFC spin-wave memories in  $^{151}\text{Eu:Y}_2\text{SiO}_5$ . Currently the control pulse is applied on the weak transition of the lambda system [20, 23, 32, 43], in order to favor the input transition in terms of optical depth. However, it is known that impedance-matched cavities can achieve 100% memory efficiency using weak input transitions [45–49]. Hence, a way forward is to use the strong transition for the control pulse, and use a cavity to compensate the low absorption on the input transition. According to the table of transition strengths in  $\text{Eu:Y}_2\text{SiO}_5$  [50], this approach would boost the HSH Rabi frequency by a factor of 2.7, giving about  $\Omega = 620 \text{ kHz}$ .

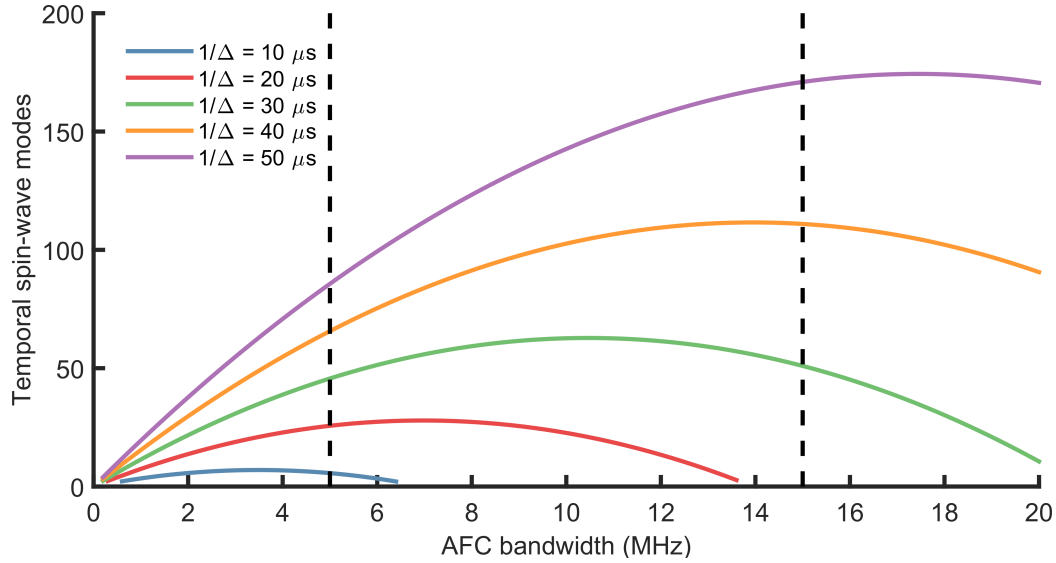


**Figure 6.** AFC spin-wave mode capacity  $N_t^{sw}$  as a function of bandwidth  $\Gamma$  according to Eq. (6), calculated using parameters  $\Omega = 620$  kHz,  $\chi = 1.36$ , and  $1/\Delta = 10 \mu\text{s}$  to  $50 \mu\text{s}$  by steps of  $10 \mu\text{s}$ . The left and right dashed, vertical lines at 5 and 15 MHz indicate the upper bandwidth limits of  $^{151}\text{Eu}$ , Pr (5 MHz) and  $^{153}\text{Eu}$  (15 MHz) in  $\text{Y}_2\text{SiO}_5$ .

In Fig. 6 the spin-wave multimode capacity is plotted as a function of memory bandwidth, over a range of excited state storage times  $1/\Delta$ , for a higher HSH Rabi frequency of  $\Omega = 620$  kHz. In general there is a maximum mode capacity for an optimum bandwidth  $\Gamma$ , given  $\Omega$  and  $1/\Delta$ , according to Eq. (6). However, one also needs to consider the maximum bandwidth supported by the physical system. The dashed lines in Fig. 6 show the approximately maximum bandwidths achievable in  $^{151}\text{Eu}:\text{Y}_2\text{SiO}_5$ , Pr: $\text{Y}_2\text{SiO}_5$  (5 MHz) and  $^{153}\text{Eu}:\text{Y}_2\text{SiO}_5$  (15 MHz), respectively. It follows from this plot that with an increased Rabi frequency, for  $^{151}\text{Eu}:\text{Y}_2\text{SiO}_5$  and Pr: $\text{Y}_2\text{SiO}_5$  the multimode capacity is chiefly limited by the system bandwidth. To reach a temporal multimode capacity of 100 or more with Europium would likely require shifting to  $^{153}\text{Eu}:\text{Y}_2\text{SiO}_5$ , and to use excited state storage times  $1/\Delta$  of  $40 \mu\text{s}$  or more. This in turn requires long AFC coherence times to simultaneously achieve high efficiencies, according to Eq. (3), which is in principle possible given the long optical coherence times in Eu: $\text{Y}_2\text{SiO}_5$  crystals. Finally we emphasize that waveguide-based quantum memories could provide a paradigm shift for higher bandwidth memories, as the mode confinement allows Rabi frequencies significantly higher than 1 MHz [51]. A particularly interesting system in this context is  $^{171}\text{Yb}:\text{Y}_2\text{SiO}_5$  [52], where memory bandwidths of at least 100 MHz are possible due to the larger hyperfine splittings [42].

## 5. Temporal multimode storage experiments in Pr: $\text{Y}_2\text{SiO}_5$

Compared to europium-doped  $\text{Y}_2\text{SiO}_5$ , praseodymium-doped  $\text{Y}_2\text{SiO}_5$  has shorter optical and spin coherence times. In the case of the optical transition, the inferred coherence

time from literature is  $152 \mu\text{s}$  at 1.4 K in the most commonly used crystallographic site [41]. However, the transition strength is larger, which can allow for shorter control pulses when performing spin wave storage. In the following two sections we will discuss the temporal multimode capacity of AFC fixed-delay and spin-wave memories in  $\text{Pr}:\text{Y}_2\text{SiO}_5$ .

### 5.1. AFC fixed-delay multimode storage in $\text{Pr}:\text{Y}_2\text{SiO}_5$

The longest reported AFC storage time in  $\text{Pr}^{3+}:\text{Y}_2\text{SiO}_5$  was  $1/\Delta = 25 \mu\text{s}$  in Ref. [18]. The bandwidth of the memory was  $\Gamma = 4 \text{ MHz}$ , limited by the hyperfine level spacing in Pr-doped  $\text{Y}_2\text{SiO}_5$ . Following Eq. (2), the maximum number of modes that can be stored is  $N_t = 40$  (where  $T_m = 625 \text{ ns}$ ). Ref. [18] contained an analysis of the concurrence and heralding rate for an experiment entangling two  $\text{Pr}^{3+}:\text{Y}_2\text{SiO}_5$  memories versus the number of possible stored temporal modes. It was shown that the heralding rate increases with the number of modes stored, demonstrating the advantage of temporal multimode storage.

In the same experiment, the  $T_2$  measured from the AFC storage efficiency was  $92 \pm 6 \mu\text{s}$ , which is very close to the  $T_2$  measured with photon echoes in the same sample of  $\text{Pr}^{3+}:\text{Y}_2\text{SiO}_5$ . The resulting relative efficiency for  $1/\Delta = 25 \mu\text{s}$  is then  $\eta_{T_2} = 0.34$ . It is not likely that the storage time can be significantly increased, given the optical coherence times in  $\text{Pr}^{3+}:\text{Y}_2\text{SiO}_5$  [41], but improvements in efficiency are still possible, which are also beneficial to obtaining high rates of entanglement distribution.

### 5.2. Spin-wave storage in $\text{Pr}:\text{Y}_2\text{SiO}_5$

The advantage in using  $\text{Pr}^{3+}:\text{Y}_2\text{SiO}_5$  for temporal multimode storage becomes more apparent when performing spin-wave storage. The higher optical transition dipole moment produces a higher Rabi frequency for the same optical intensity, as compared to Eu, thereby reducing  $T_c$  and thus allowing a larger temporal mode capacity given a similar  $\Gamma$  and  $\Delta$ .

We here present experimental results of temporal multimode spin-wave storage using  $\text{Pr}^{3+}:\text{Y}_2\text{SiO}_5$ . The experimental setup is similar to that of Ref. [16], except we used attenuated laser pulses (weak coherent states) as input modes. These had a Gaussian intensity profile, where the FWHM was  $T = 180 \text{ ns}$  and the input mode size was  $T_m = 620 \text{ ns}$ , resulting in  $\kappa = 3.4$ . The average number of photons per mode was  $0.90 \pm 0.05$ . The AFC delay was set to  $1/\Delta = 25 \mu\text{s}$  (the maximum storage time reported in the previous section), for which the AFC echo had an efficiency of  $(7.7 \pm 0.3) \%$ . The AFC bandwidth was  $\Gamma = 4 \text{ MHz}$ , and the control pulse Rabi frequency was  $\Omega = 410 \text{ kHz}$ . The control pulses were not HSH pulses, but less optimal pulses with a Gaussian profile and adiabatic frequency chirp spanning  $4.2 \text{ MHz}$ , where  $T_c = 5 \mu\text{s}$  and the FWHM is  $2.5 \mu\text{s}$ . The resulting transfer efficiency was  $(72 \pm 2) \%$ .

Figure 7 shows the retrieved temporal modes after spin-wave storage, where 20 modes were stored in (a) and 30 modes in (b). For 20 modes, the average signal to noise

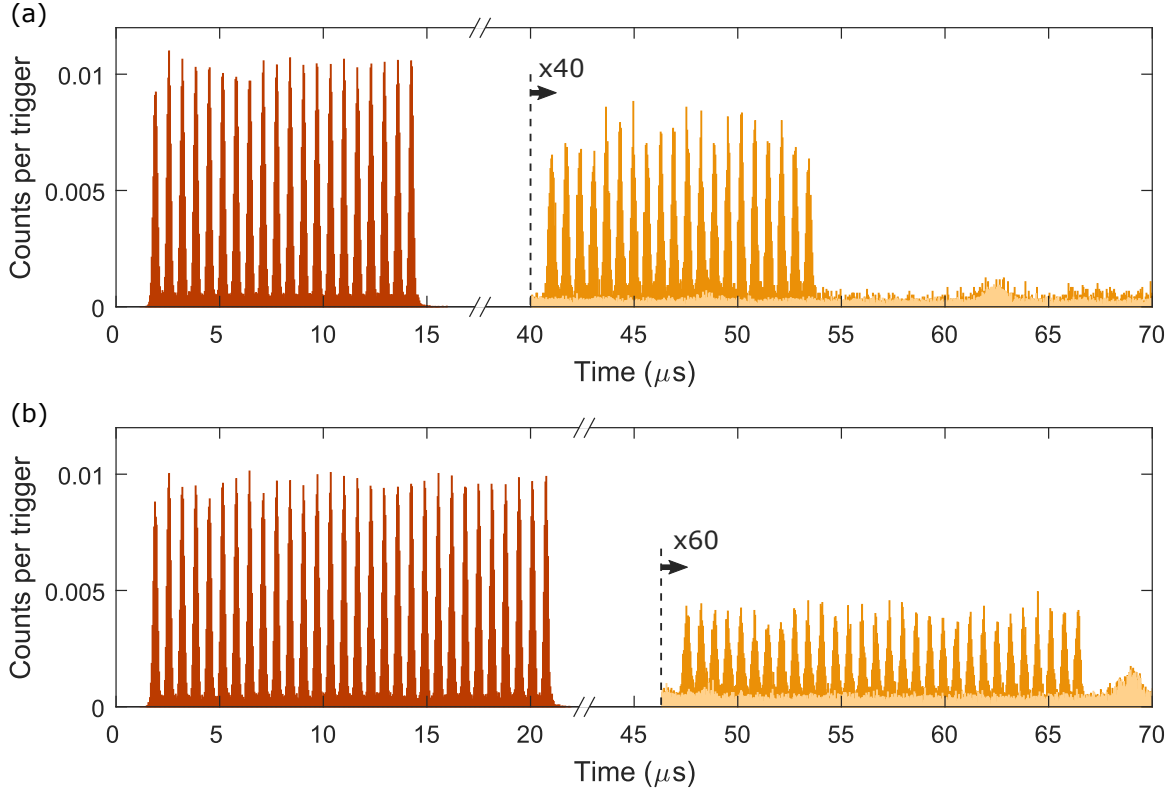


**Figure 7.** Input modes and retrieved spin-wave modes for (a) 20 input modes and (b) 30 input modes. The input modes measured through a transparency window in the memory are shown in brown, while the retrieved spin-wave modes are shown in orange, and the equivalent noise without storage is shown in light orange.

ratio,  $SNR$ , is  $17.4 \pm 0.4$ , with a corresponding spin-wave storage efficiency  $\eta_{sw}$  of  $(1.88 \pm 0.03) \%$ . For 30 modes,  $SNR = 6.7 \pm 0.1$ , with a corresponding efficiency of  $(0.63 \pm 0.01) \%$ . There is a drop in  $SNR$  and  $\eta_{sw}$  when storing more modes because different  $T_{spin}$  were used:  $14.1 \mu s$  and  $20.7 \mu s$  for 20 and 30 modes respectively. There will be a residual signal from the AFC echoes, due to the finite efficiency of the control pulses, so  $T_{spin}$  has a minimum length required to avoid the signal from the spin-wave output modes overlapping with the residual AFC echoes, which depends on the number of modes stored. The efficiency follows  $\exp(-\frac{(\pi T_{spin} \gamma_{spin})^2}{2 \ln(2)})$ , where  $\gamma_{spin}$  is the inhomogeneous broadening of the transition used for spin-wave storage, so  $\eta_{sw}$  decreases for longer  $T_{spin}$ . In this measurement,  $\gamma_{spin}$  was measured to be 26.3 kHz. We can reduce this to 16.1 kHz in more ideal experimental conditions [16], which would increase the average efficiencies to approximately 3.5 % and 2.4 % for 20 and 30 modes respectively.

Given the  $T_c$  of  $5 \mu s$ , the ideal  $T_m$ , and the AFC storage time  $1/\Delta = 25 \mu s$ , it should be possible to store  $N_t^{sw} = 32$  modes, in agreement with the 30 modes stored in Fig. 7(b). However, the control pulses have neither the ideal profile or optimum transfer efficiency. Using Eq. (6), which does assume a higher transfer efficiency (and taking  $\chi = 1.36$  like the Eu experiments), the maximum number of possible modes is

19. Although we can currently store more modes by using control pulses with a lower transfer efficiency, longer pulses are required to increase the efficiency, which reduces the number of modes. Nonetheless, this still shows the benefit of using materials allowing strong Rabi frequencies for temporally multimode spin-wave storage.

## 6. Multiplexing in other degrees of freedom

### 6.1. Spectral multimodality

*6.1.1. General discussion* The wide inhomogeneous broadening of rare earth doped crystals (REDC) offers a significant intrinsic advantage in terms of spectral multimodality. This is a static effect that increases the absorption spectrum of the system, which is enlarged by several orders of magnitude if compared to the absorption line of each single ion. For example in  $\text{Pr}^{3+}:\text{Y}_2\text{SiO}_5$  it results in an increase in absorption from 1 kHz to 10 GHz.

The maximum number of spectral modes that can be stored along the inhomogeneous absorption of REDCs can be quantified by considering the level scheme of each single ion. Each time that we perform spectral hole burning, holes and antiholes are created throughout the inhomogeneous broadening, the most distant ones appearing at the frequencies  $\Delta g + \Delta e$  and  $-(\Delta g + \Delta e)$  [34], where  $\Delta g$  ( $\Delta e$ ) represents the total spacing between the highest and the lowest ground (excited) levels. If the spectrum of the feature that we are generating is  $\Gamma$ , it will affect ions within the frequency range  $\pm(\Delta g + \Delta e + \Gamma/2)$ . Thus, to create different independent AFCs (each for a different frequency mode) in the inhomogeneous broadening of a REDC, so to avoid that the tailoring of one AFC degrades the others, we will have to place the AFCs at a distance larger than  $2(\Delta g + \Delta e) + \Gamma$  between each other (see Fig. 8). For a square inhomogeneous broadening of width  $\Gamma_{inhom}$ , the number of frequency modes that can be stored,  $N_m^f$ , shown in Fig. 8(b), can be defined as

$$N_f = \Gamma_{inhom}/(2(\Delta g + \Delta e) + \Gamma). \quad (8)$$

In reality, the inhomogeneous broadening is not flat and its shape will determine a different maximal OD for each of the spectral modes AFCs. The decrease in OD will also limit their maximal efficiency, as shown in Fig. 9 (this is not the case when using an impedance matching (IM) cavity). We calculate the maximal efficiency reachable for different ODs using the following formula [53]:

$$\eta_{afc}^b = (1 - \tilde{d})^2 \text{sinc}^2(\pi/F)$$

This formula is valid for a comb with square peaks (providing the highest efficiency) and backward retrieval from the crystal, which could be implemented by performing spin-wave storage with counter-propagating control pulses (this formula is only for the AFC and does not take into account the efficiency of the transfer pulses). Note that backward retrieval can also be reached using an IM cavity, but the calculations for the efficiency in that case would require a more complex treatment.

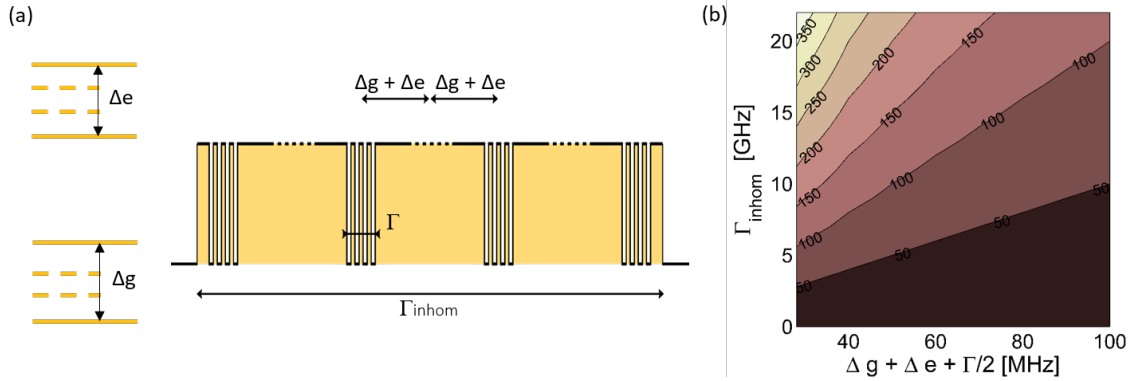


**Figure 8.** (a) (left) We assume hyperfine energy structures spanning  $\Delta g$  and  $\Delta e$  in the ground and excited states, respectively. (right) To avoid interference between side and anti-holes belonging to different AFCs, each with spectral width  $\Gamma$ , one must separate the AFCs with at least  $2(\Delta g + \Delta e) + \Gamma$  within the inhomogeneous absorption profile. (b) Contour plots of the frequency multimode capacity  $N_f$  of AFC memories (fixed-delay and spin-wave) as a function of the required frequency span of one AFC, see text for details.

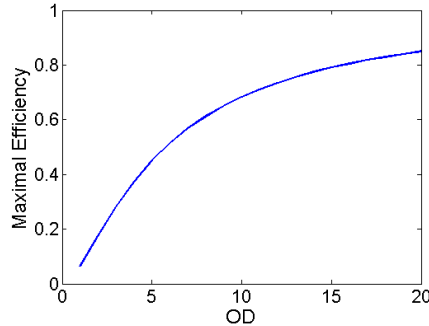


**Figure 9.** Theoretical AFC memory efficiency for backward recall as a function of peak optical depth of the AFC.

*6.1.2. Discussion for  $\text{Pr}^{3+}:\text{Y}_2\text{SiO}_5$*  The OD of a REDC can be calculated as  $\text{OD} = \alpha L$ , with  $\alpha$  being the absorption coefficient and  $L$  the length of the crystal. We consider a 5 cm long Pr:YSO crystal with a doping concentration of 0.05%. For this crystal  $\alpha = 20/\text{cm}$  in the center of the inhomogeneous broadening [34], corresponding to an  $\text{OD} = 10$ . The inhomogeneous broadening in such crystal is well described by a Gaussian distribution with a FWHM of  $\sim 10$  GHz in OD [51, 54]. From the level scheme of the ions in this crystal,  $\Delta g + \Delta e = 36.9\text{MHz}$ . The spectral feature that we need to create include the comb, but also a larger window to allow the application of control pulses, so we consider  $\Gamma = 18$  MHz. Given  $2(\Delta g + \Delta e) + \Gamma = 91.8$  MHz (we consider 92 MHz for simplicity), figure 10 shows the number of modes that can be stored in such a system with the corresponding efficiencies. Each of the frequency modes can be stored with a different maximal efficiency (panel (b)), calculated as in Fig. 9. In panel (c) we plot the mean storage efficiency of the stored modes, also for different maximal ODs of

the crystal. In Panel (d), finally, we plot the ratio between the mean efficiency of the stored modes and the single mode case (highest efficiency, storing only one mode in the center of the inhomogeneous broadening), showing therefore the lose in efficiency while increasing the number of stored modes.

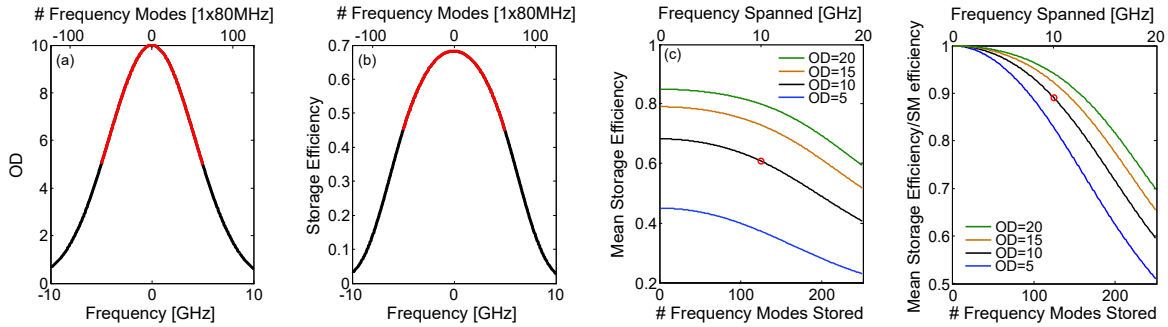


**Figure 10.** The panels show the number of frequency modes and their maximum efficiency (in the ideal case of ideal backward AFC recall) that can be achieved with Pr-doped  $\text{Y}_2\text{SiO}_5$ , see text for details.

In  $\text{Pr}^{3+}:\text{Y}_2\text{SiO}_5$  frequency multiplexing has been demonstrated in the case of storage in the excited state, where 15 frequency bins of a photon pair separated by 261 MHz and spanning almost 4 GHz have been stored simultaneously in a waveguide-integrated memory [27], and in the spin state, with the storage of weak coherent states in two spectral modes as distant as 80 MHz [55]. In a  $\text{Ti}:\text{Tm}:\text{LiNbO}_3$  waveguide storage of weak coherent states multiplexed in 26 frequency modes have been demonstrated, followed by feed-forward-controlled frequency manipulation [26].

**6.1.3. Impedance matched cavity** In the case of an impedance matched cavity, mirrors with different reflections can be chosen in order to have close to 100% storage efficiency even for very low ODs (provided that the system losses are negligible compared to the OD). In the case of frequency multimode storage, one can build the cavity to give the highest efficiency, for example, for half of the maximal OD of the system. In this case, all the modes inside  $\Gamma_{inhom}$  could be stored with the same high efficiency just by populating the higher-OD transitions with less atoms. There would be only two requirements: the linewidth of the cavity in the center of the inhomogeneous broadening (reduced due to slow light effect [47]) should be wider than the comb size; the spectral modes to be stored (and the corresponding AFCs) should be in resonance with the IM cavity (not very demanding as the slowlight will reduce massively the FSR of the cavity).

## 6.2. Spatial multiplexing

Spatial multimodality can also be employed to increase significantly the number of modes in REDC. In this case, any additional spatial mode stored would not result into a decrease in efficiency (differently from the temporal multimodality, in which either the  $T_2$  of the system or the separation between the modes would decrease the total

efficiency, or from spectral multimodality where the maximal OD would result in a different maximal efficiency per spectral mode). The efficiency would remain constant because, in REDC, the OD is flat for parallel beam paths across the surface of the crystal. This is in contrast to atomic clouds, where, depending on the beam position with respect to the center of the cloud itself, each of the spatial mode sees a different OD, similarly to the limitation that REDCs show for spectral multimodality. Nonetheless cold atomic clouds do not show a static inhomogeneous broadening, meaning that they cannot take advantage of spectral multiplexing. For this reason the spatial degree of freedom has been largely exploited in such systems [8, 56–58].

In REDCs, different spatial modes could be realised using for example electro-optical deflectors addressing different positions in the crystal, as demonstrated in atomic clouds [8]. In an integrated configuration, a matrix of waveguides could be generated along the length of the sample. In the case of integrated waveguides, one could address the different memories using commercial fiber arrays, which are at a distance of  $127\mu\text{m}$  between each other, which would result in 62 modes per  $\text{mm}^2$  of crystal surface. Note that this is not a fundamental limitation: if a glass chip would be used in the incoupling and outcoupling, then the chips could be fabricated to terminate into a much denser matrix, increasing the number of modes in the crystal by more than one order of magnitude and limited only by evanescent coupling among the waveguides.

In the discussion above we called spatial multimodality different spatial paths through the same memory. There are also other ways to exploit spatial multiplexing, which rely on using orthogonal sets of different spatial distributions of the phases of the photons (along the same optical path). Some examples of these are: twisted light (such as optical-angular momentum states [7, 55, 59, 60] or vector vortex beam), Hermite–Gaussian or Laguerre–Gaussian modes.

For quantum repeater operations [3], each of the spatial modes could be addressed by an independent photon source. This solution would make the scaling challenging. This limitation only affects the case of an external source, while would not be a problem for emissive memories [8, 24, 25]. However, even for absorptive memories the number of independent sources could be drastically reduced by using switches that could direct photons from a same source to different spatial modes at different times. With this technique, one would first fill the first spatial mode with temporal modes, and then switch to the next spatial mode. One could therefore convert spatial to temporal multiplexing and take advantage of extending the temporal multiplexing to durations much larger than the excited state AFC storage time, in principle up to the communication time between the remote ensembles. One open challenge with bulk crystals is to combine the addressing of various spatial modes with cavity enhanced quantum memories to reach high storage and retrieval efficiencies. Cavities could be in principles incorporated to waveguide arrays, but more work is needed to reduce the loss.



## 7. Conclusions

In this article we have considered a detailed model for quantifying the temporal mode capacity of AFC fixed-delay and spin-wave memories. These formulas can be used to compare different materials and experimental configurations, based on measurable experimental quantities. Comparisons with state-of-the-art experiments in both Eu and Pr doped  $\text{Y}_2\text{SiO}_5$  crystals demonstrate the utility of the theoretical models and further highlight both current limitations and future strategies for increasing the temporal multimode capacity. We further consider the possibility of frequency and spatial multiplexing to further increase the multimode capacity, a key performance factor for future quantum repeaters.

## 8. Acknowledgments

This work was financially supported by the European Union Horizon 2020 research and innovation program within the Flagship on Quantum Technologies through GA 820445 (QIA), by the Marie Skłodowska-Curie program through GA 675662 (QCALL), and by the Swiss FNS NCCR programme Quantum Science Technology (QSIT).

## Appendix A. Gaussian temporal mode profile

The intensity profile of a Gaussian pulse with FWHM of  $T$  can be written as

$$I(t) = \exp(-4 \ln 2 \cdot t^2/T^2) \quad (\text{A.1})$$

Note that the field amplitude FWHM duration is  $\sqrt{2} \cdot T$ . The corresponding power spectrum is

$$I(f) = \exp(-f^2 T^2 \pi^2 / \ln 2) \quad (\text{A.2})$$

where the FWHM (in Hz) is

$$\gamma = \frac{2 \ln 2}{\pi} \frac{1}{T} \quad (\text{A.3})$$

Note that we work with power (or intensity), and not field amplitude.

The goal here is to find an optimal relation between the pulse FWHM in time  $T$ , and the mode size  $T_m$ . One natural choice is to set  $T_m = 2T$ , for which 98.1% of the pulse energy is contained in the mode. Another natural choice is to set  $T_m$  as twice the FWHM in the field amplitude, i.e.  $T_m = 2\sqrt{2}T$ , for which 99.9% of the energy is contained in the temporal mode bin. In practice any choice between these limits would yield low mode overlap in the time domain.

To find an optimal choice one can also calculate the ratio of the AFC bandwidth to the power spectrum FWHM of the input mode,

$$\frac{\Gamma}{\gamma} = \frac{\pi}{2 \ln 2} \Gamma T = \frac{2.5\pi}{2 \ln 2} \frac{T}{T_m}, \quad (\text{A.4})$$

where in the first step we used Eq. (A.3), and in the second step Eq. (1). Let's now set  $T_m = \kappa T$  which gives us

$$\frac{\Gamma}{\gamma} = \frac{2.5\pi}{2 \ln 2} \frac{1}{\kappa} \quad (\text{A.5})$$

The choice of  $\kappa = 2$ , or  $\kappa = 2\sqrt{2}$ , results in a ratio of  $\Gamma/\gamma \approx 2.83$ , or 2, respectively. These in turn result in 99.9% and 98.1% of the power spectrum being contained in the AFC bandwidth of  $\Gamma$ . Comparing the two different choices it is clear that they either includes a larger portion in the time cut-off ( $T_m$ ), or in the power spectrum cut-off  $\Gamma$ , respectively. Interestingly one can force the same energy content in the cut-off in both domains, by requiring

$$\kappa = \frac{2.5\pi}{2 \ln 2} \frac{1}{\kappa} \quad (\text{A.6})$$

which can be solved to yield an optimum choice of  $\kappa$

$$\kappa = \sqrt{\frac{2.5\pi}{2 \ln 2}} \approx 2.38 \quad (\text{A.7})$$

With this choice, 99.5% of the power is contained in the cut-offs of both domains.

The calculations above serve to demonstrate that the precise choice of  $\kappa$  is not very critical, as soon as it is comprised between  $\kappa = 2$  and  $\kappa = 2\sqrt{2}$ . It should also be noted that all formulas were derived assuming that the Fourier spectrum follows a Gaussian profile given by an *ideal Gaussian pulse without truncation*. This is idealized, and in reality the cut-off in the time domain will slightly modify the Fourier spectrum. If  $\kappa$  is chosen in the proposed region any correction factor is still low (i.e. less than 1%). For the optimal choice of  $\kappa = 2.38$  this effect is particularly negligible, and the truncated Fourier spectrum still contains 99.4% of the pulse energy within the AFC bandwidth of  $\Gamma$ .

## Appendix B. AFC and PE coherence times recorded in $^{151}\text{Eu}:\text{Y}_2\text{SiO}_5$

The effective coherence times extracted from the AFC fixed-delay storage experiments and the corresponding photon echo (PE) coherence times are shown in Table B1, as a function of temperature. The PE data was corrected for the contribution of instantaneous spectral diffusion [38].

- [1] Briegel H J, Dür W, Cirac J I and Zoller P 1998 *Phys. Rev. Lett.* **81** 5932–5935
- [2] Duan L M, Lukin M D, Cirac J I and Zoller P 2001 *Nature* **414** 413–418
- [3] Simon C, de Riedmatten H, Afzelius M, Sangouard N, Zbinden H and Gisin N 2007 *Phys. Rev. Lett.* **98** 190503
- [4] Sangouard N, Dubessy R and Simon C 2009 *Phys. Rev. A* **79** 042340
- [5] Sangouard N, Simon C, de Riedmatten H and Gisin N 2011 *Rev. Mod. Phys.* **83** 33–80
- [6] Collins O A, Jenkins S D, Kuzmich A and Kennedy T A B 2007 *Phys. Rev. Lett.* **98** 060502–4
- [7] Nicolas A, Veissier L, Giner L, Giacobino E, Maxein D and Laurat J 2014 *Nature Photonics* **8** 234–238
- [8] Pu Y F, Jiang N, Chang W, Yang H X, Li C and Duan L M 2017 *Nature Communications* **8**
- [9] Parniak M, Dabrowski M, Mazelanik M, Leszczyński A, Lipka M and Wasilewski W 2017 *Nature Communications* **8**
- [10] Lipka M, Mazelanik M, Leszczyński A, Wasilewski W and Parniak M 2021 *Communications Physics* **4**
- [11] Heller L, Farrera P, Heinze G and de Riedmatten H 2020 *Physical Review Letters* **124** 210504
- [12] Afzelius M, Simon C, de Riedmatten H and Gisin N 2009 *Phys. Rev. A* **79** 052329
- [13] de Riedmatten H, Afzelius M, Staudt M U, Simon C and Gisin N 2008 *Nature* **456** 773–777
- [14] Clausen C, Usmani I, Bussières F, Sangouard N, Afzelius M, de Riedmatten H and Gisin N 2011 *Nature* **469** 508–511
- [15] Saglamyurek E, Sinclair N, Jin J, Slater J A, Oblak D, Bussières F, George M, Ricken R, Sohler W and Tittel W 2011 *Nature* **469** 512–515
- [16] Rakonjac J V, Lago-Rivera D, Seri A, Mazzera M, Grandi S and de Riedmatten H 2021 *Physical Review Letters* **127** 210502
- [17] Usmani I, Clausen C, Bussières F, Sangouard N, Afzelius M and Gisin N 2012 *Nature Photonics* **6** 234–237
- [18] Lago-Rivera D, Grandi S, Rakonjac J V, Seri A and de Riedmatten H 2021 *Nature* **594** 37–40
- [19] Gündoğan M, Ledingham P M, Kutluer K, Mazzera M and de Riedmatten H 2015 *Phys. Rev. Lett.* **114**(23) 230501
- [20] Laplane C, Jobez P, Etesse J, Timoney N, Gisin N and Afzelius M 2016 *New Journal of Physics* **18** 013006
- [21] Seri A, Lenhard A, Rieländer D, Gündoğan M, Ledingham P M, Mazzera M and de Riedmatten H 2017 *Phys. Rev. X* **7**(2) 021028
- [22] Usmani I, Afzelius M, de Riedmatten H and Gisin N 2010 *Nature Communications* **1** 1–7

$T$ (K)	$T_2^{\text{PE}}$ ( $\mu\text{s}$ )	$T_2^{\text{AFC}}$ ( $\mu\text{s}$ )
3.7	$707 \pm 204$	$300 \pm 30$
4.7	$651 \pm 172$	$290 \pm 20$
5.7	$423 \pm 75$	$222 \pm 13$
6.1	$256 \pm 29$	—
6.6	$140 \pm 9$	$140 \pm 3$
7.6	$38 \pm 2$	$50.1 \pm 1.1$
8.1	$23 \pm 1$	$29.0 \pm 0.4$
9.1	$8 \pm 1$	$9.7 \pm 1.2$

**Table B1.** Photon echo and AFC coherence times in  $^{151}\text{Eu}:\text{Y}_2\text{SiO}_5$ .

- [23] Jobez P, Timoney N, Laplane C, Etesse J, Ferrier A, Goldner P, Gisin N and Afzelius M 2016 *Phys. Rev. A* **93**(3) 032327
- [24] Laplane C, Jobez P, Etesse J, Gisin N and Afzelius M 2017 *Phys. Rev. Lett.* **118**(21) 210501
- [25] Kutluer K, Mazzera M and de Riedmatten H 2017 *Phys. Rev. Lett.* **118**(21) 210502
- [26] Sinclair N, Saglamyurek E, Mallahzadeh H, Slater J H, George M, Ricken R, Hedges M P, Oblak D, Simon C, Sohler W and Tittel W 2014 *Phys. Rev. Lett.* **113** 053603
- [27] Seri A, Lago-Rivera D, Lenhard A, Corrielli G, Osellame R, Mazzera M and de Riedmatten H 2019 *Physical Review Letters* **123** 080502
- [28] Thiel C, Böttger T and Cone R 2011 *Journal of Luminescence* **131** 353 – 361
- [29] Longdell J J, Fraval E, Sellars M J and Manson N B 2005 *Phys. Rev. Lett.* **95** 063601–4
- [30] Heinze G, Hubrich C and Halfmann T 2013 *Phys. Rev. Lett.* **111**(3) 033601
- [31] Holzäpfel A, Etesse J, Kaczmarek K T, Tiranov A, Gisin N and Afzelius M 2020 *New Journal of Physics* **22** 063009
- [32] Ortu A, Holzäpfel A, Etesse J and Afzelius M 2021 *arXiv:2109.06669*
- [33] Silver M S, Joseph R I and Hoult D I 1985 *Phys. Rev. A* **31**(4) 2753–2755
- [34] Rippe L, Nilsson M, Kröll S, Klieber R and Suter D 2005 *Phys. Rev. A* **71** 062328
- [35] Minář J, Sangouard N, Afzelius M, de Riedmatten H and Gisin N 2010 *Phys. Rev. A* **82** 042309
- [36] Tian M, Chang T, Merkel K D and Randall W 2011 *Appl. Opt.* **50** 6548–6554
- [37] Askarani M F, Das A, Davidson J H, Amaral G C, Sinclair N, Slater J A, Marzban S, Thiel C W, Cone R L, Oblak D and Tittel W 2021 *Physical Review Letters* **127** 220502
- [38] Könz F, Sun Y, Thiel C W, Cone R L, Equall R W, Hutcheson R L and Macfarlane R M 2003 *Phys. Rev. B* **68** 085109
- [39] Louchet-Chauvet A, Ahlefeldt R and Chaneière T 2019 *Review of Scientific Instruments* **90** 034901
- [40] Equall R W, Sun Y, Cone R L and Macfarlane R M 1994 *Phys. Rev. Lett.* **72** 2179
- [41] Equall R W, Cone R L and Macfarlane R M 1995 *Phys. Rev. B* **52**(6) 3963–3969
- [42] Businger M, Tiranov A, Kaczmarek K T, Welinski S, Zhang Z, Ferrier A, Goldner P and Afzelius M 2020 *Phys. Rev. Lett.* **124**(5) 053606
- [43] Jobez P, Laplane C, Timoney N, Gisin N, Ferrier A, Goldner P and Afzelius M 2015 *Phys. Rev. Lett.* **114**(23) 230502
- [44] Zambrini Cruzeiro E, Fröwis F, Timoney N and Afzelius M 2016 *Journal of Modern Optics* **63** 2101–2113
- [45] Moiseev S A, Andrianov S N and Gubaidullin F F 2010 *Phys. Rev. A* **82** 022311
- [46] Afzelius M and Simon C 2010 *Physical Review A* **82** 022310
- [47] Sabooni M, Li Q, Kröll S S and Rippe L 2013 *Phys. Rev. Lett.* **110** 133604
- [48] Jobez P, Usmani I, Timoney N, Laplane C, Gisin N and Afzelius M 2014 *New Journal of Physics* **16** 083005
- [49] Davidson J H, Lefebvre P, Zhang J, Oblak D and Tittel W 2020 *Phys. Rev. A* **101**(4) 042333
- [50] Zambrini Cruzeiro E, Etesse J, Tiranov A, Bourdel P A, Fröwis F, Goldner P, Gisin N and Afzelius M 2018 *Phys. Rev. B* **97**(9) 094416
- [51] Seri A, Corrielli G, Lago-Rivera D, Lenhard A, de Riedmatten H, Osellame R and Mazzera M 2018 *Optica* **5** 934–941
- [52] Ortu A, Tiranov A, Welinski S, Fröwis F, Gisin N, Ferrier A, Goldner P and Afzelius M 2018 *Nature Materials* **17** 671–675
- [53] de Riedmatten H and Afzelius M 2015 *Quantum Light Storage in Solid State Atomic Ensembles* (Springer International Publishing) chap 9, pp 241–268 Nano-Optics and Nanophotonics
- [54] Corrielli G, Seri A, Mazzera M, Osellame R and de Riedmatten H 2016 *Physical Review Applied* **5** 054013
- [55] Yang T S, Zhou Z Q, Hua Y L, Liu X, Li Z F, Li P Y, Ma Y, Liu C, Liang P J, Li X, Xiao Y X, Hu J, Li C F and Guo G C 2018 *Nature Communications* **9** 3407
- [56] Lan S Y, Radnaev A G, Collins O A, Matsukevich D N, Kennedy T A and Kuzmich A 2009 *Opt. Express* **17** 13639–13645

- [57] Chrapkiewicz R, Dąbrowski M and Wasilewski W 2017 *Physical Review Letters* **118** 063603
- [58] Tian L, Xu Z, Chen L, Ge W, Yuan H, Wen Y, Wang S, Li S and Wang H 2017 *Physical Review Letters* **119** 130505
- [59] Ding D S, Zhang W, Zhou Z Y, Shi S, Xiang G Y, Wang X S, Jiang Y K, Shi B S and Guo G C 2015 *Physical Review Letters* **114** 050502
- [60] Zhou Z Q, Hua Y L, Liu X, Chen G, Xu J S, Han Y J, Li C F and Guo G C 2015 *Physical Review Letters* **115** 070502

# Bibliography

1. Benioff, P. The computer as a physical system: A microscopic quantum mechanical Hamiltonian model of computers as represented by Turing machines. *Journal of Statistical Physics* **22**, 563–591. ISSN: 1572-9613. <https://doi.org/10.1007/BF01011339> (May 1980) (cit. on p. 2).
2. Feynman, R. P. Simulating physics with computers. *International Journal of Theoretical Physics* **21**, 467–488. ISSN: 1572-9575. <https://doi.org/10.1007/BF02650179> (June 1982) (cit. on p. 2).
3. Bennett, C. H. & Brassard, G. Quantum Key Distribution and coin tossing. *Proceedings of the IEEE International Conference on Computers, Systems, and Signal Processing.*, 175–179 (Dec. 1984) (cit. on p. 2).
4. Ekert, A. K. Quantum cryptography based on Bell's theorem. *Phys. Rev. Lett.* **67**, 661–. <http://link.aps.org/abstract/PRL/v67/p661> (Aug. 1991) (cit. on p. 2).
5. Wootters, W. K. & Zurek, W. H. A single quantum cannot be cloned. *Nature* **299**, 802–803. <http://dx.doi.org/10.1038/299802a0> (Oct. 1982) (cit. on p. 2).
6. Boaron, A. *et al.* Secure Quantum Key Distribution over 421 km of Optical Fiber. *Phys. Rev. Lett.* **121**, 190502. <https://link.aps.org/doi/10.1103/PhysRevLett.121.190502> (19 Nov. 2018) (cit. on p. 2).
7. Minder, M. *et al.* Experimental quantum key distribution beyond the repeaterless secret key capacity. *Nature Photonics* **13**, 334–338. ISSN: 1749-4893. <https://doi.org/10.1038/s41566-019-0377-7> (May 2019) (cit. on p. 2).
8. Chen, J.-P. *et al.* Sending-or-Not-Sending with Independent Lasers: Secure Twin-Field Quantum Key Distribution over 509 km. *Phys. Rev. Lett.* **124**, 070501. <https://link.aps.org/doi/10.1103/PhysRevLett.124.070501> (7 Feb. 2020) (cit. on p. 2).
9. Briegel, H.-J., Dür, W., Cirac, J. I. & Zoller, P. Quantum Repeaters: The Role of Imperfect Local Operations in Quantum Communication. *Phys. Rev. Lett.* **81**, 5932–5935. <https://doi.org/10.1103/PhysRevLett.81.5932> (Dec. 1998) (cit. on pp. 3, 7).

10. Kimble, H. J. The quantum internet. *Nature* **453**, 1023–1030. <http://dx.doi.org/10.1038/nature07127> (June 2008) (cit. on p. 3).
11. Sangouard, N., Simon, C., de Riedmatten, H. & Gisin, N. Quantum repeaters based on atomic ensembles and linear optics. *Rev. Mod. Phys.* **83**, 33–80. <http://link.aps.org/doi/10.1103/RevModPhys.83.33> (Mar. 2011) (cit. on pp. 3, 91).
12. Bussi eres, F. *et al.* Prospective applications of optical quantum memories. *Journal of Modern Optics* **60**, 1519–1537. <https://doi.org/10.1080/09500340.2013.856482> (2013) (cit. on p. 3).
13. Bock, M. *et al.* High-fidelity entanglement between a trapped ion and a telecom photon via quantum frequency conversion. *Nature Communications* **9**, 1998. ISSN: 2041-1723. <https://doi.org/10.1038/s41467-018-04341-2> (May 2018) (cit. on p. 3).
14. Meraner, M. *et al.* Indistinguishable photons from a trapped-ion quantum network node. *Phys. Rev. A* **102**, 052614. <https://link.aps.org/doi/10.1103/PhysRevA.102.052614> (5 Nov. 2020) (cit. on p. 3).
15. Langenfeld, S., Thomas, P., Morin, O. & Rempe, G. Quantum Repeater Node Demonstrating Unconditionally Secure Key Distribution. *Phys. Rev. Lett.* **126**, 230506. <https://link.aps.org/doi/10.1103/PhysRevLett.126.230506> (23 June 2021) (cit. on p. 3).
16. Pompili, M. *et al.* Realization of a multinode quantum network of remote solid-state qubits. *Science* **372**, 259–264. eprint: <https://www.science.org/doi/pdf/10.1126/science.abg1919>. <https://www.science.org/doi/abs/10.1126/science.abg1919> (2021) (cit. on p. 3).
17. Bhaskar, M. K. *et al.* Experimental demonstration of memory-enhanced quantum communication. *Nature* **580**, 60–64. ISSN: 1476-4687. <https://doi.org/10.1038/s41586-020-2103-5> (Apr. 2020) (cit. on p. 3).
18. Guo, J. *et al.* High-performance Raman quantum memory with optimal control in room temperature atoms. *Nature Communications* **10**, 148. ISSN: 2041-1723. <https://doi.org/10.1038/s41467-018-08118-5> (Jan. 2019) (cit. on p. 3).
19. Kaczmarek, K. T. *et al.* High-speed noise-free optical quantum memory. *Phys. Rev. A* **97**, 042316. <https://link.aps.org/doi/10.1103/PhysRevA.97.042316> (4 Apr. 2018) (cit. on p. 3).
20. Wang, X.-J. *et al.* Cavity-Enhanced Atom-Photon Entanglement with Sub-second Lifetime. *Phys. Rev. Lett.* **126**, 090501. <https://link.aps.org/doi/10.1103/PhysRevLett.126.090501> (9 Mar. 2021) (cit. on p. 3).

21. Corzo, N. V. *et al.* Waveguide-coupled single collective excitation of atomic arrays. *Nature* **566**, 359–362. ISSN: 1476-4687. <https://doi.org/10.1038/s41586-019-0902-3> (Feb. 2019) (cit. on p. 3).
22. Lipka, M., Mazelanik, M., Leszczyński, A., Wasilewski, W. & Parniak, M. Massively-multiplexed generation of Bell-type entanglement using a quantum memory. *Communications Physics* **4**, 46. ISSN: 2399-3650. <https://doi.org/10.1038/s42005-021-00551-1> (Mar. 2021) (cit. on p. 3).
23. Borregaard, J. *et al.* One-Way Quantum Repeater Based on Near-Deterministic Photon-Emitter Interfaces. *Phys. Rev. X* **10**, 021071. <https://link.aps.org/doi/10.1103/PhysRevX.10.021071> (2 June 2020) (cit. on p. 3).
24. Wallucks, A., Marinković, I., Hensen, B., Stockill, R. & Gröblacher, S. A quantum memory at telecom wavelengths. *Nature Physics* **16**, 772–777. ISSN: 1745-2481. <https://doi.org/10.1038/s41567-020-0891-z> (July 2020) (cit. on p. 3).
25. Kaplyanskii, A. & McFarlane, R. *Spectroscopy of Crystals Containing Rare Earth Ions* (Elsevier, 2012) (cit. on p. 3).
26. Rančić, M., Hedges, M. P., Ahlefeldt, R. L. & Sellars, M. J. Coherence time of over a second in a telecom-compatible quantum memory storage material. *Nature Physics* **14**. <https://doi.org/10.1038/nphys4254> (Jan. 2018) (cit. on pp. 4, 39).
27. Maring, N. *et al.* Storage of up-converted telecom photons in a doped crystal. *New Journal of Physics* **16**, 113021. <https://doi.org/10.1088/1367-2630/16/11/113021> (Nov. 2014) (cit. on p. 4).
28. Maring, N., Lago-Rivera, D., Lenhard, A., Heinze, G. & de Riedmatten, H. Quantum frequency conversion of memory-compatible single photons from 606nm to the telecom C-band. *Optica* **5**, 507–513. <http://www.osapublishing.org/optica/abstract.cfm?URI=optica-5-5-507> (May 2018) (cit. on p. 4).
29. Strassmann, P. C., Martin, A., Gisin, N. & Afzelius, M. Spectral noise in frequency conversion from the visible to the telecommunication C-band. *Opt. Express* **27**, 14298–14307. <http://www.osapublishing.org/oe/abstract.cfm?URI=oe-27-10-14298> (May 2019) (cit. on pp. 4, 101, 105).
30. Macfarlane, R. & Shelby, R. *Coherent Transients And Holeburning Spectroscopy In Rare Earth Ions In Solids; Spectroscopy Of Crystals Containing Rare Earth Ions* (eds Kaplyanskii, A. & Macfarlane, R.) (Elsevier Science Publishers, Amsterdam, Netherlands, 1987) (cit. on p. 4).
31. Fleischhauer, M. & Lukin, M. D. Quantum memory for photons: Dark-state polaritons. *Phys. Rev. A* **65**, 022314–. <http://link.aps.org/abstract/PRA/v65/e022314> (Jan. 2002) (cit. on p. 6).



32. Nunn, J. *et al.* Mapping broadband single-photon wave packets into an atomic memory. *Phys. Rev. A* **75**, 011401–4. <http://link.aps.org/abstract/PRA/v75/e011401> (Jan. 2007) (cit. on p. 6).
33. Moiseev, S. A. & Kröll, S. Complete Reconstruction of the Quantum State of a Single-Photon Wave Packet Absorbed by a Doppler-Broadened Transition. *Phys. Rev. Lett.* **87**, 173601. <http://link.aps.org/abstract/PRL/v87/e173601> (Oct. 2001) (cit. on p. 6).
34. Kraus, B. *et al.* Quantum memory for nonstationary light fields based on controlled reversible inhomogeneous broadening. *Phys. Rev. A* **73**, 020302. <http://link.aps.org/abstract/PRA/v73/e020302> (Feb. 2006) (cit. on p. 6).
35. Afzelius, M., Simon, C., de Riedmatten, H. & Gisin, N. Multimode quantum memory based on atomic frequency combs. *Phys. Rev. A* **79**, 052329. <http://link.aps.org/abstract/PRA/v79/e052329> (May 2009) (cit. on pp. 6, 41, 51, 52, 54).
36. Duan, L.-M., Lukin, M. D., Cirac, J. I. & Zoller, P. Long-distance quantum communication with atomic ensembles and linear optics. *Nature* **414**, 413–418. <http://dx.doi.org/10.1038/35106500> (Nov. 2001) (cit. on pp. 7, 91).
37. Samara, F. *et al.* Entanglement swapping between independent and asynchronous integrated photon-pair sources. *Quantum Science and Technology* **6**, 045024. <https://doi.org/10.1088/2058-9565/abf599> (Sept. 2021) (cit. on p. 7).
38. Kramers, H. *General theory of paramagnetic rotation in crystals* in *Proc. Acad. Sci. Amsterdam* **33** (1930), 959 (cit. on p. 11).
39. Clausen, C. *et al.* Quantum storage of photonic entanglement in a crystal. *Nature* **469**, 508–511. <http://dx.doi.org/10.1038/nature09662> (Jan. 2011) (cit. on p. 11).
40. Saglamyurek, E. *et al.* Broadband waveguide quantum memory for entangled photons. *Nature* **469**, 512–515. <http://dx.doi.org/10.1038/nature09719> (Jan. 2011) (cit. on p. 11).
41. Bussi eres, F. *et al.* Quantum teleportation from a telecom-wavelength photon to a solid-state. *Nature Photonics* **8**, 775–778. <https://doi.org/10.1038/nphoton.2014.215> (Oct. 2014) (cit. on p. 11).
42. Wolfowicz, G. *et al.* Coherent Storage of Microwave Excitations in Rare-Earth Nuclear Spins. *Phys. Rev. Lett.* **114**, 170503. <https://link.aps.org/doi/10.1103/PhysRevLett.114.170503> (17 Apr. 2015) (cit. on p. 12).

43. Welinski, S., Ferrier, A., Afzelius, M. & Goldner, P. High-resolution optical spectroscopy and magnetic properties of  $\text{Yb}^{3+}$  in  $\text{Y}_2\text{SiO}_5$ . *Phys. Rev. B* **94**, 155116. <https://link.aps.org/doi/10.1103/PhysRevB.94.155116> (15 Oct. 2016) (cit. on pp. 13, 17, 21, 27, 38).
44. Welinski, S. *et al.* Coherence Time Extension by Large-Scale Optical Spin Polarization in a Rare-Earth Doped Crystal. *Physical Review X* **10**, 031060. <https://doi.org/10.1103/PhysRevX.10.031060> (Sept. 2020) (cit. on pp. 13, 38, 39, 104).
45. Businger, M. *et al.* Optical Spin-Wave Storage in a Solid-State Hybridized Electron-Nuclear Spin Ensemble. *Physical Review Letters* **124**, 053606. <https://doi.org/10.1103/PhysRevLett.124.053606> (Feb. 2020) (cit. on pp. 13, 38, 39, 51, 67, 68, 104).
46. Cousins, A. Temperature and thermal stress scaling in finite-length end-pumped laser rods. *IEEE Journal of Quantum Electronics* **28**, 1057–1069 (1992) (cit. on p. 14).
47. Macfarlane, R. M. & Shelby, R. M. Measurement of nuclear and electronic Zeeman effects using optical hole-burning spectroscopy. *Opt. Lett.* **6**, 96–. <http://ol.osa.org/abstract.cfm?URI=ol-6-2-96> (Feb. 1981) (cit. on p. 19).
48. Hastings-Simon, S. R. *et al.* Zeeman-level lifetimes in  $\text{Er}^{3+}:\text{Y}_2\text{SiO}_5$ . *Phys. Rev. B* **78**, 085410–7. <http://link.aps.org/abstract/PRB/v78/e085410> (Aug. 2008) (cit. on pp. 19, 20, 26).
49. Chen, Y.-H., Fernandez-Gonzalvo, X., Horvath, S. P., Rakonjac, J. V. & Longdell, J. J. Hyperfine interactions of  $\text{Er}^{3+}$  ions in  $\text{Y}_2\text{SiO}_5$ : Electron paramagnetic resonance in a tunable microwave cavity. *Phys. Rev. B* **97**, 024419. <https://link.aps.org/doi/10.1103/PhysRevB.97.024419> (2 Jan. 2018) (cit. on p. 21).
50. Riesen, H., Hayward, B. F. & Szabo, A. Side-hole to anti-hole conversion in time-resolved spectral hole burning of ruby: Long-lived spectral holes due to ground state level population storage. *Journal of Luminescence* **127**, 655–664. ISSN: 0022-2313. <https://www.sciencedirect.com/science/article/pii/S0022231307001251> (2007) (cit. on p. 26).
51. Zhong, M. *et al.* Optically addressable nuclear spins in a solid with a six-hour coherence time. *Nature* **517**, 177–180. ISSN: 1476-4687. <https://doi.org/10.1038/nature14025> (2015) (cit. on pp. 30, 67, 71, 80).
52. Hahn, E. L. Spin Echoes. *Phys. Rev.* **80**, 580 (1950) (cit. on p. 33).
53. He, X.-F., Fisk, P. T. & Manson, N. B. Zeeman quantum beat in nuclear quadrupole resonance probed by Raman heterodyne spectroscopy. *Journal of Luminescence* **53**, 68–71. ISSN: 0022-2313. <https://www.sciencedirect.com/science/article/pii/002223139290108L> (1992) (cit. on p. 33).

54. Fraval, E., Sellars, M. J. & Longdell, J. J. Method of Extending Hyperfine Coherence Times in  $\text{Pr}^{3+}:\text{Y}_2\text{SiO}_5$ . *Phys. Rev. Lett.* **92**, 077601–4. <http://link.aps.org/abstract/PRL/v92/e077601> (Feb. 2004) (cit. on p. 33).
55. Fernandez-Gonzalvo, X., Horvath, S. P., Chen, Y.-H. & Longdell, J. J. Cavity-enhanced Raman heterodyne spectroscopy in  $\text{Er}^{3+}:\text{Y}_2\text{SiO}_5$  for microwave to optical signal conversion. *Phys. Rev. A* **100**, 033807. <https://link.aps.org/doi/10.1103/PhysRevA.100.033807> (3 Sept. 2019) (cit. on p. 33).
56. Horvath, S. P. *et al.* Extending Phenomenological Crystal-Field Methods to  $C_1$  Point-Group Symmetry: Characterization of the Optically Excited Hyperfine Structure of  $^{167}\text{Er}^{3+}:\text{Y}_2\text{SiO}_5$ . *Phys. Rev. Lett.* **123**, 057401. <https://link.aps.org/doi/10.1103/PhysRevLett.123.057401> (5 July 2019) (cit. on pp. 33, 39).
57. Car, B., Veissier, L., Louchet-Chauvet, A., Le Gouët, J.-L. & Chanelière, T. Selective Optical Addressing of Nuclear Spins through Superhyperfine Interaction in Rare-Earth Doped Solids. *Phys. Rev. Lett.* **120**, 197401. <https://link.aps.org/doi/10.1103/PhysRevLett.120.197401> (19 May 2018) (cit. on p. 36).
58. Lim, H.-J., Welinski, S., Ferrier, A., Goldner, P. & Morton, J. J. L. Coherent spin dynamics of ytterbium ions in yttrium orthosilicate. *Phys. Rev. B* **97**, 064409. <https://link.aps.org/doi/10.1103/PhysRevB.97.064409> (6 Feb. 2018) (cit. on pp. 37–39).
59. Rakonjac, J. V., Chen, Y.-H., Horvath, S. P. & Longdell, J. J. Long spin coherence times in the ground state and in an optically excited state of  $^{167}\text{Er}^{3+}:\text{Y}_2\text{SiO}_5$  at zero magnetic field. *Phys. Rev. B* **101**, 184430. <https://link.aps.org/doi/10.1103/PhysRevB.101.184430> (18 May 2020) (cit. on pp. 39, 104).
60. Zadrozny, J. M., Niklas, J., Poluektov, O. G. & Freedman, D. E. Millisecond Coherence Time in a Tunable Molecular Electronic Spin Qubit. *ACS Central Science* **1**. PMID: 27163013, 488–492. <https://doi.org/10.1021/acscentsci.5b00338> (2015) (cit. on p. 39).
61. Shiddiq, M. *et al.* Enhancing coherence in molecular spin qubits via atomic clock transitions. *Nature* **531**, 348–351. <https://doi.org/10.1038/nature16984> (7594 Mar. 2016) (cit. on p. 39).
62. Dolde, F. *et al.* Electric-field sensing using single diamond spins. *Nature Physics* **7**, 459–463. <https://doi.org/10.1038/nphys1969> (6 2011) (cit. on p. 39).
63. Jamonneau, P. *et al.* Competition between electric field and magnetic field noise in the decoherence of a single spin in diamond. *Phys. Rev. B* **93**, 024305. <https://link.aps.org/doi/10.1103/PhysRevB.93.024305> (2 Jan. 2016) (cit. on p. 39).

64. Probst, S. *et al.* Anisotropic Rare-Earth Spin Ensemble Strongly Coupled to a Superconducting Resonator. *Phys. Rev. Lett.* **110**, 157001–. <http://link.aps.org/doi/10.1103/PhysRevLett.110.157001> (Apr. 2013) (cit. on p. 39).
65. Bienfait, A. *et al.* Reaching the quantum limit of sensitivity in electron spin resonance. *Nature Nanotechnology* **11**, 253–257. <https://doi.org/10.1038/nnano.2015.282> (3 Mar. 2016) (cit. on p. 39).
66. Jobez, P. *et al.* Coherent Spin Control at the Quantum Level in an Ensemble-Based Optical Memory. *Physical Review Letters* **114**, 230502. <https://doi.org/10.1103/PhysRevLett.114.230502> (June 2015) (cit. on pp. 41, 54, 67, 71, 77–79, 87, 90).
67. Laplane, C., Jobez, P., Etesse, J., Gisin, N. & Afzelius, M. Multimode and Long-Lived Quantum Correlations Between Photons and Spins in a Crystal. *Physical Review Letters* **118**, 210501. <https://doi.org/10.1103/PhysRevLett.118.210501> (May 2017) (cit. on pp. 41, 79, 92, 94, 95, 100, 101).
68. Laplane, C. *Generation of non-classical correlations between spins and photons using rare-earth-ion doped crystals* eng. ID: unige:92034. PhD thesis (Dec. 2016). <https://nbn-resolving.org/urn:nbn:ch:unige-920345> (cit. on pp. 41, 53, 54, 58, 75, 79, 96).
69. Equall, R. W., Sun, Y., Cone, R. L. & Macfarlane, R. M. Ultraslow optical dephasing in  $\text{Eu}^{3+}:\text{Y}_2\text{SiO}_5$ . *Phys. Rev. Lett.* **72**, 2179. <http://link.aps.org/abstract/PRL/v72/p2179> (Apr. 1994) (cit. on pp. 41, 54, 61).
70. Könz, F. *et al.* Temperature and concentration dependence of optical dephasing, spectral-hole lifetime, and anisotropic absorption in  $\text{Eu}^{3+}:\text{Y}_2\text{SiO}_5$ . *Phys. Rev. B* **68**, 085109. <http://link.aps.org/abstract/PRB/v68/e085109> (Aug. 2003) (cit. on pp. 41, 42, 60–62, 87).
71. Arcangeli, A., Lovrić, M., Tumino, B., Ferrier, A. & Goldner, P. Spectroscopy and coherence lifetime extension of hyperfine transitions in  $^{151}\text{Eu}^{3+}:\text{Y}_2\text{SiO}_5$ . *Phys. Rev. B* **89**, 184305. <https://link.aps.org/doi/10.1103/PhysRevB.89.184305> (18 May 2014) (cit. on pp. 41, 69, 79).
72. MACFARLANE, R. & SHELBY, R. in *Spectroscopy of Solids Containing Rare Earth Ions* (eds Kaplyanskii, A. & Macfarlane, R.) 51–184 (Elsevier, 1987). <https://www.sciencedirect.com/science/article/pii/B9780444870513500092> (cit. on pp. 42, 63).
73. Cruzeiro, E. Z. *et al.* Characterization of the hyperfine interaction of the excited D05 state of  $\text{Eu}^{3+}:\text{Y}_2\text{SiO}_5$ . *Physical Review B* **97**, 094416. <https://doi.org/10.1103/PhysRevB.97.094416> (Mar. 2018) (cit. on p. 42).

74. Ma, Y. *et al.* A Raman heterodyne study of the hyperfine interaction of the optically-excited state 5D0 of Eu<sup>3+</sup>:Y<sub>2</sub>SiO<sub>5</sub>. *Journal of Luminescence* **202**, 32–37. ISSN: 0022-2313. <https://www.sciencedirect.com/science/article/pii/S0022231318301662> (2018) (cit. on p. 42).
75. Elliott, R. J. Theory of Nuclear Magnetic Resonance in Eu<sup>3+</sup>. **70**, 119–123. <https://doi.org/10.1088/0370-1301/70/1/317> (Jan. 1957) (cit. on p. 43).
76. Shelby, R. M. & Macfarlane, R. M. Measurement of the Anomalous Nuclear Magnetic Moment of Trivalent Europium. *Phys. Rev. Lett.* **47**, 1172–1175. <https://link.aps.org/doi/10.1103/PhysRevLett.47.1172> (16 Oct. 1981) (cit. on p. 43).
77. Timoney, N., Lauritzen, B., Usmani, I., Afzelius, M. & Gisin, N. Atomic frequency comb memory with spin-wave storage in 153 Eu<sup>3+</sup>:Y<sub>2</sub>SiO<sub>5</sub>. *Journal of Physics B: Atomic, Molecular and Optical Physics* **45**, 124001. <http://stacks.iop.org/0953-4075/45/i=12/a=124001> (2012) (cit. on p. 43).
78. Drever, R. W. P. *et al.* Laser phase and frequency stabilization using an optical resonator. *Applied Physics B* **31**. <https://doi.org/10.1007/BF00702605> (June 1983) (cit. on p. 44).
79. Black, E. D. An introduction to Pound–Drever–Hall laser frequency stabilization. *American Journal of Physics* **69**, 79–87 (2001) (cit. on p. 44).
80. Li, Y. *et al.* Pulsed ultrasound-modulated optical tomography using spectral-hole burning as a narrowband spectral filter. *Applied Physics Letters* **93**, 011111. eprint: <https://doi.org/10.1063/1.2952489>. <https://doi.org/10.1063/1.2952489> (2008) (cit. on p. 48).
81. Li, Y., Hemmer, P., Kim, C., Zhang, H. & Wang, L. V. Detection of ultrasound-modulated diffuse photons using spectral-hole burning. *Opt. Express* **16**, 14862–14874. <http://www.osapublishing.org/oe/abstract.cfm?URI=oe-16-19-14862> (Sept. 2008) (cit. on p. 48).
82. Beavan, S. E., Goldschmidt, E. A. & Sellars, M. J. Demonstration of a dynamic bandpass frequency filter in a rare-earth ion-doped crystal. *J. Opt. Soc. Am. B* **30**, 1173–1177. <http://www.osapublishing.org/josab/abstract.cfm?URI=josab-30-5-1173> (May 2013) (cit. on p. 48).
83. Kutluer, K., Mazzer, M. & de Riedmatten, H. Solid-State Source of Nonclassical Photon Pairs with Embedded Multimode Quantum Memory. *Phys. Rev. Lett.* **118**, 210502. <https://link.aps.org/doi/10.1103/PhysRevLett.118.210502> (21 May 2017) (cit. on pp. 48, 67, 92, 95).
84. De Riedmatten, H., Afzelius, M., Staudt, M. U., Simon, C. & Gisin, N. A solid-state light-matter interface at the single-photon level. *Nature* **456**, 773–777. <http://dx.doi.org/10.1038/nature07607> (Dec. 2008) (cit. on p. 51).

85. Bonarota, M., Ruggiero, J., Le Gouët, J.-L. & Chanelière, T. Efficiency optimization for atomic frequency comb storage. English. *Phys. Rev. A* **81**, 033803. <https://doi.org/10.1103/PhysRevA.81.033803> (Mar. 2010) (cit. on pp. 51, 52).
86. Akhmedzhanov, R. A. *et al.* Atomic frequency comb memory in an isotopically pure  $^{143}\text{Nd}:\text{Y}_7\text{LiF}_4$  crystal. **13**, 015202. <https://doi.org/10.1088/1612-2011/13/1/015202> (Nov. 2015) (cit. on p. 51).
87. Sinclair, N. *et al.* Spectral Multiplexing for Scalable Quantum Photonics using an Atomic Frequency Comb Quantum Memory and Feed-Forward Control. *Physical Review Letters* **113**, 053603 (July 2014) (cit. on p. 51).
88. Tiranov, A. *et al.* Temporal Multimode Storage of Entangled Photon Pairs. *Phys. Rev. Lett.* **117**, 240506. <https://link.aps.org/doi/10.1103/PhysRevLett.117.240506> (24 Dec. 2016) (cit. on p. 51).
89. Lago-Rivera, D., Grandi, S., Rakonjac, J. V., Seri, A. & de Riedmatten, H. Telecom-heralded entanglement between multimode solid-state quantum memories. *Nature* **594**, 37–40. ISSN: 1476-4687. <https://doi.org/10.1038/s41586-021-03481-8> (June 2021) (cit. on pp. 51, 90).
90. Afzelius, M. & Simon, C. Impedance-matched cavity quantum memory. *Phys. Rev. A* **82**, 022310. <https://doi.org/10.1103/PhysRevA.82.022310> (Aug. 2010) (cit. on p. 52).
91. Jobez, P. *et al.* Towards highly multimode optical quantum memory for quantum repeaters. *Phys. Rev. A* **93**, 032327. <https://link.aps.org/doi/10.1103/PhysRevA.93.032327> (3 Mar. 2016) (cit. on pp. 53–55).
92. Louchet-Chauvet, A., Ahlefeldt, R. & Chanelière, T. Piezospectroscopic measurement of high-frequency vibrations in a pulse-tube cryostat. *Review of Scientific Instruments* **90**, 034901. <https://doi.org/10.1063/1.5080086> (2019) (cit. on p. 55).
93. Yano, R., Mitsunaga, M. & Uesugi, N. Ultralong optical dephasing in  $\text{Eu}^{3+}:\text{Y}_2\text{SiO}_5$ . *Opt. Lett.* **16**, 1884–1886. <http://ol.osa.org/abstract.cfm?URI=ol-16-23-1884> (Dec. 1991) (cit. on p. 61).
94. Graf, F. R., Renn, A., Zumofen, G. & Wild, U. P. Photon-echo attenuation by dynamical processes in rare-earth-ion-doped crystals. *Phys. Rev. B* **58**, 5462–5478. <https://link.aps.org/doi/10.1103/PhysRevB.58.5462> (9 Sept. 1998) (cit. on p. 61).
95. Yano, R., Mitsunaga, M. & Uesugi, N. Stimulated-photon-echo spectroscopy. I. Spectral diffusion in  $\text{Eu}^{3+}:\text{YAlO}_3$ . *Phys. Rev. B* **45**, 12752. <http://link.aps.org/abstract/PRB/v45/p12752> (June 1992) (cit. on p. 63).

96. Yano, R., Mitsunaga, M. & Uesugi, N. Nonlinear laser spectroscopy of  $\text{Eu}^{3+}:\text{Y}_2\text{SiO}_5$  and its application to time-domain optical memory. *J. Opt. Soc. Am. B* **9**, 992–997. <http://josab.osa.org/abstract.cfm?URI=josab-9-6-992> (1992) (cit. on p. 63).
97. Simon, C. *et al.* Quantum Repeaters with Photon Pair Sources and Multimode Memories. *Phys. Rev. Lett.* **98**, 190503. <http://link.aps.org/abstract/PRL/v98/e190503> (May 2007) (cit. on p. 63).
98. Sabooni, M., Li, Q., Kröll S., S. & Rippe, L. Efficient Quantum Memory Using a Weakly Absorbing Sample. *Phys. Rev. Lett.* **110**, 133604. <http://link.aps.org/doi/10.1103/PhysRevLett.110.133604> (Mar. 2013) (cit. on p. 65).
99. Jobez, P. *et al.* Cavity-enhanced storage in an optical spin-wave memory. *New Journal of Physics* **16**, 083005. <https://doi.org/10.1088/1367-2630/16/8/083005> (Aug. 2014) (cit. on p. 65).
100. Holzäpfel, A. *et al.* Optical storage for 0.53 s in a solid-state atomic frequency comb memory using dynamical decoupling. *New Journal of Physics* **22**, 063009. <https://doi.org/10.1088/1367-2630/ab8aac> (June 2020) (cit. on pp. 67, 71, 79, 88, 104).
101. Heinze, G., Hubrich, C. & Halfmann, T. Stopped Light and Image Storage by Electromagnetically Induced Transparency up to the Regime of One Minute. *Phys. Rev. Lett.* **111**, 033601. <http://link.aps.org/doi/10.1103/PhysRevLett.111.033601> (3 July 2013) (cit. on p. 67).
102. Ma, Y., Ma, Y.-Z., Zhou, Z.-Q., Li, C.-F. & Guo, G.-C. One-hour coherent optical storage in an atomic frequency comb memory. *Nature Communications* **12**. <https://doi.org/10.1038/s41467-021-22706-y> (Apr. 2021) (cit. on pp. 67, 80).
103. Afzelius, M. *et al.* Demonstration of atomic frequency comb memory for light with spin-wave storage. *Phys. Rev. Lett.* **104**, 040503. <https://doi.org/10.1103/PhysRevLett.104.040503> (2010) (cit. on pp. 67, 72).
104. Ma, Y.-Z. *et al.* Elimination of noise in optically rephased photon echoes. *Nature Communications* **12**. <https://doi.org/10.1038/s41467-021-24679-4> (July 2021) (cit. on p. 67).
105. Tian, M., Chang, T., Merkel, K. D. & Randall, W. Reconfiguration of spectral absorption features using a frequency-chirped laser pulse. *Appl. Opt.* **50**, 6548–6554. <https://doi.org/10.1364/AO.50.006548> (Dec. 2011) (cit. on p. 68).
106. Allen, L. & Eberly, J. *Optical Resonance and Two-Level Atoms*, Wiley, New York 1975. (Cit. on p. 70).

107. Viola, L. & Lloyd, S. Dynamical suppression of decoherence in two-state quantum systems. *Phys. Rev. A* **58**, 2733–2744. <http://link.aps.org/doi/10.1103/PhysRevA.58.2733> (4 Oct. 1998) (cit. on p. 71).
108. De Lange, G., Wang, Z. H., Ristè, D., Dobrovitski, V. V. & Hanson, R. Universal Dynamical Decoupling of a Single Solid-State Spin from a Spin Bath. *Science* **330**, 60–63. <http://www.sciencemag.org/content/330/6000/60.abstract> (2010) (cit. on pp. 71, 83).
109. Medford, J. *et al.* Scaling of Dynamical Decoupling for Spin Qubits. *Phys. Rev. Lett.* **108**, 086802. <https://link.aps.org/doi/10.1103/PhysRevLett.108.086802> (8 Feb. 2012) (cit. on pp. 71, 83).
110. Cruzeiro, E. Z., Fröwis, F., Timoney, N. & Afzelius, M. Noise in optical quantum memories based on dynamical decoupling of spin states. *Journal of Modern Optics* **63**, 2101–2113. <https://doi.org/10.1080/09500340.2016.1204472> (2016) (cit. on p. 71).
111. Hu, S., Reimer, J. A. & Bell, A. T. Single-input double-tuned circuit for double resonance nuclear magnetic resonance experiments. *Review of Scientific Instruments* **69**, 477–478. <https://doi.org/10.1063/1.1148458> (1998) (cit. on pp. 75, 79).
112. Laplane, C. *et al.* Multiplexed on-demand storage of polarization qubits in a crystal. *New Journal of Physics* **18**, 013006. <https://doi.org/10.1088/1367-2630/18/1/013006> (Dec. 2015) (cit. on pp. 79, 90).
113. Alexander, A. L., Longdell, J. J. & Sellars, M. J. Measurement of the ground-state hyperfine coherence time of  $^{151}\text{Eu}^{3+}:\text{Y}_2\text{SiO}_5$ . *J. Opt. Soc. Am. B* **24**, 2479–2482. <http://josab.osa.org/abstract.cfm?URI=josab-24-9-2479> (Sept. 2007) (cit. on p. 79).
114. Mims, W. B. Phase Memory in Electron Spin Echoes, Lattice Relaxation Effects in  $\text{CaWO}_4:\text{Er, Ce, Mn}$ . *Phys. Rev.* **168**, 370–389. <https://link.aps.org/doi/10.1103/PhysRev.168.370> (2 Apr. 1968) (cit. on p. 82).
115. Klauder, J. R. & Anderson, P. W. Spectral Diffusion Decay in Spin Resonance Experiments. *Phys. Rev.* **125**, 912–932. <https://link.aps.org/doi/10.1103/PhysRev.125.912> (3 Feb. 1962) (cit. on p. 83).
116. Schmied, R. Quantum state tomography of a single qubit: comparison of methods. *Journal of Modern Optics* **63**, 1744–1758. <https://doi.org/10.1080/09500340.2016.1142018> (2016) (cit. on p. 89).
117. Specht, H. P. *et al.* A single-atom quantum memory. *Nature* **473**, 190–193. ISSN: 1476-4687. <https://doi.org/10.1038/nature09997> (May 2011) (cit. on p. 90).



118. Massar, S. & Popescu, S. Optimal Extraction of Information from Finite Quantum Ensembles. *Phys. Rev. Lett.* **74**, 1259–1263. <https://link.aps.org/doi/10.1103/PhysRevLett.74.1259> (8 Feb. 1995) (cit. on p. 90).
119. Matsukevich, D. N. *et al.* Entanglement of a Photon and a Collective Atomic Excitation. *Phys. Rev. Lett.* **95**, 040405–. <http://link.aps.org/abstract/PRL/v95/e040405> (July 2005) (cit. on p. 91).
120. De Riedmatten, H. *et al.* Direct Measurement of Decoherence for Entanglement between a Photon and Stored Atomic Excitation. *Phys. Rev. Lett.* **97**, 113603–4. <http://link.aps.org/abstract/PRL/v97/e113603> (Sept. 2006) (cit. on p. 91).
121. Chen, S. *et al.* Demonstration of a Stable Atom-Photon Entanglement Source for Quantum Repeaters. *Phys. Rev. Lett.* **99**, 180505. <https://link.aps.org/doi/10.1103/PhysRevLett.99.180505> (18 Nov. 2007) (cit. on p. 91).
122. Pu, Y.-F. *et al.* Experimental realization of a multiplexed quantum memory with 225 individually accessible memory cells. *Nature Communications* **8**, 15359. <https://doi.org/10.1038/ncomms15359> (May 2017) (cit. on p. 91).
123. Chrapkiewicz, R., Dąbrowski, M. & Wasilewski, W. High-Capacity Angularly Multiplexed Holographic Memory Operating at the Single-Photon Level. *Phys. Rev. Lett.* **118**, 063603. <https://link.aps.org/doi/10.1103/PhysRevLett.118.063603> (6 Feb. 2017) (cit. on p. 91).
124. Inoue, R. *et al.* Entanglement of orbital angular momentum states between an ensemble of cold atoms and a photon. *Phys. Rev. A* **74**, 053809–5. <http://link.aps.org/abstract/PRA/v74/e053809> (Nov. 2006) (cit. on p. 91).
125. Farrera, P., Heinze, G. & de Riedmatten, H. Entanglement between a Photonic Time-Bin Qubit and a Collective Atomic Spin Excitation. *Phys. Rev. Lett.* **120**, 100501. <https://link.aps.org/doi/10.1103/PhysRevLett.120.100501> (10 Mar. 2018) (cit. on p. 91).
126. Dideriksen, K. B., Schmiege, R., Zugenmaier, M. & Polzik, E. S. Room-temperature single-photon source with near-millisecond built-in memory. *Nature Communications* **12**, 3699. <https://doi.org/10.1038/s41467-021-24033-8> (2021) (cit. on p. 91).
127. Pu, Y.-F. *et al.* Experimental demonstration of memory-enhanced scaling for entanglement connection of quantum repeater segments. *Nature Photonics* **15**, 374–378. <https://doi.org/10.1038/s41566-021-00764-4> (May 2021) (cit. on p. 91).

128. Kasperczyk, M., Jorio, A., Neu, E., Maletinsky, P. & Novotny, L. Stokes-anti-Stokes correlations in diamond. *Opt. Lett.* **40**, 2393–2396. <http://www.osapublishing.org/ol/abstract.cfm?URI=ol-40-10-2393> (May 2015) (cit. on p. 92).
129. Anderson, M. D. *et al.* Two-Color Pump-Probe Measurement of Photonic Quantum Correlations Mediated by a Single Phonon. *Phys. Rev. Lett.* **120**, 233601. <https://link.aps.org/doi/10.1103/PhysRevLett.120.233601> (23 June 2018) (cit. on p. 92).
130. Velez, S. T. *et al.* Preparation and Decay of a Single Quantum of Vibration at Ambient Conditions. *Phys. Rev. X* **9**, 041007. <https://link.aps.org/doi/10.1103/PhysRevX.9.041007> (4 Oct. 2019) (cit. on p. 92).
131. Saraiva, A. *et al.* Photonic Counterparts of Cooper Pairs. *Phys. Rev. Lett.* **119**, 193603. <https://link.aps.org/doi/10.1103/PhysRevLett.119.193603> (19 Nov. 2017) (cit. on p. 92).
132. Riedinger, R. *et al.* Remote quantum entanglement between two micromechanical oscillators. *Nature* **556**, 473–477. ISSN: 1476-4687. <https://doi.org/10.1038/s41586-018-0036-z> (Apr. 2018) (cit. on p. 92).
133. Kasperczyk, M. *et al.* Temporal Quantum Correlations in Inelastic Light Scattering from Water. *Phys. Rev. Lett.* **117**, 243603. <https://link.aps.org/doi/10.1103/PhysRevLett.117.243603> (24 Dec. 2016) (cit. on p. 92).
134. Kutluer, K. *et al.* Time Entanglement between a Photon and a Spin Wave in a Multimode Solid-State Quantum Memory. *Physical Review Letters* **123**, 030501. <https://doi.org/10.1103/PhysRevLett.123.030501> (July 2019) (cit. on p. 92).
135. Sekatski, P., Sangouard, N., Gisin, N., de Riedmatten, H. & Afzelius, M. Photon-pair source with controllable delay based on shaped inhomogeneous broadening of rare-earth-metal-doped solids. *Phys. Rev. A* **83**, 053840. <http://link.aps.org/doi/10.1103/PhysRevA.83.053840> (5 May 2011) (cit. on p. 92).
136. Etesse, J., Laplane, C., Jobez, P., Gisin, N. & Afzelius, M. *Generating non-classical correlations between photons and spins in a crystal* in *Advances in Photonics of Quantum Computing, Memory, and Communication XI* (eds Hasan, Z. U., Hemmer, P. R., Craig, A. E. & Migdall, A. L.) **10547** (SPIE, 2018), 80–88. <https://doi.org/10.1117/12.2300061> (cit. on p. 94, 97).
137. Clauser, J. F. Experimental distinction between the quantum and classical field-theoretic predictions for the photoelectric effect. *Phys. Rev. D* **9**, 853–. <http://link.aps.org/abstract/PRD/v9/p853> (Feb. 1974) (cit. on p. 95).

138. Yuan, Z.-S. *et al.* Experimental demonstration of a BDCZ quantum repeater node. *Nature* **454**, 1098–1101 (Aug. 2008) (cit. on p. 95).
139. Strassmann, P. C. *Solid-state optical quantum memory: from large entanglement to telecom wavelengths* eng. ID: unige:123606. PhD thesis (Mar. 2019). <https://nbn-resolving.org/urn:nbn:ch:unige-1236060> (cit. on pp. 101, 105).
140. Mejia, T. S. *Difference Frequency Generation and Spectral Filtering for Quantum Frequency Conversion* (2021) (cit. on pp. 101, 105).
141. Zhou, X., Liu, H., He, Z., Chen, B. & Wu, J. Investigation of the Electronic Structure and Optical, EPR, and ODMR Spectroscopic Properties for 171Yb<sup>3+</sup>-Doped Y2SiO5 Crystal: A Combined Theoretical Approach. *Inorganic Chemistry* **59**, 13144–13152. ISSN: 0020-1669. <https://doi.org/10.1021/acs.inorgchem.0c01430> (Sept. 2020) (cit. on p. 103).
142. Kukharchyk, N. *et al.* Electromagnetically induced transparency in a mono-isotopic 167Er:7LiYF4 crystal below 1 Kelvin: microwave photonics approach. *Opt. Express* **28**, 29166–29177. <http://www.osapublishing.org/oe/abstract.cfm?URI=oe-28-20-29166> (Sept. 2020) (cit. on p. 104).
143. Davidson, J. H. *et al.* Measurement of the thulium ion spin Hamiltonian in an yttrium gallium garnet host crystal. *Phys. Rev. B* **104**, 134103. <https://link.aps.org/doi/10.1103/PhysRevB.104.134103> (13 Oct. 2021) (cit. on p. 104).
144. Sukhanov, A. A. *et al.* Temperature Dependencies of the Spin Relaxation Times for the Isotopically Pure Chromium Impurity 53Cr<sup>3+</sup> in the Yttrium Orthosilicate Single Crystal Y228SiO5. *Applied Magnetic Resonance* **52**, 1175–1185. ISSN: 1613-7507. <https://doi.org/10.1007/s00723-021-01366-7> (Sept. 2021) (cit. on p. 104).
145. Berkman, I. R. *et al.* *Sub-megahertz homogeneous linewidth for Er in Si via in situ single photon detection* 2021. arXiv: 2108.07090 [quant-ph] (cit. on p. 104).
146. Hu, G. *et al.* *Optical and Zeeman spectroscopy of individual Er ion pairs in silicon* 2021. arXiv: 2108.07442 [quant-ph] (cit. on p. 104).
147. LeDantec, M. *et al.* *Twenty-three millisecond electron spin coherence of erbium ions in a natural-abundance crystal* 2021. arXiv: 2106.14974 [quant-ph] (cit. on p. 104).
148. Phenicie, C. M. *et al.* Narrow Optical Line Widths in Erbium Implanted in TiO2. *Nano Letters* **19**, 8928–8933. ISSN: 1530-6984. <https://doi.org/10.1021/acs.nanolett.9b03831> (Dec. 2019) (cit. on p. 104).

149. Stevenson, P. *et al.* *Erbium-Implanted Materials for Quantum Communication Applications* 2021. arXiv: 2110.04876 [cond-mat.mtrl-sci] (cit. on p. 104).
150. Kumar, K. S. *et al.* Optical spin-state polarization in a binuclear europium complex towards molecule-based coherent light-spin interfaces. *Nature Communications* **12**, 2152. ISSN: 2041-1723. <https://doi.org/10.1038/s41467-021-22383-x> (Apr. 2021) (cit. on p. 104).
151. Casabone, B. *et al.* Dynamic control of Purcell enhanced emission of erbium ions in nanoparticles. *Nature Communications* **12**, 3570. ISSN: 2041-1723. <https://doi.org/10.1038/s41467-021-23632-9> (June 2021) (cit. on p. 104).
152. Lutz, T. *et al.* Modification of relaxation dynamics in  $\text{Tb}^{3+} : \text{Y}_3\text{Al}_5\text{O}_{12}$  nanopowders. *Phys. Rev. B* **98**, 054308. <https://link.aps.org/doi/10.1103/PhysRevB.98.054308> (5 Aug. 2018) (cit. on p. 104).
153. Serrano, D. *et al.* Coherent optical and spin spectroscopy of nanoscale  $\text{Pr}^{3+} : \text{Y}_2\text{O}_3$ . *Phys. Rev. B* **100**, 144304. <https://link.aps.org/doi/10.1103/PhysRevB.100.144304> (14 Oct. 2019) (cit. on p. 104).
154. Bartholomew, J. G. *et al.* On-chip coherent microwave-to-optical transduction mediated by ytterbium in YVO<sub>4</sub>. *Nature Communications* **11**, 3266. ISSN: 2041-1723. <https://doi.org/10.1038/s41467-020-16996-x> (June 2020) (cit. on p. 104).
155. Barnett, P. S. & Longdell, J. J. Theory of microwave-optical conversion using rare-earth-ion dopants. *Phys. Rev. A* **102**, 063718. <https://link.aps.org/doi/10.1103/PhysRevA.102.063718> (6 Dec. 2020) (cit. on p. 104).
156. Guo, A.-L., Tu, T., Guo, G.-C. & Li, C.-F. Efficient and robust collective excitation transfer in a multimode quantum memory using modulated adiabatic pulses. *Phys. Rev. A* **104**, 022404. <https://link.aps.org/doi/10.1103/PhysRevA.104.022404> (2 Aug. 2021) (cit. on p. 104).
157. Askarani, M. F. *et al.* Persistent atomic frequency comb based on Zeeman sub-levels of an erbium-doped crystal waveguide. *J. Opt. Soc. Am. B* **37**, 352–358. <http://www.osapublishing.org/josab/abstract.cfm?URI=josab-37-2-352> (Feb. 2020) (cit. on p. 105).
158. Sinclair, N. *et al.* Optical coherence and energy-level properties of a  $\text{Tm}^{3+}$ -doped  $\text{LiNbO}_3$  waveguide at subkelvin temperatures. *Phys. Rev. B* **103**, 134105. <https://link.aps.org/doi/10.1103/PhysRevB.103.134105> (13 Apr. 2021) (cit. on p. 105).
159. Seri, A. *et al.* Laser-written integrated platform for quantum storage of heralded single photons. *Optica* **5**, 934–941. <http://www.osapublishing.org/optica/abstract.cfm?URI=optica-5-8-934> (Aug. 2018) (cit. on p. 105).

160. Chen, S., Raha, M., Phenicie, C. M., Ourari, S. & Thompson, J. D. Parallel single-shot measurement and coherent control of solid-state spins below the diffraction limit. *Science* **370**, 592–595. <https://www.science.org/doi/abs/10.1126/science.abc7821> (2020) (cit. on p. 105).
161. Kindem, J. M. *et al.* Control and single-shot readout of an ion embedded in a nanophotonic cavity. *Nature* **580**, 201–204. ISSN: 1476-4687. <https://doi.org/10.1038/s41586-020-2160-9> (Apr. 2020) (cit. on p. 105).
162. Gündoğan, M. *et al.* Proposal for space-borne quantum memories for global quantum networking. *npj Quantum Information* **7**, 128. ISSN: 2056-6387. <https://doi.org/10.1038/s41534-021-00460-9> (Aug. 2021) (cit. on p. 105).
163. Ahlefeldt, R. L., Pearce, M. J., Hush, M. R. & Sellars, M. J. Quantum processing with ensembles of rare-earth ions in a stoichiometric crystal. *Phys. Rev. A* **101**, 012309. <https://link.aps.org/doi/10.1103/PhysRevA.101.012309> (1 Jan. 2020) (cit. on p. 105).
164. Grimm, M., Beckert, A., Aepli, G. & Müller, M. Universal Quantum Computing Using Electronuclear Wavefunctions of Rare-Earth Ions. *PRX Quantum* **2**, 010312. <https://link.aps.org/doi/10.1103/PRXQuantum.2.010312> (1 Jan. 2021) (cit. on p. 105).
165. Gouzien, É. & Sangouard, N. Factoring 2048-bit RSA Integers in 177 Days with 13 436 Qubits and a Multimode Memory. *Phys. Rev. Lett.* **127**, 140503. <https://link.aps.org/doi/10.1103/PhysRevLett.127.140503> (14 Sept. 2021) (cit. on p. 105).